

Diss. ETH No. 17215

Probing Coherence During Bose-Einstein Condensation

A dissertation submitted to the
SWISS FEDERAL INSTITUTE OF TECHNOLOGY
ZURICH

for the degree of
Doctor of Natural Sciences

presented by
STEPHAN RITTER
Dipl.-Phys., University of Hamburg, Germany
born 17.01.1975
citizen of Germany

examiners:
Prof. Dr. Tilman Esslinger
Prof. Dr. Claus Zimmermann

2007

Kurzfassung

In dieser Arbeit werden Experimente zu den Kohärenzeigenschaften von Bose-Einstein Kondensaten und Atomlasern vorgestellt, die durch die Entwicklung einer neuartigen Apparatur ermöglicht wurden. In dieser wird ein Bose-Einstein Kondensat (BEC) mit einem optischen Resonator extrem hoher Güte kombiniert. Einzelne aus einer magnetisch gefangenen Wolke ausgekoppelte Atome können mit sehr hoher Empfindlichkeit nachgewiesen werden, indem der Resonator als Einzelatomdetektor verwendet wird. Dies ermöglichte zum ersten Mal den zeitaufgelösten Nachweis einzelner Atome aus einem quantenentarteten Gas.

Langreichweitige Ordnung in den Nichtdiagonalelementen der Dichtematrix ist eine definierende Eigenschaft eines Bose-Einstein Kondensats und ist äquivalent zu langreichweitiger Phasenkohärenz. Sie entsteht in einem komplexen Prozess mit spontaner Symmetriebrechung. Wir konnten die Ausbildung dieser langreichweitigen Phasenkohärenz beobachten, während eine ultrakalte Wolke aus Rubidiumatomen den Phasenübergang zu einem Bose-Einstein Kondensat überschritt. Zwei überlappende Atomlaserstrahlen aus unterschiedlichen Bereichen des Kondensats fielen in den Resonator. Der Kontrast des resultierenden Materiewellen-Interferenzmusters ist durch die Kohärenz zwischen den beiden untersuchten Regionen bestimmt. Er kann aus der Modulation des Atomflusses gewonnen werden, der mit Einzelatomauflösung gemessen wird, wohingegen der Mittelwert des Flusses Rückschlüsse auf die Dichte der Wolke ermöglicht.

Mittels Schockkühlung wurde eine Atomwolke in einem Nichtgleichgewichtszustand kurz oberhalb des Phasenübergangs präpariert. Während der nachfolgenden Thermalisierung kehrte das System in ein Gleichgewicht mit einem kleinen Kondensatanteil zurück. Mittels unserer minimalinvasiven Messmethode konnten die Phasenkohärenz und die Dichte der Probe während des Phasenübergangs in Echtzeit beobachtet werden. Das Wachstum der Kohärenz begann später, verlief schneller und endete früher als der Anstieg der Dichte. Der kohärente Bereich wuchs mit einem Fünftel der Schallgeschwindigkeit.

Die vollständige Zählstatistik eines Atomstrahls wurde mithilfe von zeitaufgelöstem Einzelatomnachweis aufgenommen. Unter Verwendung eines Korrelationsverfah-

rens, das auf Hanbury Brown und Twiss zurückgeht, wurde eine konstante Korrelationsfunktion zweiter Ordnung $g^{(2)}(\tau) = 1.00 \pm 0.01$ gemessen. Hiermit konnten wir die Kohärenz zweiter Ordnung des Atomlasers und die Abwesenheit überschüssiger Intensitätsfluktuationen nachweisen, wie sie in einem pseudothermischen Strahl beobachtet wurden. Die Auswertung der Zeitabstände zwischen den einzelnen Atomen des Strahls bestätigte dieses Ergebnis. Durch den Nachweis, dass der Atomlaser eine Poissonsche Teilchenstatistik besitzt, konnte auch seine Kohärenz höherer Ordnung gezeigt werden.

Der Welle-Teilchen-Dualismus für Materie wurde in Analogie zum Doppelspalt-Experiment mit Photonen untersucht. Zwei interferierende Atomlaser wurden im Einzelatomdetektor in einen Zustand mit keinem oder einem Atom in der Resonatormode projiziert. Der Fluss von Atomen zwischen Quelle und Detektor wurde so niedrig gehalten, dass sich im Mittel nur ein einziges Atom im Interferometer befand. Nach vielen Durchläufen bildete sich ein Interferenzmuster mit hohem Kontrast. Dieser Versuch zeigt, dass die Interferenz auch für Atome ein Einteilcheneffekt ist.

Die konzeptionell neuartige Apparatur, welche die oben dargestellten Experimente ermöglicht hat, wird im Detail beschrieben und ihre Eigenschaften werden charakterisiert. Der optische Hochfinesse-Resonator befindet sich knapp unterhalb der Magnetfalle, in der das Kondensat gehalten wird. Er ist innerhalb der Vakuumapparatur auf deren austauschbaren Bodenflansch montiert, welcher viel Platz für Proben und Analysemethoden bietet. Atomlaser mit einem über sechs Größenordnungen regulierbaren Fluss können aus dem Kondensat ausgekoppelt werden. Einzelne Atome aus diesem Strahl werden mit einer Detektionseffizienz von 25 % mithilfe des Resonators nachgewiesen. Die Kopplung zwischen einem einzelnen Atom und dem Lichtfeld ist größer als alle dissipativen Prozesse. Damit ist der Resonator im Regime starker Kopplung und die Apparatur ideal geeignet für zukünftige Untersuchungen der kohärenten Wechselwirkung zwischen Materiewellen und dem quantisierten Lichtfeld des Resonators.

Abstract

This thesis features fundamental experiments on the coherence properties of Bose-Einstein condensates (BEC) and atom lasers, made possible by a newly developed apparatus combining a Bose-Einstein condensate with an ultrahigh finesse optical cavity. Using the cavity as a single atom detector, atoms extracted from a trapped cloud are detected with unprecedented sensitivity, and the first time-resolved counting of single atoms from a quantum degenerate source was demonstrated.

Off-diagonal long-range order is a defining property of a BEC and equivalent to long-range phase coherence. Its formation is a complex process accompanied by spontaneous symmetry breaking. We witnessed this formation in an ultracold cloud of ^{87}Rb atoms crossing the phase transition of BEC. Two overlapping atomic beams originating from different positions inside the condensate propagated downwards into the cavity. They showed a matter wave interference pattern with a visibility determined by the coherence of the probed regions. The modulation of the flux of atoms, recorded with single-atom resolution, yields the visibility, whereas its mean value gives information about the density of the sample.

By shock cooling, a cloud of atoms was prepared in a highly nonequilibrium state slightly above the phase transition. While the ensemble subsequently relaxed, it crossed the phase transition into an equilibrium with a small condensate fraction. Employing our minimally invasive measurement method, the growth of both the first-order coherence and the density of the sample was tracked in real time while the system crossed the phase transition. The growth of the coherence was found to start later, proceed faster and finish earlier than the increase in density. The coherent region increased at one fifth of the speed of sound.

Employing time-resolved single atom counting with the cavity detector, the full counting statistics of an atom laser beam was recorded. In a Hanbury Brown and Twiss type experiment, the second-order correlation function was found to be constant $g^{(2)}(\tau) = 1.00 \pm 0.01$, proving the atom laser's second-order coherence and the absence of excess intensity fluctuations that were observed in a pseudothermal beam. An analysis of the time interval distributions of atoms in the beam confirmed these findings. The

higher-order coherence of the atom laser was also shown, manifested in a Poissonian atom number distribution.

Matter wave-particle duality was studied in an atomic counterpart of Young's double slit experiment. Two interfering atom laser beams propagating through the detector were projected into a state with zero or one atom inside the cavity mode. The flux of atoms from the source to the detector was kept so low that on average only a single atom was in the interferometer. After many repetitions of the experiment, a high-contrast interference pattern was observed, illustrating the single-particle character of such an interference effect with atoms.

The conceptually novel apparatus facilitating the research outlined above is described in detail and its performance is characterized. The ultrahigh finesse optical cavity is located slightly below the magnetic trap confining the BEC and resides on an interchangeable "science platform" providing large spatial access for samples and probes. Atom lasers with a flux adjustable over six orders of magnitude can be output coupled from the condensate. Single atoms from this beam are detected with an efficiency of about 25% using the cavity which operates in the strong coupling regime of cavity quantum electrodynamics. Therefore the coupling between the cavity field and a single atom is much stronger than all dissipative processes. This makes the apparatus ideally suited for future studies of coherent interactions between a matter wave and the quantized light field of the cavity.

Contents

1	Introduction	1
2	Theoretical framework	7
2.1	Bose-Einstein condensation	7
2.1.1	The ideal Bose gas	8
2.1.2	The weakly interacting Bose gas	9
2.1.3	Theory of coherence and phase transitions	10
2.1.4	Quasicondensates	13
2.2	Atom lasers	15
2.2.1	The output coupling process	16
2.2.2	Radio-frequency output coupling	17
2.2.3	Two-frequency output coupling	22
2.3	Cavity QED	24
2.3.1	Optical Resonators	24
2.3.2	The Jaynes-Cummings model	28
2.3.3	The dissipative system	30
2.3.4	Single atom detection	34
3	A hybrid apparatus for BEC and cavity QED	41
3.1	Vacuum system	43
3.1.1	Main chamber	43
3.1.2	MOT chamber	44
3.1.3	Installation	46

3.2	Magnetic field configuration	46
3.2.1	Magnetic transport	47
3.2.2	QUIC trap	50
3.2.3	Magnetic shielding	52
3.2.4	Auxiliary coils	52
3.3	Science platform and cavity setup	53
3.3.1	Cavity design	53
3.3.2	Vibration isolation system	55
3.3.3	The science platform layout	55
3.4	Performance of the apparatus	56
3.4.1	BEC	58
3.4.2	Atom laser	61
3.4.3	Cavity lock	63
3.4.4	Cavity parameters	65
3.5	Single atom detection	70
3.5.1	Analysis	70
3.5.2	Identification of single atom transits	72
3.5.3	Characteristics of single atom events	73
3.5.4	Linearity	78
3.5.5	Detection efficiency	79
3.5.6	Accuracy of arrival time determination	83
3.6	Atom laser beam profile	85
3.6.1	Guiding the atom laser	87
3.7	Investigation of cold atomic gases	88
3.7.1	Thermal clouds	88
3.7.2	Quantum degenerate gases	89
3.7.3	Phase Transition	90
3.8	Precision measurement of dipole oscillations	92
3.8.1	Theoretical model	93
3.8.2	Example measurements	95

3.8.3	Potential of the method	96
3.8.4	Oscillations along the horizontal directions	97
3.8.5	Conclusions	98
4	Observing the formation of long-range order	99
4.1	Introduction	99
4.2	Background	100
4.2.1	The theory of condensate formation	100
4.2.2	Earlier experimental work	105
4.3	Methods	108
4.3.1	Setup	109
4.3.2	Filtering of atoms by the detector	110
4.3.3	Interference and first-order correlation function	113
4.3.4	Data analysis	116
4.3.5	Detector characteristics	117
4.3.6	Detection uniformity	119
4.4	Results	122
4.5	Summary	129
5	Correlations and counting statistics of an atom laser	131
5.1	Introduction	131
5.2	Methods	133
5.3	Results	136
5.3.1	Second-order correlation function and counting statistics	136
5.3.2	Time interval distributions of atoms	139
6	Cavity QED detection of interfering matter waves	143
6.1	Introduction	143
6.2	Quantum measurement in a cavity QED system	145
6.3	Single atom interference	148
6.4	Summary	150

7	Conclusions and outlook	151
A	Appendix	157
A.1	Physical constants and ^{87}Rb data	157
	Bibliography	159
	Publications related to this thesis	181
	Acknowledgements	183
	Curriculum Vitae	185

1 Introduction

More than eighty years ago, Planck, Einstein and Bohr used the quantization of energy to explain physical phenomena which at their time were not understood. Since then, this idea has developed into a sound theoretical framework: quantum mechanics. At about the same time, the idea of matter waves was introduced by de Broglie. Since then, innumerable experiments have proven the success of this theory. Even so, people are still puzzled by the consequences this theory brings about. We seem to lack some of the intuition that we have for other physical effects when it comes to the domain of very small scales. Effects on these small scales, where quantum mechanics is prevailing, are just not a part of our everyday life and experience. This explains the astonishment and enthusiasm created when quantum mechanical effects manifest themselves on a macroscopic scale. A prime example of such a system is a macroscopic matter wave. The first realization of Bose-Einstein condensation in dilute atomic gases [1, 2, 3] was a milestone in this respect. It sparked a whole new area of research and for many physicists today the observation of matter wave interference with a charge-coupled device (CCD) camera is a standard procedure.

An appealingly simple definition of a Bose-Einstein condensate (BEC) is that a macroscopic number of atoms (of the order of the total number of atoms) occupies the same quantum state of the system, usually its ground state. However, a direct verification of this criterion is rather difficult. There are other definitions of Bose-Einstein condensation suggesting more obvious experimental strategies to test a BEC. A criterion first introduced by Penrose and Onsager [4] requires off-diagonal long-range order (ODLRO) [5]. If a system shows ODLRO, the phase at one end of the system is correlated to the phase at the other end. Naturally, the existence of phase coherence in the limit of infinitely large distances can not be met by particles confined to a limited region in space. However, a non-zero first-order correlation function at distances much larger than the thermal de Broglie wavelength is a unique property of a quantum degenerate gas. The long-range order is precluded by a change of the decay of the correlation function from exponential to algebraic in the critical regime near the phase transition and can not be found in thermal atoms [6].

Phase transitions are of great interest to researchers in many, very different areas of physics, amongst other things because they show universality. At a phase transition, the properties of a system fundamentally change, evoked by only small changes in the external conditions controlling it. For instance, a slight decrease in temperature triggers the phase transition of a weakly interacting gas to a Bose-Einstein condensate. Experimental research into this specific transition seems particularly worthwhile, since the two-body interactions between the atoms are well known and the gas is free of impurities. More than sixty research groups world-wide do research on Bose-Einstein condensates and employ their unique properties. However, the intricate process of condensate formation itself is still not fully understood.

Substantial theoretical effort has been made to explain and model the stages that lead to the final Bose-Einstein condensate. In many studies, the process of condensate formation is divided into different stages [7]. During the first, the kinetic stage, collisions between the atoms induce a restructuring of the population of different energy states which leads to an increased population in low-energetic states. The quantum kinetic theory developed by Gardiner *et al.* [8] models the time-dependent population of the condensate state and hence the growth of the condensate fraction. A different approach is to numerically solve the quantum Boltzmann equation [9, 10, 11, 12]. A second, so called coherent stage plays a significant role only in the regime of very large densities or scattering lengths. It is characterized by the existence of quasicondensates, patched regions of locally constant phase. Quasicondensates are an intermediate stage of the condensation process. The relaxation of nonequilibrium phase fluctuations and the annihilation of vortices finally lead to the formation of off-diagonal long-range order [7].

Despite all this theoretical interest, condensate formation is experimentally largely unexplored. Why have so few experiments focused on gaining a deeper understanding of the condensation process? This becomes understandable when considering the experimental challenges that have to be tackled. First, the system has to be brought into a nonequilibrium situation so that during the following relaxation process it crosses the phase transition. Second, a method is needed for the time-resolved measurement either of the first-order correlation function or the coherence length of the cloud, preferably in real time and with minimal disturbance of the condensation process.

The growth of the condensate fraction [13, 14] and the change in momentum spread [15, 16] have been subject of earlier studies. During the course of this thesis, the first-order correlation function and with it the formation of long-range order were observed in real-time for the first time. The growth of the density is closely linked to the increasing population of low-energetic states of the system, whereas the occurrence of long-range phase coherence is a consequence of the extinction of density fluctuations and the formation of a uniform phase. Since the two processes are closely linked but neither the same nor necessarily synchronous, a simultaneous study of their relative progression is

particularly revealing. Off-diagonal long-range order can be found in other superfluid systems than gaseous Bose-Einstein condensates or in superconductors as well. However, a dilute degenerate Bose gas is ideally suited for experimental investigations of the formation of ODLRO because of its rather long relaxation times and the weak coupling to the environment.

In our experiment we achieved the simultaneous observation of the growth of phase coherence and density during Bose-Einstein condensation using a novel measurement setup. The results are presented in this thesis. Starting with an atomic cloud slightly above the transition temperature to BEC, we created a strongly nonequilibrium situation by removing the high energy tail of the Bose distribution. During the following relaxation process, we constantly recorded information on the first-order correlation function and the density of the atom cloud until equilibrium with a small condensate fraction was reached. The speed of the growth of coherent regions was determined as well as the times for the growth processes of coherence and density. Because the coherence was probed up to half the size of the final condensate, the formation of long-range order was directly observed.

The study of the coherence between two regions of an atom cloud was facilitated by a special matter wave interference technique: Two overlapping atomic beams are output coupled from different positions in an atom cloud. The visibility of the resulting interference pattern is proportional to the degree of phase coherence between the two regions in the condensate. To determine the visibility of the interference pattern, an accurate detection of the time-dependent atom flux is necessary. The ultrahigh finesse optical cavity which is an integral part of the setup presented here, is ideally suited for this job. In the experiment, its single-atom resolution allowed very weak output coupling with minimal influence on the condensation process. We first used this technique to realize a matter wave analogue of Young's double slit experiment. In this text book experiment we observed the build-up of a matter wave interference pattern from single atom detection events. The detection of single atoms from two interfering matter waves is a prime example of wave-particle duality. Inside the cavity the coupling between a single atom and the quantized light field is much larger than the two dissipation processes, namely decay of atomic excitation and decay of the intracavity field. This facilitates the detection of single atoms via a significant drop in the transmission of a probe laser resonant with the empty cavity. This measurement process projects the extended matter wave into a state with zero or one atom inside the cavity mode. We theoretically studied this localization process and the timescales involved.

The first evidence of Bose-Einstein condensation was the anisotropic expansion of the condensate when released from an anisotropic trap. This effect, when considering an ideal gas, is a direct consequence of the uncertainty principle and a very clear example of a quantum effect on a macroscopic length scale. However, the mutual interactions

between the atoms also lead to the anisotropic expansion of a dense classical gas in the hydrodynamic regime [17]. The observation of interference between two Bose-Einstein condensates made the wave nature of matter visible, but was likewise not sufficient to prove that the atom cloud was a true condensate, since matter wave interference can also be observed with ultracold thermal atoms [18]. So which other properties distinguish a BEC from a thermal cloud?

Generally, bosons have the tendency to bunch together. This means that the probability to find two particles at a certain distance smaller than the coherence length is higher than to find them at any other, larger distance. This was demonstrated in a groundbreaking series of experiments by Hanbury Brown and Twiss [19, 20, 21] when they evidenced the correlations between photons in two beams of light. These correlations can be envisioned as a direct consequence of the Bose-Einstein distribution. In a different description of the same physics they are due to large intensity fluctuations which themselves are a consequence of the interference of many independent elementary waves. A coherent source of bosons—atoms as well as photons—behaves differently. It obeys Poissonian statistics and therefore shows reduced intensity fluctuations that vanish in the limit of infinitely large intensities. In addition, there are no correlations between the particles. Therefore a doubtless distinction between a Bose-Einstein condensate and a thermal cloud of atoms is possible by probing the intensity correlations between the atoms.

The same properties mark the distinction between an atom laser and a thermal beam of atoms. An atom laser possesses all the distinct properties of an optical laser: it is highly directed, bright, monochromatic and obeys Poisson statistics and therefore shows minimum intensity fluctuations. While the first three properties can also be achieved for a thermal beam by filtering spatially and in the frequency domain, the counting statistics of the beam ultimately reveal its true character. In an experiment accomplished in the course of this thesis, we showed that an atomic beam output coupled from a Bose-Einstein condensate is indeed the matter wave analogue of an optical laser: its two-particle correlation function is constant unity, proving the second-order coherence of an atom laser. We also observed the absence of excess intensity fluctuations as manifested in a Poissonian counting statistics. At the same time, the absence of spatial correlations in an expanding BEC of metastable bosonic ^4He and later antibunching in fermionic ^3He was observed by another group [22, 23].

All studies mentioned above were possible because of the unique properties of our newly developed apparatus. It combines the production of Bose-Einstein condensates and atom lasers with an ultrahigh finesse optical cavity. The conflicting vacuum requirements for the initial magneto-optical trapping and subsequent evaporative cooling of the ^{87}Rb atoms are met by two nested vacuum chambers. The cavity is mounted on an interchangeable “science platform” and can be supplemented with or replaced by

additional samples and probes.

An atom coupled to an optical cavity in the strong coupling regime is a prime example of a cavity QED system. The rate at which energy is exchanged between a single electromagnetic mode of the cavity and a single atom is greater than all dissipative processes, leading to a resolvable vacuum Rabi splitting of the coupled atom-cavity system [24, 25]. The detection of single atoms [26], trapping of single atoms with single photons [27, 28], cavity cooling of atoms [29], and single photon sources [30, 31] are just a few examples of the impressive achievements with such a system. A great advantage of the cavity over other single atom detection schemes [22, 32, 33] is that the atoms are neither absorbed nor ionized. It should be possible to detect single atoms nondestructively and state preserving by implementing a heterodyne detection technique [34].

In the experiments presented in this thesis, the cavity was utilized as a time-resolving single atom detector, adding unprecedented sensitivity to the research on Bose-Einstein condensates including interferometric measurements and the investigation of particle correlations. An atom laser is a bright source of coherent atoms, allowing a precisely controllable flux of ultracold atoms with well defined internal and external degrees of freedom through the cavity. The transport of the BEC into the cavity and subsequent trapping in the cavity mode realizes a system with maximum control over the state of matter and light field and extremely strong coupling between the two.

The work presented in this thesis was carried out in close collaboration with Anton Öttl and Michael Köhl. Additional information on the experiments and the apparatus can be found in their PhD thesis [35] and habilitation thesis [36], respectively.

Outline of this thesis

- In chapter 2 an introduction to the theoretical aspects of Bose-Einstein condensation is given, with special attention to coherence and phase transitions. This is followed by a section about atom lasers and the output coupling process in particular. Furthermore, the basics of cavity QED and single atom detection using a high finesse optical cavity are discussed.
- The newly developed apparatus is presented in chapter 3. Its building blocks are described in detail and the performance of the system is characterized. We present measurements on the beam profile of an atom laser and the investigation of cold atomic gases both using the cavity-based single atom detector. The chapter closes with the introduction of a new technique to very sensitively detect and quantify dipole oscillations of a BEC via phase modulation of two atom laser beams.
- Our measurements on the formation of off-diagonal long-range order in a Bose-Einstein condensate are reported in chapter 4. It is opened by a short review of quasicondensates, the theory of condensate formation and a presentation of related experimental work. We study the specifics of the measuring method in more detail and present our results.
- The time-resolved detection of single atoms from an atom laser beam allowed us to study its second-order coherence, time interval distributions and counting statistics. The measurements and results—confirming the second-order coherence of the atom laser—are presented in chapter 5 and are contrasted with measurements on a pseudothermal beam.
- Chapter 6 reports on a matter wave analogue to Young’s double slit experiment with individual quanta. In addition, the quantum measurement performed by the cavity detector on the extended matter wave is studied theoretically.
- The thesis closes with an outlook on our very recent experiments in the critical regime of the Bose-Einstein phase transition in chapter 7. First steps towards the transport of the BEC into the ultrahigh finesse cavity are also presented.

2 Theoretical framework

In the following chapter, a brief introduction to the physics of Bose-Einstein condensates (BECs), atom lasers and cavity QED in the strong coupling regime will be given. The intention is to briefly review theoretical and experimental aspects important for the understanding of the experimental work presented in later chapters. For a more detailed and complete overview the reader is referred to the standard literature. Important articles, textbooks and reviews will be mentioned in the respective sections.

2.1 Bose-Einstein condensation

In a paper published 1924, D. Bose presented a derivation of Planck's law of black-body radiation using statistical mechanics [37]. Einstein used the same method to derive the quantum theory of an ideal gas [38]. He found that for a given temperature the non-zero energy states can only accommodate a limited number of atoms and immediately realized that this leads to the condensation of excess atoms into the zero momentum state. There is an alternative picture of Bose-Einstein condensation: The size of the wave packet of a single atom is roughly given by the thermal de Broglie wavelength

$$\lambda_{\text{dB}} = \sqrt{2\pi\hbar^2/(mk_B T)}. \quad (2.1)$$

When an ensemble of atoms is cooled to ultralow temperatures, their de Broglie wavelengths become comparable to the mean interatomic separation. Consequently the atoms overlap and become indistinguishable. The system undergoes the phase transition to a BEC (see Fig. 2.1). Already in 1938, London realized that the superfluidity of liquid ^4He was due to Bose-Einstein condensation [39, 40]. However, the strong interactions between the atoms in liquid ^4He limit the condensate fraction to below 10 %. Bose-Einstein condensates of a dilute atomic vapor, first realized in 1995 [1, 2, 3], can on the other hand be made virtually pure. They are also largely accessible for experimental investigation.

A detailed discussion of the theory of Bose-Einstein condensation can be found in review articles [41, 42] and textbooks [43, 44]. An introduction to the experimental

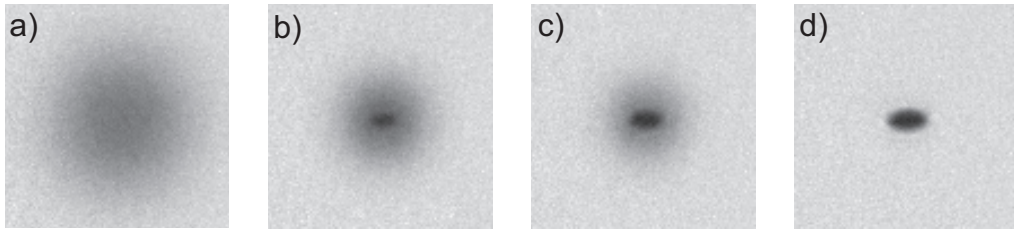


Figure 2.1: A BEC is created by evaporative cooling. All pictures were taken after ballistic expansion during 22 ms time of flight following the switch-off of the anisotropic trapping potential. Starting from a thermal cloud (a), the temperature of the ensemble is lowered by evaporative cooling. Below the critical temperature T_c , a BEC forms [(b) and (c)]. The condensate is easily distinguishable from the isotropically expanding thermal cloud by its distinctive anisotropic expansion. Cooling further leads to a virtually pure Bose-Einstein condensate (d).

aspects and methods is given in [45].

2.1.1 The ideal Bose gas

We consider a noninteracting gas of N bosons in a three-dimensional harmonic trap. At a temperature T , the mean number n_i of particles in an energy eigenstate with energy ϵ_i is given by the well known Bose-Einstein distribution

$$n_i = \frac{1}{e^{(\epsilon_i - \mu)/k_B T} - 1}. \quad (2.2)$$

k_B denotes the Boltzmann constant and the chemical potential μ is determined by the normalization to the total number of particles N : $\sum_i n_i(\mu, T) = N$. We set $\epsilon_0 \equiv 0$. Bose-Einstein condensation occurs when one (“simple BEC”) or more of the eigenvalues n_i are of the order of the total number of particles N [46]. The condensation temperature is defined as $T_c = T|_{\mu \rightarrow 0^-}$. In the case of a harmonic trapping potential

$$V_{\text{ext}}(\mathbf{r}) = \frac{1}{2}m(\omega_x^2 x^2 + \omega_y^2 y^2 + \omega_z^2 z^2) \quad (2.3)$$

and for atoms of mass m and trapping frequencies ω_x , ω_y and ω_z one finds

$$T_C = \frac{\hbar}{k_B} \left(\frac{N\omega_x\omega_y\omega_z}{\zeta(3)} \right)^{1/3}, \quad (2.4)$$

where ζ is the Riemann zeta function. For $T < T_C$ a BEC forms as a macroscopic population of the lowest single-particle state. The number of condensed atoms N_0 at a temperature T is given by

$$N_0(T) = [1 - (T/T_C)^3]N. \quad (2.5)$$

2.1.2 The weakly interacting Bose gas

The typical peak density of a BEC of a dilute gas is $n \approx 10^{20} \text{ m}^{-3}$. The scattering length of spin-polarized ^{87}Rb atoms is $a = (106 \pm 4) a_0$ [47], which is a typical value for alkali atoms. Here a_0 denotes the Bohr radius. The mean interparticle separation is thus much smaller than the scattering length, i.e. $n|a|^3 \ll 1$. This is the definition of the weakly interacting regime, where the interaction between atoms is completely characterized by the s-wave scattering length a . The true interaction potential can in general not be calculated. In the Born approximation it is replaced by an effective contact interaction

$$V_0 = \frac{4\pi\hbar^2 a}{m} \delta(\mathbf{r} - \mathbf{r}') = U_0 \delta(\mathbf{r} - \mathbf{r}'). \quad (2.6)$$

Assuming a fully condensed state, the wave function of the N-particle system can be written as a product of single-particle states $\phi(\mathbf{r}_i)$:

$$\Psi(\mathbf{r}_1, \mathbf{r}_2, \dots, \mathbf{r}_N) = \prod_{i=1}^N \phi(\mathbf{r}_i) \quad (2.7)$$

Now we introduce the wave function of the condensed state as

$$\psi(\mathbf{r}) = \sqrt{N} \phi(\mathbf{r}). \quad (2.8)$$

Taking the interaction between the atoms into account in a mean-field approximation leads to a nonlinear Schrödinger equation

$$i\hbar \frac{\partial}{\partial t} \psi(\mathbf{r}, t) = \left(-\frac{\hbar^2}{2m} \nabla^2 + V_{\text{ext}}(\mathbf{r}, t) + U_0 |\psi(\mathbf{r}, t)|^2 \right) \psi(\mathbf{r}, t), \quad (2.9)$$

the so called Gross-Pitaevskii equation [48, 49]. It describes a condensate at $T = 0$ and neglects in this form any excitations and interactions with thermal atoms.

If the interaction energy per particle is large compared to the zero-point energy of the harmonic oscillator, the kinetic energy term in the Gross-Pitaevskii can be neglected. This is the so called Thomas-Fermi approximation, which is valid for $Na/\bar{a} \gg 1$, where $\bar{a} = \sqrt{\hbar/(m\bar{\omega})}$ is the characteristic length scale for the quantum-mechanical harmonic oscillator and $\bar{\omega} = (\omega_x \omega_y \omega_z)^{1/3}$ is the geometric mean of all three oscillator frequencies. For the system studied in this thesis, this is the case for condensates of more than 10^3 atoms. In the Thomas-Fermi approximation, one can calculate the density distribution of the BEC:

$$n(\mathbf{r}) = \max \left[\frac{\mu_{\text{TF}} - V_{\text{ext}}(\mathbf{r})}{U_0}, 0 \right] \quad (2.10)$$

The chemical potential is given by

$$\mu_{\text{TF}} = \frac{1}{2} (15\hbar^2 \sqrt{m} N \bar{\omega}^3 a)^{2/5}, \quad (2.11)$$

and the condition $V_{\text{ext}}(r_{\text{TF},i}) = \mu_{\text{TF}}$ gives the radius of the condensate

$$r_{\text{TF},i} = \sqrt{\frac{2\mu_{\text{TF}}}{m\omega_i^2}}, \quad i = x, y, z, \quad (2.12)$$

the so called Thomas-Fermi radius. For large atom numbers, the results of the Thomas-Fermi approximation are excellent, apart from a small region at the border of the condensate. While the approximation predicts a sharp edge, the real wave function, that can be calculated by numerically solving the Gross-Pitaevskii equation, falls off exponentially on a length scale given by $1/\sqrt{8\pi na}$, the so called healing length.

The Gross-Pitaevskii equation was introduced here to describe the wave function of the condensed state. This approach neglects quantum fluctuations, which are taken into account by the Bogoliubov theory. It can be used to describe elementary excitations in a BEC, which are found to behave like noninteracting quasiparticles. Their dispersion relation reads

$$\epsilon(\mathbf{p}) = \sqrt{(cp)^2 + \left(\frac{p^2}{2m}\right)^2} \quad (2.13)$$

where $c = \sqrt{U_0 n/m}$ denotes the speed of sound. For small momenta ($p \ll mc$), eqn. (2.13) becomes $\epsilon(\mathbf{p}) \approx cp$, i.e. phonon-like, whereas for $p \gg mc$ one finds the dispersion law for free particles $\epsilon(\mathbf{p}) \approx p^2/(2m) + U_0 n$. Quantum fluctuations lead to excitations even at zero temperature, with the consequence there is a quantum depletion of the condensate. Because dilute atomic gases are usually very weakly interacting, the depletion is negligible in these experiments. In liquid helium however it is responsible for the low condensate fractions of only about 10%.

2.1.3 Theory of coherence and phase transitions

For a non-interacting gas of Bosons, the criterion for Bose-Einstein condensation is simply the macroscopic population of one of the single-particle energy states, usually the ground state. This collection of atoms in the ground state is called a Bose-Einstein condensate, whereas atoms occupying higher energy levels are attributed to the thermal fraction. This simple and intuitive picture becomes problematic when the interactions between the particles are of importance. It no longer makes sense to use the one-particle states as eigenfunctions of the trapping potential. As an alternative, the condensate can be described as a macroscopic wave function ψ , which is a complex quantity with amplitude and phase. This wave function takes the role of an order parameter. The idea of introducing an order parameter is a general concept in physics. Often one is interested in specific properties of a many-body systems, as, e.g., the magnetization of a magnet. Trying to understand this property of the bulk by keeping track of all properties of its constituents is a hopeless endeavor. Instead, one uses the concept of

an order parameter to describe the interesting property of the system. In the case of a BEC, the order parameter is given by its wave-function.

Spontaneous symmetry breaking

The description of the interacting condensate starts from a pure, bosonic N -body state of fixed particle number and energy. In second quantization, one uses the equivalence between a system of N particles and a quantized field [6] generated by the quantized boson field operator $\Psi(\mathbf{r})$. The Hamiltonian describing the system is invariant under the global gauge transformation $\Psi(\mathbf{r}) \rightarrow e^{i\theta}\Psi(\mathbf{r})$ with θ being real and independent of position. The system is characterized by $\psi(\mathbf{r}) \equiv \langle \Psi(\mathbf{r}) \rangle = a(\mathbf{r}) e^{i\phi(\mathbf{r})}$, the complex order parameter of the transition, also called the condensate wave function. For temperatures above the critical temperature $\psi(\mathbf{r}) = 0$ shows global phase symmetry. When Bose-Einstein condensation happens, the global gauge invariance is spontaneously broken, i.e. ψ becomes finite with a certain phase ϕ . This is in close analogy to the magnetization of a ferromagnet: While the Hamiltonian describing the system is rotationally invariant in the absence of external fields, the ground state possesses a spontaneously broken symmetry and the magnetization points in a definite direction. An immediate consequence of the spontaneous symmetry breaking is that no phase correlations between completely independent condensates can be expected [50]. However, the appearance of a fixed relative phase between two initially independent, interfering condensates is not in contradiction with the two condensates initially being in a Fock state [51, 52]. Lieb *et al.* have proven the equivalence between spontaneous gauge symmetry breaking and Bose-Einstein condensation in the quasi average sense [53].

Penrose-Onsager criterion of Bose-Einstein condensation

The one particle density matrix of a system of bosons can be written as

$$\rho_1(\mathbf{r}, \mathbf{r}') = \langle \hat{\Psi}^\dagger(\mathbf{r}) \hat{\Psi}(\mathbf{r}') \rangle, \quad (2.14)$$

where $\langle \dots \rangle$ denotes the ensemble average. Since $\hat{\Psi}(\mathbf{r})$ is the Bose field annihilation operator and $\hat{\Psi}^\dagger(\mathbf{r})$ the creation operator, $\rho_1(\mathbf{r}, \mathbf{r}')$ is the probability to find a particle at \mathbf{r} after removing one at \mathbf{r}' . For a homogeneous, ideal Bose gas, one finds [6]

$$\rho_1(\mathbf{r}, \mathbf{r}') = \frac{\langle n_0 \rangle}{V} + \int \frac{d^3k}{(2\pi)^3} e^{i\mathbf{k} \cdot (\mathbf{r} - \mathbf{r}')} \langle n_k \rangle. \quad (2.15)$$

The interpretation of this result is instructive. The existence of a Bose-Einstein condensate, i.e. a macroscopic number of atoms n_0 occupying the same momentum state, implies

$$\rho_1(\mathbf{r}, \mathbf{r}') \xrightarrow{|\mathbf{r} - \mathbf{r}'| \rightarrow \infty} \frac{\langle n_0 \rangle}{V}, \quad (2.16)$$

i.e. in a homogeneous, noninteracting system and for large separations ρ_1 is given by the number of condensed atoms. In the case of a thermal gas in the critical regime (see chapter 7) and for $r \gg \lambda_{dB}$, correlations decay as

$$\rho_1(\mathbf{r}, \mathbf{r}') \propto \frac{1}{r} e^{-r/\xi}. \quad (2.17)$$

The correlation length is given by $\xi = \hbar/\sqrt{2mk_B T |\ln z|}$ and the fugacity z related to the chemical potential μ via $z = \exp[\mu/(k_B T)]$. In a three-dimensional harmonic oscillator potential z is defined via $g_{3/2}(z) = (T_C/T)^{3/2} g_{3/2}(1)$, with the Bose or polylogarithm function $g_p(z)$ given by $g_p(z) = \sum_{l=1}^{\infty} \frac{z^l}{l^p}$. Close to the critical temperature, that is for $t = (T - T_c)/T_c \rightarrow 0$, the correlation length diverges as $\xi \propto |t|^{-\nu}$. The critical exponent ν characterizes the divergence and is 1 for a homogeneous and 1/2 for a trapped noninteracting system.

For interacting particles, Penrose and Onsager [54, 4] and Yang [5] proposed a criterion for Bose-Einstein condensation:

$$\langle \hat{\Psi}^\dagger(\mathbf{r}) \hat{\Psi}(\mathbf{r}') \rangle \xrightarrow{|\mathbf{r}-\mathbf{r}'| \rightarrow \infty} \langle \hat{\Psi}^\dagger(\mathbf{r}) \rangle \langle \hat{\Psi}(\mathbf{r}') \rangle. \quad (2.18)$$

This is also the definition of the existence of off-diagonal long-range order (ODLRO) in ρ_1 [5]. The concept of ODLRO describes a defining property of a BEC and is equivalent to long-range phase coherence of the system. When the spatial extension of the off-diagonal elements is as large as or larger than the spatial extension of the diagonal elements, i.e. the density of the system, it is said to possess off-diagonal long-range order.

In summary, a condensate can be described by an order parameter, its (macroscopic) wave function. The concept of broken gauge symmetry is one of the fundamental principles for understanding BEC. Off diagonal long-range order or long-range phase coherence describe the same concept [55].

Coherence and correlation functions

The normalized first- and second-order correlation functions, measuring the degree of coherence, can be defined as [56]

$$g^{(1)}(\mathbf{r}, \mathbf{r}') = \frac{\rho_1(\mathbf{r}, \mathbf{r}')}{\sqrt{\rho_1(\mathbf{r}, \mathbf{r})} \sqrt{\rho_1(\mathbf{r}', \mathbf{r}')}}, \quad (2.19)$$

and

$$g^{(2)}(\mathbf{r}, \mathbf{r}') = \frac{\langle \hat{\Psi}^\dagger(\mathbf{r}) \hat{\Psi}^\dagger(\mathbf{r}') \hat{\Psi}(\mathbf{r}') \hat{\Psi}(\mathbf{r}) \rangle}{\rho_1(\mathbf{r}, \mathbf{r}) \rho_1(\mathbf{r}', \mathbf{r}')}. \quad (2.20)$$

Both functions yield one in the case of perfect coherence. $g^{(1)}$ characterizes fluctuations in the phase of the field amplitude. It is experimentally directly accessible as the visibility

$$V = \frac{I_{\max} - I_{\min}}{I_{\max} + I_{\min}} \quad (2.21)$$

of an interference pattern in an experiment with perfect detectors. This interference is a single-particle effect. In contrast, $g^{(2)}$ is proportional to the joint probability to measure one atom at \mathbf{r} and another at \mathbf{r}' and therefore a two-particle effect. The two-particle correlation function is an ideal measure for the bunching behavior of thermal bosons [57, 58], that is their tendency to cluster. In chapter 5, we present a measurement of the temporal two-particle correlation function of an atom laser beam. An important difference between the theory of coherence in a BEC and optical coherence [59] is given by the interactions of the atoms. They strongly influence the second-order correlations on small length scales. The first-order correlation function $g^{(1)}$ is of great importance for the measurement of the condensate formation presented in chapter 4.

2.1.4 Quasicondensates

A quasicondensate is distinct from a true condensate in that it shows large phase fluctuations and therefore no long-range phase coherence, even though it possesses the same density profile and local correlation properties as a true condensate. The presence of quasicondensates could be revealed by the momentum distribution of a gas below the critical temperature. Large phase fluctuations are very common in low-dimensional systems. In very elongated 3D condensates axial phase fluctuations exist even well below T_c [60]. In such a geometry, the wavelength of the elementary excitations can become larger than the radial size of the system. In the axial direction low-energy excitations then show a 1D behavior and strong phase fluctuations can be observed. Neglecting correlations in the thermal cloud, the correlation function is given by

$$\langle \hat{\Psi}^\dagger(\mathbf{r}) \hat{\Psi}(\mathbf{r}') \rangle = \sqrt{n_0(\mathbf{r}) n_0(\mathbf{r}')} e^{-\langle [\delta\hat{\phi}(\mathbf{r}, \mathbf{r}')]^2 \rangle / 2}. \quad (2.22)$$

The mean square thermal fluctuations of the phase in the center of the cloud are found to be

$$\langle [\delta\hat{\phi}(z, z')]^2 \rangle = \delta_L^2 \frac{|z - z'|}{L}, \quad (2.23)$$

where L denotes the axial size of the cloud. Therefore it depends on the magnitude of δ_L^2 whether phase fluctuations control the system. For $\delta_L^2 \geq 1$ this is surely the case. δ_L^2 is given by [60]

$$\delta_L^2 = \frac{T}{T_c} \left(\frac{N}{N_0} \right)^{3/5} \delta_c^2, \quad (2.24)$$

where δ_c^2 depends on atomic properties, particle number N and trapping frequencies

$$\delta_c^2 = \frac{32\mu(N_0 = N)}{15N^{2/3}\hbar\bar{\omega}} \left(\frac{\omega_\rho}{\omega_l}\right)^{4/3}. \quad (2.25)$$

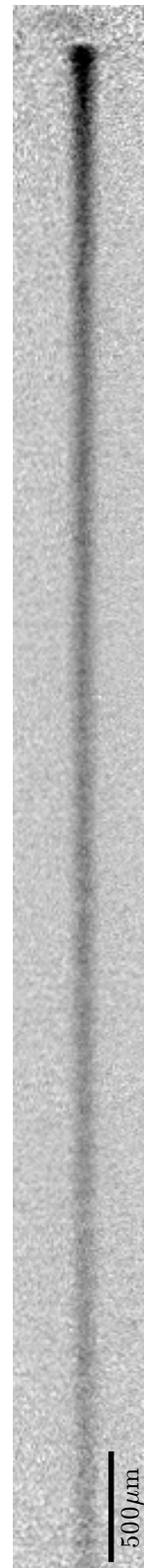
Experimentally, quasicondensates have been observed in very elongated traps [61, 62, 63]. The phase fluctuations lead to stripes in the density distributions of the atom cloud after ballistic expansion. These could be observed in traps with aspect ratios exceeding 25 and for temperatures not too far below T_c . In a similar trapping geometry the Hannover group measured the spatial second-order correlation function of phase fluctuating condensates [64, 65]. Using two Bragg pulses a condensate was split in two parts with a separation determined by the time between the two pulses. The absorption images of the interfering clouds showed strong modulations in the density profile due to interference which could be quantified by the intensity correlation function. From this the coherence length of the sample was inferred.

2.2 Atom lasers

Quantum optics and research on ultracold atoms would not be conceivable without lasers. They have become reliable workhorses for cooling, trapping, manipulating and detecting single atoms as well as ensembles and they provide the experimentalist with a true realization of a coherent state, sometimes also called Glauber state [59]. It is the closest quantum mechanical realization of a classical wave with fixed intensity and phase. Laser light has many desirable properties which one also wants for atomic beams. An atom laser should likewise be bright, highly directed, largely monochromatic and on the quantum level obey Poissonian statistics [66]. Since the atoms in a Bose-Einstein condensate all occupy the same mode, they make a perfect source for an atom laser.

Atom lasers draw their desirability from their unique properties. For example in interferometry, the coherence and reduced intensity fluctuations of the atom laser as compared to a thermal beam will enable experiments with formerly unthinkable precision. With atom interferometers, inertial sensing and the precise measurement of fundamental constants is possible and they considerably benefit from the outstanding properties of an atom laser. In atom lithography, one can gain from the high brightness and directionality of the beam. Foci of about 1 nm, well below what is feasible with optical beams, seem possible. Using holography, the diffraction of atoms can be used to produce very small structures due to the much smaller wavelengths of atoms compared to light [67, 68].

The analogy between an optical laser and an atom laser not only pertains to the properties of the beam. All the important components of an optical laser can also be found in an atom laser. Atoms trapped in the ground state of a confining potential are the analogue of photons occupying a single mode of an optical cavity. In the same way that a mirror with higher transmission acts as an output coupler for the intracavity photons, there are several possible mechanisms of coupling the trapped matter wave to the continuum of untrapped states. These mechanisms will be presented in the next paragraph. At the heart of both lasers lies the effect of Bose stimulation, constituting the necessary gain mechanism. The presence of N bosons in one particular mode leads to a transition probability into this state proportional to $N + 1$. This leads to an enhanced population of an already highly occupied state, which is the cavity mode in an optical laser and the ground state in an atom laser. The idea of producing a matter wave analog to the optical laser goes back to ideas from the early



times of the experimental realization of BEC in atomic vapors and even before that [69, 70, 71, 72, 73]. A review on the theory of atom lasers is given in reference [74].

2.2.1 The output coupling process

The first realization of a pulsed output coupler for atoms [75] from a BEC marked the beginning of the experimental realization and research on atom lasers. Atoms in a “low-field seeking” internal state are trapped in the minimum of a magnetic field configuration. The principle idea is to couple the trapped state the atoms are in to a second state that is magnetically insensitive. Then the atoms will fall under the influence of gravity, forming the (possibly pulsed) atom laser beam. Several other output coupling mechanisms are possible. Lowering the trap depth for atoms confined in a vertical optical standing wave potential for example also produces a pulsed atom laser [76]. Two counter propagating Raman laser beams can be used to output couple atoms while at the same time imparting a momentum of $2\hbar k$ [77]. This allows for propagation directions different from the one given by gravity. Also, the interaction time between output coupled atoms and the trapped condensate can be drastically reduced, therefore facilitating the production of beams with extremely low divergence [78]. Due to the temporal change in the magnetic field of the trap used in [77], the stimulated Raman process needs to be pulsed. A quasi-continuous beam can be created by pulsing with a repetition rate equal to an integer fraction of the phase evolution of the output coupled matter wave. The first atom laser with a truly continuous wave (cw) output coupler was demonstrated in a magnetically shielded setup of a Bose-Einstein condensate in a QUIC trap [79]. The shielding allowed for the stable output coupling with only one radio frequency from a definite region within the condensate. This is the method used in the setup presented in this thesis. Continuous output coupling was also demonstrated for a BEC trapped in a horizontally oriented, tightly focused dipole trap [80]. It is achieved by simply lowering the power in the trapping beam. In such a setup, magnetic field fluctuations only enter via the second-order Zeeman effect, but the stability of the atom laser now crucially depends on the stability of the trapping laser intensity. The atom lasers we have called “continuous” so far share the property that their coherence length can be much longer than the size of the condensate they stem from. In all experiments up to date, the final limit on the length of the atom laser is given by the size of the reservoir they are output coupled from. Producing a truly continuous atom laser with no principle limit to its length and duration mainly requires a continuous replenishment of the trapped BEC [81]. A different route pursued is to create a magnetically guided beam of optically pre-cooled atoms, that might in the future be cooled to quantum degeneracy by evaporation [82, 83].

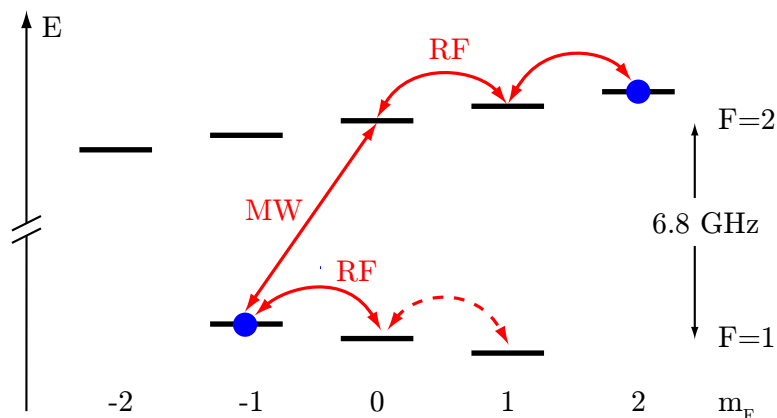


Figure 2.2: Hyperfine structure of the $5^2S_{1/2}$ ground state of ^{87}Rb in a weak magnetic field. Starting with atoms in the trapped $|F=2, m_F=2\rangle$ state, output coupling of an atom laser can be achieved via two radio-frequency transitions into the untrapped $|F=2, m_F=0\rangle$ state. The same final state can be reached with a microwave transition from the $|F=1, m_F=-1\rangle$ state. Alternatively, an atom laser in the $|F=1, m_F=0\rangle$ state can be produced starting with a trapped cloud in the $|F=1, m_F=-1\rangle$ state.

2.2.2 Radio-frequency output coupling

In the experiments presented in this thesis, atom laser output coupling from a magnetic trap using radio- or microwaves was used. A theoretical description of atom lasers produced by rf output coupling is based on a set of coupled generalized Gross-Pitaevskii equations and has led to a one-dimensional model [84, 85]. A fully quantum mechanical calculation (assuming a source with a Gaussian density distribution) in three-dimensions confirms the basic results for condensate sizes exceeding $1\ \mu\text{m}$ [86, 87]. Here, we will present a semi-classical picture for the case of a BEC of ^{87}Rb atoms trapped in the harmonic potential of a magnetic trap.

The $5^2S_{1/2}$ ground state of ^{87}Rb has two hyperfine states, $F=1$ and $F=2$. Their splitting in the presence of a magnetic field is depicted in Fig. 2.2. Magnetic trapping of atoms in the “low-field-seeking” states $|F=1, m_F=-1\rangle$, $(|F=2, m_F=1\rangle$ and $|F=2, m_F=2\rangle$ is possible. These are the states whose energy is lowered when the magnetic field is decreased. The splitting of the two hyperfine states at zero magnetic field is $\Delta E_{\text{hfs}} = h\nu_{\text{hfs}} \approx h \times 6.8\ \text{GHz}$ [88]. In the limit of weak magnetic fields, the splitting of the different m_F states is called anomalous Zeeman effect and is—to lowest order—given by $\Delta E_{|F, m_F\rangle} = m_F \mu_B g_F B$ with Landé factors given by $g_{F=1} \approx -1/2$ and $g_{F=2} \approx 1/2$. The exact energy eigenvalues are given by the Breit-Rabi formula [89, 88],

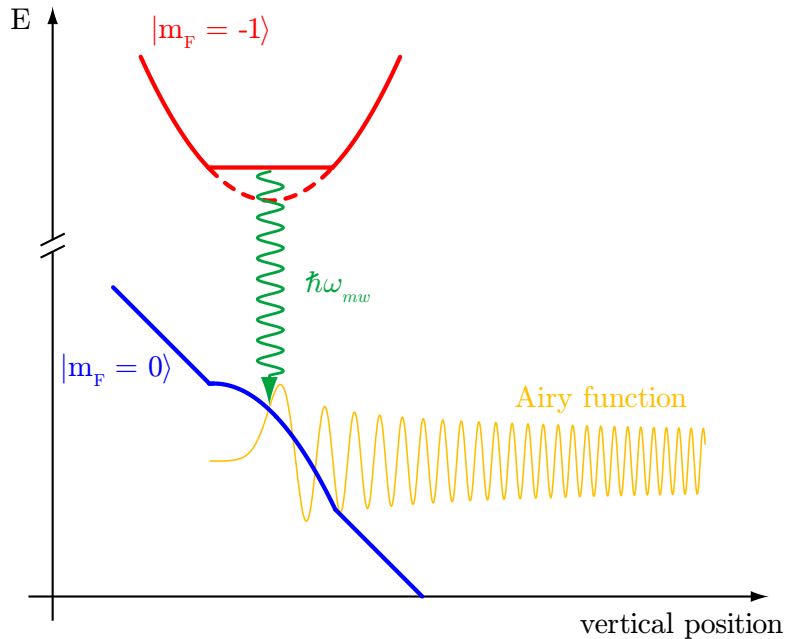


Figure 2.3: Energy diagram illustrating the output coupling mechanism used for producing an atom laser beam from a magnetically trapped BEC. The potentials for trapped (red) and untrapped (blue) atoms are coupled via a radio or microwave frequency (green). The wave function of the atom laser beam in the gravitational potential is an airy function (yellow). Note that the potential for trapped atoms has been scaled up by about a factor of twenty to bring out the contribution of the mean-field.

which also incorporates the second-order Zeeman shift. As one can see from Fig. 2.2, with a radio-frequency $\nu = \frac{1}{2}\mu_B B/h$ and the selection rule $\Delta m_F = 0, \pm 1$, transitions from the trapped $|F = 1, m_F = -1\rangle$ to the untrapped $|F = 1, m_F = 0\rangle$ state are possible. However, the same frequency couples the $|F = 1, m_F = 0\rangle$ to the $|F = 1, m_F = 1\rangle$ state. Only if the second-order Zeeman effect is significant, the $m_F = 0 \rightarrow m_F = 1$ transition is suppressed [90]. From $|F = 2, m_F = 2\rangle$ a transition into the untrapped state $|F = 2, m_F = 0\rangle$ involves two radio frequency (rf) photons. In a 1D mean-field model, an atom laser based on the latter transition was shown to exhibit significant density fluctuations even for weak output coupling [91]. To realize a clean two-level system, for most of the experiments presented here we use a microwave frequency (mw) to couple atoms from the trapped $|F = 1, m_F = -1\rangle$ into the untrapped $|F = 2, m_F = 0\rangle$ state. There is no other transition at the same resonance frequency.

Fig. 2.3 illustrates the position dependence of the output coupling resonance. For simplicity, only the dependence on the vertical position with the horizontal location kept constant is shown. Atoms in the low-field seeking $|m_F = -1\rangle$ state are trapped

magnetically. The harmonic potential of this trap (red line) is altered by the mean-field due to the repulsive interaction of the atoms so that all condensate atoms have the same energy equal to the chemical potential μ . Output coupling is achieved using a radio or microwave of frequency ν_{mw} . It couples the trapped atoms to the untrapped state $|m_F = 0\rangle$. The potential for the $|m_F = 0\rangle$ atoms (blue line) is the sum of the linear gravitational potential and a mean-field contribution. In ^{87}Rb , trapped and untrapped atoms experience the same mean field, because their scattering lengths are approximately equal. The energy difference between the minimum of the trapping potential and the energy of the untrapped atoms is given by the anomalous Zeeman effect and therefore proportional to the magnetic field. From the figure it is apparent that there is a unique relationship between the energy $h\nu_{\text{mw}}$ of the rf or mw photon and the vertical position. In a classical picture, output coupling occurs in a region where the energy difference between the two potentials is equal to the energy of the photon. The eigenfunction of the atom laser beam in the linear gravitational potential are given by Airy functions (plotted in yellow) $\Phi_E \sim Ai(\zeta_E(z))$ with $\zeta_E = (z - E/(mg))/l$ and the length scale given by $l = (\hbar^2/(2m^2g))^{1/3}$. The classical inflection point of a particle of energy E coincides with the inflection point of the first maximum of the Airy function at $\zeta_E = 0$. The probability for an atom to be output coupled is given by [92]

$$W_{oc} = \frac{h\Omega_0^2}{4} |\langle \Psi_{\text{BEC}} | \Phi_E \rangle|^2 \quad (2.26)$$

with $|\langle \Psi_{\text{BEC}} | \Phi_E \rangle|^2$ being the Franck-Condon factor between the bound and free state Φ_E . The Rabi frequency is given by

$$\Omega_0 = \mu_{12} B_{\text{mw}} / \hbar, \quad (2.27)$$

where μ_{12} is the magnetic dipole matrix element between the two coupled states and B_{mw} the magnetic field of the microwave radiation [93].

The overlap integral between the bound state and the Airy function is non-zero only in a very narrow region of order $l = 0.3 \mu\text{m}$ around $\zeta_E = 0$. Therefore the region of output coupling is well defined by the classical resonance condition [84].

The classical resonance condition is a consequence of energy conservation. This is of course not only true in the one-dimensional situation considered so far but also in three dimensions. Output coupling occurs at positions within the condensate at which the local magnetic field $B(\mathbf{r})$ fulfills the resonance condition $\nu_{\text{mw}} = (\Delta E_{\text{hfs}} - g_F \mu_B B(\mathbf{r})) / h$. In Fig. 2.4, cuts through the minimum of the combined magnetic and gravitational potential are plotted. The magnetic potential is that produced by the quadrupole Ioffe configuration (QUIC) trap [94] used in this work. The lines indicate regions of constant magnetic field. Without gravity, the atoms would sit in the harmonic potential around the minimum of the B-field. The effect of the linear gravitational potential however is

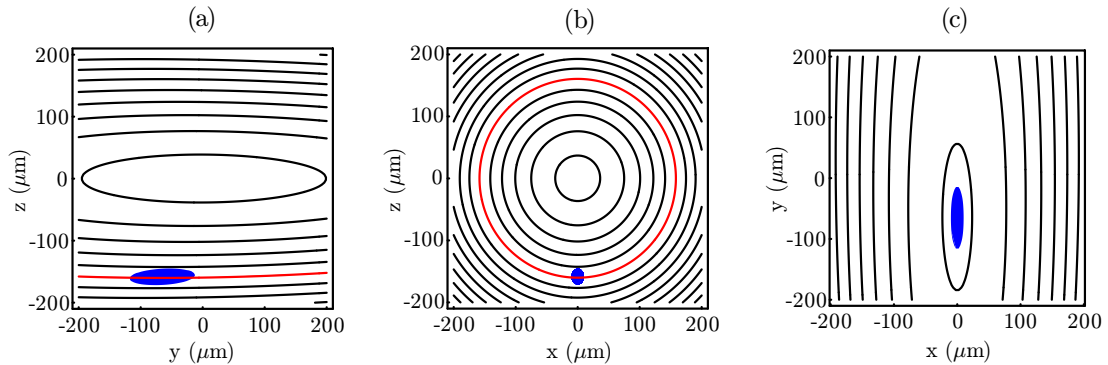


Figure 2.4: Location of the trapped BEC in the magnetic field of the QUIC trap. (a), (b) and (c) show a section through the minimum of the trapping potential in x , y and z direction, respectively. y is the Ioffe axis and gravity acts along $-z$. The black lines are regions of constant magnetic field. Due to gravity, the position of the condensate (blue ellipse) is shifted downwards by about $159\mu\text{m}$ with respect to the minimum of the magnetic field. Because of this large gravitational sag, the degeneracy of the trapping frequencies ω_x and ω_z is lifted and the long axis of the condensate is tilted by 3.2° with respect to the horizontal. The drawing is to scale for a pure condensate of 10^6 atoms.

a shift downwards of the trapping potential. This gravitational sag amounts to $z_{\text{sag}} = g/\omega_z^2$, where g is the acceleration due to gravity. If the sag is smaller than the region of linearly varying magnetic field, the harmonicity of the trap is preserved. We simulate the magnetic field in our trap configuration using the experimentally determined values for the trapping frequencies to fine adjust the positions of the coils. From this we find a gravitational sag of $z_{\text{sag}} = 159\mu\text{m}$. This is much larger than the size of a condensate. For 10^6 atoms the Thomas-Fermi radii are $(10, 53, 13)\mu\text{m}$ along the two horizontal axes and the vertical axis of the trap, respectively. Therefore the sections between the condensate and the shells of constant magnetic field (see for example the red lines in Fig. 2.4) are nearly planar, horizontal surfaces. The smaller the condensate, the more these cuts resemble horizontal planes, because their radius of curvature, given by z_{sag} , is much larger than the size of the condensate.

As can be seen from equations (2.26) and (2.27), the output coupling rate is proportional to the power of the microwave. Hence the flux of an atom laser is approximately proportional to the product of the number of atoms in the output coupling slice and the mw power [95]. However, this is only true for a two-level system and small Ω_0 . In this case, the flux of the atom laser beam is homogeneous as can be seen in Fig. 2.5(a). The residual fluctuations visible in the image are due to atomic shot noise and the noise of the imaging system. This was confirmed in a measurement presented in chapter 5 of this thesis. We measured the two-particle correlation function $g^2(\tau)$ of a weakly output

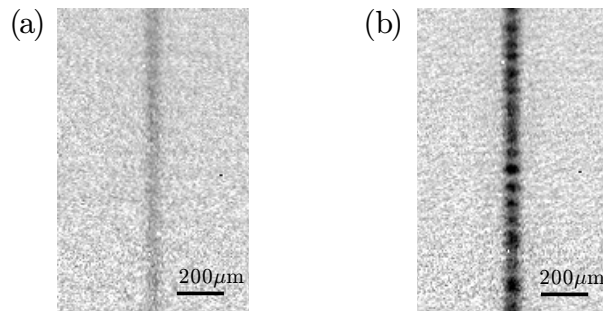


Figure 2.5: Sections of an atom laser in the $|F = 2, m_F = 0\rangle$ state. (a) Weak output coupling. (b) Du to a very strong microwave, the atom laser shows a substructure. Both images show the same field of view and have been scaled equally concerning brightness and contrast.

coupled atom laser beam and found it to be constant within our measurement accuracy of 1%. We can call Ω_0 small as long as it is less than the inverse coupling time. This is the time it takes for an atom to leave the region in which it is resonant with a photon of the output coupling frequency ν_{mw} [78].

When the Rabi frequency is increased, the regime of strong coupling is reached. Figure 2.5(b) shows the effect of such strong output coupling. The beam appears fragmented due to large density fluctuations originating from the complex coherent output coupling dynamics. Atoms already in the untrapped $|m_F = 0\rangle$ state of the atom laser beam but still in the spatial region where the output coupling resonance is fulfilled are being coupled back into the condensate (in the trapped $|m_F = -1\rangle$ state). Complex coherent dynamics are to be expected even in a two state system. They have already been observed in the five-state system of a condensate and an atom laser both in the $F = 2$ manifold (see Fig. 2.5(b) and [96]). The three state system of the $F = 1$ manifold was found to be comparable to the two-state system ($|F = 1, m_F = -1\rangle \leftrightarrow |F = 2, m_F = 0\rangle$) in terms of density fluctuations when the output coupling was weakly enough to avoid strong density fluctuations [91]. However, the highest coupling efficiency can clearly be achieved with the two-state system, i.e. by output coupling using a microwave frequency.

The spatial structure of an atom laser beam has been studied theoretically [97] as well as experimentally [98, 99]. Moreover, the temporal coherence of an atom laser beam has been found to be Fourier limited by its length [100]. The final and maybe most exclusive property of an atom laser left to be proven experimentally is its higher-order coherence. This was achieved as a part of this thesis (see chapter 5 and [101]). More detailed studies of the amazing general properties of atom lasers as well as of the tailoring of its specific features, e.g., by applying feedback [102, 103], are one interesting future direction of research. What seems even more appealing is to use the atom laser

to advance other fields in physics. In an experiment presented in this thesis, we have used the interference between two atom lasers to study the process of Bose-Einstein condensation itself. While section 2.2.3 will give a short introduction to this technique, the main results on the condensate growth are presented in chapter 4.

2.2.3 Two-frequency output coupling

When output coupling with two frequencies ω_1 and ω_2 from the trapped condensate, two overlapping atom laser beams are generated [see Fig. 2.6(a)]. They interfere and a high-contrast interference pattern can be observed [see the absorption image in Fig. 2.6(b)]. Their difference in energy $\Delta E = \hbar(\omega_2 - \omega_1)$ is fixed by the difference of the two frequencies, which also determines the periodicity of the interference pattern. As a result of energy conservation, atoms resonant with ω_1 are spatially separated from those resonant with ω_2 by $\Delta z = \Delta E/(mg)$, where m denotes the mass of an atom and g the acceleration due to gravity. Two nearly planar and parallel, horizontal surfaces are the sources of two atom laser beams. As the beams overlap, a high-contrast interference pattern forms. The frequency of this interference pattern only depends on the vertical distance Δz between the regions the atom lasers originate from. This is analogous to Young's double slit experiment, where equivalently only the displacement between the two slits has to be considered. In particular, the distance between two arbitrarily picked point sources, one from each slit, is irrelevant. For the situation considered here, the interference occurs along the propagation direction of the atom lasers given by gravity. The interference between two point sources will occur at a frequency solely determined by their difference in the gravitational potential, because this energy difference controls the relative phase evolution relevant for the beat frequency.

A detector at a fixed position in space, as for example an ultrahigh finesse optical

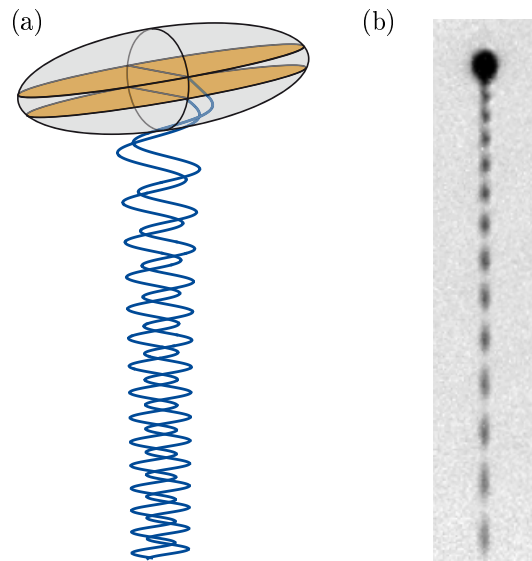


Figure 2.6: Using two frequencies, atom lasers originating from two different planes in the condensate (a) are output coupled, forming an interference pattern (b).

cavity sensitive to single atoms, will detect a sinusoidally modulated flux of atoms

$$f(t) = A (1 + V \sin [(\omega_2 - \omega_1)t + \phi]) \quad (2.28)$$

at exactly the difference frequency of the two output coupling waves. In absorption imaging [see Fig. 2.6(b)], when an image of the interference pattern is taken at a particular time, the interference pattern is not equidistant, because the velocity of the atoms increases due to gravity. The resulting vertical density distribution as a function of position is given by [104, 85]

$$n(z) = \frac{A}{\sqrt{|z|}} \left[1 + V \cos \left(\sqrt{\frac{2}{g}} (\omega_2 - \omega_1) \sqrt{|z|} + (\omega_2 - \omega_1)t + \phi \right) \right]. \quad (2.29)$$

The contrast of the interference pattern is characterized by its visibility V and depends on the coherence between the two regions the atom lasers originate from. Unequal intensities in the two beams, non-perfect mode overlap, and other effects can lead to a reduction in V that might especially be dependent on Δz . These effects and their influence on V are discussed in Sec. 4.3.6 of this thesis. Neglecting their residual curvature, the regions of output coupling are identified by their position z along the vertical axis. Using two frequencies, we can probe the condensate at z and z' and find the associated visibility $V(z, z')$. Starting from equations (2.14) and (2.19) it was shown that the visibility is very well approximated by the normalized first-order correlation function:

$$V(z, z') \approx g^{(1)}(z, z'). \quad (2.30)$$

This is an extremely important result, since it presents a method to map out the first-order correlation function of a BEC. The method is not limited to pure condensates, but can equally well be applied to partially condensed ensembles and thermal gases well above T_C or even in the critical regime. For all these different situations, a measurement of the visibility of the interference pattern gives information on the correlation function of the sample. It is especially worth noting that these measurements can be done time resolved.

2.3 Cavity QED

The theory of quantum electrodynamics (QED) describes the interaction between electrically charged particles by the exchange of photons and therefore the interaction between light and matter. Several phenomena in atomic physics, as e.g. spontaneous emission, can be described by the coupling of an atom to the radiation field of free space. In cavity QED, the mode spectrum of free space is altered by introducing boundary conditions and the quantization of the electromagnetic field is a natural consequence. Inside an optical resonator for example, only a fraction of all modes of the free space continuum can exist. The light field inside the cavity can be described as a superposition of Fock states, which are states with a fixed photon number that form a quantum mechanical basis of the electromagnetic field. If the reflectivity of the mirrors is sufficiently high, the interaction between an atom and one of the cavity modes can be larger than its coupling to all other modes including those of free space.

The coupling between the atom and the one particular mode of the cavity is characterized by the atom-cavity coupling constant g_0 . There are two loss-processes in the system: The decay of the electromagnetic field inside the resonator is described by the cavity decay rate $\kappa = \Delta\nu/2$, which is half the linewidth of the cavity. It is due to transmission through the mirrors and additional scattering or absorption losses not caused by the atom. The decay of the atomic dipole moment due to coupling to the environment $\gamma = \Gamma/2$ is given by half the linewidth of the atomic transition. If the atom-cavity coupling is larger than all other loss processes and the inverse dwell time τ^{-1} of the atom inside the cavity, i.e. $g_0 \gg \gamma, \kappa, \tau^{-1}$, the system is in the strong coupling regime of cavity QED. The good isolation of such a strongly coupled system from the environment greatly minimizes decoherence rates and allows for the study of coherent dynamics, as for example required for the implementation of quantum logic gates.

In the following sections, we will first review basic resonator theory. It is followed by an introduction to the Jaynes-Cummings model which is subsequently extended to incorporate dissipation. A discussion on how single atom detection can be achieved using a high-finesse optical cavity and the influence of different parameters on the detection efficiency closes the chapter. For additional information the reader is referred to the comprehensive review articles on the subject [105, 106, 107, 108].

2.3.1 Optical Resonators

To quantize the electromagnetic field, boundary conditions need to be introduced. In the experiment, this is achieved with a cavity. Many different types of cavities used for this purpose exist, ranging from superconducting cavities in the microwave range to microspheres, photonic bandgap cavities, monolithic microtoroidal resonators, or

Bragg mirrors in the optical and near-infrared spectrum. The resonator used in the work presented in this thesis consists of two macroscopic, concave Bragg mirrors. The characteristics of such a cavity will be presented in the following section.

Fabry-Pérot interferometer

A Fabry-Pérot interferometer consists of two planar, parallel and highly reflecting mirrors. The mirrors need not but in many cases are assumed to be identical. The interferometer is characterized by its length l_{res} and the properties of the two mirrors. These properties are their reflectivity \mathcal{R} , their transmission \mathcal{T} , and their losses \mathcal{L} . The losses can be due to scattering, diffraction or absorption. We have $\mathcal{R} + \mathcal{T} + \mathcal{L} = 1$ and in general, all three are wavelength dependent. Light incident on a Fabry-Pérot interferometer (in the following often shortly called “resonator” or “cavity”) will be reflected or transmitted depending on its wavelength. By superimposing the incident electromagnetic wave with the reflected part and the part leaking out of the resonator, constructive and destructive interference can occur. In case that one round trip of length $2l_{\text{res}}$ is equal to an integer multiple of the wavelength,

$$2l_{\text{res}} = n\lambda, \quad n \in \mathbb{N}, \quad (2.31)$$

maximum transmission $T_{\text{FP}}^{\text{max}}$ occurs. However, the maximum transmission is very different from the transmission \mathcal{T} of a single mirror because of interference at the resonator. The frequency dependent transmission of an empty cavity with identical mirrors is given by [109]

$$T_{\text{FP}}(\nu) = \frac{T_{\text{FP}}^{\text{max}}}{1 + \frac{4\mathcal{R}}{(1-\mathcal{R})^2} \sin^2\left(\frac{2\pi l_{\text{res}}\nu}{c}\right)} \approx \left(\frac{\mathcal{T}}{1-\mathcal{R}}\right)^2 \frac{1}{1 + \left(\frac{2\mathcal{F}}{\pi} \sin\left(\frac{2\pi l_{\text{res}}\nu}{c}\right)\right)^2}, \quad (2.32)$$

where \mathcal{F} denotes its finesse and c is the speed of light.

The distance between two neighboring frequencies with maximum transmission is called the free spectral range

$$\Delta\nu_{\text{FSR}} = \frac{c}{2l_{\text{res}}} \quad (2.33)$$

which is equal to the inverse of the round trip time of a photon. The finesse is defined as the ratio of the free spectral range $\Delta\nu_{\text{FSR}}$ and the linewidth $\Delta\nu_c$ of a cavity, i.e. the full width at half maximum of a transmission peak,

$$\mathcal{F} = \frac{\Delta\nu_{\text{FSR}}}{\Delta\nu_c}. \quad (2.34)$$

If there are no intracavity losses, the finesse depends on the reflectivity of the mirrors only

$$\mathcal{F} = \frac{\pi\sqrt[4]{\mathcal{R}_1\mathcal{R}_2}}{1 - \sqrt{\mathcal{R}_1\mathcal{R}_2}}, \quad (2.35)$$

where the indices 1 and 2 denote the first and second mirror, respectively. The decay rate of the field in the resonator is $\kappa = \pi \Delta \nu_{\text{FSR}} / \mathcal{F} = \frac{\pi c}{2l_{\text{res}} \mathcal{F}}$. This is half the decay rate of the intensity inside the resonator, which in turn is equal to the inverse of the lifetime of a photon in the cavity. The power inside the resonator is \mathcal{F}/π times larger than the input coupled power, because an atom traverses the resonator \mathcal{F}/π times on average.

In the following, we consider two identical mirrors and assume that there are no losses due to scattering or absorption inside the cavity other than those on the mirror substrates denoted by \mathcal{L} . This is a good assumption when the cavity resides in an ultrahigh vacuum environment. We will also assume perfect spatial mode matching of the incident beam. Under these conditions, the maximum transmission of a Fabry-Pérot interferometer on resonance $T_{\text{FP}}^{\text{max}}$ can be calculated using basic resonator theory (see for example [110])

$$T_{\text{FP}}^{\text{max}} = \left(\frac{\mathcal{T}}{1 - \mathcal{R}} \right)^2 = \left(\frac{\mathcal{T}}{\mathcal{T} + \mathcal{L}} \right)^2. \quad (2.36)$$

The fraction of light reflected on resonance is $R_{\text{FP}} = \mathcal{L}^2 / (\mathcal{T} + \mathcal{L})^2$, and therefore the maximally achievable input coupling is given by

$$\eta_{\text{in}} = 1 - R_{\text{FP}} = 1 - \left(\frac{\mathcal{L}}{\mathcal{T} + \mathcal{L}} \right)^2. \quad (2.37)$$

For very high reflectivities and using eqn. (2.35), the finesse can be approximated by

$$\mathcal{F} = \frac{\pi \sqrt{\mathcal{R}}}{1 - \mathcal{R}} \stackrel{\mathcal{R} \rightarrow 1}{\approx} \frac{\pi}{1 - \mathcal{R}} = \frac{\pi}{\mathcal{T} + \mathcal{L}} \quad (2.38)$$

Equation (2.38) provides an easy way to determine the reflectivity of the mirrors by measuring the finesse of the cavity: $\mathcal{R} = 1 - \pi/\mathcal{F}$. Combining equations (2.36) and (2.38) yields for the transmissivity of the mirrors

$$\mathcal{T} = \frac{\pi}{\mathcal{F}} \sqrt{T_{\text{FP}}^{\text{max}}}. \quad (2.39)$$

$\mathcal{T} + \mathcal{L} + \mathcal{R} = 1$ gives

$$\mathcal{L} = 1 - (\mathcal{T} + \mathcal{R}) = \frac{\pi}{\mathcal{F}} \left(1 - \sqrt{T_{\text{FP}}^{\text{max}}} \right). \quad (2.40)$$

$T_{\text{FP}}^{\text{max}}$ is measurable if one can ensure perfect spatial mode matching. The finesse can be determined from measurements of the free spectral range and the cavity linewidth. Therefore using equations (2.39) and (2.40), the properties of the mirrors constituting the cavity can be inferred from measured properties of the Fabry-Pérot resonator.

To calculate \mathcal{T} and \mathcal{L} using the above equations, a precise determination of $T_{\text{FP}}^{\text{max}}$ with perfect mode matching is necessary. Since the latter is very difficult to achieve and not necessary for all other purposes, another method independent of the mode matching is

better suited. The power P_{in} incident on the cavity, the reflected and the transmitted power, labeled by P_{r} and P_{t} respectively, can easily and accurately be measured. Then the transmission of each mirror is given by

$$\mathcal{T} = \frac{2\pi}{\mathcal{F} \left(1 + \frac{P_{\text{in}} - P_{\text{r}}}{P_{\text{t}}} \right)}, \quad (2.41)$$

and by inserting equation (2.41) into equation (2.38) and solving for \mathcal{L} one finds the losses at each mirror to be

$$\mathcal{L} = \frac{\pi}{\mathcal{F}} - \mathcal{T} = \frac{\pi}{\mathcal{F}} \left(1 - \frac{2}{1 + \frac{P_{\text{in}} - P_{\text{r}}}{P_{\text{t}}}} \right). \quad (2.42)$$

Transverse modes

For practical purposes, a Fabry-Pérot resonator with its two plane parallel mirrors has the critical disadvantage of only being marginally stable. This means that minute deviations from the parallel configuration result in an unstable cavity. In a ray optics picture no closed trajectory for a light ray exists in such a situation. Therefore concave mirrors with a radius of curvature R_{C} are usually used instead of plane ones. They support discrete resonator modes — Gaussian beams — which are solutions of the paraxial wave equation [111, 110]. To make a symmetric resonator stable, the radius of curvature of the mirrors has to be chosen such that $\infty > R_{\text{C}} > l_{\text{res}}/2$ with l_{res} being the cavity length. The two limiting cases are the planar cavity $R_{\text{C}} = \infty$ and the concentric resonator with $R_{\text{C}} = l_{\text{res}}/2$ and are both only marginally stable.

In principle, an infinite number of spatial modes can be supported by the cavity. A resonator mode is characterized by the three integers l, m, n , where l and m describe the field variations in the transverse direction, i.e. the transverse modes, whereas n describes the order of the longitudinal mode. The transverse modes are classified as TEM_{lm} (“transverse electromagnetic”). The lowest-order transverse mode called TEM_{00} has a purely Gaussian profile $\propto \exp\left(-\frac{x^2+y^2}{w(z)^2}\right)$, while the higher orders are given by Hermite functions. The radius of the beam is a function of the distance z from the waist

$$w(z) = w_0 \sqrt{1 + \left(\frac{z}{z_R} \right)^2}, \quad (2.43)$$

with the waist radius w_0 and the Rayleigh range given by [111]

$$z_R = \frac{\pi w_0^2}{\lambda}. \quad (2.44)$$

In a cavity, the curvature of the wavefronts

$$R(z) = z + \frac{z_R^2}{z} \quad (2.45)$$

at the position of the mirrors needs to match their radius of curvature R_C . For a symmetric cavity with concave mirrors this determines the mode waist radius via

$$w_0^2 = \frac{\lambda l_{\text{res}}}{2\pi} \sqrt{\frac{2|R_C|}{l_{\text{res}}} - 1}. \quad (2.46)$$

The mode volume V_m of a cavity can be calculated by integrating the mode function over the length of the cavity along its axis (z direction) and over all space radially. In addition, the standing wave structure needs to be accounted for. The exact result is

$$V_m = \frac{1}{4}\pi w_0^2 l_{\text{res}} + \frac{1}{48\pi} \left(\frac{\lambda}{w_0}\right)^2 l_{\text{res}}^3 = \frac{1}{4}\pi w_0^2 l_{\text{res}} \left(1 + \frac{1}{3(2R_C/l_{\text{res}} - 1)}\right). \quad (2.47)$$

In a near-planar cavity the radius of curvature R_C of the mirrors is much larger than the length of the cavity l_{res} . This leads to a Rayleigh range z_R much larger than the length of the cavity and therefore the divergence of the Gaussian mode within the cavity can be neglected. Then the cavity mode volume can very well be approximated by

$$V_m = \frac{\pi}{4} w_0^2 l_{\text{res}}. \quad (2.48)$$

The frequency spectrum of a near-planar cavity is given by

$$\begin{aligned} \nu_{lmn} &= \frac{c}{2l_{\text{res}}} \left[n + \frac{(1+l+m)}{\pi} \arccos\left(1 - \frac{l_{\text{res}}}{R_C}\right) \right] \\ &\approx \frac{c}{2l_{\text{res}}} \left[n + \frac{(1+l+m)}{\pi} \sqrt{\frac{2l_{\text{res}}}{R_C}} \right]. \end{aligned} \quad (2.49)$$

2.3.2 The Jaynes-Cummings model

The system of a single, stationary two-level atom interacting with the single mode of a perfect cavity is described by the Jaynes-Cummings model [112, 113, 114, 115]. The atom is modeled as a two level system with its ground state $|g\rangle$ and excited state $|e\rangle$ split by $\hbar\omega_A$ (see Fig.2.7). The basis of the light field consists of Fock states $|n\rangle$, $n \in \mathbb{N}$ separated by the energy of a single intracavity photon $\hbar\omega_C$. The Jaynes-Cummings Hamiltonian in the rotating wave approximation reads

$$H_{\text{J.C.}} = \frac{1}{2}\hbar\omega_A \hat{\sigma}_z + \hbar\omega_C \left(\hat{a}^\dagger \hat{a} + \frac{1}{2}\right) + \hbar g(\mathbf{r})[\hat{\sigma}_+ \hat{a} + \hat{a}^\dagger \hat{\sigma}_-], \quad (2.50)$$

where \hat{a}^\dagger and \hat{a} are the photon creation and annihilation operators, respectively and $\hat{\sigma}_+$, $\hat{\sigma}_-$ and $\hat{\sigma}_z$ are the Pauli matrices of the atomic pseudospin. The eigenvalues of $\hat{\sigma}_z$ applied to $|e\rangle$ and $|g\rangle$ are $+1$ and -1 , and $\hat{\sigma}_+ = |e\rangle\langle g|$ and $\hat{\sigma}_- = |g\rangle\langle e|$ are the raising and lowering operators, respectively. Without interaction, the states $|g, n+1\rangle$ and

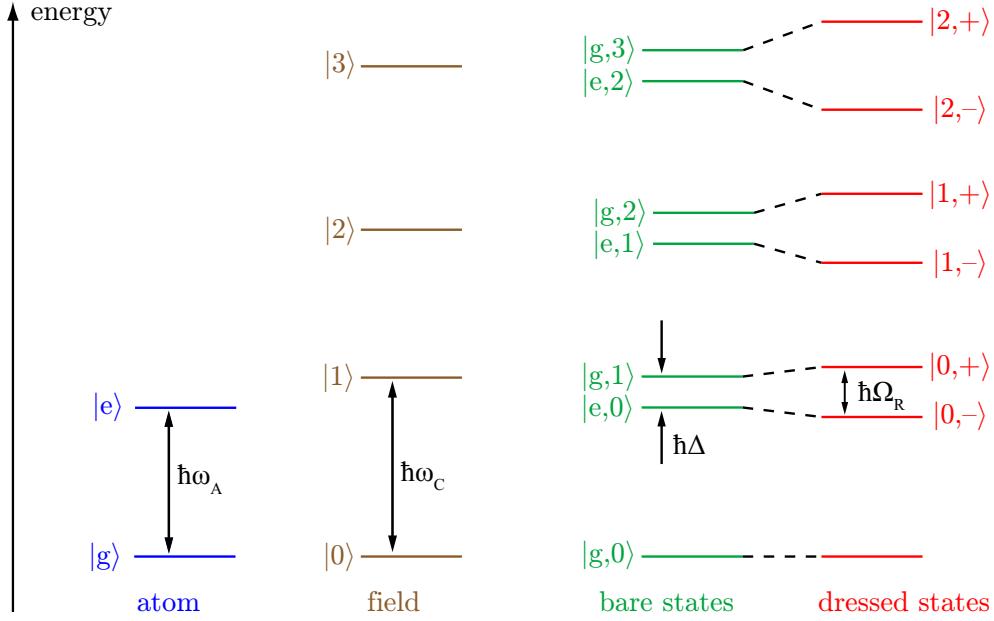


Figure 2.7: Energy diagram of the James-Cummings model. The combined system of a two-level atom (blue) and a single cavity mode (yellow) can be expressed in the bare state basis (green). Introducing a coupling between the two systems leads to the dressed states (red) of the atom-cavity molecule.

$|e, n\rangle$ are split by $\hbar\Delta$, where $\Delta = \omega_C - \omega_A$ is the detuning between the cavity resonance frequency and that of the atomic transition. The coupling between the two systems leads to a splitting of $\hbar\Omega_R$ with the Rabi frequency given by $\Omega_R = \sqrt{\Omega^2 + \Delta^2}$. The atom-field coupling constant $\Omega = 2\sqrt{n+1}g_0\psi(\mathbf{r})$ is a function of the photon number n and the position \mathbf{r} of the atom in the cavity mode. The position dependence of the coupling constant $g(\mathbf{r}) = g_0\psi(\mathbf{r})$ is due to the Gaussian standing wave profile

$$\psi(\mathbf{r}) = \cos(2\pi z/\lambda) \exp[-(x^2 + y^2)/w_0^2] \quad (2.51)$$

determined by λ and the cavity mode waist radius w_0 . The cavity axis is oriented along the z -axis. $2g_0$ is called the single-photon Rabi frequency and g_0 is given by

$$g_0 = \mathbf{d} \cdot \boldsymbol{\mathcal{E}}/\hbar = \frac{d}{\hbar} \sqrt{\frac{\hbar\omega_C}{2\epsilon_0 V_m}} \cos(\angle[\mathbf{d}, \boldsymbol{\mathcal{E}}]), \quad (2.52)$$

where \mathbf{d} is the dipole matrix element of the atomic transition, $\boldsymbol{\mathcal{E}}$ the maximum electric field of a single photon in the cavity and their directions are given by the polarization of the atom and the field mode, respectively.

In Fig. 2.8 the eigenenergies of the bare states (dashed green lines) and the dressed states (solid red lines) are plotted. The energies of the states $|g, 0\rangle$ and $|e, 0\rangle$ are independent of the detuning Δ . The energies of all other bare states $|g, n\rangle$ and $|e, n\rangle$ change

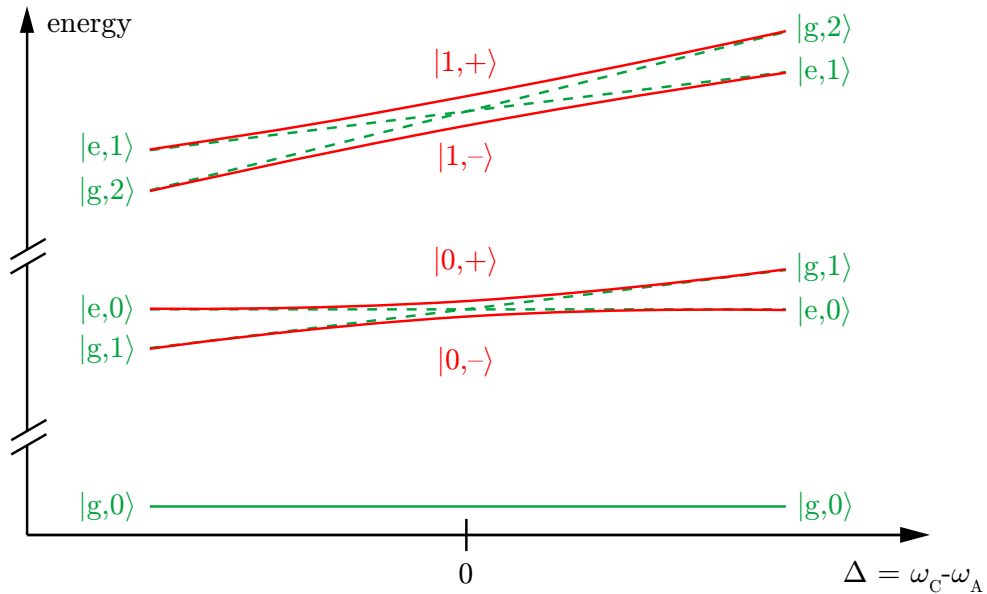


Figure 2.8: Energy diagram of the Jaynes-Cummings model as a function of the detuning Δ . The green dashed lines are the bare states valid for the uncoupled system. The dressed states (solid red lines) result from the coupling between atom and cavity field.

as $n\hbar\Delta$, proportional to the number of field quanta in the cavity mode n . The dressed states $|n, \pm\rangle = c_i |g, n+1\rangle + c_j |e, n\rangle$ are introduced by the coupling between pairs of states $|g, n+1\rangle$ and $|e, n\rangle$. At $\Delta = 0$, there is an avoided crossing and the two dressed states $|n, \pm\rangle$ are split by $\hbar\Omega$.

2.3.3 The dissipative system

The Jaynes-Cummings model describes a closed system. The real-world system however exhibits two dissipative processes, namely the decay of the population of the excited state of the atom due to coupling to the free-space electromagnetic background and cavity losses due to transmission through the mirrors, absorption other than by the atom or scattering. They are characterized by the decay rate of the excited state γ and the decay rate of the field inside the cavity κ , respectively. In addition, the cavity might be excited by an external laser field. To incorporate these couplings to the environment, the Jaynes-Cummings model has to be extended [116, 114].

The atom-cavity system is modeled as being coupled to two baths, which are continua of harmonic oscillators. In the Born-Markov approximation¹, the dynamics of the

¹In the Born approximation, a weak coupling between the system and the environment is assumed, i.e. the influence of the system on the environment is small and the density matrix of the complete

system is governed by the master equation for the density operator ρ of the joint atom-cavity system. In the electric dipole and rotating wave approximation it reads [117, 118]:

$$\dot{\rho} = -\frac{i}{\hbar} [\hat{H}_0, \rho] + \gamma (2\hat{\sigma}_- \rho \hat{\sigma}_+ - \hat{\sigma}_+ \hat{\sigma}_- \rho - \rho \hat{\sigma}_+ \hat{\sigma}_-) + \kappa (2\hat{a} \rho \hat{a}^\dagger - \hat{a}^\dagger \hat{a} \rho - \rho \hat{a}^\dagger \hat{a}) \quad (2.53)$$

$$\begin{aligned} \hat{H}_0 &= H_{\text{J.C.}} + H_{\text{pump}} \\ &= -\hbar \Delta_c \hat{a}^\dagger \hat{a} - \hbar \Delta_a \hat{\sigma}_+ \hat{\sigma}_- + \hbar g [\hat{a} \hat{\sigma}_+ + \hat{a}^\dagger \hat{\sigma}_-] + \hbar \epsilon (\hat{a} + \hat{a}^\dagger) \end{aligned} \quad (2.54)$$

$\Delta_c = \omega_L - \omega_C$ is the detuning between the probe field of frequency ω_L and the cavity resonance frequency ω_C . The detuning between ω_L and the atomic resonance frequency ω_A is denoted by $\Delta_a = \omega_L - \omega_A$. Note that the coupling constant is in general position dependent, even though we have omitted it here for clarity. \hat{H}_0 is the Hamiltonian of the system without dissipation. It consists of the Jaynes-Cummings Hamiltonian and a pump term. The pump rate ϵ is defined such that the mean number of photons inside the resonator without any atom present (i.e. $g = 0$) is given by

$$n = \frac{\epsilon^2}{\kappa^2 + \Delta_c^2}. \quad (2.55)$$

The quantum master equation can be solved numerically, e.g. using a Monte-Carlo wave function approach [119, 120]. It is valid for arbitrarily large photon numbers and therefore takes saturation effects into account. In the weak pump limit, i.e. when the excitation of the atom is small, an analytical solution for the stationary state of a strongly coupled system can be found. The expectation value of the intracavity photon number becomes [118]

$$\tilde{n} = \langle a^\dagger a \rangle = \epsilon^2 \frac{\Delta_a^2 + \gamma^2}{(\Delta_c \gamma + \Delta_a \kappa)^2 + (g^2 - \Delta_a \Delta_c + \gamma \kappa)^2}. \quad (2.56)$$

It is proportional to the cavity transmission and plotted in Fig. 2.9 as a function of the detuning of a probe laser of frequency ω_L from $\omega_0 \equiv \omega_C = \omega_A$. The blue graph shows the spectrum of the bare cavity ($g = 0$) with a maximum at zero detuning and a linewidth of 2κ . The red curve is the spectrum for $g = g_0$. Due to the coupling, the peak is split into two much smaller peaks separated by $2g_0$. This is the so called vacuum Rabi splitting, first observed in 1992 [24]. The two peaks are well separated if the splitting is larger than the width of the peaks.

system can be written as a tensor product of the reduced density matrix and a stationary state of the environment. In the Markov approximation the temporal evolution of the state of the system at time t is assumed to only depend on the current state $\rho(t)$. This approximation is justified if the timescale on which the state of the system changes is large compared to the timescale on which correlations between the system and the environment decay.

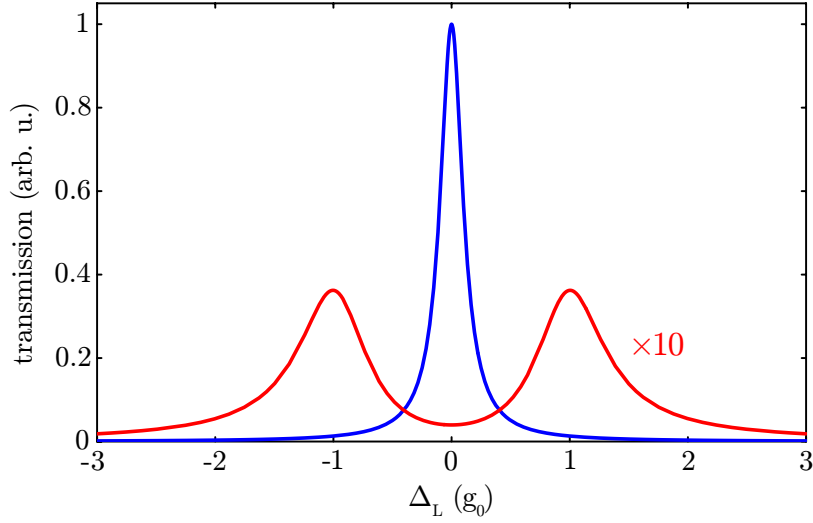


Figure 2.9: Spectrum of the coupled atom-cavity system for $\Delta_L = \omega_L - \omega_0$ with $\omega_0 \equiv \omega_C = \omega_A$. The blue curve shows the transmission of the empty cavity, i.e. with no atom present. The red curve is the transmission with one atom maximally coupled to the cavity ($g = g_0$). Note that the red curve has been enlarged by a factor 10 to make it better visible.

The mean excitation of the atom in the weak pump limit is given by

$$\langle \hat{\sigma}_+ \hat{\sigma}_- \rangle = \epsilon^2 \frac{g^2}{(\Delta_c \gamma + \Delta_a \kappa)^2 + (g^2 - \Delta_a \Delta_c + \gamma \kappa)^2} = \tilde{n} \frac{g^2}{\Delta_a^2 + \gamma^2}. \quad (2.57)$$

The criterion of low atomic excitation can be quantified as $\langle \hat{\sigma}_+ \hat{\sigma}_- \rangle \ll 1$. On resonance and for a system in the strong coupling regime, empty cavity driving fields of $n \ll g^2/\kappa^2$ give a weak field response. Only in this regime the semiclassical theory is valid [121, 122].

Two important dimensionless parameters are frequently used to characterize the coupling in an atom-cavity system. The critical atom number

$$N_0 = \frac{2\gamma\kappa}{g_0^2} \quad (2.58)$$

determines how many atoms are required to alter the intracavity light intensity significantly. The critical photon number

$$m_0 = \frac{\gamma^2}{2g_0^2} \quad (2.59)$$

gives the number of photons necessary to create the saturation intensity I_{sat} in the cavity mode volume V_m with the resonant single-photon interaction rate g_0 . The criterion for low excitation on resonance can be restated as $\tilde{n} \ll m_0$.

Strong coupling regime

Loosely speaking, one enters the strong coupling regime of cavity QED when a photon emitted into the cavity mode is more likely to be reabsorbed by the atom than to escape the resonator and when an excited atom is more likely to emit the photon into the cavity mode than into free space. This is equivalent to N_0 and m_0 both being much smaller than unity. In addition, the coupling time τ , which is the time the atom interacts with the cavity mode, needs to be larger than the inverse coupling strength $1/g$, so that coherent dynamics can evolve. This last criterion is usually easily fulfilled. All these requirements can be combined to give a definition of the strong coupling regime:

$$g \gg \gamma, \kappa, \tau^{-1} \quad (2.60)$$

An atom and a cavity in the strong coupling regime constitute a true quantum system whose properties are drastically changed by the addition or subtraction of a single atom or photon. This immediately implies that the presence of a single atom within the cavity mode volume is easily detected via a large change in the properties of the coupled system. Since in the strong coupling regime the critical photon number m_0 is much smaller than one, only one mean intracavity photon is sufficient to take the system into the regime of strong driving. The strongly coupled system of a single atom and a cavity is instructively called “atom-cavity molecule”. The coupling creates a new system with properties very different from those of its constituents, similar to a molecule formed by two atoms. Because of the large coherence times, a cavity QED system in the strong coupling regime is ideally suited for the implementation of quantum gates and quantum information processing.

Design considerations for optimal coupling

To have an atom-cavity system deep in the strong coupling regime, some design considerations for the cavity are important. The single photon cooperativity parameter

$$C_1 = \frac{g_0^2}{2\gamma\kappa} \propto \frac{\mathcal{F}\lambda^2 l_{\text{res}}}{V_m} \quad (2.61)$$

should be made as large as possible. Because g_0^2 and γ are both proportional to the square of the dipole matrix element d , it cancels. Therefore C_1 is not dependent on d or the linewidth of the transition and consequently the special properties of the atom and the specific transition chosen only enter via the dependence on the wavelength of the transition. The finesse \mathcal{F} is only dependent on the reflectivity of the mirrors [see eqn. (2.35)], so if large cooperativity is the only demand, the highest reflectivity available should be chosen.

When analyzing the best parameter range in the complete region of stable cavities $0 < l_{\text{res}} \leq 2R_C$, the exact formula for the cavity mode volume [eqn. (2.47)] needs to be used instead of the approximate expression in equation (2.48). Inserting eqn. (2.47) into eqn. (2.61), one finds that the cooperativity parameter increases with decreasing cavity length. For a given cavity length, C_1 has a maximum with respect to R_C at $R_C = \frac{2}{3}l_{\text{res}}$. However, both l_{res} as well as R_C can not be made arbitrarily small. Concerning the radius of curvature of the mirrors, the surface quality of the substrate limits the reflectivity via scattering losses, and polishing substrates with very small R_C is technically difficult. Therefore a tradeoff between maximal reflectivity and minimal radius of curvature has to be made. Usual extremely low-loss mirrors are available with radii of curvature down to $R_C = 75$ mm. Consequently, in order to be able to enter the strong coupling regime, a near-planar configuration has to be chosen. In that case

$$C_1 \propto \frac{\mathcal{F}\lambda^2}{w_0^2} \propto \frac{\mathcal{F}\lambda}{\sqrt{R_C l_{\text{res}}}} \quad \text{for } l_{\text{res}} \ll R_C. \quad (2.62)$$

The wavelength of the transition only enters linearly and the cooperativity is inversely proportional to the square root of the cavity length l_{res} . Taking the best mirrors available, the cavity length is the last free parameter and should be made as small as possible. However, a lower bound on l_{res} is set by the requirement of enough space between the cavity mirrors to allow for the transmission of several trapping and imaging beams perpendicular to the cavity axis.

2.3.4 Single atom detection

In the course of this PhD project, the first detection of single atoms from quantum degenerate gases was presented. The interaction of a single atom with the light field inside an ultrahigh finesse cavity is so strong, that the latter is significantly altered by the presence of a single atom [26, 123]. Therefore an atom can be detected via a drastic change in the light transmitted through the cavity.

Several other methods to detect single atoms exist. For a single atom trapped in an optical dipole trap, detection of its fluorescence has been successful [124, 125]. For freely falling atoms, the collection efficiency for the fluorescence photons has been increased using a special mirror setup [126]. For metastable noble gas atoms, another technique exists. Because they are in a metastable excited state, they contain a large amount of internal energy and individual atoms can be detected spatially resolved using a microchannel plate detector [127, 22]. Proposals to use impact ionization of the atoms using a scanning electron microscope [33] or photoionization [32] both followed by detection of the resulting ion have been published lately.

In the following, the qualities of a cavity QED detector will be considered in more detail. The transmission of a probe laser beam through the cavity is monitored, and the

presence of one or several atoms can be inferred from the change in this transmission. From equations (2.55) and (2.56) one finds for the relative cavity transmission

$$\frac{T(\mathbf{r})}{T_0} = \frac{\tilde{n}}{n} = \frac{\kappa^2 (\gamma^2 + \Delta_a^2)}{(\Delta_c \gamma + \Delta_a \kappa)^2 + (g^2(\mathbf{r}) - \Delta_a \Delta_c + \gamma \kappa)^2}, \quad (2.63)$$

with $T_0 = (\epsilon/\kappa)^2$ being the transmission of the empty cavity ($g(\mathbf{r}) = 0$) for the on-resonant probe laser ($\Delta_c = 0$). The position dependence of the coupling constant is due to the Gaussian standing wave profile. Because of this dependence, the position of an atom inside a cavity can (with some ambiguity) be inferred from the transmission [121, 27, 28, 128].

On resonance, i.e. with $\Delta_a = \Delta_c = 0$ one finds

$$\frac{T(\mathbf{r})}{T_0} = \frac{1}{\left(1 + \frac{g^2(\mathbf{r})}{\kappa\gamma}\right)^2} \stackrel{g(\mathbf{r}) \rightarrow g_0}{=} \frac{1}{(1 + 2C)^2}. \quad (2.64)$$

It is obvious that with C on the order of one or larger, the presence of a single atom in the cavity can clearly be detected. The cooperativity parameter $C = NC_1$ is the product of the number of atoms N and the single atom cooperativity parameter C_1 [see eqn. (2.61)]. In a more intuitive picture, as e.g. developed in the framework of optical bistability, the atomic cooperativity parameter C is given by the ratio of the round trip atomic absorption loss divided by the round trip cavity loss due to the transmissivity of the mirrors: $C = \frac{\alpha_0 l}{2\mathcal{T}}$ with α_0 being the absorption coefficient, l the length of the medium and \mathcal{T} the transmissivity of the mirrors [129].

A system is called optically bistable [129, 130, 131, 132] if for one input power two output powers can be observed. It depends on the history of the input which of the two output states is found. Classical theory predicts optical bistability for a cavity with a cooperativity parameter $C > 4$ if the intracavity intensity is on the order of the saturation intensity. In the experiments described in this thesis however, optical bistability is not expected. In the weak field limit the bistability is not observable and for larger driving strengths, the quantization of the cavity field has to be taken into account explicitly. Because this quantization is not included in the semi-classical theory, it is no longer a correct description of the system [133, 121].

The detunings Δ_a and Δ_c are in principle free parameters when setting up a cavity system to detect single atoms. However, there is a certain range of parameters that guarantees high detection efficiency and a large signal-to-noise ratio. To identify those, eqn. (2.63) is plotted in Fig. 2.10(a) for one maximally coupled atom, i.e. with $g(\mathbf{r}) = g_0$. The plot is related to Fig. 2.8, which shows the dressed states $|0, \pm\rangle$ of the atom-cavity molecule. Spectroscopy of the dressed states, setting $E = \hbar\omega_L$ and including dissipation leads to the graph in Fig. 2.10(a). Note however that the axes have been changed. The

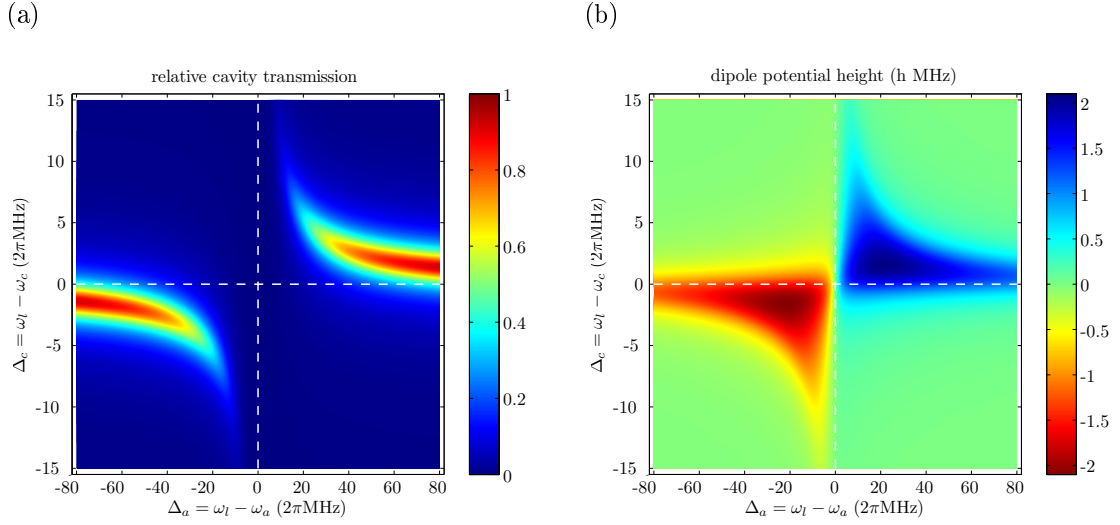


Figure 2.10: (a) Transmission through the cavity with one atom maximally coupled to the light field. This is the solution of equation (2.63), normalized to the transmission of a cavity with no atom and $\Delta_c = 0$. (b) Height of the dipole potential inside the high finesse optical cavity due to the detection light. Negative values of the potential height indicate an attractive potential. The parameters used for both graphs are the same as given in Table 3.2.

red curve in Fig. 2.9 is a cut through Fig. 2.10(a) with $\omega_C = \omega_A$. Two regions of high transmission of the coupled atom-cavity system can be identified.

Forces inside the resonator

When an atom enters the cavity, it is no longer only subject to gravity, but intracavity forces become important [134, 135]. Of course, the situation in a cavity is much more complex than the channeling in a classical standing wave [136], since the position of the atom influences the light field intensity. Velocity dependent forces [117, 118] and diffusion due to spontaneous emission and dipole fluctuations will not be discussed here, even though they can influence the atom's dynamics [137, 138]. Of great importance is the conservative dipole force exerted by the intracavity light field [139, 140]. The associated potential is depicted in Fig. 2.10(b):

$$U = \begin{cases} \frac{-\epsilon^2 \hbar \Delta_a}{\text{Im}(A)} \arctan\left(\frac{\text{Re}(A)}{\text{Im}(A)}\right) & \text{if } \text{Im}(A) \neq 0, \\ \frac{-2\epsilon^2 \hbar \Delta_a}{\text{Re}(A)^3} & \text{if } \text{Im}(A) = 0, \end{cases} \quad (2.65)$$

with $\text{Re}(A)$ and $\text{Im}(A)$ denoting the real and imaginary part of $A = \gamma\kappa + g^2 - \Delta_a\Delta_c - i(\Delta_c\gamma + \Delta_a\kappa)$ respectively [128]. The plot is for one intracavity photon, i.e. with $\epsilon = \kappa$, for maximum coupling $g = g_0$ and with the potential set to zero for vanishing coupling.

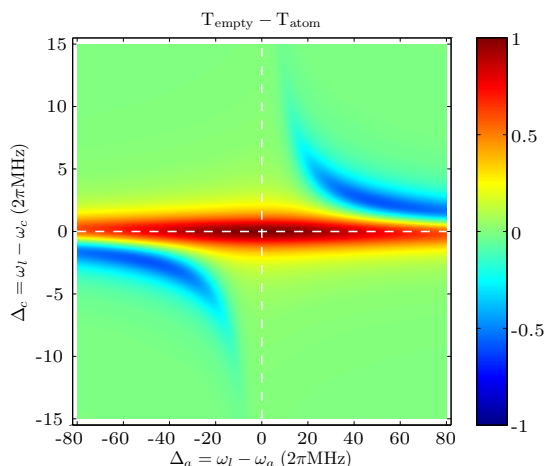


Figure 2.11: Difference between the transmission of the empty cavity and the coupled atom-cavity system. Positive values denote larger transmission for the empty cavity, and therefore in this parameter range atoms manifest themselves as dips in the cavity transmission. In the blue regions (negative values), the presence of an atom shifts the cavity closer to resonance and consequently the signature of an atom inside the cavity is a peak in the cavity transmission.

As can be seen from the plot, the potential strongly depends on the detunings. For $\Delta_a < 0$ (red-detuned) it is attractive, whereas for $\Delta_a > 0$ (blue-detuned) it is repulsive.

The potential is also position dependent, because the coupling strength g varies with the spatial structure of the cavity mode [see eqn. (2.51)]. Therefore the dipole force can be used to trap an atom inside the cavity by ramping up the intensity of the probe laser once the atom enters the resonator [27, 28, 141]. Alternatively, a second, far-detuned laser beam copropagating with the probe beam has been used [142]. The trapped atom is strongly heated, which finally limits the trapping times. To overcome this problem, several cooling schemes for single atoms inside a high-finesse optical cavity have been experimentally tested [143, 144, 145, 146, 29, 147, 148].

Choice of optimal detunings

The detection efficiency of a cavity QED detector strongly depends on the detunings of the probe laser and the cavity with respect to the atomic resonance. Because an atom transit is identified via a change in cavity transmission, a large difference in transmission between the empty cavity (T_{empty}) and a maximally coupled atom-cavity system (T_{atom}) is desirable. The first can be inferred from eqn. (2.32) setting $\nu = \Delta_c$ and is independent of Δ_a . The latter is given by eqn. (2.63) plotted in Fig. 2.10 (a). The difference is proportional to the strength of the signal in single atom detection and is

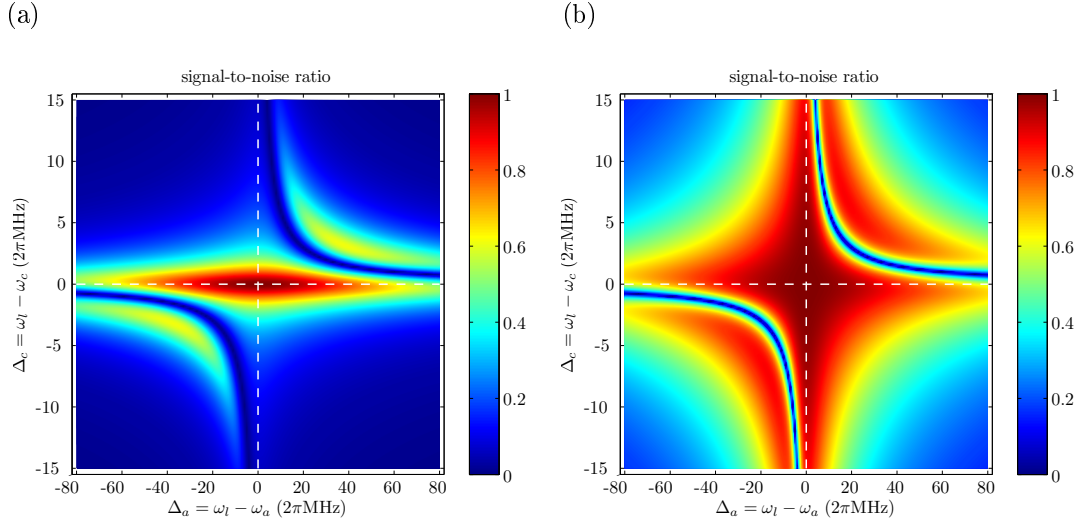


Figure 2.12: Detectability of single, maximally coupling atoms (see text). (a) The power of the probe light incident on the cavity is constant [eqn. (2.66)]. (b) The intracavity photon number is held constant [$\bar{n} = 1$, eqn. (2.67)], independent of whether there is an atom in the cavity or not.

plotted in Fig. 2.11. Two main parameter ranges can be identified. Close to $\Delta_c = 0$ the empty cavity transmission is high and the coupling to an atom will lead to a decrease in transmission. This decrease will be large for $\Delta_a = 0$ and decrease with increasing detuning from the atomic resonance. The second range of parameters is in the vicinity of the dressed states of the coupled atom-cavity system. Since they are significantly away from the cavity resonance for modest Δ_a , the empty cavity transmission will be very small. With an atom present it will increase and peaks will be the resultant manifestation of an atom transit through the cavity. Note that the latter signal is much smaller than the first due to the reduced height of the resonance maxima with an atom present.

The size of the signal alone is not significant to characterize the detectability of single atoms. The shot noise of the probe light constitutes an inevitable uncertainty that has to be taken into account to identify optimal parameters. Determination of this noise depends on the concrete mode of operation. We consider two cases. In the first, the power of the probe light incident on the cavity is held constant, independent on the detunings chosen. The shot noise on T_{empty} and T_{atom} individually is proportional to their square root, because the detected number of photons is proportional to the transmission. Then error propagation gives the total noise as the square root of the sum of the squares of the individual errors. The resulting detectability [128]

$$\tilde{D} = \frac{|T_{\text{empty}} - T_{\text{atom}}|}{\sqrt{T_{\text{empty}} + T_{\text{atom}}}} \quad (2.66)$$

is plotted in Fig. 2.12(a). Obviously, a small parameter range around $\Delta_a = \Delta_c = 0$ yields best results, with the dependence on Δ_a being much weaker than on Δ_c . For every $\Delta_a \neq 0$ there exists a Δ_c so that the transmission of the empty cavity and that with one atom are equal and therefore the detection of single atoms is impossible. In Fig. 2.12(b) the detectability is plotted for an intracavity photon number $\bar{n} = 1$ which is kept constant, independent of whether an atom is in the cavity or not:

$$\tilde{\mathcal{D}}^* = \frac{|T_{\text{empty}} - T_{\text{atom}}|}{\max(\sqrt{T_{\text{empty}}}, \sqrt{T_{\text{atom}}})}. \quad (2.67)$$

In this mode of operation, the power of the light incident on the cavity is not independent on the detunings chosen. It is adjusted such that the intracavity photon number is never larger than one. For detunings where the atom leads to a reduction in the cavity transmission (“dips”), the intracavity photon number of the empty cavity is set to one. If the presence of an atom increases the transmission (“peaks”), $\bar{n} = 1$ when the atom couples maximally to the cavity. This choice of the probe light intensity ensures that a certain power level behind the cavity is never exceeded. This is important for example when a single photon counter is used as a detector and a maximum power level should not be crossed to avoid saturation effects. As can be seen from the plot, this increases the parameter range where single atom detection can be performed with good efficiency. Especially the dependence of the detectability on Δ_c is less pronounced as compared to the case with constant probe power.

Of course, the absolute signal-to-noise ratio (SNR) will to a great extent depend on the number of photons that constitute the signal. The signal is proportional to the integration times and the intensity of the detection light as long as saturation or spontaneous effects are avoided. Therefore long interaction times between atom and cavity and high light intensities are desirable. Their influence on the signal-to-noise ratio and definite values thereof, specific for the apparatus presented in this thesis, will be calculated in Sec. 3.5.5.

3 A hybrid apparatus for BEC and cavity QED

We have designed and built the first apparatus to integrate an ultrahigh finesse optical cavity in a Bose-Einstein condensation system, which—despite recent significant progress [149, 150]—still is a pending, central goal for atom chip experiments [151, 152]. With this experimental setup we are able to detect single atoms from a quantum degenerate source with high efficiency by output coupling an atom laser aimed into the cavity mode. The atom laser allows for a very high rate and controllable delivery of atoms into the cavity mode, which facilitates research of cavity QED in the strong coupling regime with single atoms. Moreover, the cavity as a single atom detector opens up the field of quantum atom optics and is especially useful to probe ultracold atomic clouds *in situ* and time resolved, particularly near the phase transition [153, 154]. Furthermore it is an extremely sensitive tool to detect atomic beams for high precision interferometry measurements and to investigate particle correlations [101].

The experimental difficulties in merging the two research fields of quantum degenerate gases and cavity QED arise mainly from adverse vacuum prerequisites and sophisticated topological requirements on both of these state-of-the-art technologies. For example, limited spatial access prevents the inclusion of a high finesse optical cavity in conventional Bose-Einstein condensation setups.

Our apparatus (Fig. 3.1) overcomes these experimental challenges with a conceptually novel design. It provides good access to the condensate for diverse samples and probes which are modularly integrable on an exchangeable “science platform.” This is rendered feasible by means of a nested vacuum chamber design with a high vacuum (HV) enclosure inside the ultrahigh vacuum (UHV) main chamber and a short *in vacuo* magnetic transport. Two distinct pressure regions are required since the two common stages towards Bose-Einstein condensation, a magneto-optical trap (MOT) for laser cooling and trapping a large number of atoms and evaporative cooling, have conflicting requirements on their vacuum environment. We utilize a short magnetic transport [155, 156] to convey the cloud of cold ^{87}Rb atoms from the MOT to the main chamber, where we perform evaporative cooling to quantum degeneracy. From the Bose-Einstein conden-

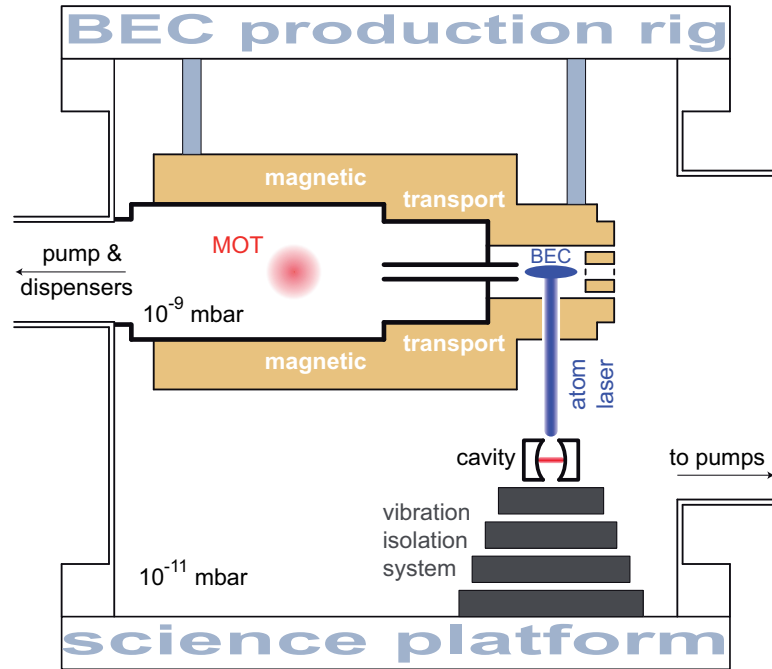


Figure 3.1: Schematic sketch of the experimental setup illustrating the nested vacuum chambers, the short magnetic transport and the “science platform” bearing the ultrahigh finesse optical cavity on top of the vibration isolation system. The atomic cloud captured in the magneto-optical trap (MOT) is transferred through a differential pumping tube into the ultrahigh vacuum region and evaporatively cooled towards quantum degeneracy. We output couple a continuous atom laser from the BEC and direct it to the cavity mode where single atoms are detected.

sate we output couple a continuous atom laser and direct it into the cavity mode. The ultrahigh finesse optical cavity is integrated on the science platform and rests on top of an UHV compatible vibration isolation system which is vital for its stable operation. The cavity is located 36 mm below the BEC and enables us to detect single atoms from thermal and quantum degenerate sources. In the following, the modular experimental building blocks of our hybrid BEC and cavity QED apparatus are presented in more detail, before we describe the operation and highlight the performance of our quantum atom optics experiment.

Parts of this chapter have been published as [157]: A. Öttl, S. Ritter, M. Köhl, and T. Esslinger. ‘Hybrid apparatus for Bose-Einstein condensation and cavity quantum electrodynamics: Single atom detection in quantum degenerate gases’. *Review of Scientific Instruments* **77**, 063118 (2006).

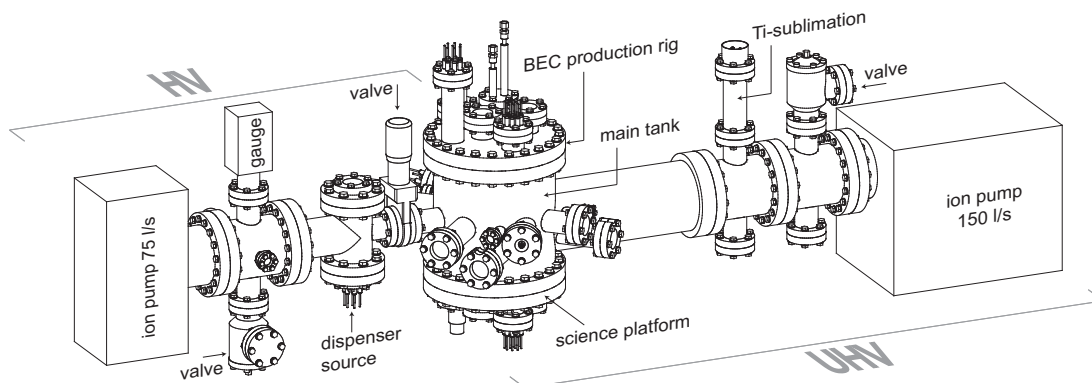


Figure 3.2: Overview of the complete vacuum system showing the pumping sections for the two nested vacuum regions, high vacuum (HV) and ultrahigh vacuum (UHV), respectively. The overall length is close to 2 m. The main tank offers multiple optical and electrical access and is sealed off by two CF 200 cluster flanges called “BEC production rig” and “science platform.”

3.1 Vacuum system

The vacuum system presented here consists of two nested steel chambers, where the higher pressure (HV) MOT chamber is situated inside the lower pressure (UHV) main tank. The HV region houses the alkali dispenser source. Both vacuum regions are pumped separately and a differential pumping tube maintains a pressure ratio of 10^2 . The setup grants multiple optical access for laser cooling as well as for observation and manipulation of the resulting Bose-Einstein condensate.

3.1.1 Main chamber

The objective of the vacuum system (Fig. 3.2) is to attain an UHV environment at 10^{-11} mbar for efficient evaporative cooling of the laser precooled atomic cloud. Center-piece of our vacuum system is the custom-welded, cylindrical main tank of nonmagnetic stainless steel (AISI type 316). It has a diameter of 20 cm and features multiple access in form of optical grade viewports and electrical feedthroughs with standard CF sealing. The viewports are antireflection coated on both sides (see Fig. 3.3). Two custom-made CF 200 cluster flanges cap the main chamber from above and below. The top flange (called “BEC production rig”) features optical and electrical access (see Fig. 3.3), since most of the electromagnetic coil configuration is mounted on this flange and placed inside the UHV. In addition a liquid nitrogen compatible feedthrough is supplied for cooling the magnet coils, and resistive temperature sensors (PT 100) are used to monitor their temperature. The bottom flange (called science platform) serves as an exchange-

able mount for the inclusion of samples and probes into our system. Besides viewports and electrical feedthroughs (Fig. 3.3) to connect to electromagnetic coils, PT100 sensors and the piezo element of the optical cavity design, it includes a cold finger and a 300 l/s nonevaporable getter (NEG) vacuum pump. The core vacuum pumping is performed by a titanium sublimation pump and a 150 l/s ion getter pump. A right angle valve is included in this pumping section for rough pumping the system.

The HV part of the system (Fig. 3.2) connects to the MOT chamber which protrudes into the UHV main chamber and serves as a repository for rubidium atoms. It can be shut off with a gate valve between the MOT chamber and the rubidium dispenser source [158, 159]. The HV region is pumped by an ion getter pump (75 l/s) whose pumping speed can be derated by a rotatable disk inside the tube reducing its conductance. This serves to control the rubidium vapor pressure which is monitored with a wide range pressure gauge. Also a right angle valve is included for rough pumping purposes.

Our rubidium repository consists of seven alkali metal dispensers fixed in star shape to the tips of an eight pin molybdenum electrical feedthrough where the center pin serves as the common ground. Beforehand, the conductors were bent by 90° so that the dispensers aim towards the MOT chamber. Dispenser operation may be viewed through a viewport mounted from above. The dispensers can easily be exchanged without breaking the ultrahigh vacuum in the main chamber by closing the gate valve between the MOT chamber and the dispenser source.

3.1.2 MOT chamber

The MOT chamber as part of the high vacuum region is situated inside the ultrahigh vacuum main tank (Fig. 3.3). However, the fact that both pressure regions are well in the molecular flow regime allows for relatively simple sealing techniques. The purpose of the MOT chamber is to contain a higher background vapor pressure of rubidium atoms for an efficient loading of the magneto-optical trap.

Our MOT chamber was milled out of a single block of nonmagnetic stainless steel (AISI type 316). This material was chosen to reduce eddy currents produced by fast switching of the magnetic fields. Bores of 35 mm diameter give optical access for the six pairwise counterpropagating laser beams forming the magneto-optical trap. These bores are sealed off by standard optical grade laser windows (BK 7) with double-sided antireflection coating and are clamped to the MOT chamber by stainless steel brackets. At the metal glass interface we use thin (0.2 mm) Teflon rings to protect the windows. We also took precautions in the form of ceramic screens to prevent coating of the windows by the titanium sublimation pump. An additional bore provides the connection of the MOT chamber to the HV pumping section and the dispenser source. This connection is sealed against the UHV main tank with a tight fit stainless steel bushing inside

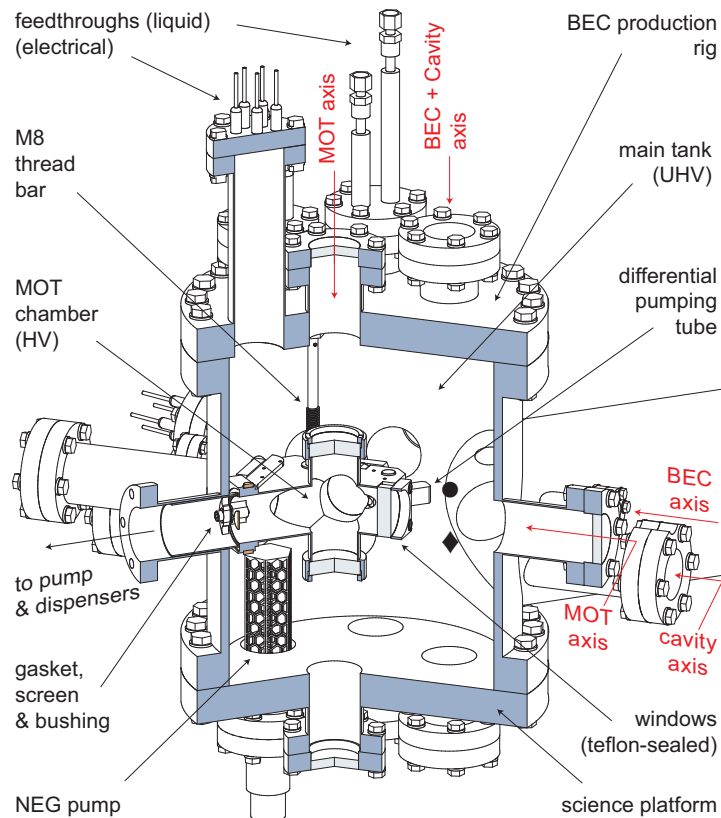


Figure 3.3: Section through the UHV system illustrating the realization of the nested chambers design and revealing the details and objectives of the divers optical axes. The position of the BEC and cavity are marked by (●) and (◆), respectively. The high vacuum MOT chamber is suspended from the “BEC production rig” and sealed by a tight fit bushing against the UHV main tank. The “science platform” provides space for additional components such as the ultrahigh finesse optical cavity. Note that for clarity in the illustration, the magnet coil configuration (Fig. 3.5) and the optical cavity assembly (Fig. 3.8) are omitted in this figure.

the CF 40 socket. The bushing is tightened to the MOT chamber thereby pressing its circular knife edge into a custom-made annealed copper gasket. A screen to prevent a direct line of sight from the hot dispensers to the center of the MOT is included in the laser cut gasket.

The MOT chamber is sandwich mounted between the two magnet coil brackets for the magnetic transport (see Sec.3.2) and simultaneously functions as a spacer for the magnet coil assembly. The whole structure is suspended from the top flange by four M8 thread bars and represents our BEC production rig. A differential pumping tube interfaces the MOT chamber with the main tank. It serves for conveying the cloud of cold

atoms with the magnetic transport from the MOT into the UHV main chamber. The aluminum differential pumping tube is mounted with a press fit in the MOT chamber and can be exchanged. It has an inner diameter of 6 mm over a length of 45 mm and can maintain a differential pressure of 10^2 - 10^3 depending on the actual pumping speed in the UHV main chamber. Its conductance for rubidium at room temperature is about 0.31/s.

3.1.3 Installation

All components of the system were electropolished (the custom-welded parts were pickled afore), cleaned, and air baked at 200°C before assembly [160]. Additionally, all critical *in vacuo* materials like Stycast 2850 FT and Kapton used for the magnet coil brackets (see Sec.3.2), Viton A, and Wolfmet utilized for the vibration isolation stack (see Sec.3.3) as well as plastic (Teflon and Vespel) and ceramic (Macor and Shapal) parts were externally outgassed by vacuum baking them at 200°C. The bakeout [161] of the fully assembled system was performed at 120°C which is the maximum temperature rating of the piezotube used in our optical cavity assembly. The ultimate attainable pressure in the UHV system is 3×10^{-11} mbar. It is measured directly inside the main chamber in close proximity of the magnetic trap for Bose-Einstein condensation. In the HV part we maintain a pressure in the range of 10^{-9} mbar.

3.2 Magnetic field configuration

A magnetic transport [155, 156] is a reliable and controlled way to transfer the cold atomic cloud from the MOT to a region of considerably lower background pressure for evaporative cooling. Only an *in vacuo* magnet coil arrangement in conjunction with nested vacuum domains allows for a short transport design and grants spacious access volume inside the main chamber. However, care must be taken to meet the UHV requirements with the materials chosen for the magnet coil structure.

Besides spatial and optical accessibility, the requirement on the magnetic trap is mainly magnetic field stability to enable stable atom laser output coupling. Therefore we employ a magnetic quadrupole Ioffe configuration (QUIC) trap [94], because its simplicity allows for a compact design and ensures an easy and stable operation at very low power consumption (~ 2 W). A magnetic shielding enclosure and additional *in vacuo* coils for manipulating atoms in connection with the cavity round off the magnetic configuration of the system.

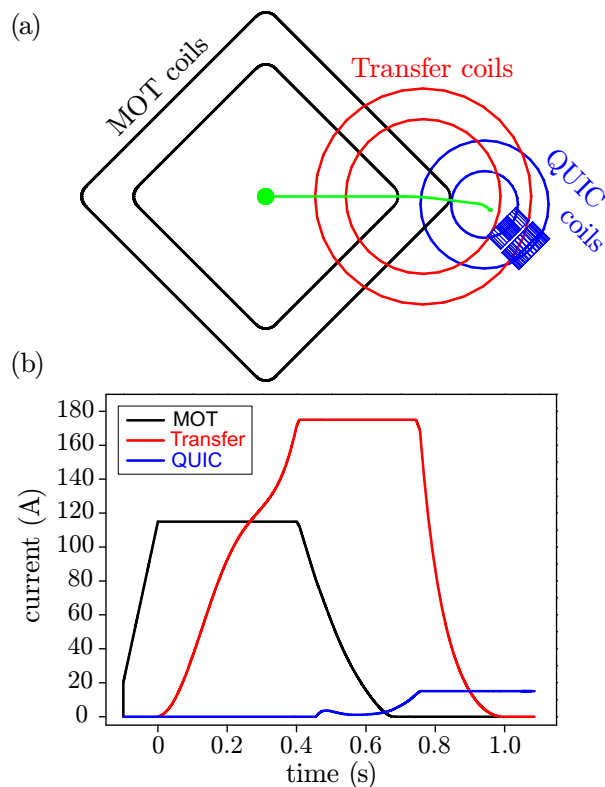


Figure 3.4: (a) Top view of the arrangement of coils for the magnetic transport. The green line denotes the trajectory of the atomic cloud from the MOT (filled circle) into the QUIC trap. (b) Temporal sequence of currents through the different coils to realize the compression of the cold atomic cloud (negative times) and the magnetic transport.

3.2.1 Magnetic transport

The magnetic transport design consists of two partially overlapping electromagnetic coil pairs (called “MOT coils” and “transfer coils”) producing quadrupole potentials and the final QUIC trap coils [Fig. 3.4(a)]. The overall potential minimum can be moved over a distance of 82 mm so that the cold atoms in a low field seeking Zeeman state are conveyed from the position of the MOT directly into the final magnetic QUIC trap. The transfer coil pair provides sufficient overlap between the two to achieve a smooth transfer of the magnetic potential without significant heating of the cold atomic cloud.

The magnet coils were wound from rectangular copper wire (3×1 and 1×1 mm) for optimal filling fraction. We chose Kapton film isolated wire which is temperature durable and suitable in the ultrahigh vacuum environment. The coils were integrated in two mirror-inverted, custom-made copper brackets and encapsulated with Stycast 2850 FT, a

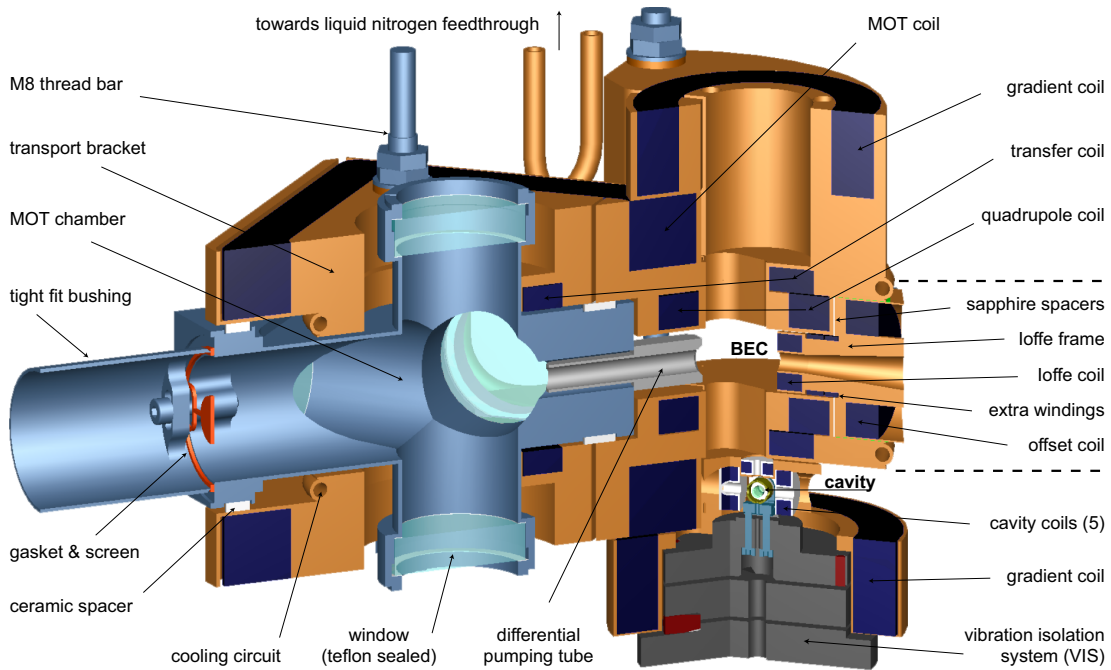


Figure 3.5: Section through the complete assembly inside the main vacuum chamber. It illustrates the arrangement of magnet coils, the inner chamber, and the cavity with respect to each other. Functional units of the magnet coil configuration are the two transport brackets that sandwich the inner chamber and the laterally mounted Ioffe frame (elements between dashed lines). These parts, including the top gradient coil, are fixed to each other and mounted from the top flange. The optical cavity on top of the vibration isolation system, the surrounding coils, and the bottom gradient coil are mounted on the science platform.

thermally conductive epoxy. The brackets are slotted in order to suppress eddy currents from switching the magnetic field. The magnet coil assembly was fixed in a sandwich structure around the MOT chamber and suspended from the top flange by M8 thread bars (Fig.3.5). The complete assembly including the QUIC trap represents the BEC production rig.

A cooling system to remove the heat dissipated by the electromagnetic coils is supplied in form of a copper pipe with 4 mm inner diameter. It is soldered in a loop around each coil bracket and connected to the liquid nitrogen feedthrough. A temperature stabilized recirculating chiller permanently pumps pure ethanol cooled to -90°C through the system. Thereby we maintain a maximum operating temperature below 0°C . This in turn lowers the power consumption of the magnet coils whose surface temperature is monitored with PT 100 sensors and interlocked to the power supplies.

The geometry and arrangement of the magnetic transport coils [Fig. 3.4(a)] are dominated mainly by constraints set by the size of the MOT chamber, the required length

of the differential pumping tube, and the optical access to the MOT, BEC, and cavity. For instance, the square shape of the MOT coils best achieves a large overlap with the transfer coils while granting optical access to the cavity axis. The aspect ratio A/R of the coil separation ($2A$) to the coil radius (R) could be tuned to a balanced tradeoff between a maximally strong ($A/R = 0.5$) and a maximally long ($A/R = 0.87$) linear gradient region [162]. The anti-Helmholtz configuration is advantageous for tight confinement and deep trap depths whereas long linear gradients yield large handover regions between two coil pairs. Furthermore, the power consumption of a coil pair for a given field gradient can be minimized by choosing a well matched ratio of axial to radial windings.

In order to find an optimum current sequence for the magnetic transport [155] we calculate the magnetic field of the coil configuration analytically and discretize it along the transport axis on a $100\ \mu\text{m}$ grid. The currents needed to transfer the magnetic minimum smoothly from the MOT to the QUIC are then computed numerically in accordance with several constraints. Limited by a maximum available electrical current we optimized the magnetic field gradients and trap depths especially during the handover. Furthermore, we tried to minimize deformations of the trapping potential. The resulting spatial sequence of currents per coil is converted into a temporal sequence including an acceleration and deceleration phase by taking into account the limited bandwidth of the current control servo [Fig. 3.4(b)].

The magnetic transport sequence initiates with a fast ($400\ \mu\text{s}$) ramp to 20 A in the MOT coils after magneto-optical trapping and optical pumping the cold atoms into a low field seeking state. The ramp needs to be fast with respect to the expansion of the cloud but adiabatic on the spin degree of freedom. It is followed by a slow (100 ms) compression of the atomic cloud to the maximum field gradients. Increasing the current in the transfer coils pulls the atoms towards their center, and by decreasing the MOT coil current the zero of the potential is handed over [Fig. 3.4(b)]. The field of the QUIC is aiding at this point to maintain a constant aspect ratio. The magnetic transport finishes by ramping down the current through the transfer coils in favor of the QUIC coils. The atomic cloud is conveyed through the differential pumping tube directly into the magnetic QUIC trap which stays on for the subsequent evaporative cooling stage.

The trajectory of the magnetic transport [Fig. 3.4(a)] is slightly bent so that atoms in the final magnetic trap position have no direct line of sight into the higher pressure MOT chamber. This suppresses background gas collisions which would shorten the lifetime of the Bose-Einstein condensate. The bend is achieved by laterally offsetting the center of the QUIC trap by 3 mm from the differential pumping tube.

The MOT and transfer coils are powered by 5 kW dc power supplies. However, since their internal current control bandwidth is too slow to sample the time-current sequence

		MOT	Transfer	QUIC
Resistance	(m Ω)	200	50	300
Inductance	(μ H)	1000	70	450
Maximum current	(A)	115	170	15
Maximum field gradient	(G/cm)	310	290	320

Table 3.1: Electromagnetic properties of the magnet coils.

for the MOT coils, we externally feedback control it by a closed-loop servo. It is implemented with a current transducer and a MOSFET bench. The fast initial ramp to 20 A is additionally supported by current from four large capacitors (15 mF each) charged to 60 V. The electromagnetic properties of the coils with resulting maximum currents and field gradients are listed in Table 3.1.

The magnetic transport is performed over a period of 1 s. We maintain a minimum trap depth of ~ 70 G equivalent to about 2 mK. The total power required is approximately 2 kW which corresponds to an average power consumption of ~ 34 W at a duty cycle of 1/60.

3.2.2 QUIC trap

The magnetic QUIC trap consists of three coils connected in series. This is advantageous to diminish relative current fluctuations and therefore magnetic field fluctuations. Two coils (called “quadrupole coils”) produce a quadrupole field, and one smaller coil (called “Ioffe coil”) mounted orthogonally between the quadrupole coils lifts the magnetic zero to a finite value and adds a curvature to the resulting potential [94]. Having a nonzero magnetic field minimum is crucial when evaporatively cooling atoms towards quantum degeneracy in order to circumvent losses due to Majorana spin flips.

The geometry of the QUIC trap potential is approximately cylindrically symmetric with respect to the Ioffe coil axis. Along this direction the curvature and therefore the confinement is weaker than in the radial directions. In our case this results in cigar shaped Bose-Einstein condensates with an aspect ratio of 5:1. The exact position and dimension of the Ioffe coil are very critical to yield the desired magnetic bias field B_0 which should be on the order of a few Gauss. A low bias field is preferential because the trap frequencies scale as $B'/\sqrt{B_0}$, where B' is the magnetic field gradient and high trap frequencies permit faster and more efficient evaporative cooling.

The construction of the Ioffe coil is done in the same way as for the transport coils. It is integrated in a slotted copper frame and potted with Stycast. The Ioffe frame is mounted laterally between the transport coil brackets which hold the quadrupole



Figure 3.6: Photograph of the preassembled mu-metal hull before it is mounted around the main vacuum tank. It consists of seven large and several small individual pieces.

coils. Additionally, the Ioffe frame serves as a spacer for the two transport brackets. The mechanical contact is accomplished with sapphire sheets in order to prevent eddy currents by simultaneously maintaining good thermal conductivity (Fig. 3.5). The large mass of the complete magnet coil structure functions as a thermal low-pass filter which contributes to the good temperature stability. In the Ioffe frame we have integrated additional coils on the same axis as the Ioffe coil to be able to manipulate the final trap geometry inside the vacuum system after bakeout. Two few-winding coils are employed to fine-tune the value of the magnetic field minimum B_0 . One larger coil (called “offset coil”) a little further away from the trap center can be used to change the aspect ratio of the trap and make it approximately spherical. Furthermore, the Ioffe frame features a conical bore which allows us to image the BEC through the center of the Ioffe coil.

The electrical connections of the coils forming the magnetic QUIC trap are realized outside the vacuum. We have included a 1.4 MHz low-pass filter in parallel to the Ioffe coil to avoid any radio frequency pickup because of its low inductance of 4 μH . The QUIC trap is operated with a 150 W power supply specifically tuned to our inductive load. The average power consumption of the magnetic trap is maximally 60 W but can be as low as 2 W when operated at 3 A (see Sec. 3.4).

3.2.3 Magnetic shielding

We clad the main vacuum chamber in a mu-metal shielding (Fig. 3.6) of 1 mm thickness to minimize the influence of residual external magnetic field fluctuations on the cold atoms. A magnetically quiet environment is essential for stable continuous wave (cw) operation of the atom laser.

Mu-metal is a magnetically soft nickel alloy with a very high relative magnetic permeability $\mu_r \sim 10^5$ which attenuates magnetic fields inside an enclosure. The magnetic shielding factor S of a sphere of mu-metal with a thickness d and an inner radius of r_i is roughly $S = \frac{2\mu_r d}{3r_i} + 1$ [163]. Magnetic field lines penetrate an opening roughly as far as its diameter. Therefore we have attached a stub around the pumping tube of the main vacuum tank to attain a better aspect ratio at the position of the BEC. The design of the mu-metal hull was aided by computer simulations using an electromagnetic CAD program. The mu-metal was machined and cured as recommended by the manufacturer. After demagnetization we have measured a dc magnetic extinction ratio of ~ 40 in the vertical and ~ 100 in the horizontal direction at the position of the BEC.

3.2.4 Auxiliary coils

Since the mu-metal shielding prevents any manipulation of the atoms with external magnetic fields, we have arranged supplementary magnet coils inside the mu-metal enclosure. All extra coils were potted with Stycast either in a slotted copper or Shapal frame for good thermal conductivity and mechanical sturdiness.

Two large coils (called “gradient coils”) are included in the main vacuum chamber to compensate the gravitational force for the weakest magnetic sublevel (30.5 G/cm) with 22 A. Their total resistance and inductance is about 0.2Ω and 0.9 mH, respectively. The gradient coils were mounted inside the vacuum chamber on the transport bracket (Fig. 3.5) and on the science platform around the cavity (Fig. 3.8), respectively. With the latter we should be able to reach the widest Feshbach resonance of ^{87}Rb (at ~ 1008 G) [164] at the position of the cavity.

Around the cavity we have placed two pairs of tiny coils (4Ω , 0.4 mH) along and perpendicular to the cavity axis (Fig. 3.5). They can be used to create magnetic field gradients of about 200 G/cm (with 1 A) for tomography experiments. In combination with a fifth tiny coil (1Ω , 0.1 mH) mounted above, a magnetic trap at the position of the cavity can be formed. These five small coils (called “cavity coils”) were wound from 0.04 mm^2 Kapton isolated copper wire on Shapal frames to be penetrable by radio frequency.

In addition to the magnet coils inside the vacuum tank we have wound three mutually orthogonal pairs of large extra coils around the main tank. They are still within the mu-

metal hull and serve to produce homogeneous magnetic fields, for example for optical pumping.

3.3 Science platform and cavity setup

We have designed this apparatus with attention to versatile access for samples and probes to the BEC. Therefore we have implemented two independent sections of complementary functionality, i.e. the BEC production rig (see Secs. 3.1 and 3.2) and the science platform. The latter is a modular, interchangeable flange, which in the current configuration supports our single atom detector in form of the ultrahigh finesse optical cavity. The design of the cavity was guided by the need for stability, compactness, and ultrahigh vacuum compatibility. It rests on top of a passive vibration isolation stack which can be positioned on the science platform.

3.3.1 Cavity design

The Fabry-Pérot optical cavity is formed by two dielectric Bragg mirrors of ultrahigh reflectivity and ultralow scattering losses. They consist of $\text{SiO}_2/\text{TiO}_2$ coating on BK7, specified by the manufacturer to provide $\mathcal{T} < 4 \times 10^{-6}$ and $\mathcal{L} < 10^{-5}$ (“best effort”). The reflection band is 40 nm wide and centered around 780 nm. We have determined a final quality factor of $Q = 1.6 \times 10^8$ after bakeout from the linewidth of the cavity ($\Delta\nu_c = 2.4$ MHz). The initial Q immediately after cleaning the mirrors was higher by about a factor of two. The cylindrical mirrors (3 mm diameter, 4 mm length) having a radius of curvature of 75 mm are separated by 176 μm which results in a Gaussian mode waist of $w_0 = 25.5 \mu\text{m}$. A detailed characterization of the optical properties of the cavity is given in section 3.4.4.

Each mirror was bonded with superglue into a specifically fabricated ceramic (Shapal) ring structure. It positions and fixes the mirror inside the piezoceramic tube [123]. A piezoelectric actuator is required to fine-tune the length of the cavity and as the actuator for the cavity lock (see Sec. 3.4.3). The $l = 7$ mm long piezo tube has inner and outer diameters of $d_i = 5.35$ mm and $d_o = 6.35$ mm, respectively. It is equipped with nonmagnetic wraparound electrodes (silver) which allow the inner electrode to be contacted from the outside. Additionally, the piezo tube features four radial holes of 1 mm diameter for lateral access of atoms and lasers perpendicular to the cavity axis. The piezo is made of BM532 which features an especially high charge constant of $d_{31} = -270 \times 10^{-12}$ C/N. The excursion can be calculated as $\Delta l/V = d_{31}l/t = 3.8$ nm/V, with $t = (d_o - d_i)/2$ being the wall thickness of the tube. To be able to set the cavity at resonance with light of arbitrary frequency, the cavity length needs to be changeable by $\lambda/2$, which is 415 nm. The effective length of the piezo tube is reduced by the wrap

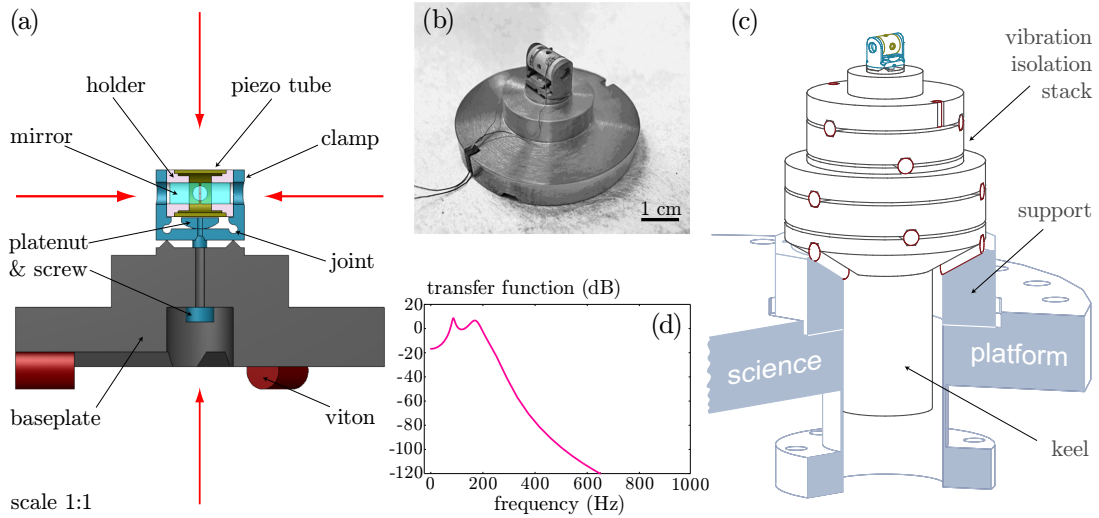


Figure 3.7: Elements of the optical cavity implementation. (a) Plane cut through the assembled cavity design where the arrows indicate optical access. (b) Photograph of the cavity setup. The electrical leads for the piezotube are pinched in a slotted Viton piece to efficiently decouple the cavity from the environment. (c) The cavity assembly resting on top of the vibration isolation stack which is positioned on the science platform. (d) Modeled frequency response of our vibration isolation stack.

around electrodes and the four holes. We experimentally find that tuning over a free spectral range at 830 nm is accomplished by changing the applied voltage by about 190 V (~ 2.2 nm/V).

The cavity assembly is mounted by a specifically designed compact fixture (called “clamp”) making use of mechanical joints [Fig. 3.7(a)]. It was manufactured by spark erosion from titanium in order to be nonmagnetic while having good elastic properties. Further design considerations aimed at high mechanical eigenfrequencies to avoid resonances within the bandwidth of the cavity lock (~ 40 kHz), that means a small size and high stiffness are favorable. We estimate the lowest eigenfrequency of our fixture with a simple mechanical fixed-hinged beam model [165] to be ~ 50 kHz.

Our design of the cavity mount consists of the \sqsubset -shaped clamp and a baseplate with integrated bearings to which the clamp is tightened with a plate nut. It transfers the downward force onto the cavity assembly and firmly holds it together. Moreover, it provides the piezo with a load. A hole of 1.2 mm diameter in the baseplate and plate nut grants optical access to the cavity from below. This cavity setup is highly modular and easily interchangeable because it freely rests on the vibration isolation stack [Fig. 3.7(b)].

3.3.2 Vibration isolation system

The aforementioned baseplate simultaneously acts as the top mass of our vibration isolation stack [166] which consists of five layers of massive plates (Wolfmet) with rubber dampers (Viton A) in between [Fig. 3.7(c)]. Viton has good vibration damping properties and is suitable for an ultrahigh vacuum environment. The 5 mm diameter Viton pieces rest in hexagonal grooves that are radially arranged in 120° graduations. Consecutive layers are rotated by 60° to prevent a direct “line of sound.” Hexagonal shaped grooves best avoid squeezing and creeping of the rubber and provide good lateral stability. Position, angle, and tilt reproducibility of this structure are excellent because of the frustum shaped bottom mass with keel. It centers the stack in an inverted, truncated conelike support and assures mechanical stability by lowering the center of mass to below the support points. The complete stack has a central 10 mm bore for vertical optical access to the cavity.

Its damping properties can be modeled by regarding the structure as a system of coupled masses and springs [167] and calculating its frequency dependent transfer function [Fig. 3.7(d)]. For attenuation at low frequencies large masses and small spring constants are favorable [168, 169]. Therefore we have fabricated the plates from a heavy metal alloy (Wolfmet) and employed short (10 mm) Viton pieces. Our vibration isolation stack works well for acoustic frequencies above 200 Hz.

Additional precautions to counter low-frequency excitations such as building vibrations include setting up the experiment on a damped rigid optical table in a basement laboratory having its own independent foundation and choosing a position with little floor vibration within this laboratory. The quality of the vibration isolation system is such that we could easily operate the cavity in the vicinity of a turbo-molecular pump. Furthermore the vibration isolation stack kept the cavity in place when the whole optical table accidentally dropped by about 2 cm as we tried to tilt it.

3.3.3 The science platform layout

The self-contained, interchangeable science platform flange was prepared to support and align the complete cavity mount. Its layout provides manual positioning ability of the cavity mount by ± 2 mm along and perpendicular to the cavity axis, respectively. This is rendered feasible by an octagonal support (nonmagnetic steel) of the vibration isolation stack which can be deterministically moved and fixed in a larger octagonal cutout on the flange.

The second objective of the support is to sustain the arrangement of cavity coils and the gradient coil (see Sec. 3.2.4), which are positioned around the cavity without direct contact to it. The coil assembly is mounted on two nonmagnetic steel sustainers which

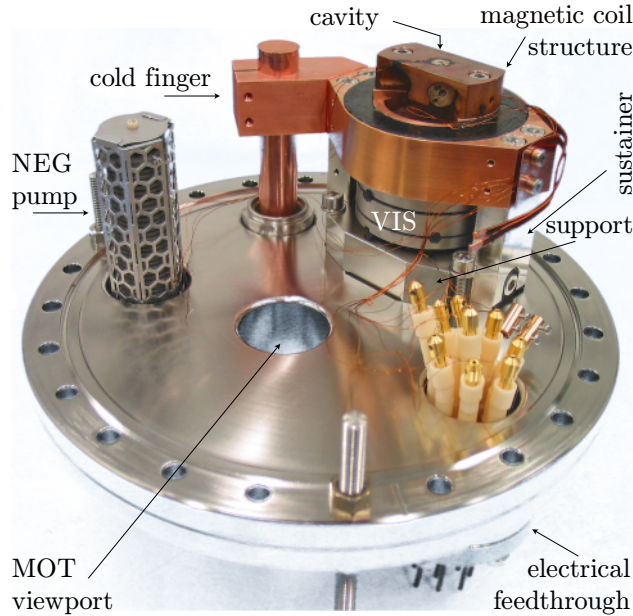


Figure 3.8: Photograph of the mounted science platform. The support bears the vibration isolation system (VIS) and the magnetic coil structure which surrounds the optical cavity.

are fixed to the vibration isolation support.

In order to remove the heat dissipated by the electromagnetic coils, we have connected the copper bracket of the gradient coil to a power feedthrough serving as a heat bridge (“cold finger”). Outside the vacuum the 19 mm diameter copper conductor can be connected to the cooling circuit and cooled to -90°C . The copper rod serves as the main drain for the heat because of the low thermal conductivity of the steel sustainers and support.

The mounting of the independent BEC production rig and science platform within the main vacuum chamber has to be noncontact but within a fraction of a millimeter. This results in a final position of the optical ultrahigh finesse cavity being 36.4 mm below the BEC. The orientation of the cavity axis is at 90° with the symmetry axis of the magnetic trap (Ioffe axis).

3.4 Performance of the apparatus

The design of our setup has been carried out along complex performance objectives, yielding the device presented in the preceding sections. The capabilities of the apparatus will become clear in the following sections, where we characterize its performance and

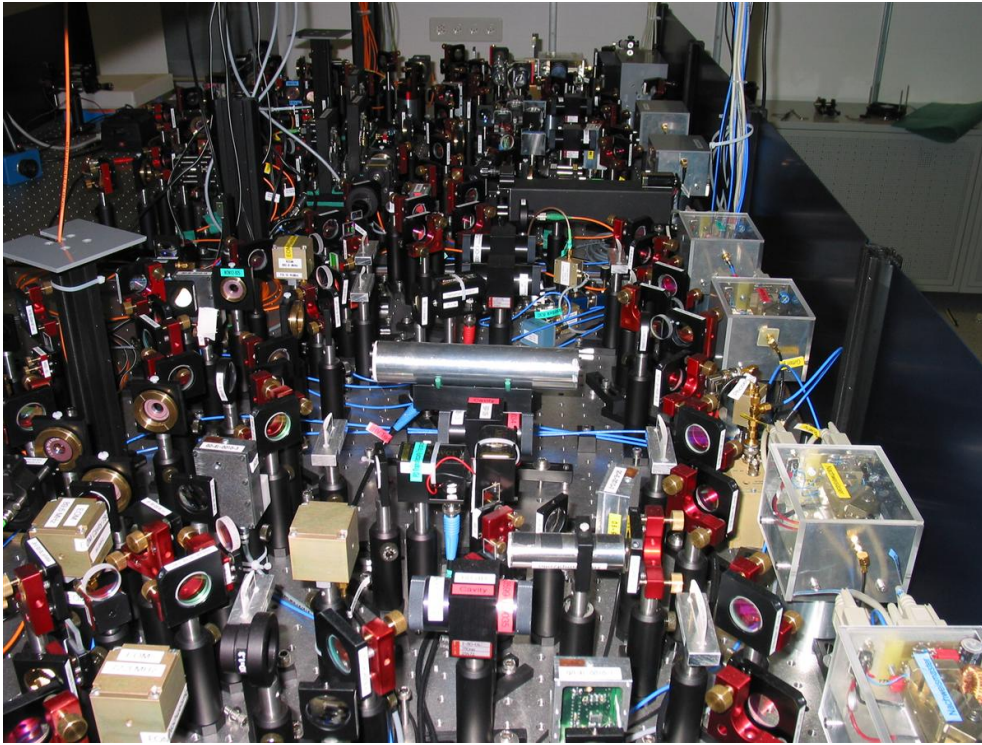


Figure 3.9: Photograph of the laser setup. The square boxes on the right side of the table are grating stabilized diode lasers. The four lasers in the foreground and the corresponding optics are used for stabilization and probing of the ultrahigh finesse cavity. The laser system used for laser cooling, optical pumping and imaging resides in the rear part of the table.

present initial experiments highlighting the new experimental possibilities. One example is the first detection of single atoms from a quantum degenerate gas using a cavity QED detector.

The experiment is operated periodically with a cycle time of 60 s. During each cycle we produce a new BEC from which we output couple an atom laser. It is directed to the ultrahigh finesse optical cavity situated 36.4 mm below the BEC where single atoms are detected. The cavity is probed by a resonant laser and its length is actively stabilized by an off-resonant laser with respect to the atomic transition. The experimental sequence is fully computer controlled using a software developed in Borland C++. 64 digital channels, 16 analog channels (8×12 bit and 8×16 bit), and a General Purpose Interface Bus (GPIB) for control of frequency synthesizers via the IEEE 488 interface connect the computer with the elements of the experimental setup.

The experiment is distributed on two self-contained optical tables, one for the laser system and one for the vacuum apparatus. They are linked by optical fibers. A picture

of the laser table is shown in Fig. 3.9. The laser setup for locking and probing the ultrahigh finesse optical cavity covers the front half, whereas the optics for laser cooling and probing the BEC are at the rear end of the table.

3.4.1 BEC

We form a Bose-Einstein condensate of ^{87}Rb in dilute atomic vapor, starting with a dispenser-loaded magneto-optical trap (MOT). After loading the atoms into a magnetic trap and subsequent magnetic transport, the atoms are cooled to quantum degeneracy by means of rf-induced evaporation [45, 156].

The MOT operates on the D_2 line of ^{87}Rb ($5^2S_{1/2} \rightarrow 5^2P_{3/2}$) with a linewidth of $\Gamma = 2\pi \times 6$ MHz at a wavelength of $\lambda = 780$ nm. About 100 mW of light at the cooling transition $|F = 2\rangle \rightarrow |F' = 3\rangle$ are available from a tapered amplifier which is injection seeded with a home built external cavity diode laser [170]. To allow for frequency tuning, the laser is offset-locked [171] to the $|F = 2\rangle \rightarrow |F' = 2\rangle$ transition with an offset of about 250 MHz. An additional laser (called “repumper”), directly locked to the $|F = 1\rangle \rightarrow |F' = 2\rangle$ transition by Doppler-free rf-spectroscopy [172], is used to avoid atomic losses into the $|F = 1\rangle$ dark state and delivers a power of 1 mW in each MOT beam.

An important design parameter is the size of the MOT beams. For a given laser power, the MOT beam diameter D should be chosen such that an intensity of about $5 \times I_{\text{sat}}$ at the center of the MOT beams is reached [173]. The maximum number of atoms that can be trapped in a MOT is proportional to $D^{3.6}$ if the intensity is kept constant [174, 175]. We chose a beam diameter of $D = 31.2$ mm; small enough to not lose more than 3% of the laser power at the windows in the inner chamber with a diameter of 34 mm. With 17 mW in each of the six MOT beam one finds an intensity of about $2.7 \times I_{\text{sat}}$ at the center of the beam and even at its edges (limited by the windows of the inner chamber) there is still an intensity of about I_{sat} to assure efficient cooling. For optimum collection efficiency the detuning of the cooling laser from the $|F = 2\rangle \rightarrow |F' = 3\rangle$ transition is set to -3Γ .

During the first 20 s of each cycle we load the magneto-optical trap with atoms from the pulsed alkali dispenser source [159]. The dispensers are operated at ~ 7 A with a temporal offset of -3 s to the actual MOT phase. Only atoms with a velocity below the calculated capture velocity $v_c = \Gamma/k = 4.7$ m/s for the ^{87}Rb D_2 line are captured and cooled. The number of atoms with $v < v_c$ in the Boltzmann distribution is proportional to v_c^4 .

For the magneto-optical trap we set a magnetic field gradient of 10 G/cm by running a current of 3.5 A through the MOT coils. No earth field compensation is required

because of the mu-metal shielding. We collect about 1×10^9 atoms in the MOT before we switch off the magnetic field and sub-Doppler cool the atoms in a 10 ms optical molasses phase. While the lowest achievable temperature in the MOT is the Doppler temperature $T_D = \hbar\Gamma/(2k_B) = 146 \mu\text{K}$ for the ^{87}Rb D₂ line, polarization gradient cooling in the optical molasses decreases the temperature under optimal conditions by a factor $2\delta/\Gamma$. Here δ is the detuning from the atomic transition. The minimal kinetic energy is certainly limited to a few times the recoil energy with $T_{\text{recoil}} = 362 \text{ nK}$ [176, 88]. In contrast to the optimal detuning $\delta = -\Gamma/2$ for a standard optical molasses, we therefore choose a large detuning of -19Γ , which was experimentally found to yield optimal results.

The atoms in the MOT and molasses populate all Zeeman levels of the $5^2S_{1/2} |F = 2\rangle$ state. The $|F = 1\rangle$ manifold is not populated, since the repumper light is on even a few ms after the end of the MOT phase. Before magnetically trapping and transporting the cold atomic cloud, the atoms are optically pumped into the low field seeking $|F = 1, m_F = -1\rangle$ hyperfine state. For that purpose we first apply σ^- -polarized light resonant with the $|F = 2\rangle \rightarrow |F' = 2\rangle$ transition in addition to the repumping light, until all atoms populate the $|F = 2, m_F = -2\rangle$ state. After switching off the repumper, a short pulse of π -polarized light resonant again with the $|F = 2\rangle \rightarrow |F' = 2\rangle$ transition excites the atoms to the $5^2P_{3/2} |F' = 2, m_{F'} = -2\rangle$ state. From there they can decay to the $5^2S_{1/2} |F = 2, m_F = -2\rangle$ or $|F = 2, m_F = -1\rangle$ state, which will lead to another excitation by the π - or σ^- -polarized light, respectively. Or they fall into the $5^2S_{1/2} |F = 1, m_F = -1\rangle$ state we want to populate, which is a dark state for the $|F = 2\rangle \rightarrow |F' = 2\rangle$ light. Optical pumping is performed over 2 ms at a homogeneous magnetic field of 4 G. All light fields are off when the transport sequence starts with adiabatically compressing the cloud [Fig. 3.4 (b)]. The magnetic transport conveys the atoms within 1 s through the differential pumping tube over a distance of 8 cm directly into the magnetic QUIC trap. We estimate a transport efficiency of $> 90\%$ by transferring the atoms back into the magneto-optical trap and measuring their fluorescence. The losses are mainly due to background collisions and depend on the pressure in the MOT chamber.

We operate the magnetic QUIC trap initially with a maximum current of 15 A. This yields the highest trap frequencies of $\omega_x = \omega_z = 2\pi \times 135 \text{ Hz}$ and $\omega_y = 2\pi \times 28 \text{ Hz}$ with a bias field B_0 of 4.7 G and a field gradient B' of $\sim 300 \text{ G/cm}$. Here ω_y and ω_x denote the trapping frequencies along and perpendicular to the Ioffe axis, respectively and ω_z is in the vertical direction. Over a period of 23 s we perform rf-induced evaporative cooling with an exponential frequency ramp and a radio frequency power of 24 dBm. The radio frequency is radiated by a coil inside the vacuum chamber which consists of ten turns of Kapton clad copper wire (1 mm^2) encircling an area of 3 cm^2 . It is mounted 2 cm away from the center of the trap and is oriented at 90° with respect to the Ioffe axis. This

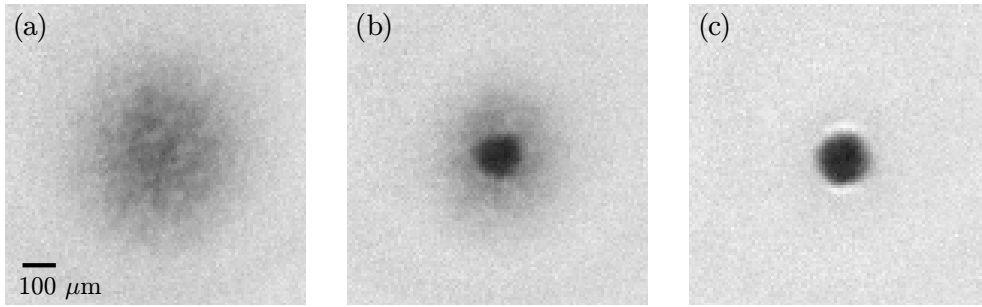


Figure 3.10: Absorption images of cold atom clouds. (a) Thermal cloud at a temperature T above the critical temperature T_c . (b) Bimodal distribution for $T < T_c$. (c) “Pure” Bose-Einstein condensate at $T \ll T_c$. The images were taken after 30 ms time of flight with a detuning of 2Γ to avoid saturation.

results in a B_{rf} of about 30 mG at the position of the cold atoms.

Before reaching the critical phase space density for Bose-Einstein condensation we relax the trap to the final parameters of $\omega_x = 2\pi \times 38.6 \text{ Hz}$, $\omega_y = 2\pi \times 7.2 \text{ Hz}$ and $\omega_z = 2\pi \times 29.1 \text{ Hz}$ with $B_0 = 1.2 \text{ G}$ and $B' = 60 \text{ G/cm}$ by powering the QUIC trap with 3 A. The initial trap symmetry is lifted by the large gravitational sag. For a perfectly harmonic trap it is given by $z_{\text{sag}} = g/\omega_z^2 \approx 290 \mu\text{m}$, where g is Earth’s gravitational acceleration. However, taking the anharmonicity of the trap far from the center of the magnetic field minimum into account, combined measurements on and simulations of our setup yield $z_{\text{sag}} = 159 \mu\text{m}$. Furthermore, the long axis of the BEC is inclined by about 3.2° with respect to the horizontal plane (see Sec. 2.2.2 and Fig. 2.4). The opening of the trap is performed adiabatically ($\dot{\omega}/\omega \ll \omega$) over a period of 1 s. During this time an rf shield limits the trap depth to prevent heating of the cold atomic cloud. In the weak trap we further cool the atoms evaporatively over 5 s and achieve Bose-Einstein condensates of up to 5×10^6 atoms (see Fig. 3.10). The density in the weak trap is considerably lower so that the losses due to inelastic collisions are reduced. We have measured a $1/e$ -lifetime for condensates of about 30 s. The typical size of the Bose-Einstein condensate is $(23 \times 120 \times 30) \mu\text{m}^3$ (Thomas-Fermi diameter) with a chemical potential μ of about 1 kHz.

Resonant absorption imaging of the cold atoms after a free expansion time of 30 ms allows us to extract the number of atoms in the cloud and its temperature. We fit the resulting density distribution with the sum of a Gaussian and a Thomas-Fermi profile. The spatial resolution of our imaging system ($f/10$) is limited to $9 \mu\text{m}$ by the diameter of the windows. We employ a charge coupled device (CCD) camera with an according pixel size.

3.4.2 Atom laser

An atom laser is a coherent atomic beam extracted from a Bose-Einstein condensate (Fig. 3.11). The trapped condensate, being in a quantum degenerate state, serves as the source for the freely propagating atom laser. A steady-state output coupling process establishes a coupling between the ground state of the trap and the energy eigenfunctions of the linear gravitational potential and produces a continuous atom laser. The resulting cw atom laser [79], in contrast to optical lasers, consists of interacting massive particles propagating downwards in the gravitational field. But like an optical laser it is a matter wave in a coherent state as defined by Glauber in the quantum theory for optical lasers [59] and exhibits higher-order coherence [101].

In order to output couple atoms we locally change their internal spin state from the magnetically trapped $|F = 1, m_F = -1\rangle$ into the untrapped $|F = 2, m_F = 0\rangle$ hyperfine state. The spin flip is induced by a coherent microwave field at the hyperfine splitting frequency of ^{87}Rb ($\Delta E_{\text{hfs}}/h = 6.8 \text{ GHz}$) [88]. This microwave output coupling scheme is equivalent to a two-level system because of the Zeeman splitting ($\sim 1 \text{ MHz}$) in the hyperfine niveaus (see Sec. 2.2.2). Therefore it is superior to rf output coupling which mutually couples all states from a Zeeman manifold [96]. The microwave signal is produced by a synthesizer locked to a 10 MHz global positioning system (GPS) reference. We use a home-built resonant helix antenna with 14 dB gain [Fig. 3.11(a)] placed inside the ultrahigh vacuum chamber to radiate the microwave field. The antenna is connected and impedance matched to a commercial microwave feedthrough.

The energy conservation for the resonance condition of the microwave output coupling is only satisfied at regions of constant magnetic field where $\Delta E_{\text{hfs}} - g_F \mu_B B(\mathbf{r}) = h\nu_{\text{mw}}$. Here ν_{mw} is the microwave frequency, $B(\mathbf{r})$ the magnetic field of the trap at position \mathbf{r} , and μ_B the Bohr magneton. The hyperfine Landé g factor g_F applies to the BEC state. The magnetic moment of the output coupled atoms is zero to the first order.

The resonant regions for output coupling are ellipsoidal shells given by the geometry of the magnetic field, centered at the minimum of the magnetic potential. However, the center of the actual harmonic trapping potential for massive particles is lowered by the gravitational sag with respect to the magnetic field minimum. For our experimental conditions the resonant output coupling shells intersect the Bose-Einstein condensate almost as horizontal planes (see Fig. 2.4).

The Rabi frequency Ω of the microwave output coupling process is given by $\mu_{12} B_{\text{mw}}/\hbar$, where μ_{12} is the magnetic dipole matrix element between the two coupled states and B_{mw} the magnetic field of the microwave radiation [93]. The magnetic dipole transition has selection rules $\Delta m_F = \pm 1$. In the weak output coupling regime ($\Omega \ll \omega_z$) an atom leaves the condensate much faster than the Rabi frequency and does not undergo Rabi oscillations [95]. The atom laser output coupling rate depends on the number of atoms

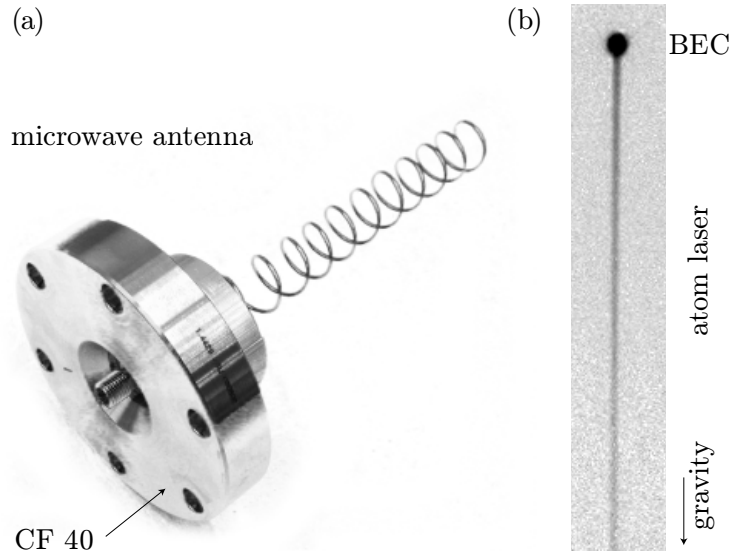


Figure 3.11: Coherent microwave output coupling of a continuous atom laser. (a) Helix antenna built for 6.8 GHz mounted on a vacuum feedthrough. (b) Resonant absorption image of the atom laser after a propagation of 2 mm.

in the condensate N_{BEC} and the overlap $|\langle \Psi_{\text{BEC}} | \Phi_{\text{E}} \rangle|^2$ between the BEC wave function Ψ_{BEC} and the energy eigenfunction Φ_{E} of the free atom laser [92, 74]. For given atom number N_{BEC} and microwave frequency the output coupling rate is proportional to Ω^2 and therefore to the power of the incident microwave radiation [84].

Producing a coherent cw atom laser crucially depends on the temporal stability of the resonance condition. We take experimental care to avoid any fluctuations or drifts of the magnetic resonance position. A temperature controlled cooling circuit for the large mass magnet coil structure and a GPS locked synthesizer permit excellently reproducible conditions. The magnetic shielding enclosure together with the hermetic steel vacuum chamber eliminate external electromagnetic field fluctuations (see Secs. 3.1.1 and 3.2.3). The only detectable noise source is the low noise current supply powering the magnetic QUIC trap. We have measured a magnetic field stability of better than $5 \mu\text{G}/\sqrt{\text{Hz}}$ (at 3 kHz) or $50 \mu\text{G}$ overall (bandwidth: 50 kHz). This enables us to produce second-order coherent atom lasers and output couple a cw atom laser over the duration of the BEC lifetime. Due to the extremely low atom fluxes measurable with the cavity detector we do not have to deplete the condensate significantly.

The atom laser freely propagates downwards for 86.1 ms before entering the ultrahigh finesse optical cavity where single atoms are detected. The cavity is placed 36.4 mm below the BEC which results in a velocity of 0.84 m/s for the atoms traversing the cavity mode. This velocity corresponds to a de Broglie wavelength of about 5 nm which

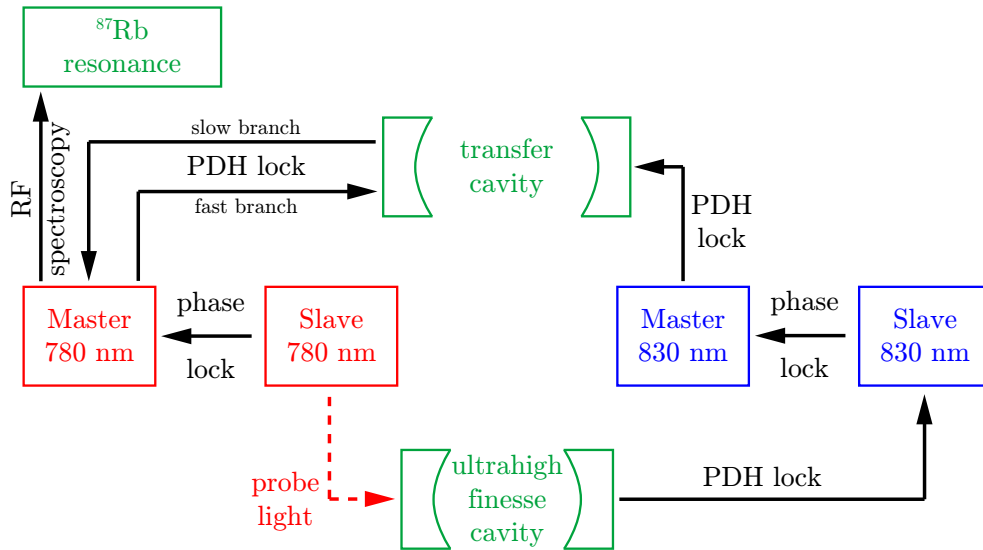


Figure 3.12: Locking scheme of the detection setup. Black solid lines represent a lock with the device the arrow starts from stabilized to the one it points to (PDH = Pound-Drever-Hall, RF = radio frequency).

could be useful for applications in coherent atom lithography [177] or as an atom laser microscope [178, 179].

3.4.3 Cavity lock

In order to engage the ultrahigh finesse optical cavity as a single atom detector we have to stabilize its length to better than $0.5 \lambda / \mathcal{F} \approx 1$ pm with respect to the wavelength of the probe laser.

We choose a cavity locking scheme [34] that allows us to independently adjust the frequencies of the cavity resonance (ω_C) and of the probe laser (ω_L). Furthermore it enables us to keep the cavity permanently locked even during atom detection since the effect of a single atom transit on the far-detuned stabilization laser is negligible and vice versa. A sketch of the locking scheme is depicted in Fig. 3.12. The 780 nm master laser is stabilized to a D₂ line of ⁸⁷Rb using radio frequency spectroscopy. Its absolute frequency stability is transferred to a transfer cavity with a free spectral range $\Delta\nu_{\text{FSR}}$ of 1 GHz by locking the latter to the 780 nm master laser using the Pound-Drever-Hall (PDH) technique [180, 181]. The transfer cavity consists of two identical mirrors with radius of curvature $R_C = 25$ cm. Its length is 15 cm and the resulting mode waist radius $w_0 = 169$ μm . The PDH lock acts on a piezo in between the two mirrors, keeping the optical path length at the locking wavelength constant. The so called 830 nm master laser is locked to the transfer cavity and therefore inherits its

absolute frequency stability. The 830 nm and 780 nm slave lasers are used to stabilize and probe the ultrahigh finesse cavity, respectively. In order to be freely tunable, the actual probe and stabilization slave lasers are phase locked [182] with a frequency offset of $\pm(0\text{--}500)$ MHz to their respective master lasers. The length of the science cavity is then actively controlled by a Pound-Drever-Hall lock to the stabilization slave laser with a bandwidth of 38 kHz. We create the necessary sidebands for the lock with a home-built electro-optical modulator (EOM) [183]. It works at 362 MHz to have the sidebands well off-resonant with the cavity, which has a finesse of only $\mathcal{F} = 3.8 \times 10^4$ at 830 nm and therefore a linewidth of 22 MHz.

One advantage of the Pound-Drever-Hall technique is its insensitivity against intensity fluctuations. The slope of the error signal is $4\sqrt{P_C P_S}/(\pi\Delta\nu_c)$, with $\Delta\nu_c$ being the cavity linewidth and P_C and P_S the power in the carrier and one of the (equally intense) sidebands, respectively. The signal is maximal when the combined power in both sidebands is equal to the power in the carrier. With an EOM, a maximum of 34 % of the total incident power can be transferred into each of the first-order sidebands, leaving 10 % in the carrier. For many experiments it is desirable to minimize the power inside the cavity to minimize the interaction between stabilization light and atoms. Both the scattering rate and the dipole potential should be as low as possible. However, a certain minimal size of the PDH error signal is needed in order to stabilize the cavity. The ratio between the size of the error signal and the power inside the resonator for a given total power is $\sqrt{1/P_c - 1}$, which suggests making the carrier very small. There is however the limit of the minimum relative carrier power of 10 % mentioned above. The solution to this problem is to lock the cavity to one of the sidebands, which is possible because the PDH lock also works with only a single sideband. The sidebands can in principle be made arbitrarily small without any restriction on the power of the carrier. Since only the weak sideband is resonant with the cavity, the strong carrier is not coupled into the cavity and therefore does not interact with the atoms. We have stabilized the cavity to one of the sidebands containing only 3.2 % of the total power. This yields only 2 nW of power behind the cavity, which corresponds to 35 μ W of light at 830 nm inside the resonator. Consequently, the scattering rate is as low as 1 mHz and is about a factor of 150 better than what we typically achieve by locking to the carrier.

We actively control the power of the stabilization and probe laser incident on the cavity to about 2 μ W and 3 pW, respectively. In order to have a good spatial overlap, the two lasers are guided through the same optical fiber. Their power ratio of 10^{-6} is realized with an optical color filter that transmits most of the light at 830 nm but strongly attenuates the probe light. We can couple about 25% of the incident probe laser power into the cavity TEM₀₀ mode being limited by the non-optimal impedance matching.

The transfer cavity only serves as a rigid frequency linker as long as the refractive

index in between its two cavity mirrors is constant. The refractive index of air however depends on environmental parameters α_i like temperature, pressure, and its composition in a wavelength dependent manner. In case one of these parameters changes, the PDH lock counteracts changes of the optical path length at 780 nm by changing the cavity length. At 830 nm however, the index of refraction might have changed by a different amount and therefore the frequency of the 830 nm master laser is shifted. The change in its frequency f with the physical quantity α is in general given by

$$\frac{\partial f}{\partial \alpha_i} = \left(\frac{\partial n_1}{\partial \alpha_i} n_2 - \frac{\partial n_2}{\partial \alpha_i} n_1 \right) \frac{f}{n_1 n_2} \quad (3.1)$$

where n_1 and n_2 denote the refractive index of air at 780 nm and 830 nm, respectively [184]. For typical conditions (T=20 °C , p=1013 mbar and a relative humidity of 50 %) we find a change of the 830 nm laser frequency of -0.4 MHz/°C and 0.1 MHz/mbar. The refractive indices were calculated using a program provided by the National Institute of Standards and Technology (NIST)[185]. Since ambient temperature drifts in the lab of 1–2 °C during the day and daily variations of the atmospheric pressure of one millibar are common, we observe a drift of the 830 nm laser with respect to the 780 nm laser of up to 1 MHz. This is especially annoying since all the locks employed in stabilizing the relative frequency between cavity and detection laser offer much better stability. Putting the transfer cavity in vacuum should eliminate this problem and a chamber to hold it has already been designed. Another advantage would be an improved decoupling of the cavity from changes in ambient temperature. Even though expansion of the spacer supporting the mirrors is counteracted by the piezo, once its maximum length change is reached, the lock collapses and the cavity and 830 nm lasers need to be relocked. This would happen less often if the cavity was isolated thermally from the environment by putting it inside a vacuum chamber.

3.4.4 Cavity parameters

Since the ultrahigh finesse cavity is a central part of the experiment, measurements done to determine its parameters are presented in the following section. The results are summarized in Table 3.2.

Cavity length

We have determined the length of the ultra-high finesse optical cavity in two different ways. The length of a near-planar cavity can be calculated by determining the ratio of the frequency interval between two neighboring transverse modes $\Delta\nu_{tr}$ [see eqn. (2.49)]

to the free spectral range $\Delta\nu_{\text{FSR}}$ of the cavity, to be

$$l_{\text{res}} \approx \frac{\pi^2 R_C}{2} \left(\frac{\Delta\nu_{\text{tr}}}{\Delta\nu_{\text{FSR}}} \right)^2, \quad (3.2)$$

where R_C is the radius of curvature of the two equal mirrors. However, this method is not very accurate, since it relies on the linearity of the change in cavity length with the piezo voltage.

The second method yields much more accurate results but requires not only one but two freely tunable lasers. Their wavelengths λ_1 and λ_2 need to be tuned in resonance with two TEM₀₀ modes that are simultaneously resonant with the cavity. Then the length of the resonator can be calculated as

$$l_{\text{res}} = \frac{\Delta n \lambda_1 \lambda_2}{2(\lambda_2 - \lambda_1)} = \frac{c \Delta n}{2(\nu_1 - \nu_2)}, \quad (3.3)$$

where Δn is an integer characterizing the difference in longitudinal modes between the two wavelengths. Taking two neighboring modes ($\Delta n = 1$) with $\lambda_1 = 825.605$ nm and $\lambda_2 = 827.526$ nm we find $l_{\text{res}} = 177.8$ μm .

The same calculation can be done for the two wavelengths used during operation of the cavity as a single atom detector. They are 780.246 nm for the detection laser resonant with the ⁸⁷Rb D₂ transition and 829.689 nm for the stabilization laser used for locking the high-finesse cavity. From the measurement with two adjacent longitudinal modes we can reason that $\Delta n = 27$ in this case. The resulting cavity length is $l_{\text{res}} = 176.8$ μm . Following the results from [186], the discrepancy results from the leakage of the cavity mode into the mirror coatings. Wavelengths differing from the center wavelength leak deeper into the coating, which explains why a longer resonator length is measured with both laser detuned about 45 nm from the center frequency of the coatings of 780 nm. Extrapolating to the cavity length at the center wavelength we find $l_{\text{res}} = 175.9$ μm . The maximum length change achievable with the piezo is 0.4 μm , and therefore the definite cavity length depends on the precise operation conditions.

One needs to discriminate the mechanical length of the cavity, given by the distance between the inner sides of the two mirrors and the effective cavity length. The latter is larger by about 0.6 μm for our parameters than the first because the electromagnetic mode extends into the stack of coating layers. The effective cavity length is determined with the methods described above. It is the physically relevant quantity as for example required to calculate the cavity mode volume V_m .

Linewidth and finesse

After assembly, the cavity was tested in a separate vacuum chamber. Its linewidth was determined in a cavity ringdown measurement, whose results are shown in Fig. 3.13.

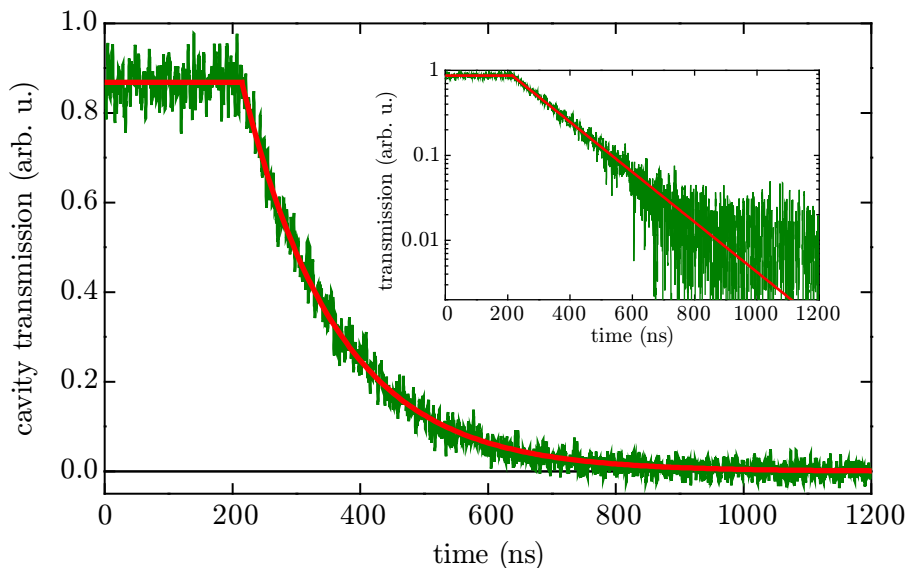


Figure 3.13: Cavity ringdown to determine the lifetime of a photon in the cavity. The inset shows a logarithmic plot of the same data as in the main graph. The red line is a fit to the data.

A probe laser is locked to the cavity, leading to a constant transmission of light. At $t_0 = 215$ ns, it is switched off and the decay of the intracavity light field can be observed. Fitting an exponential $I(t) = A \exp(-(t - t_0)/\tau_c)$ to the data, the time constant for the intracavity intensity can be determined as $\tau_c = (147 \pm 0.3)$ ns. From this, the linewidth is calculated as $\Delta\nu_c = 1/(2\pi\tau_c)$ and the decay rate of the electromagnetic field inside the cavity is

$$\kappa = 2\pi \frac{\Delta\nu_c}{2} = \frac{1}{2\tau_c}. \quad (3.4)$$

The system to measure the cavity ringdown was characterized independently. Without the cavity in the optical path, the decay of the photo diode signal from 90 % to 10 % took only 11 ns. It was limited by the switching time of the AOM and not by the photodiode. Therefore the influence of the systems switching time on the ringdown measurement is very small. This is confirmed by the strictly linear shape of the cavity transmission in the semilogarithmic plot shown as an inset in Fig.3.13. As a supplementary evidence we fitted the decay starting only at $t_0 = 315$ ns, which is 100 ns after the beginning of the switch off. By then the effect of the switching time of the AOM should be completely negligible. A decay time of $\tau_c = (141 \pm 5)$ ns is found, basically confirming the result of the fit to the complete data range. Using the independently measured cavity length of $l_{\text{res}} = 176$ nm, we find a finesse $\mathcal{F} = \frac{\pi c \tau_c}{l_{\text{res}}} > 7.5 \times 10^5$.

Unfortunately, the finesse dropped to $\mathcal{F} = 4 \times 10^4$ over a period of about three months following its installation in the main vacuum chamber and the subsequent bake-out. Several attempts to clean the cavity mirrors without having to break the vacuum were carried out. However, neither local heating nor illumination of the cavity mirrors with ultraviolet light increased the finesse. Therefore the cavity was taken out of the vacuum chamber and disassembled. The mirrors were thoroughly cleaned mechanically, using lens cleaning tissue, acetone and isopropanol. After reinstallation and bake-out the result was a finesse of 3.4×10^5 which has now been stable for about three years.

Even though a cavity ringdown measurement is the method of choice to determine the finesse once its length is known, in the final setup the signal to noise of the ringdown was not sufficient. The optical setup is optimized for very low light intensities and therefore only about 20 μW of light were available for input coupling. Since the photodiode used for detection needs to be very fast (the single photon counter's count rate is much too low for this), the photo current needs to be monitored as a voltage drop over a very small resistor ($\sim 50 \Omega$). But then the signal is simply too small for a sufficient signal-to-noise ratio.

We therefore chose to measure the cavity linewidth directly by determining the width of the decrease of reflected light on resonance, using the sidebands created by an EOM for the Pound-Drever-Hall stabilization as frequency markers. The choice of the right scan speed of the piezo is crucial for accurate results. Nonlinearities in the voltage to length conversion by the piezo were taken into account as well as heating of the cavity once it fills with resonant light, which leads to a slightly asymmetric transmission curve. When scanning over the resonance by increasing the cavity length, the resonance curve appears slightly narrower because the heating of the substrates increases the growth in cavity length. The opposite effect can be observed when scanning from shorter to longer cavity lengths. Scanning both ways and averaging as well as using low light intensities minimizes these effects. A linewidth of $\Delta\nu_c = 2.5 \text{ MHz}$ at 780 nm and $\Delta\nu_c = 22.4 \text{ MHz}$ at 830 nm are measured. This factor of 9 difference in the linewidths is a property of the mirror coatings. They are optimized for 780 nm (design wavelength) and 50 nm away from the design wavelength a significantly higher transmission is to be expected.

We found that the cavity mirrors are birefringent, which leads to a splitting of the resonance frequencies between two orthogonal axes of linear polarization by about the cavity linewidth $\Delta\nu_c$ at 780 nm.

The maximum fraction of light that can be input coupled into the cavity has been determined as $\eta_{\text{in}} = 1 - R$, with R being the measured fraction of light reflected from the input coupling mirror. The theoretical value ("theory") of η_{in} has been calculated from eqn. (2.37). The discrepancy between the theoretical and experimental values is due to imperfect mode matching. The same is true for the maximum transmission on

Cavity parameters		
	wavelength λ	
	780.246 nm	829.689 nm
length l_{res}	175.9 μm	177.8 μm
free spectral range $\Delta\nu_{\text{FSR}}$	852 GHz	843 GHz
linewidth $\Delta\nu_c$	2.5 MHz	22.4 MHz
finesse \mathcal{F}	342×10^3	38×10^3
max. input coupling η_{in} (exp.)	24 %	57 %
max. input coupling η_{in} (theory)	43 %	91 %
$T_{\text{FP}}^{\text{max}}$ (exp.)	3.4 %	30 %
$T_{\text{FP}}^{\text{max}}$ (theory)	6.1 %	49 %
mirror transmission \mathcal{T}	2.3 ppm	58 ppm
mirror losses \mathcal{L}	6.9 ppm	25.3 ppm
mirrors, radius of curvature R_C	75 mm	
mode waist radius w_0	25.25 μm	26.11 μm
mode volume V_m	$88 \times 10^3 \mu\text{m}^3$	$95 \times 10^3 \mu\text{m}^3$
decay rate of the atomic dipole moment γ	$2\pi \times 3.0 \text{ MHz}$	
decay rate of the intracavity field κ	$2\pi \times 1.3 \text{ MHz}$	$2\pi \times 11.2 \text{ MHz}$
atom-cavity coupling constant g_0	$2\pi \times 10.6 \text{ MHz}$	
cooperativity parameter \mathcal{C}	29.5	

Table 3.2: Properties of the ultrahigh finesse cavity. Details are given in the text.

resonance $T_{\text{FP}}^{\text{max}}$, with the theoretical value calculated from eqn.(2.36). \mathcal{T} , \mathcal{L} , w_0 , and V_m have been determined using equations (2.41), (2.42), (2.46), and (2.47), respectively. The atomic resonance (ω_A) we employ for single atom detection is the cycling transition $|F = 2\rangle \rightarrow |F' = 3\rangle$ of the D₂ line of ⁸⁷Rb. The decay rate of the atomic dipole moment is given by half the natural linewidth $\gamma = \Gamma/2$ [88] and is much smaller than the atom field coupling rate g_0 . The same is true for the cavity field decay rate κ and the inverse atom transit time $\tau^{-1} = 2\pi \times 3 \times 10^{-3}$, The latter means that the atom is always in a quasi steady state with the cavity field during the transit. g_0 has been calculated using eqn. (2.52) and assuming an isotropic dipole matrix element [88]. Since $g_0 \gg (\gamma, \kappa, \tau^{-1})$, we operate in the strong coupling regime of cavity QED (see section 2.3.3).

3.5 Single atom detection

The detection of single atoms with an ultrahigh finesse optical cavity [26] can heuristically be viewed as the refractive index of a single atom being sufficient to significantly shift the cavity resonance. Consequently, the transmission of an initially resonant, weak probe laser is measurably reduced. In quantum mechanical terms the coupling of a single atom with the quantized electromagnetic field in the cavity mode dominates the dissipation losses (strong coupling regime) which means the level splitting of the Jaynes-Cummings model [112, 113] can be resolved (see section 2.3.4). On the other hand, the quantum mechanical detection process on the longitudinally delocalized atom within the atom laser beam projects and localizes them inside the cavity mode [187].

We can efficiently study these cavity QED interactions of single atoms having an atom laser as an unprecedentedly bright, controllable, reproducible, and well defined source of atoms. Here, we present experimental results that characterize the performance of our combined BEC and ultrahigh finesse optical cavity system.

3.5.1 Analysis

In order to identify single atom transits, we record the transmission of a weak, resonant probe laser beam through the cavity with a single-photon counting module (SPCM). A typical recording showing single atom transits is presented in Fig. 3.14.

Photon detection system

The light coming from the cavity is filtered with a 780 nm bandpass and a 830 nm notch filter to block the stabilization light. Their combined relative optical density (OD) at 830 nm is 12. The SPCM employs a silicon avalanche photodiode [188] with a nominal dark count rate $< 50 \text{ s}^{-1}$ and a nominal photon detection efficiency of 60 %. It is located inside a light-tight enclosure (“blackbox”) and we experimentally find an overall photon dark count rate of $\sim 100 \text{ s}^{-1}$. An accurate determination of the quantum efficiency of the SPCM would be desirable. Comparing the SPCM output with the reading of a calibrated power meter gives $\eta_{\text{SPCM}} \approx 50 \%$ which is not a very accurate number. Using correlated photon pairs would be far superior and is especially independent of an external standard [189, 190, 191], but has not been deployed due to its minor relevance for the work presented here. The SPCM produces TTL pulses of 35 ns length for each detected photon and has a measured dead time of 58 ns. Therefore the maximally achievable count rate is about $2 \times 10^7 \text{ s}^{-1}$ and already at a count rate of $5 \times 10^6 \text{ s}^{-1}$ the typical linearity correction factor is 1.4. The pulses are counted by a Multiscaler (Fast ComTec P7882) with a minimum dwell time of 100 ns. In the current mode of

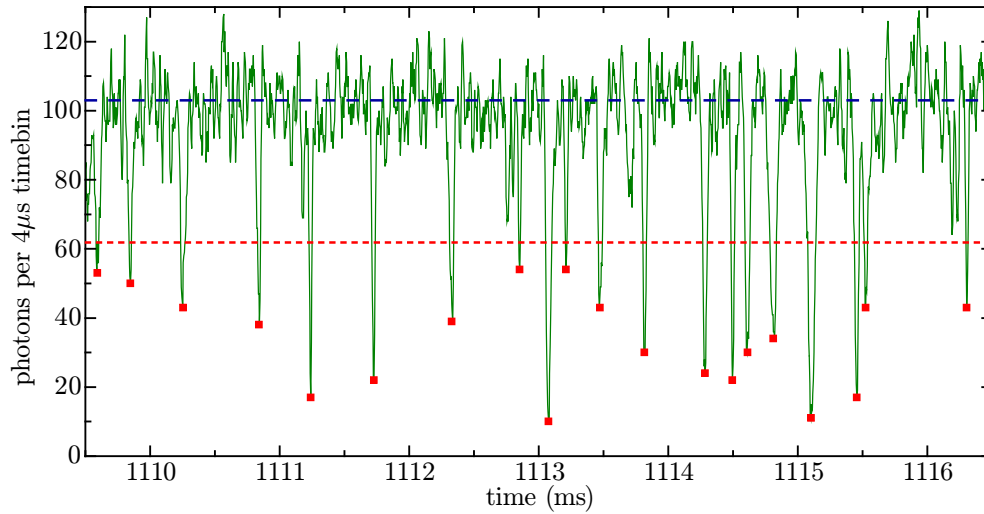


Figure 3.14: Cavity detection of atoms from an atom laser. The atom flux is about four orders of magnitude lower than in Fig. 3.11(b). Single atom transits through the cavity are clearly identified as dips in the cavity transmission (green data). Dips larger than 4 times the shot noise (4σ , red dotted line) of the empty cavity transmission (blue dashed line) are identified as single atoms transits by a custom-made software algorithm (red squares).

operation the maximum recording time is limited by the amount of on-board memory of the card allowing the storage of 5×10^5 time bins. Therefore 2 s of continuous recording are possible with a resolution of 4 μ s. We found the existence of very short intervals of insensitivity between adjacent time bins, contrary to the manufacturers specification of zero dead time. For practical purposes however, they can be neglected.

Photon detection efficiency

The intracavity intensity on its axis is given by

$$I_c = \frac{2P_c}{\pi w_0^2}, \quad (3.5)$$

where $P_c = \bar{N}_{ic} h\nu c / l_{res}$ is the power inside the cavity of length l_{res} given by the average number of intracavity photons \bar{N}_{ic} of frequency ν . Every time a photon hits the output coupling mirror, it is transmitted with a probability given by the transmission of the output coupling mirror \mathcal{T} . Therefore the power behind the output coupling mirror P_{oc} is the product of \mathcal{T} and the power inside the cavity: $P_{oc} = \mathcal{T}P_c$. The rate at which photons impinge on the output coupling mirror is given by the free spectral range $\Delta\nu_{FSR}$. Therefore one intracavity photon is equivalent to an optical power of $P = h\nu\Delta\nu_{FSR}\mathcal{T}$ behind the cavity.

The detection efficiency for an intracavity photon is

$$\eta_{\text{ic}} = \frac{\mathcal{T}}{\mathcal{T} + \mathcal{L}} \times \frac{1}{2} \times \eta_{\text{o}} \times \eta_{\text{SPCM}} \times (1 - \tau_{\text{d}}c_{\text{r}}). \quad (3.6)$$

The two contributions coming from the cavity are the ratio of mirror transmission to total cavity losses and a factor 1/2 to account for equal transmission probability through both mirrors. $\eta_{\text{o}} = 85\%$ accounts for the losses of photons at the optical elements between the cavity and the SPCM and $\eta_{\text{SPCM}} \approx 0.5$ is the photon detection efficiency of the single photon counter at low count rates. The last factor in eqn. (3.6) represents the reduced detection efficiency of the SPCM for large count rates c_{r} due to its dead time of $\tau_{\text{d}} = 58$ ns. The cumulative detection efficiency is $\eta_{\text{ic}} = 5.2\%$ if the count rate is so low that the detector dead time can be ignored.

At a count rate c_{r} of the SPCM, the mean intracavity photon number \bar{N}_{ic} is given by

$$\bar{N}_{\text{ic}} = \frac{2l_{\text{res}}}{c\eta\mathcal{T} \left(\frac{1}{c_{\text{r}}} - \tau_{\text{d}} \right)}, \quad (3.7)$$

where $\eta = \eta_{\text{o}} \times \eta_{\text{SPCM}} \times (1 - \tau_{\text{d}}c_{\text{r}}) = 43\%$ is the detection efficiency for photons leaving the cavity via the output coupling mirror. Solving eqn. (3.7) for c_{r} gives

$$c_{\text{r}} = \left(\tau_{\text{d}} + \frac{2l_{\text{res}}}{\bar{N}_{\text{ic}}\eta\mathcal{T}c} \right)^{-1} \approx \frac{\eta\mathcal{T}c}{2l_{\text{res}}} \bar{N}_{\text{ic}}, \quad (3.8)$$

where we have ignored the dead time of the SPCM in the last term. In order to achieve a large signal-to-noise ratio for single atom detection, we usually work with an SPCM count rate of about 5 photons/ μs , which is equivalent to an average intracavity probe photon number of about 8. This corresponds to an intensity on the cavity axis of about 100 I_{sat} using the saturation intensity for isotropically polarized light $I_{\text{sat}} = 35.8$ W/ m^2 . The detection efficiency for an intracavity photon is $\eta_{\text{ic}} = 3.8\%$ in this case.

3.5.2 Identification of single atom transits

We integrate the signal from the SPCM over 20 μs with a temporal resolution between 1–4 μs . In Fig. 3.14 the mean empty cavity transmission of $\bar{n} = 103$ atoms per 20 μs timebin is marked by the dashed blue line. The threshold for single atom detection, defined as a reduction by at least 4 times the shot noise (4σ), is $\bar{n} - 4\sqrt{\bar{n}} = 62$ and plotted as a red dotted line. Single atom transits are automatically identified using custom-made software and are marked in the figure by a red square. The rate of false atom detection events is reduced to less than 0.5 s $^{-1}$ due to the 4σ criterion.

In typical detection routines, a certain number of events (missing photons in this case) must be reached for the detection to be valid. The optimal width of the integration region is dependent on the ratio between peak and background amplitude and

in the case considered here approximately 1.2 times the full width at half maximum (FWHM) of the transmission dip. For our average coupling time of 45 μs (also defined as FWHM) this would be 54 μs . However, a smaller integration time can be advantageous. Integrating over a large time leads to a severe decrease in the maximum dip depth and therefore entail an underestimation of the reduction in transmission at maximum coupling strength. In addition, we deduce information about the presence of the peak and especially its maximum from its shape, which gets increasingly distorted with larger integration times. 20 μs was found to be a good compromise between the different requirements.

3.5.3 Characteristics of single atom events

The coupling of a single atom with the cavity mode can be characterized by the magnitude and duration of the resulting transmission dips. A recorded typical single atom transit is shown in Fig. 3.17(a). The 4σ threshold here corresponds to about 50 % reduction in the probe light transmission of about 70 photons per 20 μs . We analyze detected events and show histograms in Figs. 3.17(b) and 3.17(c) for atom laser data taken in 184 iterations of the experiment. The atom flux was set to $\sim 1 \times 10^3 \text{ s}^{-1}$, so the probability [101] for unresolved multiatom events within the dead time of our detector ($\sim 70 \mu\text{s}$) is less than 0.3 %.

Atom trajectories inside the cavity

The power of the 780 nm probe laser and the 830 nm stabilization laser in the cavity are 1.46 μW and 5.15 mW, respectively. From this we can calculate the intensity on the cavity axis to be $I_c^{780} = 2P_c/(\pi\omega_0^2) = 1.43 \times 10^3 \text{ W/m}^2 = 40s_0$ and $I_c^{830} = 5.05 \times 10^6 \text{ W/m}^2$, respectively. The resulting maximum dipole potential for the 780 nm light is reached at a red detuning of $3.3 \Gamma_{D_2}$ and equals $-4200 E_{\text{recoil}}$ for an atom at an antinode. For the stabilization light at 830 nm one finds a potential depth of $-71 E_{\text{recoil}}$. Since the potential due to the detection light is about 60 times larger than that due to the stabilization laser, in the following we will only consider the effects of the detection light at 780 nm, which is assumed to be red detuned to give the maximum possible potential depth. This is also the detuning for which we experimentally find the highest detection efficiency (see above). The scattering rates are 0.13 Hz for 830 nm and 10^7 Hz for the probe laser red detuned by 3.3Γ from the D_2 line. The latter is half the maximally possible scattering rate. The number of photons scattered during an atom transit is thereby rather limited by the decay of atoms into the $F=1$ state, which is not resonant with the detection light, and we do not scatter 450 atoms as one would naively calculate from the mean time atoms spend in the cavity. The scattering rate of the stabilization laser can be reduced by about a factor of 150 to 10^{-3} Hz when fully exploiting the

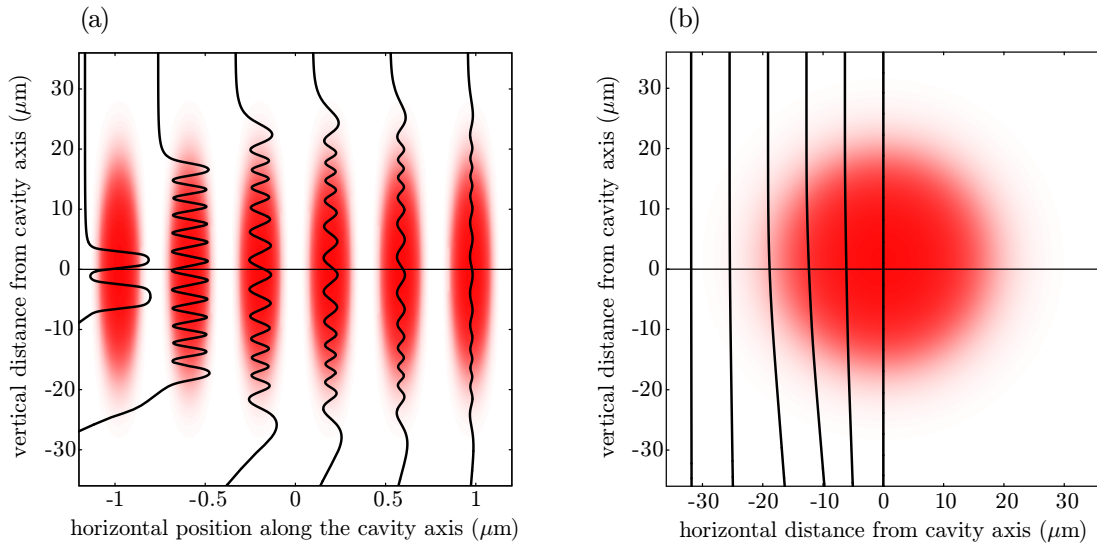


Figure 3.15: Trajectories of atoms through the cavity mode. The red shading indicates the depth of the dipole potential where darker red marks a deeper potential. In (a) the cavity is viewed from the side. The six trajectories plotted are those of atoms entering the cavity at a horizontal distance of $(0.98, 0.9, 0.7, 0.5, 0.3, 0.1) \times \lambda/4$ from an antinode of the cavity and on axis along the other direction. Note that the horizontal axis shows only $1/30$ of the region of the vertical axis and therefore the oscillations are greatly enhanced. (b) View along the cavity axis. Perpendicular to it, the dipole force is weak and leads to a small deflection of the atoms. The atoms are injected at an antinode with a distance $(1.25, 1, 0.75, 0.5, 0.25, 0) \times w_0$ from the cavity axis. w_0 is the waist radius of the cavity mode.

potential of stabilizing the cavity with very low light intensities (see section 3.4.3).

To be able to better understand the cavity transmission signals, the trajectories of atoms in the cavity need to be studied [192, 193]. They determine the position- and therewith time-dependent coupling. In chapter 6 we show that upon entering the cavity an atom is localized in less than a microsecond. Therefore it is justified to use a semiclassical model, where the internal state of the atom and the cavity mode are treated quantum mechanically but the motion of the atom is treated classically. In the case of a weakly driven cavity the force on an atom is given by [118]

$$\langle F(\vec{r}) \rangle = \frac{-2\bar{n}\hbar\kappa^2\Delta_a g(\vec{r})\nabla g(\vec{r})}{(\Delta_C\gamma + \Delta_A\kappa)^2 + (g^2(\vec{r}) - \Delta_A\Delta_C + \gamma\kappa)^2}. \quad (3.9)$$

The mean number of photons in the empty cavity is set to $\bar{n} = 3.4$. Therefore the condition of weak driving is strictly speaking only fulfilled in the case of a strongly coupling atom. The condition of low excitation of the atom is well fulfilled. We ignore all velocity dependent forces and all forces associated with spontaneous emission.

Solving the coupled equations of motion for an atom in three dimensions, subject to gravity and the position dependent dipole force [eqn. (3.9)] yields the trajectories of atoms in the cavity. As one can see from Fig. 3.15(a), the dipole forces along the cavity axis can alter the trajectories considerably because of the large intensity gradients. Atoms entering the cavity between a node and an antinode oscillate around the nearest node, leading to an effectively higher coupling of the atom to the light field as compared to the case without dipole forces. In the y-direction, which is perpendicular to the cavity axis and gravity, the forces are much weaker [see Fig. 3.15(b)]. Even though the deflection of the atom is noticeable, the coupling is only slightly increased.

The influence of the light force on the trajectory depends strongly on the position at which the atom enters the cavity. The transit time is shortened most when an atom traverses the cavity at the center of an antinode, coupling maximally to the light field. The shortest transit time is found for $\Delta_a = 2\pi \times 12 \text{ MHz}$ and $\Delta_c = 2\pi \times 1.1 \text{ MHz}$, reducing it by $1.6 \mu\text{s}$. The effect is quite small due to the high vertical velocity of the atoms of 0.84 m/s upon entering the cavity mode. It can be understood in a classical, one-dimensional model. Due to the attractive potential the velocity of an atom is always higher than or equal to what it would be in free fall. Since the potential is assumed to be conservative in the simulations, the total velocity of the atom well below the cavity does not differ from the free fall case. The overall effect is a faster transit of the atom through the cavity compared to free fall.

In three dimensions however, an extension of the transit time can also be observed. In this case, the z-component of the velocity is reduced because the atom is deflected by the potential. The effect is largest when the atom traverses the cavity close to the cavity axis and very close to a node of the standing wave (within 7% of $\lambda/4$). In this case, the atom is accelerated towards the antinode but not trapped in it. This results in a large deflection of the atom and a slower transit. The maximum increase in transit time is of the same magnitude as the maximum decrease. Considering atoms injected radially on axis and averaging over all possible positions along the cavity axis, one finds an average decrease in transit time of about $1.3 \mu\text{s}$. When the atom enters with a horizontal distance to the cavity axis, the decrease in transit time diminishes approximately proportional to the decrease in coupling.

Dead time of the single atom detector

The dead time of the single atom detector can be inferred from the two-particle correlation function $g^{(2)}(\tau)$ of an atom laser at small τ . Figure 3.16 shows a histogram of the time differences τ between single atom events detected in an atom laser beam (see chapter 5). The limited measurement time and atom flux lead to an average number of 80 entries per time bin of $1 \mu\text{s}$. The resulting shot noise for time intervals larger than

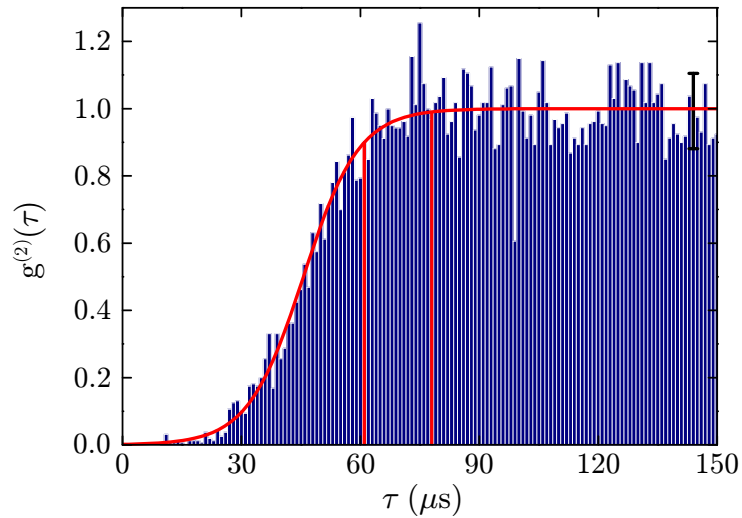


Figure 3.16: The beginning of the two-particle correlation function $g^{(2)}(\tau)$ gives valuable information on the dead time of the single atom detector. The red curve is a fit to the data with the 90 % and the 99 % point marked by the vertical red lines. The error bar indicates the size of shot noise on the data.

the dead time of the detector is indicated by the exemplary error bar. The red curve is a sigmoidal Boltzmann fit to the data giving $g^{(2)}(\tau) = (1 + \exp[-(\tau - 46\mu\text{s})/7\mu\text{s}])^{-1}$. The 90 % and 99 % points are indicated by the two vertical red lines at 61 μs and 78 μs , respectively. From this we can infer that for atom arrivals separated by more than 80 μs no reduction in detection efficiency due to preceding atoms is present. The atom detection routine used here discriminates between dips caused by single and multiple atoms. For single atom dips, a maximally allowed full-width at half-maximum (FWHM) can be set. It is usually chosen to be 90 μs , the minimal size of a dip at which one can hope to accurately discriminate between the arrival times of two atoms. 1.3 % of all dips are found to be wider than this threshold.

The origin of the detector dead time is the insensitivity to a second atom during the coupling times of a preceding atom. The distribution of the coupling times, defined as FWHM of the transmission dips, is shown in Fig. 3.17(b). It is mainly determined by the radial size of the Gaussian cavity mode and the velocity of the atoms during their transit. For a radial coupling strength $g(r) = g_0 e^{-r^2/w_0^2}$ with $w_0 = 25.5 \mu\text{m}$ and an initial velocity of 84.1 cm/s we find from numerical simulations an average coupling time of $45 \pm 12 \mu\text{s}$ [Fig. 3.17(b), gray]. Note that for two atoms separated by this time interval a detection efficiency of 50 % was determined by analyzing $g^{(2)}(\tau)$. Taking the classical free fall velocity is justified since the induced momentum uncertainty by projecting the longitudinally delocalized atom into the cavity mode is on the order of 10 $\mu\text{m/s}$.

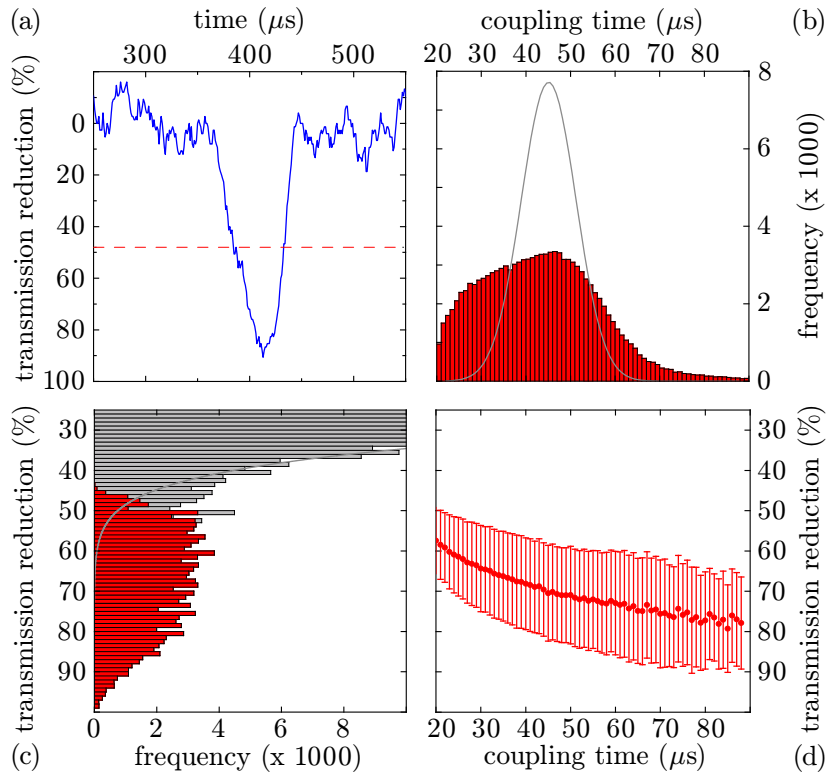


Figure 3.17: Characteristics of detected single atom events. (a) The transit of a single atom significantly reduces the probe light transmission through the cavity. We integrate the signal with a $20\ \mu\text{s}$ sliding average and set the detection threshold to 4σ of the photon shot noise. (b) Distribution of measured coupling times (FWHM) (red) compared to the distribution of simulated events (gray). (c) Distribution of measured transmission reduction magnitudes. An evaluation with a 4σ threshold (red) is compared to a 2σ threshold (gray) revealing the discrimination of the events from the photon shot noise. (d) Dependency of the transmission reduction on the coupling time due to the non-Gaussian shape of the dips.

In the numerical simulations (see section 3.5.3) we take into account photon shot noise and the features of our peak detect routine, namely, the $20\ \mu\text{s}$ sliding average. The effect of the dipole potential on the transit time is small, because the slight gain in velocity ($< 2\ \mu\text{s}$) is counteracted by an effectively stronger and therefore longer coupling [Fig. 3.17(d)]. The mean of the measured coupling time distribution [Fig. 3.17(b), red] is in accordance with the expected value. However, the distribution deviates from the expected shape and exhibits an excess of short and long transit times. We attribute the shorter transits to optical pumping of atoms into the dark state $|F = 1\rangle$ because their number is intensity dependent on the probe light. Longer transit times could be explained by diffraction of the atomic beam, scattering of spontaneous photons or cavity

cooling effects, if the cavity axis is slightly nonorthogonal with respect to the atom laser (possibly 10^{-2} rad) and by unresolved multiatom events.

Maximum coupling

The magnitudes of the cavity transmission dips [Fig. 3.17(c)] reflect the different maximum coupling strengths for single atom transits. Depending on its radial position, an atom will experience a varying peak coupling strength according to the Gaussian profile of the cavity mode. In the axial direction, however, the light force is strong enough to channel the atoms towards the intensity maxima of the standing wave [136]. Arbitrarily weak coupling transits cannot be resolved due to the shot noise in the empty cavity transmission. We set the single atom detection threshold to 4σ of the original transmission to achieve a large signal-to-noise ratio.

The resulting histogram of peak depths is displayed in Fig. 3.17(c)(red) compared to data for a lower threshold level of 2σ in Fig. 3.17(c)(gray) unveiling the photon shot noise. The weakest detectable single atom events correspond to peak atom field coupling strengths of $g_0^{\min} = 2\pi \times 6.5$ MHz. The strongest attainable coupling strengths for our cavity are $g_0^{\max} = 2\pi \times 10.4$ MHz, which would be equivalent to a reduction of 80% in the cavity transmission [187]. We do not observe a sharp cutoff in the histogram but rather an equal distribution of transmission reductions from 50–80% with smeared out edges due to the comparatively large photon shot noise at the minimum of the transmission dip. This is consistent with numerical simulations for single atom events.

The dependence of the probe light transmission of the coupled atom-cavity system is nonlinear in the atom-field coupling strength [187]. Therefore the shape of the transmission dips is not Gaussian as the cavity mode and we observe a dependency of the magnitude in transmission reduction on the coupling time and vice versa [Fig. 3.17(d)].

The knowledge about the signatures of single atom events facilitates the discrimination of “true” single atom events from “false” shot noise events or unresolved multiatom events. However, the broad distributions make it difficult to distinguish two weakly coupling atoms from a strongly coupling one. Yet, the observed characteristics of the detected events are in good agreement with the theoretical predictions for single atom transits.

3.5.4 Linearity

Having an atom laser as the source for atoms that couple with the cavity mode offers several advantages. For instance it provides well reproducible starting conditions and allows us to precisely control the flux of atoms over a wide range by varying the microwave output coupling power. The attainable atom flux is orders of magnitude larger

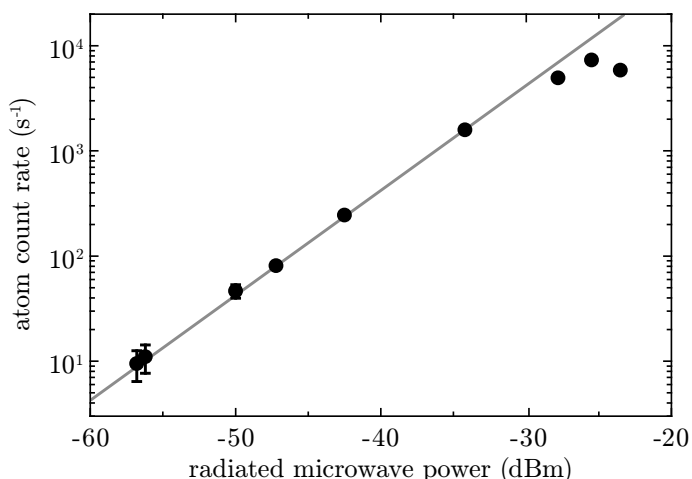


Figure 3.18: The ultrahigh finesse optical cavity functions as a linear detector on the output coupling rate, which is the atom flux, over three orders of magnitude. Saturation occurs at a count rate of about 5×10^3 atoms per second.

than in experiments employing a magneto-optical trap as the source of cold atoms.

We have confirmed that our single atom detector functions as a linear detector on the atom flux over three orders of magnitude (Fig. 3.18). The measured count rate of atoms is proportional to the microwave output coupling power (see Sec. 3.4.2). Saturation occurs at a flux of about 5×10^3 atoms per second. At higher rates multiatom arrivals within the dead time of our detector become dominant and single atom events cannot be resolved anymore. At a very low atom flux the error bars become increasingly large due to atom shot noise, which is determined by the Poissonian distribution of atom numbers. Additionally, a very weak atom “dark count” rate without intentional output coupling may be present. It is likely due to stray magnetic or optical fields and depends on the size of the Bose-Einstein condensate. However, the dark count rate is still less than 5 atoms per second on average for a BEC with 2×10^6 atoms.

3.5.5 Detection efficiency

The theoretical aspects of single atom detection have been described in section 2.3.4. Here, we extend those considerations to yield concrete results for the signal-to-noise ratio, and we will present measurements determining the optimum parameters for single atom detection.

In order to determine the detection efficiency for single atoms from the Bose-Einstein condensate we make use of the linear behavior of the atom flux on the microwave output coupling power (Fig. 3.18). We output couple a significant number of atoms

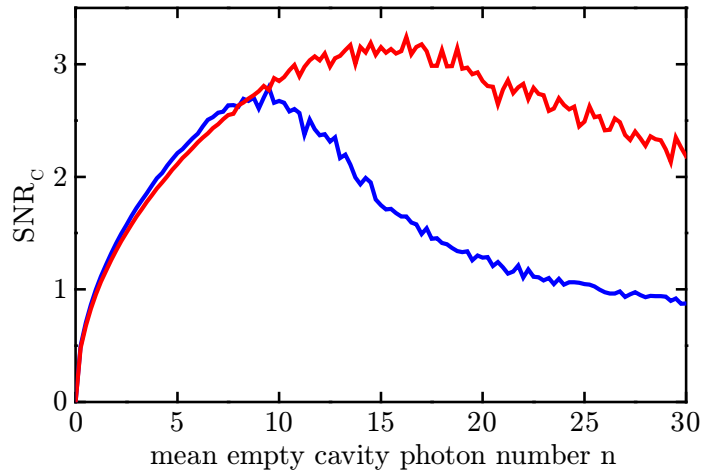


Figure 3.19: Detectability \mathcal{D} (see equation 3.10) as a function of the mean number of photons inside the empty cavity n . Both curves are results of numerical simulations with a resolution of $0.25 n$. The blue curve shows the behavior for cavity and probe laser tuned to the atomic resonance ($\Delta_a = \Delta_c = 0$). The red curve has been obtained for the those parameters typically used in the experiments and yielding the maximum detection efficiency ($\Delta_a = -3\Gamma = -18$ MHz and $\Delta_c = 1$ MHz).

measurable by absorption imaging while being still in the weak output coupling regime. This number is compared to the number of atoms detected by the cavity at a much lower microwave power and the resulting lower atom flux, including the corresponding ratio of the output coupling powers. The atom number in absorption imaging has been calibrated with the atom number at the critical temperature which is well known for our trap frequencies. For optimum settings of the cavity and laser detunings we are able to detect $(24 \pm 5)\%$ of the output coupled atoms with the cavity detector. This number is mainly limited by the spatial extent of the atom laser beam being larger than the cavity mode (see Sec. 3.6).

Signal-to-noise ratio

Because of the very stable and low-noise cavity lock, the cavity transmission is shot noise limited. Therefore the noise of our cavity transmission signal is given by $\sqrt{c_r \tau}$, where c_r is the mean count rate of the single photon counter for the empty cavity transmission and τ is the duration of an atom transit. In the experiments presented here, the mean interaction time $\tau = 45 \mu\text{s}$ is predetermined by the cavity mode diameter and the velocity of the atoms after falling the 36 mm from the position of the QUIC trap. c_r however can be tuned by changing the power of the probe laser. In the following, we will investigate the dependence of the signal-to-noise ratio on the probe power intensity.

Since the above considerations suggest working with high intracavity photon numbers, the system might no longer be in the weak pump limit. Therefore universal results from numerically solving the quantum master equation [see eqn. (2.53)] are required. In analogy to the definition of the detectability \mathcal{D} introduced in eqn. (2.66) we define

$$\mathcal{D} = \frac{|n - \langle \hat{a}^\dagger \hat{a} \rangle|}{\sqrt{\sigma_n^2 + \sigma_{\langle \hat{a}^\dagger \hat{a} \rangle}^2}}. \quad (3.10)$$

Here, n is the mean number of photons in the empty cavity, $\langle \hat{a}^\dagger \hat{a} \rangle$ is the mean number of photons in the cavity maximally coupled to a single atom and σ_n and $\sigma_{\langle \hat{a}^\dagger \hat{a} \rangle}$ denote their respective standard deviations. Figure 3.19 shows the dependence of \mathcal{D} on n with the parameters listed in Table 3.2 and for two different sets of detunings. On resonance (blue curve), it shows a pronounced maximum at $n \approx 9$. An even higher value of $\mathcal{D} \approx 3.2$ is found for the typical parameters used in the experiment, which are $\Delta_a = -3\Gamma = -18$ MHz and $\Delta_c = 1$ MHz (red curve). The maximum is reached at $n \approx 16$. This simulation is oversimplified in that we have assumed a constant coupling of the atom to the cavity mode during the whole transit. It is assumed to be equal to the maximum coupling and therefore the results constitute an upper limit on the signal-to-noise ratio.

The ultimate signal are the photons detected with the SPCM. Therefore, to get absolute values for the signal-to-noise ratio, \mathcal{D} has to be multiplied with the square root of the number of photons detected during an average atom transit for a cavity with no atom and one mean intracavity photon. We obtain

$$\text{SNR} = \mathcal{D} \times \sqrt{c_r \tau} = \mathcal{D} \times \sqrt{\frac{\mathcal{T} \eta c}{2l_{\text{res}}} \tau}, \quad (3.11)$$

where c_r denotes the count rate of the single photon counter [eqn. (3.8)] for one intracavity photon ($\bar{N}_{\text{ic}} = 1$). With the mean coupling time $\tau = 45 \mu\text{s}$ and ignoring the SPCM dead time this gives $\text{SNR} = \mathcal{D} \times 6$. The dead time of the SPCM however limits the maximum count rate via a declining detection efficiency [see eqn. (3.8)], so that working at $n = 8$ gives best results, even though the maximum of \mathcal{D} is at larger n (see red curve in Fig. 3.19). Including the dead time and for $n = 8$ we get $\text{SNR} = \mathcal{D} \times 5 = 14$. This is a very large value if one considers that a signal-to-noise ratio of 3 already gives a 95 % probability of detecting an event that is truly present if there is no background [194].

In principle, the discrimination between different numbers of atoms inside the cavity should be possible with our apparatus [195]. It was unnecessary for the work presented here, because the typical flux of atoms was so low that the probability of simultaneously having two atoms inside the cavity mode volume is negligible. In addition, the discrimination between different atom numbers would require to work at a set of detunings Δ_a and Δ_c which are not optimal for single atom detection.

Optimal parameters

The single atom detection efficiency of the ultrahigh finesse optical cavity strongly depends on the frequencies chosen [128] for the probe laser (ω_L) and the cavity resonance (ω_C) with respect to the atomic transition (ω_A). Furthermore, the effective coupling strength g_0 and therefore the detection probability are determined by the polarization of the probe light with respect to the quantization axis of the atomic spin.

In our experimental configuration we have a residual vertical magnetic field at the position of the cavity of about 16 G which represents the quantization axis for the atoms. The field originates from the magnetic QUIC trap which is on during the detection of single atoms from the atom laser.

We set the probe light to horizontal (within 10°) polarization which yields a four times higher atom count rate as vertically (within 10°) polarized light. Only these two distinct polarization settings are feasible, since we experience birefringence of the mirrors leading to a splitting of the cavity resonances for these two polarizations by about its linewidth. The horizontal polarization of the probe light produces a higher atom field coupling rate because it drives σ^+ and σ^- transitions compared to the fewer and weaker π transitions for vertically polarized light. The exact atom field interactions are more complex because of the Zeeman splitting and the resulting optical pumping dynamics inside the cavity. However, for red detuned probe light the atoms entering the cavity in the $|F = 2, m_F = 0\rangle$ state will predominantly be pumped into the $|F = 2, m_F = -2\rangle$ stretched state and undergo cycling transitions driven by the σ^- polarization component. Therefore this cycling transition will be the main contribution in the single atom detection process. The imbalance is due to a redshift for the σ^- component and a blueshift for the σ^+ component of ~ 22 MHz in the magnetic field of 16 G at the cavity.

The number of detected atoms critically depends on the detuning between probe laser and atomic resonance $\Delta_a = \omega_L - \omega_A$ and probe laser-cavity detuning $\Delta_c = \omega_L - \omega_C$ as illustrated in Fig. 3.20. Here ω_A refers to the bare atomic transition without magnetic field. For most efficient single atom detection we work with a probe laser-atom detuning Δ_a between -30 and -40 MHz and a probe laser-cavity detuning $\Delta_c \approx 0.5 - 1$ MHz. By taking into account the 22 MHz Zeeman shift of the cycling transition $|F = 2, m_F = -2\rangle \leftrightarrow |F' = 3, m_{F'} = -3\rangle$ (vertical dashed line in Fig. 3.20) the probe laser red detuning for optimum single atom detection is about 3Γ . This value is close to the maximum of the dipole potential created by the probe laser [see section 2.3.4 and Fig. 2.10(b)]. That means the dipole force channels the atoms in the axial direction towards the antinodes of the standing wave [136] which are simultaneously the areas of the highest atom field coupling strength. In the radial direction the dipole force is too weak to significantly modify the trajectory of the atoms within the cavity mode (see above).

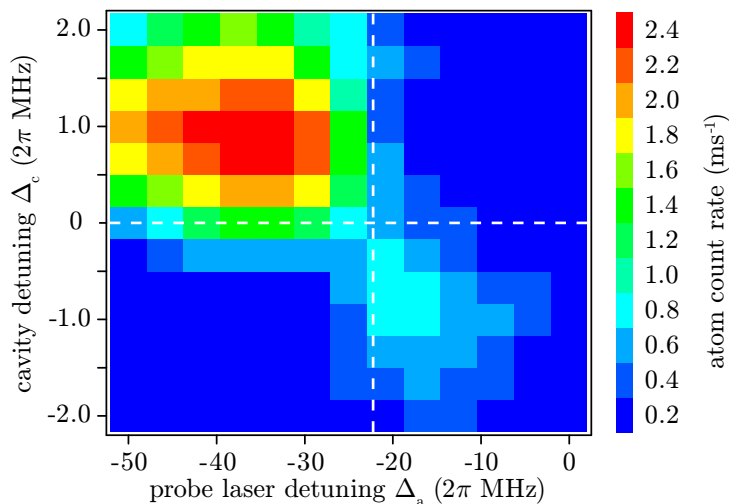


Figure 3.20: Dependence of the single atom detection efficiency on the detunings Δ_a and Δ_c . The vertical dashed line represents the cycling transition which is Zeeman shifted by 22 MHz from the zero field atomic transition. Best single atom detection is achieved with a probe laser red detuned by about 3Γ from the cycling transition (close to the maximum of the dipole potential created by the probe laser) and a cavity detuning of about $\Delta\nu/2$. The second local detection maximum corresponds to a blue detuned probe laser. Therefore the dipole potential is repulsive and the atom count rate reduced.

The second set of parameters in Fig.3.20 where single atom transits are detected is around $\Delta_a \approx -18$ MHz and $\Delta_c \approx -1$ MHz. However, the count rate is reduced considerably because the probe light is blue detuned from the cycling transition and therefore the dipole potential is repulsive. In the other two quadrants spanned by the resonances of the cavity and the cycling transition of Fig.3.20 (dashed lines), atom transits result in increased probe laser transmission versus the empty cavity transmission [28]. We do not use those events for single atom detection because the efficiency is reduced as compared to evaluating dips. Additionally, the peaks exhibit a substructure consisting of single photon bursts which makes it more difficult to discriminate single consecutive atom transits.

3.5.6 Accuracy of arrival time determination

Once an atom transit is identified, a precise determination of the time when the atom traverses the cavity axis in z-direction (“atom arrival time”) is necessary. The method employed determines the two points in time when the decrease in transmission is half maximum and sets the atom arrival time to be halfway between these times. We have

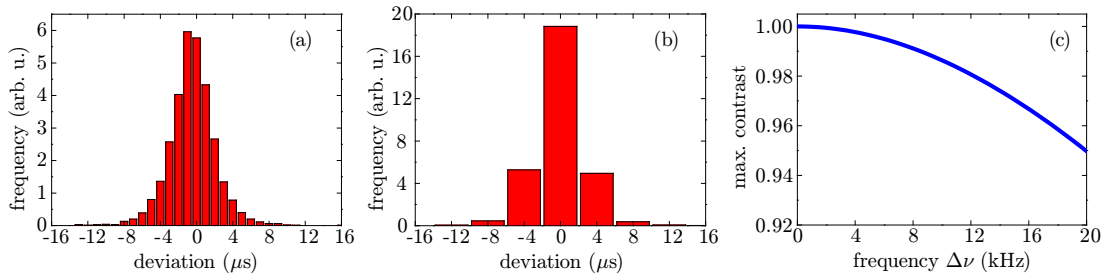


Figure 3.21: Jitter in the determination of atom arrival times. The mean deviation from the true atom arrival time is $1.9\ \mu\text{s}$ for a resolution of $1\ \mu\text{s}$ (a) and $2.6\ \mu\text{s}$ for $4\ \mu\text{s}$ resolution (b). (c) Fourier transform of (a). It is equivalent to the maximally observable contrast of a fully modulated matter wave interference pattern of frequency $\Delta\nu$ due to timing jitter.

compared this method with two alternatives. The first was taking the time of the minimum of the transmission as the atom arrival time. In the second method, the arrival time is the intersection of the two straight lines through the half minimum points with their respective slopes equal to those in the half minimum points. Using simulated atom transits (see below), both methods were found to be inferior to the main one in that they show an increased jitter in the determined atom arrival times. This is immediately plausible for the first alternative method, since the exact position of the minimum is subject to the strong fluctuations in photon flux due to shot noise. The second alternative method also showed a systematic offset of the determined atom arrival times which was not present when comparing the main and the first alternative method. This is probably due to the asymmetry of the peaks with differing magnitudes of the slopes on both sides of the dip.

We have characterized the accuracy of the determination of atom arrival times by analyzing artificial data. The position dependent coupling strength $g(\vec{r})$ between atom and cavity was calculated for atoms falling through the cavity mode at a mean velocity of $\bar{v}_z = 0.84\ \text{m/s}$. Starting positions are equally distributed over both transverse axes of the cavity, resulting in traces of all possible maximum coupling strengths. The coupling strengths are translated into relative cavity transmission using the relation found from numerically solving the quantum master equation of the system. Finally, multiplying the value for the relative transmission with a shot noise limited empty cavity transmission yields a list of numbers of photons per timebin, as usually recorded from the SPCM. These data are fed into our detection software. The resulting atom arrival times are compared to the true values used in the simulation. The resulting difference is plotted in Fig. 3.21. In (a), the timebin width and therefore the resolution was set to $1\ \mu\text{s}$, whereas in (b) the dwell time is $4\ \mu\text{s}$. The mean deviation of the automatically determined atom arrival times is $1.9\ \mu\text{s}$ for (a) and $2.6\ \mu\text{s}$ for case (b), respectively. The reason for the

offset of about $0.5\ \mu\text{s}$ of the distribution from zero in (a) is due to the quantization of time by $1\ \mu\text{s}$. When an atom arrival time is determined to lie between two timebins it is by convention assigned to the upper one. This minimizes the error in determining time intervals between atom arrivals, which is e.g. important when measuring the two-particle correlation function $g^{(2)}(\tau)$ (see chapter 5). This offset is not present in the data with a dwell time of $4\ \mu\text{s}$. The mean deviation of the atom arrival times is nearly a factor of two smaller for maximally coupling atoms than for an ensemble with all possible couplings.

From the simulation we find that about once in 2s shot noise leads to an atom detection event without any being present, which is about what one expects from the classically unavoidable Poissonian fluctuations in the detection light. From 10^4 fake atoms coupling maximally to the cavity each was detected. The same is true for atoms coupling with 75 % of the maximum value. This success rate of course decreases dramatically when atoms coupling less strongly are considered. Therefore in selecting a specific threshold for the coupling one can optimize between a minimum number of false detections and maximum detection efficiency.

The timing jitter leads to a decrease in the achievable contrast when output coupling from a BEC with two different frequencies (see section 2.2.3). The larger the separation between the two frequencies, the smaller the achievable contrast. This dependency is described by the Fourier transform of the timing jitter. For the data of Fig. 3.21(a) it is plotted in (c). At a frequency difference of 20 kHz the contrast is limited to 95 %.

3.6 Atom laser beam profile

Obviously, in order to see single atoms with the cavity, the atom laser has to propagate through the cavity mode. However, this is technically demanding, because the BEC production rig and the science platform are completely independent entities of the experimental apparatus and the alignment has to be better than a few millirad without knowing the exact position of the cavity mode. Furthermore, the second-order Zeeman effect slightly bends the trajectory of the atom laser in the $|F = 2, m_F = 0\rangle$ state and modifies its final lateral position by hundreds of micrometers. Although we have aligned the cavity with respect to the BEC position as accurately as possible with plummets during the assembly of the apparatus, the atom laser did not innately hit the cavity mode. We correct these deviations by tilting the whole optical table on which the experiment rests employing its height adjustable legs. The tilt is monitored with a dual-axis inclinometer having its axes aligned along and perpendicular to the cavity axis. With this method we direct the atom laser exactly into the cavity mode and maximize the atom count rate [Fig. 3.22(a)].

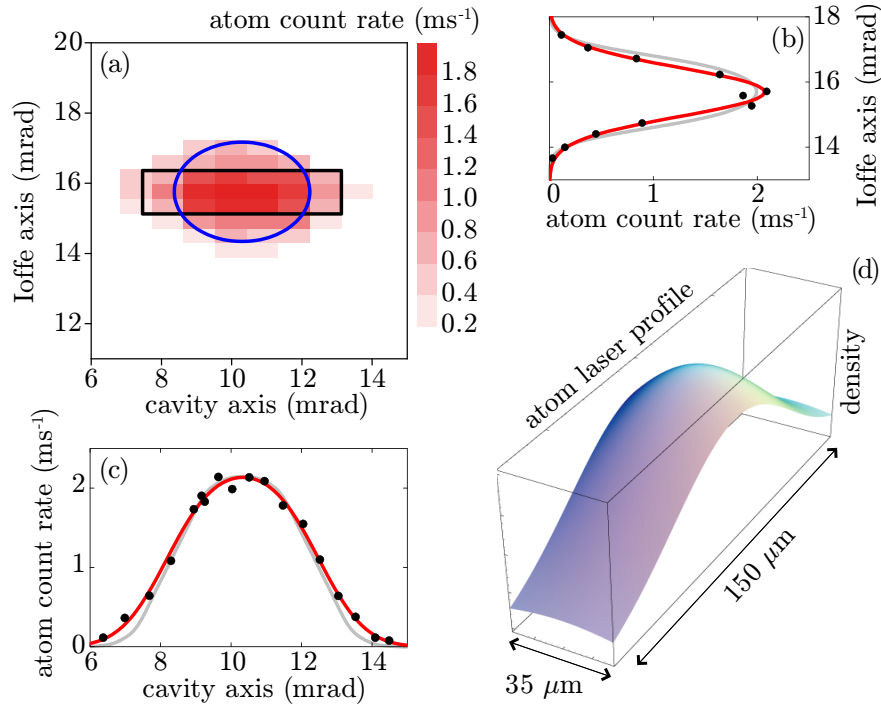


Figure 3.22: (a) The detected atom count rate for a constant atom flux is shown with respect to the inclination of the optical table along the two axes. The rectangle represents the active area of the cavity mode and the ellipse is the reconstructed size ($1/e$ diameter) of the atom laser at the position of the cavity. [(b) and (c)] Fit (red) to the measured data (black) by the convolution of the active size of the cavity mode with a Gaussian beam profile along the Ioffe (b) and cavity (c) axes. It is compared to the expected shape from numerical simulations of the Gross-Pitaevskii equation (gray). (d) Visualization of the extracted two-dimensional atom laser beam profile clipped by the active area of the cavity mode.

Moreover, tilting the setup enables us to experimentally deduce the diameter of the atom laser after a propagation of 36.4 mm. The active area of the cavity mode is approximately $(35 \times 150) \mu\text{m}^2$. The size in the radial direction is determined by the weakest coupling $g_0^{\text{min}} = 2\pi \times 6.5 \text{ MHz}$ at which an atom transits can still be detected. In the axial direction it is given by the projection of the cavity length clipped by the curved mirrors.

A deconvolution of the measured angle dependent count rates with this active area assuming a Gaussian atom laser beam profile yields $1/e$ diameters of $80 \mu\text{m}$ and $110 \mu\text{m}$ along and perpendicular to the Ioffe axis, respectively [Figs. 3.22(b) and 3.22(c), red]. The mapped atom laser, being output coupled from the center of a Bose-Einstein condensate with 1×10^6 atoms, is slightly inverted compared to the trap geometry but

almost round at the cavity. Here, its divergence is about 2 mrad along the (“fast”) cavity axis and less than 0.5 mrad along the Ioffe axis, which makes it the best collimated atom laser to date [79, 77, 90].

The repulsive mean field interaction from the remaining trapped BEC is considerable only along the fast axis where it acts as a defocusing lens for the atom laser beam. This results in an expansion about four times larger than expected from Heisenberg’s uncertainty principle. Along the weakly confining Ioffe axis the lensing effect is negligible and the size of the atom laser is consistent with a free expansion of the initial ground state in the trap. The size of the atom laser and therefore its divergence can be reduced further, especially along the fast axis, by output coupling below the center plane of the BEC [90] and by using smaller condensates (see Sec. 3.7.2).

We compare the measured atom laser profiles along its symmetry axes with numerical simulations of its time evolution using the Gross-Pitaevskii equation. The resulting density distributions of the atom laser deviate slightly from a Gaussian shape [99], but the measured convolutions with the cavity mode agree very well with the simulated curves [Figs. 3.22(b) and 3.22(c), gray]. The overestimated width along the Ioffe axis can be explained by the angle of the BEC axis with respect to the horizontal plane, reducing the spatial width of the output coupling region along the Ioffe axis. Along the cavity axis the slight deviation at the edges is probably due to pointing variations, i.e. transverse oscillations of the atom laser beam. Small collective oscillations in the trap are translated into deflections of the atom laser beam over which we integrate with our detection method. The collective oscillations, mainly dipole oscillations in the trapped Bose-Einstein condensate, can be excited by radio frequency evaporation or incautious relaxation of the magnetic trap.

3.6.1 Guiding the atom laser

The reason for the single atom detection efficiency not being unity is mainly the mismatch of the atom laser and cavity mode sizes [Fig. 3.22(d)]. Their overlap is only about 50 % when replacing the cavity mode by a box given by the projected length of the cavity mode and a minimum peak atom field coupling strength of $g_0^{\min} = 2\pi \times 6.5$ MHz in the radial direction [see Fig. 3.22(a)]. We have performed classical simulations of atom trajectories inside the cavity. The sensitivity of the cavity-based atom detector is highly position dependent due to the standing wave structure of the cavity mode. By taking into account the channeling effect of the dipole potential, from our simulations we find a maximum single atom detection efficiency of 80 % and an averaged efficiency of about 50 % within the aforementioned box. Therefore the overlap of the atom laser beam and the “sensitive area” of the cavity is only about 25 % to 40 %. Comparing this to the measured detection efficiency of about 1/4 (see Sec. 3.5.4), we find an efficiency close to

unity for atoms traversing the sensitive area of the cavity detector to be detected.

In order to increase the overlap and therefore the number of detectable atoms it is possible to funnel the atoms with a dipole potential created by a far red-detuned guiding laser (850 nm, up to 100 mW, beam waists of $(30 \times 60) \mu\text{m}^2$) into the cavity mode. By doing so we are able to improve the single atom detection efficiency by about a factor of two to around 50 %. This number still differs from a perfect detection efficiency because the dipole potential formed by the probe laser is simply not strong enough to perfectly localize the atoms in the axial direction at the antinodes of the standing wave.

Although we are able to increase the single atom detection efficiency, employing the guiding laser involves some disadvantages. Scattering and heating rate in the dipole potential formed by the guiding laser can influence the atom arrival times which is undesirable for many experiments [101]. Furthermore, the guiding laser acts on both thermal and quantum degenerate atoms and therefore diminishes a characteristic feature of our detector, namely, the very sensitive discrimination between thermal and condensed atom count rates (see Sec. 3.7).

3.7 Investigation of cold atomic gases

The combination of a Bose-Einstein condensate with an ultrahigh finesse optical cavity enables us to detect single atoms from a quantum degenerate gas with very high sensitivity. Therefore we can employ the cavity as a minimally invasive probe for cold atomic clouds. This allows us to perform nondestructive measurements on the ensemble of cold atoms *in situ* and time resolved.

Assuming a constant, weak output coupling power, the atom count rate of the cavity detector depends on the properties of the source via two factors. First, the number of output coupled atoms is proportional to the number of atoms fulfilling the resonance condition, which in turn is proportional to the density at the output coupling plane. Second, the atom count rate depends on the probability for an output coupled atom to hit the cavity mode. Because of its finite active area the cavity functions as a filter in momentum space.

3.7.1 Thermal clouds

For a thermal cloud the density at the output coupling central plane is proportional to $N_{\text{th}} T^{-1/2}$ and the probability to hit the detector is proportional to $1/T$ assuming Gaussian density and momentum distributions. Therefore the thermal atom count rate detected with the cavity is proportional to $N_{\text{th}} T^{-3/2}$. This dependency is shown in Fig. 3.23. At the critical temperature of $T_c \approx 180 \text{ nK}$ for 10^7 atoms only about 0.6% of

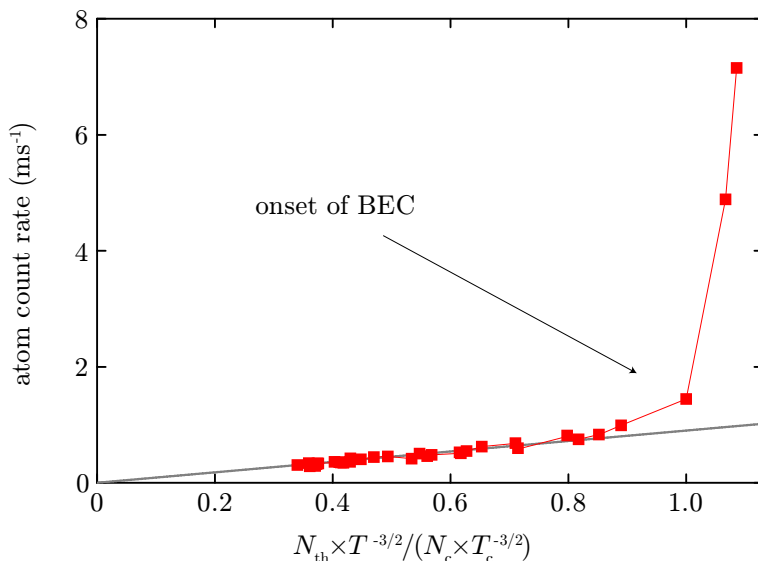


Figure 3.23: Investigation of atom count rates for thermal beams. The count rate is proportional to $N_{\text{th}} T^{-3/2}$ for temperatures above the critical temperature and sharply increases when cooling across the phase transition. Just above T_c the density and momentum distributions of the thermal cloud are governed by a Bose distribution and obey a different scaling law than expected for a Gaussian distribution.

the output coupled thermal atoms will fly through the cavity mode and can possibly be detected. The onset of Bose-Einstein condensation can be clearly seen in the sharp increase in the number of detected atoms [196, 197]. Close to the critical temperature however, the detected atom flux slightly deviates from the expected behavior because the Gaussian distributions for density and momentum are not valid approximations anymore near T_c . The thermal cloud is correctly described by the more peaked Bose distribution which yields an increased atom detection rate of about 30 % near the critical temperature of 180 nK compared to the Gaussian distribution (see also Sec. 4.3.2).

3.7.2 Quantum degenerate gases

For Bose-Einstein condensates the probability for an atom to hit the cavity mode and therefore the atom count rate detected with the cavity is independent of temperature. The number of resonant atoms participating in the output coupling process is proportional to the density of the BEC and the area of the output coupling plane. This means the atom flux is proportional to $N_{\text{BEC}}^{4/5}$ (when output coupling from the center of the BEC with respect to the vertical axis), because the Thomas-Fermi radius of a BEC scales as $N_{\text{BEC}}^{1/5}$. However, this dependency is only true for Bose-Einstein condensates of interme-

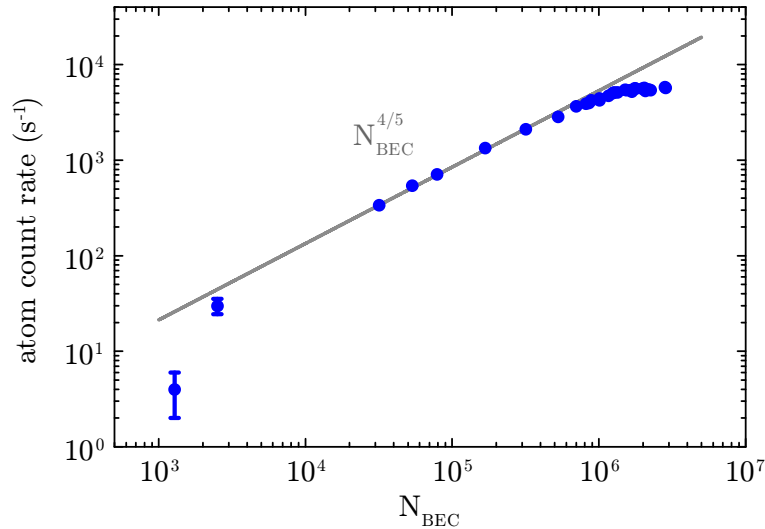


Figure 3.24: Investigation of measured atom count rates for pure quantum degenerate samples. The scaling with the atom number in a pure BEC and at constant output coupling power exhibits three different regimes. The expected $N_{\text{BEC}}^{4/5}$ behavior is only valid for intermediate particle numbers. Very small and very large condensates obey different scaling laws due to an increased Heisenberg limited momentum spread and the mean field repulsion of the remaining condensate, respectively.

diante size (Fig. 3.24) and deviates for very small and very large condensates. Output coupling from small condensates accounts for a faster quantum mechanical expansion of the initial ground state wave function in the atom laser. Therefore the overlap between the transverse atom laser wave function and the cavity mode is reduced. Large condensates on the other hand exhibit increased divergence because of the mean-field repulsion exerted on the atom laser propagating through the BEC. The condensate acts as an imperfect diverging lens and displaces the maximum density outwards [90, 99, 98]. This results in a weaker scaling of the detected atom flux with the number of atoms in the BEC and possibly a decrease when the atom laser profile becomes more “donut-mode-like.” These three regimes are displayed in Fig. 3.24 for measured atom count rates versus the number of atoms in the “pure” BEC. The exact position of the crossover between these regimes depends on the active area of the single atom detector.

3.7.3 Phase Transition

Our single atom detector in form of the ultrahigh finesse optical cavity is extremely sensitive and selective to quantum degenerate atoms not only because of the increased density at the output coupling region but also due to the filtering in transverse momentum space. This means we can more accurately observe the onset of Bose-Einstein

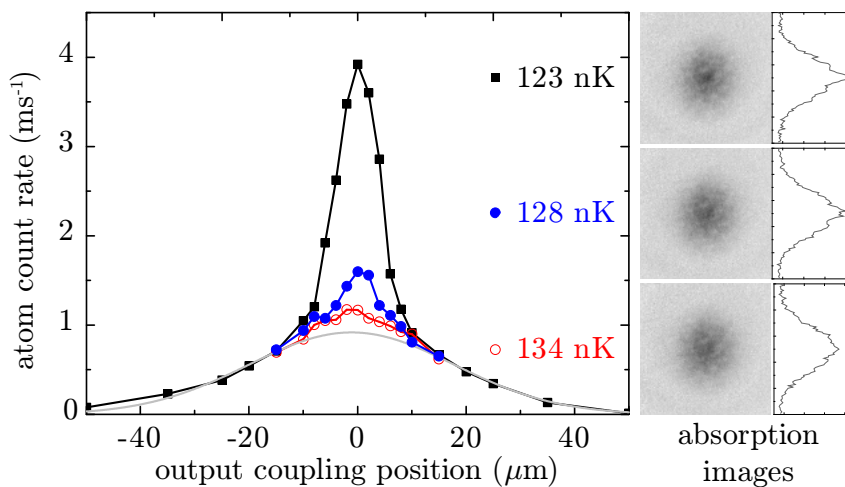


Figure 3.25: Analysis of the density distribution of the trapped ultracold atomic gas by output coupling at different vertical positions relative to the center of the BEC and measuring the resulting atom count rate with the cavity. The profiles for three different temperatures around T_c are shown in comparison with the absorption images. The high sensitivity of the cavity detector to quantum degenerate atoms allows for the precise observation of the onset of Bose-Einstein condensation and the deviations from a Gaussian profile (gray curve).

condensation as compared to absorption imaging techniques. The exact determination of the critical temperature in combination with the precisely measured trap frequencies (Fig. 3.28) allows one in turn to calibrate the atom number obtained by the absorption images. Furthermore we are able to survey the density distribution in the trap along the vertical direction by scanning the resonant plane for the output coupling process through the trapped cloud of cold atoms (Fig. 3.25). For temperatures close to the critical temperature the density distribution of the thermal cloud already deviates from the Gaussian shape and has to be described by the more peaked Bose distribution (Fig. 3.25, 134 nK). For temperatures slightly below T_c single atom detection with the cavity allows us to observe and map very small condensates that are not visible in absorption images (Fig. 3.25, 128 nK and 123 nK). This is a valuable tool to study the temporal and spatial evolution of a bosonic gas at the phase transition.

3.8 Detecting phase modulation of an atom laser beam—A new tool for precision measurements of dipole oscillations

The measurement of collective excitations has been a tool to study condensate physics from right after its first experimental realization [198, 199, 200]. It was further used to characterize a BEC of molecules [201], the superfluid to Mott insulator transition in 1D [202] and a degenerate gas of fermions at the BEC–BCS crossover [203]. To determine the oscillation frequency, all these measurements rely on the accurate detection of the position (dipole oscillation) and shape (quadrupole oscillations) of the atom cloud after different times with respect to the start of the oscillation. This is usually achieved by absorption imaging. *In situ* imaging allows for the direct observation in position space but requires a high-resolution imaging system and a rather large oscillation amplitude. An alternative is to switch off the trapping potential after a variable time delay and wait for some constant time of flight before imaging. In this case the momentum distribution of the sample can directly be imaged and in principle even very small momenta are detectable when allowing for very long flight times. Since momentum and position are conjugate variables, both techniques offer the same information on the oscillations.

Complementary to the methods described above, we have developed a technique to determine the amplitude and frequency of the center of mass oscillation along the vertical axis of one and the same trapped Bose-Einstein condensate *in situ*. Applying two microwave frequencies, we output couple atoms from the BEC which will subsequently form two overlapping atom laser beams. These atomic beams show an interference pattern at the difference $\Delta\nu$ between the two microwaves (see Sec. 2.2.3). Using the cavity-based single atom detector, we record the arrival times of all atoms falling through the cavity mode. This constitutes a flux measurement of extremely high efficiency and accuracy on the single atom level. In the case of a BEC at rest, the Fourier transform of the histogram exhibits a peak exactly at $\Delta\nu$. Due to the high temporal coherence of the atom laser [100], the width of this Fourier peak is given by the inverse of the duration of output coupling. Certainly, the precision in determining its center frequency is much higher.

The appearance of the frequency spectrum changes when collective, vertical dipole oscillations are present. In this case, the interference pattern of the two atom lasers gets phase modulated. In addition to the carrier, sidebands at the vertical trap frequency and multiples thereof are present (see Fig. 3.26). Their heights are dependent on the amplitude of the oscillation and the difference frequency $\Delta\nu$ of the two microwaves.

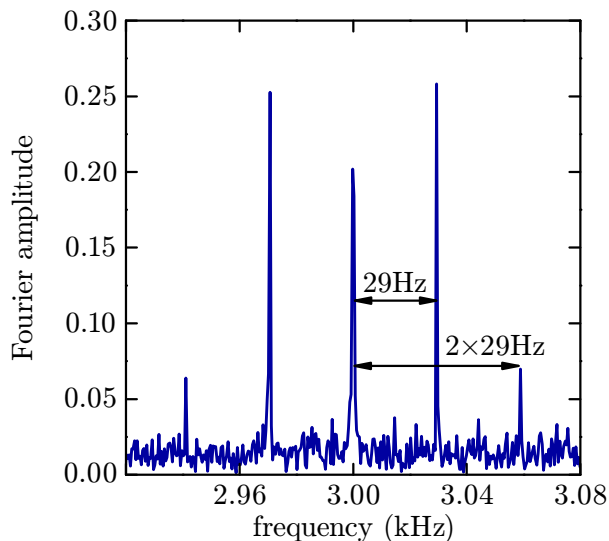


Figure 3.26: Fourier transform of the atom flux in an experiment to determine the frequency and amplitude of vertical oscillations (see text). The sidebands are separated from the carrier at 3 kHz by multiples of the oscillation frequency.

3.8.1 Theoretical model

In a semi-classical picture neglecting interactions, one can understand this effect as being due to different times of flight for atoms from the two atom lasers. Due to energy conservation, atoms are output coupled from regions which can be well approximated as the intersection of a horizontal plane and the BEC (see Sec. 2.2.2). For the following considerations, a one-dimensional model along the direction given by gravity is sufficient. Each atom laser originates from a well defined position in space. At a frequency difference $\Delta\nu$ between the two microwave frequencies used for output coupling, the separation between the two origins is given by $\Delta x = h\Delta\nu/(mg)$, with m being the atomic mass and g the acceleration due to gravity (see Sec. 2.2.3).

The time it takes for a particle with initial velocity v to fall the distance l from its position of output coupling into the cavity is given by

$$t_f = \sqrt{\frac{2l}{g} + \left(\frac{v}{g}\right)^2} - \frac{v}{g}. \quad (3.12)$$

The output coupling frequencies are chosen such that the origins of the atom laser beams are symmetric with respect to the center of the trapped cloud. Let d be the distance between this center and the cavity axis. Δx is much smaller than d and we let $l = d \pm \Delta x/2$. If the cloud oscillates in the trap, the atoms will have a time dependent initial velocity $v = v_0 \cos \omega_z t$ which oscillates at the vertical trap frequency ω_z . The

maximal velocity of a harmonic oscillator is given by $v_0 = A\omega_z$, where A is the spatial amplitude of the oscillation.

The difference in time of fall t_f from the upper and the lower slit is given by

$$\Delta t = \sqrt{\frac{2(d + \Delta x/2)}{g} + \left(\frac{v_1}{g}\right)^2} - \frac{v_1}{g} - \left(\sqrt{\frac{2(d - \Delta x/2)}{g} + \left(\frac{v_2}{g}\right)^2} - \frac{v_2}{g} \right), \quad (3.13)$$

assuming initial velocities v_1 and v_2 for the atoms from the upper and lower origin, respectively. It can be approximated by

$$\Delta t \approx \frac{\Delta x}{\sqrt{2dg}} + \frac{v_2 - v_1}{g} \quad (3.14)$$

to first order in Δx and Δv in case $v \ll \sqrt{2lg}$. This is equivalent to $A \ll \sqrt{2lg}/\omega_z = 4.6$ mm. This criterion is easily fulfilled.

Δt needs to be evaluated for atoms reaching the cavity at the same time, because only these will interfere. If an atom from origin 1 reaches the cavity at time t , it was output coupled at time $t - t_{f,1}$. At that time, the cloud in the trap and therefore also the atom under consideration had the velocity $v_1 = v_0 \cos(\omega_z(t - t_{f,1}))$. Equivalently, for an atom from the second slit we get $v_2 = v_0 \cos(\omega_z(t - t_{f,2}))$. This means that atoms arriving at the cavity at the same time were output coupled at different times and therefore with different velocities. The difference between v_2 and v_1 oscillates in time. So we get

$$\begin{aligned} \Delta t &\approx \frac{\Delta x}{\sqrt{2dg}} + \frac{v_0}{g} [\cos(\omega_z(t - t_{f,2})) - \cos(\omega_z(t - t_{f,1}))] \\ &= \frac{\Delta x}{\sqrt{2dg}} - 2\frac{v_0}{g} \sin\left[\frac{\omega_z}{2}((t - t_{f,2}) + (t - t_{f,1}))\right] \sin\left[\frac{\omega_z}{2}\Delta t\right] \\ &= \frac{\Delta x}{\sqrt{2dg}} - 2\frac{v_0}{g} \sin[\omega_z t + \phi_0] \sin\left[\frac{\omega_z}{2}\Delta t\right]. \end{aligned} \quad (3.15)$$

where $\phi_0 = -\omega_z(t_{f,1} + t_{f,2})/2$ is constant to zero order in v . We replace Δt in the argument of the second sine by equation (3.14) to zeroth order in v and finally find

$$\Delta t \approx \frac{\Delta x}{\sqrt{2dg}} - 2\frac{v_0}{g} \sin(\omega_z t + \phi) \sin\left(\frac{\omega_z \Delta x}{\sqrt{8dg}}\right). \quad (3.16)$$

We look at the interference of the two atom lasers by adding two plane waves of energy $\hbar\omega_i$ at the position of the cavity:

$$\begin{aligned} |\psi|^2 &\propto |e^{i\omega_1(t-t_{f,1})} + e^{i\omega_2(t-t_{f,2})}|^2 \\ &= 2(1 + \cos[\omega_1(t - t_{f,1}) - \omega_2(t - t_{f,2})]) \\ &= 2(1 + \cos[(\omega_1 - \omega_2)t - \omega_1 t_{f,1} + \omega_2 t_{f,2}]) \\ &= 2\left(1 + \cos\left[(\omega_1 - \omega_2)(t - \bar{t}_f) - \frac{\omega_1 + \omega_2}{2}\Delta t\right]\right), \end{aligned} \quad (3.17)$$

where we have used $t_{f,1} = \bar{t}_f + \Delta t/2$ and $t_{f,2} = \bar{t}_f - \Delta t/2$. The energy difference between the two atom lasers and between the two microwaves ($\hbar\Delta\omega$) are the same and equal to the potential difference of the atom laser origins: $\hbar(\omega_1 - \omega_2) = \hbar\Delta\omega = mg\Delta x$. Using the same argument we find $\hbar(\omega_1 + \omega_2)/2 = mgd$ for atoms of mass m . Assuming \bar{t}_f to be constant and inserting equation (3.16) into (3.17) we find

$$|\psi|^2 \propto 1 + \cos \left[\Delta\omega t + \frac{2mdv_0}{\hbar} \sin \left(\frac{\omega_z \hbar \Delta\omega}{m\sqrt{d}(2g)^{3/2}} \right) \sin(\omega_z t + \phi_0) + \Phi_0 \right], \quad (3.18)$$

having absorbed all terms in the cosine which are not time dependent into the global phase Φ_0 . This is the formula of a sinusoidally phase modulated signal (often also called frequency modulated) with carrier frequency $\Delta\nu = \Delta\omega/(2\pi)$, modulation frequency $\omega_z/(2\pi)$ and modulation index

$$\beta = \frac{2mdv_0}{\hbar} \sin \left(\frac{\omega_z \hbar \Delta\omega}{m\sqrt{d}(2g)^{3/2}} \right) \approx \frac{v_0 \omega_z \sqrt{d} \Delta\omega}{\sqrt{2}g^{3/2}} = \frac{2\pi A \omega_z^2 \sqrt{d} \Delta\nu}{\sqrt{2}g^{3/2}}. \quad (3.19)$$

We have linearized the sine, which is a very good approximation since its argument is typically three orders of magnitude smaller than one.

Now we are in a position to understand the frequency spectrum in Fig. 3.26: Rewriting equation (3.18) and setting all phases to zero we get

$$\begin{aligned} |\psi|^2 &\propto 1 + \cos(2\pi\Delta\nu t + \beta \sin(2\pi\nu_z t)) \\ &= 1 + \sum_{k=-\infty}^{\infty} J_k(\beta) \cos(2\pi(\Delta\nu + k\nu_z)t), \quad k \in \mathbb{Z}. \end{aligned} \quad (3.20)$$

The signal contains a peak at zero frequency due to the constant offset, the carrier at $\Delta\nu$, and sidebands around this carrier spaced by ν_z . The amplitudes of the frequency components are given by Bessel functions of the first kind $J_k(\beta)$.

3.8.2 Example measurements

Figure 3.27 shows the amplitudes of the Fourier peaks at $\Delta\nu$ and $\Delta\nu \pm \nu_z$ as a function of the microwave frequency difference $\Delta\nu$. They are well fitted by the zero order and first-order Bessel functions respectively. The solid lines are fits of $J_{0,1}(\beta)$ to the data. The agreement is very good for $\Delta\nu < 14$ kHz. For larger slit separations the signal gets too small to be accurately discriminated from the noise. The trap frequency $\nu_z = 29.4$ Hz can be determined very accurately by fitting the peaks in Fig. 3.26. The error is certainly below one percent. We find $\beta/\Delta\nu = (0.497 \pm 0.003)$ ms for the data presented in Fig. 3.27. From this we can infer the amplitude of the oscillation to be

$$A = \frac{\sqrt{2}g^{3/2}}{2\pi\omega_z^2\sqrt{d}} \frac{\beta}{\Delta\nu} = 0.54 \mu\text{m} \quad (3.21)$$

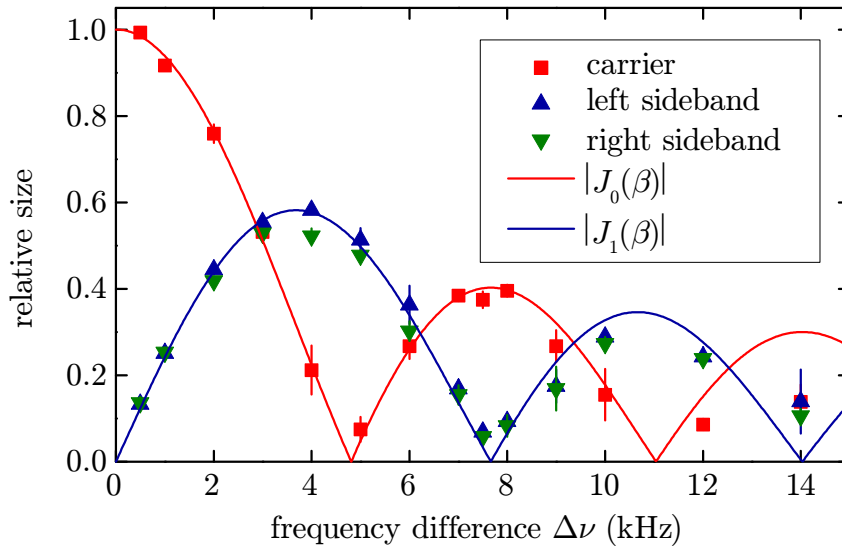


Figure 3.27: Dependence of the relative amplitudes of carrier and sidebands on the carrier frequency $\Delta\nu$. The data points are extracted from Fourier transforms of flux measurements like the one in Fig. 3.26. The error bars indicate statistical errors of the mean of three measurements. By fitting Bessel functions to the data (solid lines), the amplitude of the oscillation can be deduced.

We can measure d very accurately by transporting the atoms from the QUIC trap into the cavity and counting the number of half-wavelengths necessary to shift the atoms by this distance. Since the transport laser wavelength is stabilized to an atomic transition, it is accurately known. The uncertainty in g is also much smaller than 1%, and therefore the error in A is dominated by the errors in $\beta/\Delta\nu$ and ν_z . It is on the order of 1%, demonstrating a measurement of the oscillation amplitude on the nm scale.

3.8.3 Potential of the method

What are the limits in the determination of extremely small amplitudes? In principle, increasing d , ν_z and $\Delta\nu$ all improve the sensitivity. However, increasing d is experimentally rather difficult and also not very efficient since the sensitivity only shows a square root dependence on d . Increasing the trapping frequency however is easily achieved. At the maximally available current for our QUIC-trap, we find $\omega_z = 2\pi \times 135$ Hz, which results in a 20-fold increase in sensitivity. For difference frequencies of up to 6 kHz we find 100% visibility of the interference fringes, signified by a carrier peak of half the height of the peak at zero frequency. For larger separations the signal decreases faster than $\Delta\nu$ increases. The smallest modulation index β_{\min} we can detect depends on the signal-to-noise ratio in the Fourier transform. Following a usual convention, we assume

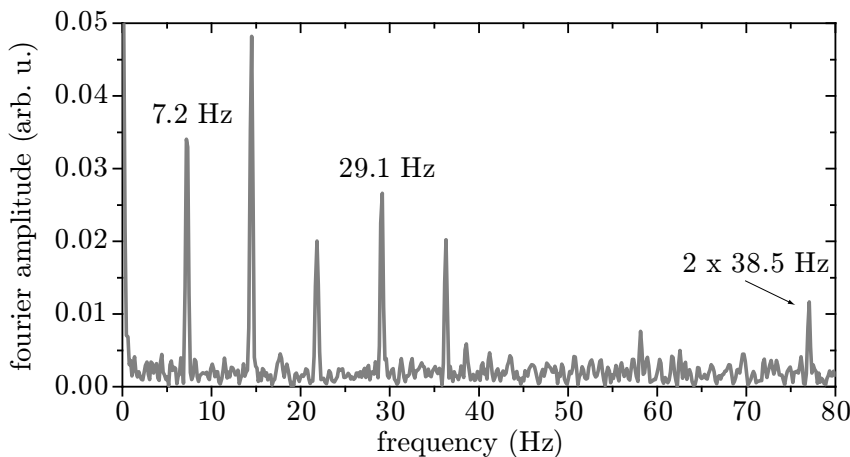


Figure 3.28: The Fourier spectrum of the detected atom laser flux exhibiting the trapping frequencies and their harmonics. A fast and precise tool to measure frequencies of collective oscillation in the trap.

that a signal-to-noise ratio of at least three is necessary to accurately discriminate the sidebands from the noise, which is roughly given by the square root of the number of detected atoms. We can detect up to 2000 atoms per second without significant decrease in detection efficiency. Therefore the maximum detection time and ultimately the damping rate of the oscillation limits the sensitivity of our measurement. The same is true for the accuracy in determining the oscillation frequencies. The width of the peaks is Fourier limited, i.e. given by the inverse of the recording time, and their center can be determined with much higher accuracy.

At a vertical trapping frequency of $\omega_z = 2\pi \times 135 \text{ Hz}$ and within only one second of measurement time, we are sensitive to amplitudes as small as $A = 2 \text{ nm}$. To get the same resolution in absorption imaging, assuming an imaging resolution of $1 \mu\text{m}$, a time of flight of 590 ms during which the cloud falls by 1.7 m would be necessary and is rather impractical. The larger the trapping frequency in the vertical direction, the greater the advantage of the new detection method employing the cavity, because the smallest detectable amplitude scales as ω_z^{-2} compared to ω_z^{-1} in absorption imaging.

3.8.4 Oscillations along the horizontal directions

So far, we have presented a method to measure the frequency and amplitude of oscillations in the vertical direction. The same is possible for the two horizontal axes. As mentioned earlier, transverse oscillations of the BEC are translated into deflections of the atom laser. Because the beam is larger than the active area of the cavity and has an approximately Gaussian density profile, pointing variations will lead to changes in

the atom flux detected with the cavity. This effect can be exploited to precisely determine the frequencies of excited collective oscillations in the trap by analyzing the Fourier spectrum of the atom count rate. The baseband of such a spectrum is shown in Fig. 3.28 exhibiting harmonics of the trap frequencies (dipole oscillations) and mutual sidebands. The frequencies can be measured in situ with one and the same experimental implementation of a Bose-Einstein condensate to high precision (mHz), Fourier limited by the duration of the atom laser recording. Even the vertical trapping frequency is visible, because the region of output coupling is fixed in space whereas the BEC oscillates. Therefore the local density at the position of output coupling and with it the atom flux changes periodically.

3.8.5 Conclusions

We have presented an extremely sensitive method to detect the amplitude and frequency of collective oscillations of a magnetically trapped Bose-Einstein condensate. It relies on the precise detection of the time-dependent flux of an atom laser beam output coupled from the BEC. It is important to note that even though a small reduction in the number of condensate atoms due to the output coupling is inevitable, the remaining cloud is not heated. Also the influence of the output coupling on the oscillations is very weak. Therefore experiments with a pure BEC directly following the accurate determination of its oscillation amplitude and frequency are feasible. Oscillations along all three trap axes can be resolved simultaneously and with minimum disturbance of the atom cloud. The detection of vertical oscillations is especially sensitive. The method presented here was used to determine the trapping frequencies of our apparatus. In addition, it was essential for the experiments on condensate formation presented in chapter 4. Oscillations induced by shock cooling an ultracold atom cloud had to be minimized to allow for the accurate determination of coherence and density growth during condensate formation. The high sensitivity of the method allowed to test and descry procedures to avoid the excitation of oscillations. In addition, it facilitated the determination of a quantitative upper limit for residual oscillations and their effect on the measurement (see Sec. 4.3.6).

4 Observing the formation of long-range order during Bose-Einstein condensation

We experimentally investigated the formation of off-diagonal long-range order in a gas of ultracold atoms. A magnetically trapped atom cloud prepared in a highly nonequilibrium state thermalized and thereby crossed the Bose-Einstein condensation phase transition. The evolution of phase coherence between different regions of the sample was constantly monitored and information on the spatial first-order correlation function was obtained. We observed the growth of the spatial coherence and the formation of long-range order in real time and compared it to the growth of the atomic density. Moreover, we studied the evolution of the momentum distribution during the nonequilibrium formation of the condensate.

Parts of this chapter have been published as [153]: S. Ritter, A. Öttl, T. Donner, T. Bourdel, M. Köhl, and T. Esslinger. ‘Observing the Formation of Long-Range Order during Bose-Einstein Condensation’. *Physical Review Letters* **98**(9), 090402 (2007).

4.1 Introduction

When a gas of atoms is undergoing Bose-Einstein condensation a macroscopic number of particles start to occupy the same quantum mechanical state—it seems like the randomly colliding atoms are suddenly forced into a lock-step motion. The understanding of this process in which phase coherence spreads over the whole gaseous cloud has intrigued physicists long before Bose-Einstein condensation has been demonstrated [204, 7]. In particular, the question when the characteristic long-range phase coherence is established is the key point for understanding the condensation process. The trajectory into the state of a Bose-Einstein condensate [204, 7, 205, 206] is much more intricate than its equilibrium properties.

The transition to a superfluid or a superconducting quantum phase is a remarkable process in which the properties of the system undergo a fundamental change. The conceptual link between quantum phases in various systems is the off-diagonal long-

range order in the density matrix which describes phase correlations over macroscopic distances [4, 5]. The first-order spatial correlation function $G^{(1)}(r, r') = \langle \hat{\Psi}^\dagger(r) \hat{\Psi}(r') \rangle$ [56] quantifies the characteristic length scale over which phase correlations exist. Here $\hat{\Psi}$ ($\hat{\Psi}^\dagger$) denotes the annihilation (creation) operator of the atomic field. To experimentally study how long-range order is established in space and time, real time access to this process is required. Yet, due to the short relaxation times and the strong coupling to the environment this seems troublesome in condensed matter samples, such as liquid helium or superconducting materials.

In a trapped atomic Bose gas the situation is distinctly different. It forms an almost closed system with negligible coupling to the environment and the relaxation time scales are experimentally accessible. [104].

4.2 Background

Even though the question how the phase transition itself takes place in such a system is of fundamental interest, surprisingly little experimental studies have addressed this topic. On the theoretical side, much more work has been done. Some of the results however are still inconsistent and no complete description covering all aspects has emerged. In the following we will give a brief summary of the recent theoretical and experimental work related to the subject.

4.2.1 The theory of condensate formation

The process of Bose-Einstein condensation can be divided into different stages. In a first kinetic stage with no condensate yet present, collisions between the atoms lead to a restructuring of the distribution function and the occupation numbers of the low-energetic states grow. It is governed by elastic collisions and the characteristic time scale is set by the collision time $\tau_{\text{col}} = (n\sigma v_T)^{-1}$ with n being the peak density of the gas, σ the elastic collision cross section, and v_T the average thermal velocity. The second stage is also called coherent stage and only plays a significant role in the regime of very large density or scattering length. This is when the initiation of the condensate and the actual phase transition characterized by the formation of long-range order take place. The coherent stage describes the existence and subsequent merging of quasicondensates, patched regions of locally constant phase, into a full Bose-Einstein condensate. The growth of the condensate, associated with the decay of vortices and phase fluctuations constitutes the final stage of condensate formation [7].

Several authors studied the kinetic stage by numerically solving the quantum Boltz-

mann equation [9, 10, 11, 12]. The growth of the condensate is described by

$$n_0(t) = n_0(\infty) \left(1 - e^{-t/\tau_0}\right) \quad (4.1)$$

in [207] and [12]. However, due to computational complexity the simulations included only a small number of atoms. This model does not reproduced a delay until atoms start to macroscopically occupy the ground state, however, such a delay is surely to be expected. In a full dynamical treatment Bijlsma *et al.* [208] find the same functional behavior but with an onset time t_{onset} already predicted by their theory, so that in eqn. (4.1) t has to be replaced by $t - t_{\text{onset}}$. Kagan *et al.* give the inverse of the collision rate c_R , which is the mean collision rate $\tau_{\text{col}} = c_R^{-1}$ for each thermal atom, as the order of magnitude for the duration of the kinetic stage.

During the coherent stage, the kinetic energy of the atoms is smaller than their average potential energy. Here, the kinetic equation is not valid anymore. The coherent stage is characterized by an instability mechanism that favors the macroscopic population of the lowest energy state [209]. Due to critical fluctuations, the ground state acquires an energy less than the instantaneous chemical potential. This leads to a coherent transfer of population from the low-lying excited states to the ground state. Stoof [209] states a timescale of order

$$\left(\frac{\lambda_{\text{dB}}(T = T_c)}{a}\right)^2 \frac{\hbar}{k_B T_c} \quad (4.2)$$

for this process, which is a few hundred ms.

The existence of quasicondensates during the coherent stage is predicted by Kagan *et al.* . They show suppressed density fluctuations and particles occupying a small range of low-lying excited states with energies $\epsilon < n_0 U_0$ [204]. Large phase fluctuations are still present though, and therefore there is no off-diagonal long-range order. The correlation time $\tau_c = \hbar/(n_0 U_0)$ is found to be the time scale for evolution on the length scale of the correlation length $r_c = \hbar/\sqrt{2mn_0 U_0}$ for this stage, so that the coherence grows approximately at the speed of sound

$$v_s = \sqrt{\frac{nU_0}{m}} \sim \frac{r_c}{\tau_c}. \quad (4.3)$$

Therefore the coherent stage (and the time for formation of a quasicondensate) is much faster than the kinetic stage, with the latter hence setting the time scale for the whole process. The formation of off-diagonal long-range order is determined by the relaxation of very long sound waves [7, 210]. Whether quasicondensates are an intermediate stage of the condensation process depends on the speed of the formation of off-diagonal long-range order compared to that of topological long-range order. The first is related to the relaxation of nonequilibrium phase fluctuations, while the latter is determined by the time needed for the annihilation of vortices. This happens during the last stage of the condensation process.

A quantum theory for the nucleation of a BEC, describing the kinetic and coherent stage in a unified way, was developed by Stoof [211]. He claims that the existence of quasicondensates is not compatible with the results of that microscopic calculation [209].

It is important to stress that the above results have been obtained for homogeneous systems. Svistunov [205] considers the case of a weakly interacting trapped Bose gas. He states that in the hydrodynamic (“*anti*-Knudsen”) regime, where the formation of quasicondensates takes place, the external potential becomes irrelevant. The hydrodynamic regime is characterized by $\tau_{\text{col}}\omega \ll 1$, with ω being the trapping frequency. This is equivalent to demanding that the mean free path of the atoms is small compared to the size of the cloud. However, typical BEC experiments and also the one presented here are not in the hydrodynamic regime. Svistunov finds that in the Knudsen regime, the behavior of the trapped system is qualitatively similar to an isotropic homogeneous one, apart from the difference in the density of states. Once the coherent regime is reached, the discreteness of the trap levels becomes important, which leads to a slowing down of the evolution towards lower energies, followed by a fast equilibration on a time scale determined by the collision time τ_{col} . In the hydrodynamic regime, a quasihomogeneous picture of evolution is found. However, one interesting difference compared to the truly homogeneous case exists: The process of quasicondensation starts at the center of the trap and from thereon grows outwards. Also the excitation of breathing modes of the quasicondensate are to be expected.

Khlebnikov [212] finds that in the coherent stage of BEC formation the correlation length ξ should grow linearly in time at a speed on the order of the speed of sound. For the relaxation time t_r , which is the duration of the kinetic stage, he gives a rough estimate of

$$t_r \sim \frac{\hbar k_B T}{U_0^2 n^2}. \quad (4.4)$$

Opposed to the prediction of a linear growth of the coherence length ξ by Khlebnikov, Lacaze *et al.* [213] expect a growth of $\xi(t) \sim \sqrt{\hbar t/m} = 27 \mu\text{m s}^{-1/2} \times \sqrt{t}$.

Quantum kinetic theory

In a series of papers, Gardiner *et al.* have developed a substantial description of the kinetics of Bose-Einstein condensation in a trap. While they treat a spatially homogeneous, weakly condensed system in [214, 207], in [8, 215], a strongly condensed, trapped gas was considered. In the following, we want to briefly describe the latter theory and results.

A Bose gas trapped in an isotropic harmonic oscillator potential is described by a field in second quantization. The field is divided into a so called condensate band, which hosts

all atoms with energies below a certain threshold value E_R , and the noncondensate band occupied by all atoms with energies above E_R . The noncondensate band is modeled as a fully thermalized heat bath containing most of the atoms, even after condensation. Its dynamics in interaction with the condensate band is described by a master equation. The condensate band consists of the trap energy levels modified by the presence of the condensate, i.e. by its mean field. These energy levels are described by a Bogoliubov spectrum. The state of the condensate band can—at any time—be completely described by the number N of atoms in the band and the set of occupation numbers of all its energy levels $\{n_m\}$, where $m = 0$ is the condensate and all other m denote the quasiparticle levels. While the total number of particles is conserved, quasiparticles corresponding to excitations are not. Phononlike quasiparticles are neglected, because the lower of these represent spatial oscillations of the condensate. Even though this can experimentally be observed, it should only have a small influence on the growth process. Growth processes describe collisions that change N . These are mainly collisions between two atoms from the noncondensate band with one of them ending up in the condensate band. Scattering processes do not change N and are predominantly given by collisions between one atom from the condensate and one from the noncondensate band.

Initially there is no condensate present, and, due to preceding cooling, the chemical potential μ in the noncondensate band has become nonnegative, ultimately driving the condensation process. In the simplest approximation, the condensate band only consists of one level and all fluctuations are neglected. In this case a differential equation for the growth of the condensate is found

$$\dot{n}_0 = 2W^+(n_0)\left[\left(1 - e^{\frac{\mu_c(n_0) - \mu}{k_B T}}\right)n_0 + 1\right]. \quad (4.5)$$

μ and $\mu_c(n_0)$ are the chemical potential of the bath and the condensate, respectively. Note that the bath is assumed to have constant chemical potential μ and temperature T and not to be depleted by the condensation process. Equation (4.5) depicts some important aspects of the condensation process: The spontaneous emission term given by the $+1$ in the squared brackets starts the condensate formation. Once there is some population in the lowest level, the gain term, and therefore the difference in the chemical potentials between condensate and bath, dominates the process. A steep rise in the condensate number is followed by a slow approach towards the final condensate number because the chemical potential of the condensate $\mu_c(n_0)$ approaches the chemical potential of the bath μ .

Assuming a Maxwell-Boltzmann distribution for the Wigner function of the noncondensed atoms, the prefactor in (4.5) is given by

$$W^+(n_0) = \frac{4m(ak_B T)^2}{\pi \hbar^3} e^{2\mu/(k_B T)} \left[\frac{\mu_c(n_0)}{k_B T} K_1 \left(\frac{\mu_c(n_0)}{k_B T} \right) \right] \approx \frac{4m(ak_B T)^2}{\pi \hbar^3} e^{2\mu/(k_B T)}, \quad (4.6)$$

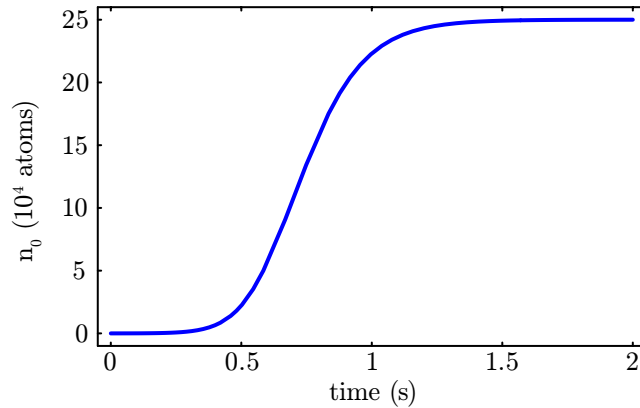


Figure 4.1: Growth of the condensate occupation n_0 according to the simple growth model [eqn. (4.5)]. $W^+(n_0)$ has been calculated using the parameters typical for the apparatus used in this thesis with a final condensate number of 2.5×10^5 atoms and is a factor of 3 larger than given by eqn. (4.6) to resemble the result of a more realistic model (see text).

where $K_1(z)$ is a modified Bessel function and the approximation on the right hand side is well fulfilled for realistic parameters. While the exponential in eqn. (4.6) is close to one for our parameters, the other factor is approximately equal to the elastic collision rate

$$c_R = \frac{1}{\tau_{\text{col}}} = \sqrt{2}\bar{n}\sigma_{th}\bar{v} = \frac{4a^2mN\omega_x\omega_y\omega_z}{\pi k_B T}. \quad (4.7)$$

Here $\bar{n} = N\omega_x\omega_y\omega_z (m/(4\pi k_B T))^{3/2}$ is the mean density for a harmonically trapped gas in equilibrium, $\sigma_{th} = 8\pi a^2$ is the scattering cross section between thermal atoms and $\bar{v} = \sqrt{8k_B T}/(\pi m)$ the mean velocity of thermal atoms at temperature T [216]. The equality between $\frac{4m(ak_B T)^2}{\pi\hbar^3}$ and c_R is easily seen when evaluating the first expression at the transition temperature given by eqn. (2.4) and setting $\zeta(3) \approx 1$. For our parameters with a final condensate size of 2.5×10^5 atoms, the collision rate is $c_R \approx 33 \text{ s}^{-1}$.

A more accurate extension of the theory [217, 215] takes more energy levels of the condensate band into account. Furthermore, the full Bose-Einstein distribution is used to give a more realistic Wigner function. Equation (4.5) stays valid, but $W^+(n_0)$ is about a factor of three larger. This results in a speedup in all stages of the condensation process by this factor. A growth curve as described by this theory is plotted in Fig. 4.1. The S shape of the curve is characteristic for a growth process. The first stage is very slow, since spontaneous transitions to the lowest level are the only mechanism by which the condensate can grow. Once there is a substantial population of condensate atoms, there is a stage of fast growth due to stimulated transitions. Subsequently, as the chemical potential of the condensate approaches the chemical potential of the bath, n_0

slowly approaches its equilibrium value.

Neglecting fluctuations and quasiparticle effects is not a good approximation during the initial stage of the condensation process—the “nucleation” of a very small condensate consisting of a few atoms. Without scattering processes the only way for population of the condensate level is directly from the noncondensate band. However, during the thermalization process, excess population in the other levels of the condensate band develops. By including scattering effects atoms from these higher condensate levels can now directly be transferred into the condensate. This significantly speeds up the first stage of the growth process until a very small condensate has formed. The rest of the process however is basically unaltered [218].

Also the full quantum dynamics of the system have been solved numerically, i.e. the bath of the noncondensate band has been replaced by the discrete energy levels of the system [219]. Good agreement with the model described here was found for final condensate fractions of up to 10 %, and only for larger final condensate fractions the depletion of the thermal cloud had a significant influence on the growth process. Because the final condensate fractions in the experiments to be presented here are only of the order of 3 %, the above description is sufficient.

4.2.2 Earlier experimental work

Most previous experimental work has either concentrated on the growth of density and condensate fraction or on the coherence properties of a BEC in thermal equilibrium. In contrast, we here report on the time-resolved observation of the coherence properties of an atom cloud crossing the phase transition to BEC. We nevertheless want to give a short overview of the main previous work and results.

Growth of the condensate fraction

Two experiments on the dynamics of the growth of the number of condensate atoms have been performed. The earlier one studied the growth following a sudden remove of atoms during a shock cooling stage of 10 ms duration [13]. The number of condensate atoms was inferred from phase-contrast images of the trapped cloud by fitting the density distributions with a bimodal function. Condensates smaller than 10^5 atoms could not be detected with this method. A typical S shape curve similar to the solution of eqn. (4.5) was found to fit the growth of the number of condensate atoms well for those experimental runs where no condensate existed immediately after the shock cooling stage. The final condensate fraction was between 5 % and 20 %, depending on the precise conditions chosen. However, the speed of the condensate formation was found to be 3 to 15 times slower than predicted in [8]. A more detailed analysis of the theory

and the same experimental data [217, 218] gives better agreement between theory and experiment, but some discrepancy still remains.

The growth of the condensate size in a situation of continuous cooling of the atom cloud was studied by Köhl *et al.* [14]. After preparing the sample closely above T_c , they abruptly lowered the radio frequency used for evaporative cooling to a value limiting the trap depth to $\epsilon_{\text{cut}} = \eta k_B T_i$. Here, T_i is the temperature of the thermal cloud before the jump and the evaporation parameter η was varied to study different situations. For a period of 6 s the radio-frequency field was held constant and the growth of the number of condensed atoms was observed by fitting the density distribution of the atoms after 17 ms time-of-flight. When limiting the trap depth to very low values corresponding to final condensate fraction exceeding 30 %, a fit of eqn. (4.1) showed good agreement with the theory [12, 208, 217, 177]. In the case of slow cooling with $\eta \sim 4.6$ however, a largely increased initiation time and a two-stage growth process were observed. During a first stage, the condensate number grows approximately linearly. It then proceeds with an eight times larger rate and can be described by eqn. (4.1). The transition between the first and the second stage is always observed at condensate fractions in the range between 1.5 % and 3.5 %. The authors give two possible reasons for the discrepancy between theory and experiment for slow cooling. On the theoretical side, assumptions like the ergodicity of the system and other approximations might fail in accurately describing the complex physics of the system. Secondly, the formation of quasicondensates in the early stage of the condensation process might lead to a significant reduction in the growth rate compared to the quantum kinetic calculation.

Experiments on coherence properties of condensates

A landmark experiment was the first observation of interference between two initially separated Bose-Einstein condensates [17]. They were released from separate traps and overlapped during the subsequent ballistic expansion. A high-contrast interference pattern was observed as a consequence of the coherence of the condensates.

Using Bragg spectroscopy, the momentum distribution of an atom cloud can be measured. The minimum momentum spread is given by the coherence length of the sample, provided that the contribution of other effects like the mean-field energy of the sample are small. The presence of phase fluctuations leads to a broadening of the momentum distribution, because the velocity field of a Bose-Einstein condensate is proportional to the gradient of its phase. In practice, the inhomogeneous density distribution leads to an inhomogeneous mean-field shift of the Bragg resonance and therewith to a broadening of the momentum distribution. Depending on the precise properties of the investigated system, it can be the largest contribution to the momentum width and therefore render an accurate measurement impossible. In [220], Bragg spectroscopy was applied to a

BEC and a momentum spread dominated by the radial size of the condensate was measured. This confirmed a coherence length equal to the size of the sample and therewith the long-range order of the condensate. A complementary measurement using Bragg scattering in the time domain was also demonstrated [221]. A 1D optical lattice was used to diffract a part of the condensate. The fraction of diffracted atoms as a function of the delay between two such Bragg pulses showed an oscillatory behavior. The slow decay of the fringe amplitude with increasing temporal separation between the two pulses was found to be consistent with a uniform global phase of the trapped BEC.

Bragg spectroscopy in the frequency domain was also used to study the coherence properties of an elongated condensate in equilibrium [222]. For an extremely elongated BEC, a Lorentzian shape of the resonance was found. This is to be expected for a quasicondensate with its momentum distribution dominated by phase fluctuations. At the same time, density fluctuations were found to be suppressed, supporting the existence of quasicondensates in the investigated system.

A very successful method to study the coherence properties of a thermal gas or a BEC is the atomic analog to Young's double slit experiment. Two atomic beams are output coupled from slit-like regions of an atom cloud and the interference between the two beams falling under the influence of gravity can be observed [104]. The distance between the two slits can be varied and therefore the first-order coherence of the atom cloud can be probed as a function of distance. This method was presented in detail in Sec. 2.2.3 of this thesis. It was introduced in [104] and used to measure the spatial correlation function of a trapped Bose gas above and below the phase transition. They found a Gaussian decay of the correlation function for a purely thermal sample and a decay to a constant value given by the condensate fraction below T_c . The contrast of the interference pattern was determined by absorption imaging. A significant extension of the method is achieved by replacing the destructive imaging technique. Utilizing a cavity based single atom detector, the coherence of the atom cloud can be probed continuously with negligible back-action on the investigated sample.

The method of condensate focussing was introduced in [15]. By a shock cooling procedure, clouds with a small condensate fraction were produced, showing large, strongly damped shape oscillations. By switching off the trapping potential during an inward phase of such an oscillation, the axial size of the condensate reached a focus after a specific time of ballistic expansion, when the compression was balanced by the increasing mean-field due to the growing chemical potential. Much larger foci than theoretically expected for a true BEC were found and attributed to local variations in the expansion velocity due to the presence of phase fluctuations, indicating local thermalization and the existence of quasicondensates.

Investigations of local second- [223] and third-order [224] correlations in Bose-Einstein

condensates found evidence for the theoretically expected reduced correlations compared to thermal ensembles. In the study of the second-order correlations, the dependence of the interaction energy on the probability for two atoms to be close together was exploited by analyzing time-of-flight measurements. A corresponding relation between measured three body recombination rates and $g^{(3)}(\Delta r = 0)$ was used in the second experiment.

Dynamical studies of phase coherence

Hugbart *et al.* have studied the growth process of a BEC in a largely anisotropic trap ($\omega_z/\omega_\perp \approx 100$) [16]. By shock cooling, they have produced an over-saturated thermal cloud. They then measured the temporal evolution of the number of condensed atoms in absorption imaging and the momentum width of the sample using Bragg spectroscopy. Apart from an initial delay, the growth of the number of condensed atoms could quite nicely be explained by a theoretical model based on [225]. The momentum width was compared to the expected equilibrium value and a decaying excess momentum width could be observed and explained by the excitation of a quadrupole mode. Measurements during the first 100 ms after the end of the shock cooling process were impossible, and therefore the existence of quasicondensates in an early stage of BEC formation could not be observed. For times larger than 100 ms after the onset of condensation they were not present in the data. This is in qualitative agreement with the theoretical predictions by Kagan *et al.* [204, 7, 226]. The method of Bragg spectroscopy used requires condensate fractions in excess of 5 % to work. Therefore the very interesting initial stage of the condensate formation could not be investigated. In order to acquire data for later stages of the condensation process, a final equilibrium state with a larger condensate fraction needed to be achieved. This requires the extraction of a larger fraction of atoms during shock cooling and also a sample prepared closer to T_c before shock cooling. This might imply that condensate nucleation has already taken place before the end of the shock cooling stage.

4.3 Methods

Here we present an experimental study of the evolution of off-diagonal long-range order during the formation of a Bose-Einstein condensate out of a nonequilibrium situation. We start from a Bose gas above the phase transition temperature and suddenly quench the gas into a strongly nonequilibrium state [13, 14, 15, 16]. Subsequently, the gas can be regarded as a closed system which evolves into a Bose-Einstein condensed phase. The off-diagonal long-range order is measured by studying the interference pattern of atomic matter waves originating from two different locations in the atom trap [104].

The visibility of this interference pattern measures the phase coherence between the two regions and its temporal evolution uncovers the formation of long-range order. We continuously monitor the visibility of the interference pattern and the time-dependent atom flux during the formation using a single atom counter with high temporal resolution [101]. Varying the vertical distance Δz between the two locations allows us to experimentally map out the evolution of the phase coherence and density in the trapped Bose gas.

With this method, the coherence of the trapped sample is probed *in situ* and the growth can be monitored real time. Because of the high detection efficiency, the disturbance of the atom cloud and the condensation process is kept at a minimum and is orders of magnitude smaller than in the case of absorption imaging [104].

4.3.1 Setup

We start by preparing a thermal cloud of atoms in the $|F = 1, m_F = -1\rangle$ hyperfine ground state of ^{87}Rb in the harmonic trapping potential of the magnetic QUIC trap. The trapping frequencies are $(\omega_x, \omega_y, \omega_z) = 2\pi \times (39, 7, 29)$ Hz, where z denotes the vertical axis. The temperature of the atom cloud $T = 240$ nK is slightly above the transition temperature $T_c = 215$ nK for Bose-Einstein condensation for the given number of atoms $N = 1.3 \times 10^7$. This results in a collision time of $\tau_{\text{col}} \approx 30$ ms. Temperature and atom number are measured by absorption imaging. The atom cloud is then brought into a strong nonequilibrium situation by rapidly lowering the trap depth to 620 nK and removing the high-energy tail of the Maxwell-Boltzmann distribution. This “shock cooling” experimentally reproduces the theoretical situation of a thermal bath and a condensate band. The usual way of producing a condensate by slow adiabatic cooling is not suitable to observe the intrinsic dynamics of condensate formation, because the evaporation is done so slowly that the vapor stays close to thermodynamic equilibrium. To study the fundamental processes underlying the condensate formation, a freely evolving system is preferable. Many authors show that the shock cooling will first lead to a thermalization of the high-energy atoms from the noncondensate band with the lower levels following later [207, 226, 12]. Within the 100 ms of shock cooling we remove 30% of the atoms. Subsequently, the cloud relaxes from its highly nonequilibrium state and within a few hundred milliseconds 3% of the atoms form a Bose-Einstein condensate. During the relaxation process particle number and total energy are conserved with minimal disturbance due to the detection process. Moreover, we take great care to not excite oscillations of the condensate as a consequence of the shock cooling.

We detect the evolution of both the density and the long-range order of the cloud simultaneously and in real time using radio frequency output coupling (Sec. 2.2.2 and [79]) and single atom counting (Sec. 3.5 and [101, 187]). For output coupling we ap-

ply a weak monochromatic microwave frequency field which spin-flips atoms from the magnetically trapped state into the untrapped state $|F = 2, m_F = 0\rangle$. The untrapped atoms form a downwards propagating atomic beam. The output coupling region is defined by a surface of constant magnetic field and can be approximated by a horizontal plane within the atom cloud (Sec. 2.2.2 and [79]). Applying two microwave fields with different frequencies realizes output coupling from two vertically separated surfaces of constant magnetic field (Sec. 2.2.3 and [104]) which are chosen symmetric about the center of the cloud. The two overlapping atomic beams interfere with each other. The mean flux reflects the local density of atoms at the position of output coupling within the transverse momentum interval measured by our detector. The visibility of the interference pattern reflects the phase coherence. The interference pattern is detected in time with single atom resolution using the ultrahigh finesse optical cavity. Our system permits a precise measurement of the time-dependent atom flux.

4.3.2 Filtering of atoms by the detector

The cavity detector is a filter for the atoms output coupled from the magnetic trap. The probability for an atom to reach the detector depends on its position and momentum at the time of output coupling. Since those atoms that enter the detector are a subset of the complete thermal ensemble, their velocity distribution is markedly different. In the following, the two are compared, which gives important insight into the properties of our single atom detector.

We consider an ideal gas trapped in a three-dimensional harmonic oscillator potential $V(\vec{r}) = \frac{1}{2}m(\omega_x^2 x^2 + \omega_y^2 y^2 + \omega_z^2 z^2)$. In the local density approximation¹, the Wigner function² of the system is given by [56]

$$\mathcal{W}(\mathbf{r}, \mathbf{p}) = \frac{1}{(2\pi\hbar)^3} \frac{1}{\exp[(\mathbf{p}^2/2m + V(\mathbf{r}) - \mu)/k_B T] - 1}. \quad (4.8)$$

Free parameters are the temperature T and the chemical potential μ . The chemical potential μ determines how far the system is above the condensation temperature T_c via

$$\left(\frac{T}{T_c}\right)^3 = \frac{g_3(1)}{g_3(\mathfrak{z})}, \quad (4.9)$$

¹The local density approximation here assumes that the momentum dependence in the Wigner function is that of a spatially homogeneous system with the potential energy equal to the local value. It is valid as long as the de Broglie wavelength is small compared to the variations in the confining potential.

²The Wigner function is the quantum mechanical analogue of the phase space probability distribution. Due to the uncertainty principle in quantum mechanics only a phase space *quasi*-probability distribution exists—the Wigner function. For a given state it can be calculated from its density matrix.

with the fugacity $\mathfrak{z} = e^{\mu/(k_B T)}$. The analytical density distributions for thermal atoms are

$$n_T(\mathbf{r}) = \frac{1}{\lambda_{\text{dB}}^3} g_{3/2} \left(e^{[\mu - V(\mathbf{r})]/k_B T} \right) \quad (4.10)$$

in position space after integration in momentum space and

$$n_T(\mathbf{p}) = \frac{1}{\omega_x \omega_y \omega_z (\lambda_{\text{dB}} m)^3} g_{3/2} \left(e^{[\mu - \mathbf{p}^2/(2m)]/k_B T} \right) \quad (4.11)$$

in momentum space after integration in position space. For the thermal component at or below T_c one has to set $\mu = 0$. The Bose or polylogarithm function $g_p(z)$ is given by

$$g_p(z) = \frac{1}{\Gamma(p)} \int_0^\infty \frac{x^{p-1}}{z^{-1}e^x - 1} dx = \sum_{l=1}^\infty \frac{z^l}{l^p}, \quad (4.12)$$

where $\Gamma(p)$ is the Euler gamma function.

Only atoms with a certain combination of position and momentum at the moment of output coupling will finally fall into the cavity. To get results incorporating these velocity filtering properties of our geometry as well as the coupling between position and momentum, a Monte-Carlo simulation was performed. While z denotes the vertical axis, x and y are along and perpendicular to the long axis of the cavity, respectively. The cavity is modeled to have a horizontal, square shaped sensitive area of $(150 \times 35) \mu\text{m}^2$ (see Sec. 3.6). We simulate a thermal gas at 200 nK, 0.2 % above the critical temperature ($\mu/(k_B T) = -0.005$).

We output couple atoms from a nearly planar, horizontal surface perpendicular to gravity close to the center of the magnetic trap ($z \approx 0$). In the following we will therefore only consider atoms with $z = 0$.

Figure 4.2 shows the distribution of positions and velocities at the moment of output coupling. The red squares show the distributions of the complete trapped atom cloud. Only 0.97 % of all atoms will finally traverse the sensitive area of the cavity. Their distributions in the magnetic trap are shown as blue histograms. Note that all distributions have been normalized to their peak values to make their shapes comparable. The most striking difference between the two ensembles is the strongly reduced velocity spread for the atoms that will traverse the cavity, which is a consequence of the small size of the cavity compared to its distance from the magnetic trap.

To calculate the momentum distribution $n_{z=0}(\mathbf{p})$ of all output coupled atoms, the Wigner function [eqn. (4.17)] is evaluated at $z = 0$ and integrated over the two remaining spatial coordinates. This gives

$$n_{z=0}(\mathbf{p}) \propto g_1(e^{[\mu - \mathbf{p}^2/(2m)]/k_B T}). \quad (4.13)$$

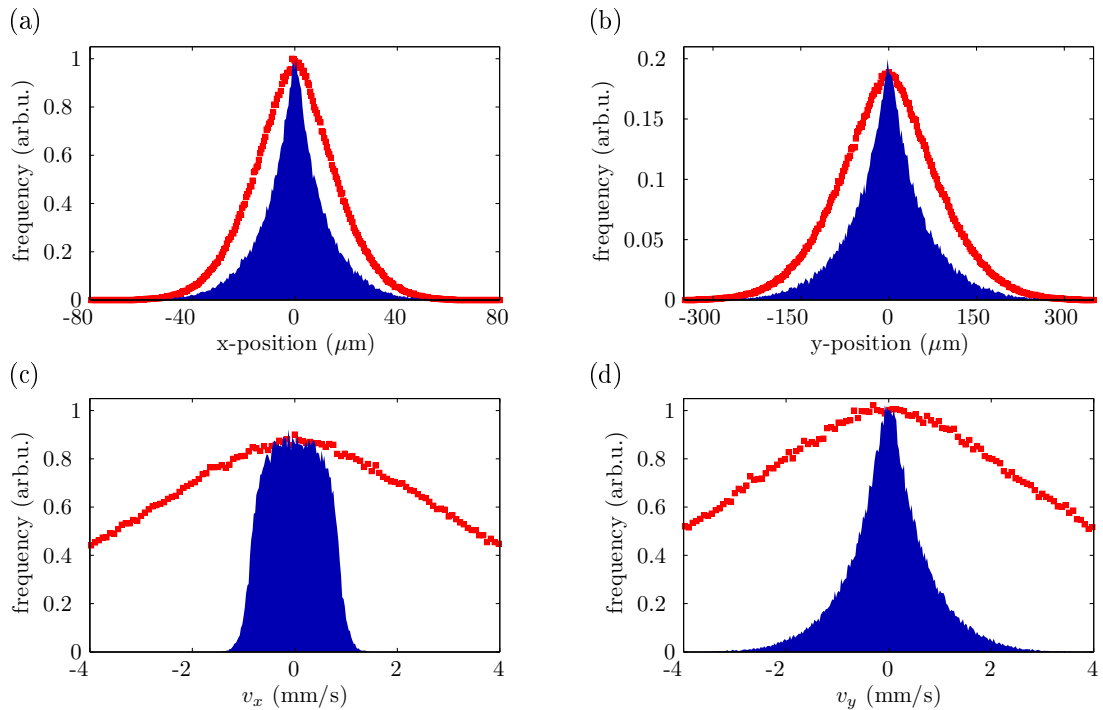


Figure 4.2: Comparison of position [(a) and (b)] and velocity [(c) and (d)] distribution in the magnetic trap of all atoms versus those detected by the cavity. The red squares show the distribution of all atoms, whereas the blue histogram includes only the subclass of those atoms that will later hit the cavity. The curves have been normalized to their respective peak values to make the shapes of the distribution comparable. The total number of atoms in the subclass (blue data) is only about 1% of the complete ensemble of all trapped atoms (red data).

Integration over p_x and p_y yields the velocity distribution along gravity of all atoms output coupled at $z = 0$

$$v_z(z = 0) \propto g_2(e^{-(\frac{1}{2}mv^2 - \mu)/k_B T}). \quad (4.14)$$

In Fig. 4.3, only atoms from a horizontal plane with $z = 0$ in the cavity are considered. This closely matches the situation of atoms output coupled from the center of the trapped cloud. The distribution of the vertical velocity v_z of these atoms is plotted as black squares and a red line in Fig. 4.3(a). While the black squares are the result of a Monte-Carlo simulation, the red line is a fit of eqn. (4.14). The good agreement between the two confirms the accuracy of the simulation. This distribution of all output coupled atoms can now be compared to v_z for those atoms from the beam that will traverse the cavity. While the change of the velocity in z-direction is much less pronounced than in the two horizontal directions, it is nevertheless found to be significantly altered by the filtering process.

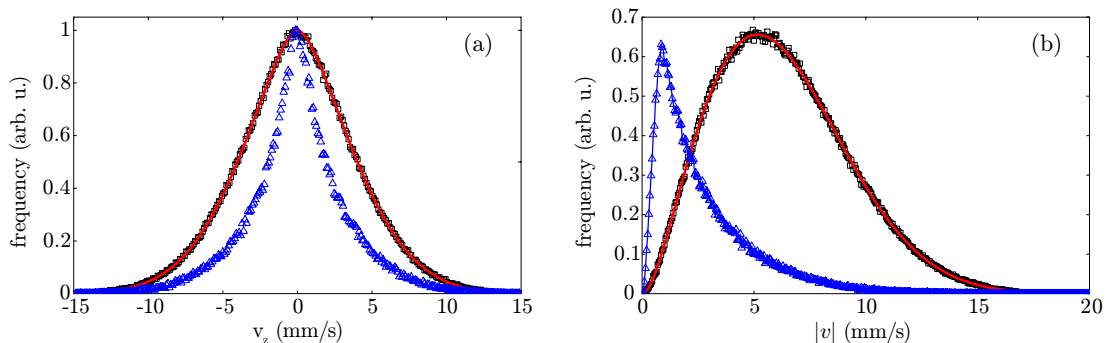


Figure 4.3: Velocity distributions of atoms in the magnetic trap. In contrast to Fig. 4.2, only atoms with $z = 0$ are considered. These are the atoms addressed by output coupling. While in (a) only the z -component is plotted, graph (b) shows the magnitude of the total velocity. The black squares are the results of a Monte-Carlo simulation while the red line is an analytical fit. The blue triangles are the velocities in the trap of that subclass of atoms which will fall into the cavity.

In Fig. 4.3(b), the absolute value $|\mathbf{v}| = \sqrt{v_x^2 + v_y^2 + v_z^2}$ of the velocity is compared for all output coupled atoms (black data) to those filtered by the cavity (blue data). Transforming eqn. (4.13) into spherical coordinates yields

$$|\mathbf{v}| \propto v^2 g_1(e^{-(\frac{1}{2}mv^2 - \mu)/k_B T}). \quad (4.15)$$

and has been fitted as a red line to the black data in Fig. 4.3(b). The filtering process strongly changes the distribution and especially reduces the mean energy of the filtered ensemble (blue triangles) compared to the primal entity.

In the derivation of the first-order correlation function from the Wigner function (see Sec. 4.3.3), we assume to only detect atoms with $p_x = p_y = z = 0$, independent of their initial radial position. Both assumptions are not completely fulfilled. Neither do we only collect atoms with zero horizontal momentum [see Fig. 4.2(c) and (d)] nor is the detection probability independent of the horizontal position of the atoms at the time of output coupling. To ensure that it still is a very good approximation, we compare in Fig. 4.4 the distribution of v_z for atoms that will hit the detector (blue circles) to an ensemble with arbitrary x and y and $p_x = p_y = 0$ (red squares). Both curves have been normalized to the same number of atoms. The agreement is very good, apart from the approximated curve being slightly more peaked, resulting in a slightly larger fraction of atoms around $v_z = 0$.

4.3.3 Interference and first-order correlation function

The visibility of the interference pattern of two overlapping atomic beams along their propagation axis is approximately given by the normalized first-order correlation func-

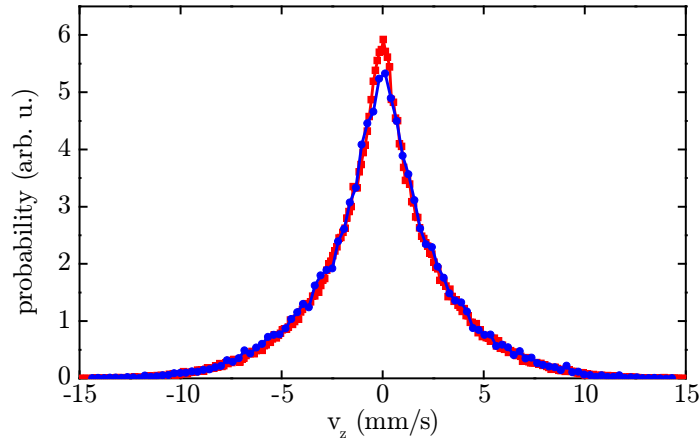


Figure 4.4: Probability distribution for the vertical velocity v_z of atoms output coupled from $z = 0$. Atoms that reach the cavity detector (blue circles) are compared to those with $p_x = p_y = 0$ (red squares). All data are the result of a Monte-Carlo simulation (see text).

tion $g^{(1)}(z, z')$ along the same axis [104]. The (non-normalized) first-order correlation function $G^{(1)}$ of a partly condensed gas is given by [56]

$$G^{(1)}(\mathbf{r}, \mathbf{r}') = \psi^*(\mathbf{r})\psi(\mathbf{r}') + \int d\mathbf{p} e^{-i\mathbf{p}\cdot(\mathbf{r}-\mathbf{r}')/\hbar} \mathcal{W}\left(\mathbf{p}, \frac{\mathbf{r} + \mathbf{r}'}{2}\right). \quad (4.16)$$

$\psi^*(\mathbf{r})\psi(\mathbf{r}')$ is basically the condensate density [6], and the second term is the Fourier transform of the Wigner function of the uncondensed part. The Wigner function of an ideal, thermal gas in a three-dimensional harmonic trapping potential in the local density approximation is given by

$$\mathcal{W}(\mathbf{p}, \mathbf{r}) = \frac{1}{(2\pi\hbar)^3} \frac{1}{\exp[(\mathbf{p}^2/2m + V(\mathbf{r}) - \mu)/k_B T] - 1}, \quad (4.17)$$

with $\mathbf{p} = (p_x, p_y, p_z)$ and $\mathbf{r} = (x, y, z)$.

Our measuring method has got some specifics that require a closer analysis to understand the connection between the measured visibility and the correlations in the atom cloud. Atoms are output coupled from two nearly planar, horizontal planes symmetric about the center of the trapped cloud along the z -axis defined by gravity. With the origin at the center of the cloud, this implies $z + z' = 0$. The distance between two output coupling planes is $\Delta z = z - z' = 2z$. In principle atoms from everywhere in the trapped cloud can contribute to the signal of detected atoms. It can be modeled by integrating over the whole space along x and y . This is an approximation because the detection probability of atom is not independent from its position at output coupling [see Fig. 4.2(a) and (b)]. Atoms with arbitrary momentum along the z -axis are detected,

whereas the velocity filtering properties of our detector geometry are such that we can approximate it to only detect atoms with $p_x = p_y = 0$ [see Fig. 4.2(c) and (d)].

The phase of an atom or a matter wave only depends on its vertical position, because only along this z -axis a potential gradient exists and therefore a phase shift can only be acquired along this axis. Consequently, the frequency of an interference pattern between two matter waves only depends on the vertical separation of their regions of origin and not on their absolute spacing.

We will first consider the thermal component only, which is described by the second term in eqn. (4.16). Under the approximations given above, we measure

$$\int_{-\infty}^{\infty} dp_z \int_{-\infty}^{\infty} dx \int_{-\infty}^{\infty} dy e^{-ip_z \cdot \Delta z / \hbar} \mathcal{W}(p_x = 0, p_y = 0, p_z; x, y, z = 0). \quad (4.18)$$

This can be shown to be equivalent to

$$G_T^{(1)}(z, z') = \int_{-\infty}^{\infty} d^3 \mathbf{p} e^{-ip_z \cdot \Delta z / \hbar} \mathcal{W}(\mathbf{p}; x = 0, y = 0, \frac{z + z'}{2}), \quad (4.19)$$

which in turn is equal to the second term in eqn. (4.16) for $x = y = 0$. The important result is, that for an ideal, thermal gas the visibility we measure with the cavity detector is equivalent to the first-order correlation function

$$g_T^{(1)}(\mathbf{r} = [0, 0, z], \mathbf{r}' = [0, 0, z']) , \quad (4.20)$$

which is the correlation function along the vertical axis, radially in the center of the cloud. The same basic argument is valid for a strongly interacting gas.

Concerning the condensed part, which is described by the first term in eqn. (4.16), again interference will only occur along the gravitational axis. Perpendicular to it the atoms will not acquire a phase shift because there is no potential gradient and therefore no interference pattern will occur. For the condensate part we measure

$$G_C^{(1)}(z, z') = \int_{-\infty}^{\infty} dx \int_{-\infty}^{\infty} dy \psi^*(x, y, \frac{-\Delta z}{2}) \psi(x, y, \frac{\Delta z}{2}). \quad (4.21)$$

The visibility of a pure BEC is 100 % (see Sec. 4.3.6) assuming perfect mode overlap of the two atom laser beams and for not too large Δz (see Sec. 4.3.6). The first-order correlation function of a partly condensed system is the sum of equations (4.19) and (4.20) with their corresponding scaling factors (see Sec. 4.3.5). In equilibrium, it will show a constant offset due to the condensed part and proportional but not equal (see Sec. 4.3.5) to the condensate fraction.

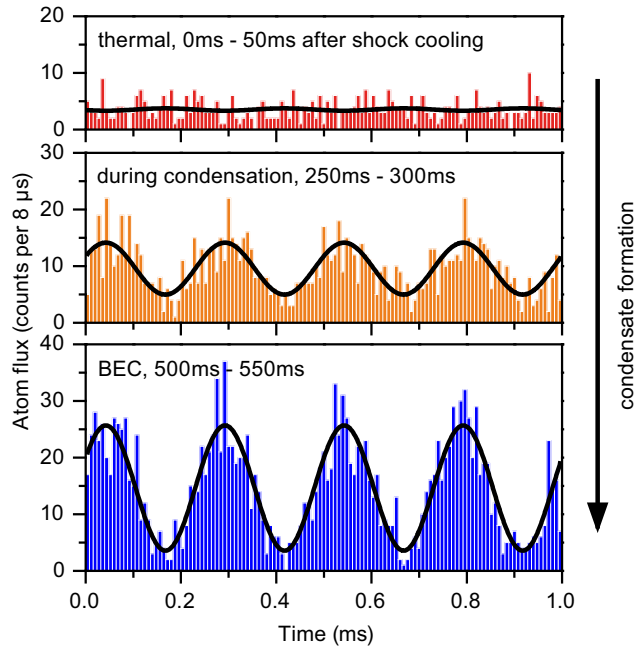


Figure 4.5: Buildup of density and off-diagonal long-range order during condensate formation. We plot the histogram of the atom arrival times modulo 1 ms for $\nu = 4$ kHz. The data are summed over 18 repetitions of the experiment. The black lines are fits to the data with a fixed phase to extract the mean atom flux A and the visibility V of the interference pattern (see text).

4.3.4 Data analysis

The mean atom flux and the visibility of the atomic interference pattern are determined in time bins of 50 ms length. In Fig. 4.5 three different situations of the condensate formation are shown. For the cloud immediately after shock cooling [Fig. 4.5(a)], the visibility is zero and the mean atom flux is low. As the condensation process develops [Fig. 4.5(b)], the atom flux increases and interference arises. Both continue to grow up to a final value [Fig. 4.5(c)] determined by the condensate fraction and detector function. The black lines are a fit of

$$f(t) = A [1 + V \sin(2\pi\nu t + \phi)] \quad (4.22)$$

to the data. The frequency ν is the difference of the two microwave frequencies used for output coupling. The phase ϕ is determined by the relative phase of the two microwave fields which is locked to the experimental cycle. It is determined once for our setup and therefore only A and V are free parameters in the fit. The output coupling of atoms with a rate $\approx 5 \times 10^4$ atoms per second is essentially not perturbing the density dynamics of the condensate formation. In particular, it has no detectable influence on

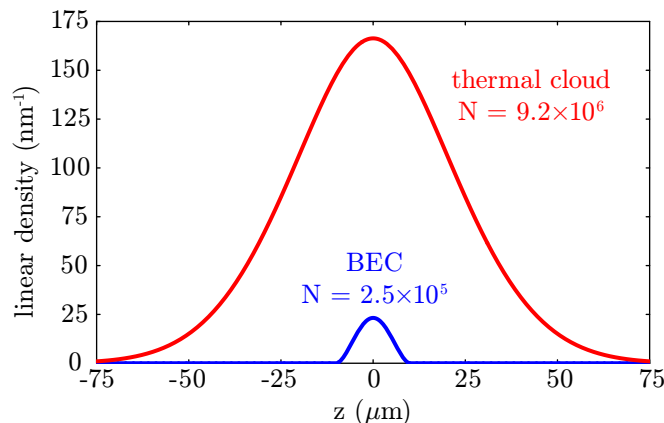


Figure 4.6: Linear density distribution of a thermal cloud and a BEC of the given number of atoms in our magnetic trap. The linear density is obtained by integrating the three-dimensional density over both horizontal coordinates.

the final condensate fraction.

4.3.5 Detector characteristics

The observation of long-range order even at a very small condensate fraction poses a severe technical challenge. Our detection scheme has specific properties which render the present measurement possible.

Even in equilibrium after shock cooling the condensate fraction is only 2.7%. The peak density of a BEC of 2.5×10^5 atoms in the Thomas-Fermi approximation is $48 \mu\text{m}^{-3}$ while that of a thermal cloud of 9.2×10^6 atoms is $22 \mu\text{m}^{-3}$. It can be shown that when output coupling with a certain frequency, the atom flux is proportional to the integrated density in a horizontal slice through the cloud of trapped atoms [86, 87]. The above statement is valid under the reflection approximation, which is analogous to the local density approximation and neglects the kinetic energy of the output coupled atoms unlike their energy in the gravitational potential. The probabilities to be output coupled are equal for a condensed and a thermal atom that both fulfill the resonance condition. Therefore the number of output coupled atoms is proportional to the number of atoms in resonance with the microwave or radio frequency. The ratio between output coupled thermal and condensed atoms will therefore be given by the ratio of their radially integrated density distributions. Changes to the density distribution of one component induced by the presence of the other component are neglected. As a result, the radially integrated, linear density of the BEC and the thermal cloud are plotted as a function of the vertical position z in Fig. 4.6. Two features are important. First, the linear density of the BEC even at its maximum is about 7 times smaller than that

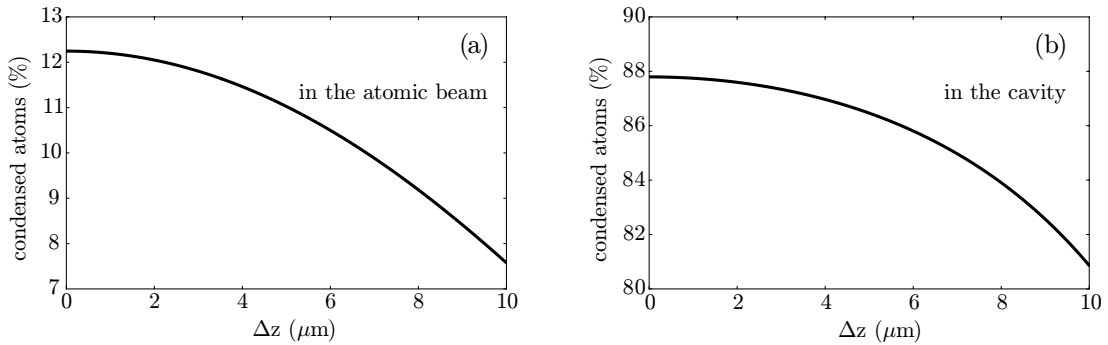


Figure 4.7: We examine a system with 9.2×10^6 thermal and 2.5×10^5 (2.7%) condensed atoms in our magnetic trap. Atoms are output coupled from two horizontal slices separated by Δz symmetrically around the center of the trap. (a) The fraction of condensed atoms in the atomic beam as a function of Δz . (b) Taking only those atoms from the atomic beam that fall into the cavity detector, the percentage of atoms from the condensate is shown as a function of Δz . It is drastically increased as opposed to the fraction in the beam, because of the much lower probability for a thermal atom to traverse the cavity mode volume.

of the thermal cloud. Secondly, due to the much smaller size of the condensate, the ratio of condensed to thermal atoms within one horizontal slice through the condensate drops to zero when the distance of the slice from the center of the cloud equals the Thomas-Fermi radius $R_z = 10 \mu\text{m}$.

The fraction of condensed atoms from the total number of output coupled atoms is plotted in Fig. 4.7(a) as a function of the separation Δz of the two horizontal planes symmetric with respect to the center of the trap. Therefore each plane has a distance of $\Delta z/2$ from the center. It is instructive to relate the condensate fractions in the beam and in the trapped cloud. One finds that the total fraction of condensed atoms is a factor of four larger in the beam than in the trapped cloud. In other words, the output coupling probability for a condensed atom is a factor of four larger than for a thermal atom. The reason is the higher local density of the BEC in the center of the trap.

Moreover, we observe unequal detection efficiencies for condensed and noncondensed atoms. For thermal atoms the transverse velocity spread is larger which reduces the probability for an atom to be detected in the cavity. The detection efficiency for condensed atoms is about 25%. Taking into account the standing wave structure of the cavity mode and the threshold on coupling used in single atom detection, we find a probability of 50% for an atom traversing the rectangular “active area” of the cavity (see Sec. 3.6) to be detected. Therefore the probability to hit the cavity mode is about 50% for a condensed atom, whereas for a thermal atom it is only about 1% (see Sec. 4.3.2). For this reason the fraction of condensed atoms hitting the cavity detector, as plotted in Fig. 4.7(b), differs dramatically from the same quantity in the atomic beam [see

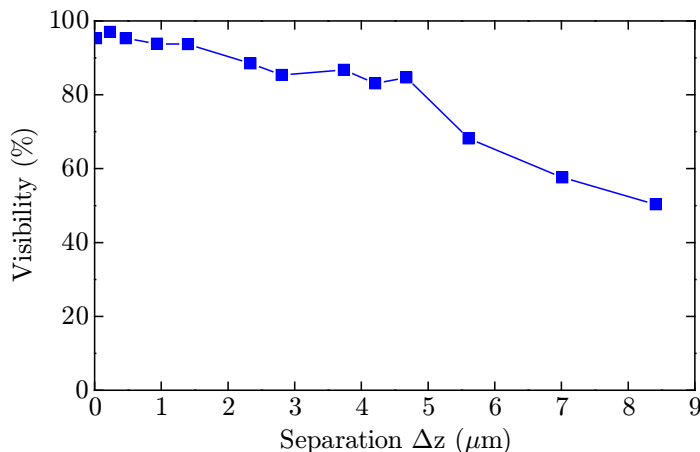


Figure 4.8: Visibility of a matter wave interference pattern. Two overlapping atom lasers are output coupled from two regions separated by Δz in a cloud of 2.4×10^6 atoms with a condensate fraction of 75 %. The visibility declines with increasing Δz to about 50 % for the largest separation measured.

Fig. 4.7(a)]. Because of these effects the visibility of the interference pattern greatly exceeds the condensate fraction and reaches a maximum of 70 % for $\Delta z > \lambda_{\text{dB}}$.

4.3.6 Detection uniformity

To understand the specifics of our measuring method, it is instructive to study the visibility of an interference pattern from a quantum degenerate ensemble in thermal equilibrium. Unfortunately, no data for a pure condensate are available. The largest condensate fraction for which we measured the dependence of the visibility on the separation of the two output coupling regions is 75 %. The data is shown for a cloud of 2.4×10^6 atoms in Fig. 4.8. Two important observations can be made. First, the observed visibility greatly exceeds the condensate fraction, which has been explained in Sec. 4.3.5. Second, the visibility declines with increasing Δz , which is not obviously explained by the properties of our setup discussed so far. In the following, we will discuss several effects that all contribute to this decay and estimate their magnitude. In an independent measurement we have confirmed that with a pure condensate and for $\Delta z < 3 \mu\text{m}$ perfect visibility (100 % within the measurement accuracy of a few percent) can be observed.

In the following, we will discuss and quantify some of the effects that lead to a decay of the visibility with increasing Δz . All numbers refer to the parameters specific for the measurement presented here, i.e. 9.4×10^6 atoms and a condensate fraction of 2.7 %.

Small condensate size

From Fig. 4.7(b) it can be seen that the fraction of detected condensed atoms reduces with increasing separation Δz , because the condensate is much smaller, both in particle number and in size, than the thermal cloud (see Sec. 4.3.5). In a simple model, one can treat the thermal and condensate fraction separately. While atoms from the condensate are assumed to show perfect interference, the thermal component is assumed to show no interference for separations Δz much larger than the de Broglie wavelength. Then the decrease in the fraction of atoms from the condensate will lead to a decrease in the visibility for increasing Δz . It amounts to about 5% for the largest $\Delta z = 8.4 \mu\text{m}$ measured in the experiment.

Time resolution of the detector

We have discussed the temporal accuracy of the cavity detector in section 3.5.6. The shot noise on the detection light leads to an uncertainty in the determination of the atom arrival times with a mean of $1.9 \mu\text{s}$ for a recording time of 0.5 s and $2.6 \mu\text{s}$ for 2 s, respectively. This limits the achievable contrast as a function of slit separation as shown in Fig. 3.21(c). For 18 kHz one finds a reduction of 5%.

The cavity detector might be slightly tilted from the horizontal. Atoms entering the detector on the higher side would be detected earlier than those entering on the lower side. This effectively leads to an additional uncertainty in arrival time determination, which for a moderate tilt of 0.5° is already of the same size as the jitter due to shot noise.

Residual oscillations of the trapped atoms

During initial experiments, large oscillations in the atom flux detected by the cavity were observed. Dipole oscillations perpendicular to the cavity axis were observed as large peaks in the Fourier transform of the atom flux at the lowest trapping frequency $\omega_y/(2\pi)$ and its second and third harmonic. Oscillations in this direction are expected to have relatively large amplitude due to the low confinement. In addition, the cavity detector has a size of only $35 \mu\text{m}$ in this direction and therefore spatial oscillations of the beam lead to large changes in the atom flux. By starting the shock cooling stage of constant duration at the right time of the experimental cycle, we find that we can suppress the oscillations so that no detectable periodic change in atom flux remains. Starting the shock cooling process $\tau = 2\pi/\omega_y$ later was found to bring back the oscillations at maximum amplitude.

We attribute the origin of these oscillations to changes in the trapping potential in-

duced by the strong microwave frequency used for shock cooling [227]. This is supported by several observations. First, there are no oscillations present before shock cooling. Second, oscillations induced by the condensation process would be random, which contradicts with the observation that they are stoppable with a single choice of the shock cooling timing. Third, they are stoppable without changing the duration of the shock cooling stage just by changing its temporal position in the experimental cycle.

For the shock cooling experiments presented here, the effect of vertical oscillations could be eliminated. In the horizontal direction however, the temporal behavior of the atom flux is extremely sensitive to oscillations of even smallest amplitudes due to phase modulation of the beam (see section 3.8). This phase modulation leads to a theoretical upper limit for the contrast, since power from the carrier frequency is shifted into the sidebands. We find that for the largest measured slit separations of 18 kHz, residual oscillations lead to a reduction in visibility of 5%. This corresponds to an amplitude of 0.03 μm . The theoretical limit for the visibility due to this effect is a function of the frequency difference and given by the zero order Bessel function $J_0(\beta)$, with β given by equation (3.19).

Vibrations of the detector

A change in the distance between the magnetically trapped atoms and the detector would influence the detected signal. The reason for such a change can either be due to variations in the position of the magnetic trap or due to vibrations of the cavity. The first would cause center-of-mass oscillations of the trapped atoms, which we can detect with very high sensitivity as explained in the last section. Since we only observe oscillations of extremely small amplitude, we do not expect this to be a significant contribution. The cavity rests on a vibration isolation stack which effectively damps vibrations above 200 Hz (see chapter 3). In principle, one expects a time dependent Doppler shift in the detected frequency of the interference pattern. This would decrease the visibility of the interference pattern, however we observe full contrast for frequencies of a few kHz. Also no broadening of the Fourier peaks at the difference frequency can be observed. Therefore we conclude that this effect has no relevant influence on the measurement.

Atom laser mode overlap

The mode overlap of the two atom laser beams produced by the two output coupling frequencies is not perfect. We have taken care to equalize the power of the two microwave frequencies and therefore the flux in both beams. However, several effects reduce the mode overlap as the difference between the two frequencies increases.

First, the trapped cloud acts as a diverging lens for an atom laser beam, leading to a strong influence of its mode profile on the position of output coupling [90, 97, 99, 98]. While the beam originating from the lower part of the condensate stays well collimated, the upper one is spread by the mean field potential of the trapped atoms. From numerical simulations we find this to reduce the overlap by 10 % for a frequency separation of 18 kHz.

A second contribution is due to the geometry of our trapping potential resulting in a tilt of the long axis of the condensate by 3.2° with respect to the horizontal (see Sec.2.2.2 and Fig.2.4). We estimate this to lead to an additional decrease in mode overlap by 4 %. Additional effects include the finite size of the output coupling regions and the residual curvature of the surfaces of constant magnetic field.

4.4 Results

The evolution of phase coherence in the trapped Bose gas as a function of separation Δz of the two output coupling regions is shown in Fig.4.9. Neglecting the specific properties of our detection setup, the plot shows the temporal evolution of the first-order correlation function for a Bose gas crossing the phase transition to a BEC. As described in Sec.4.3.6, the main influence of our detector is an underestimation of the coherence at large Δz , which however does not affect the temporal behavior.

In the initial nonequilibrium state just after the quench we observe purely thermal-like short-range correlations which decay on a characteristic length scale given by the thermal de Broglie wavelength $\lambda_{\text{dB}} \approx 0.4 \mu\text{m}$. After the first 200 ms during which little changes are detected, the length scale over which phase correlations exist expands rapidly and the long-range order of a Bose-Einstein condensate is established after a further 100 ms. Subsequently, a stage of gradual condensate growth towards equilibrium is observed.

The evolution of the flux of atoms through the cavity is plotted in Fig.4.10. It is proportional to the density of atoms in the region of output coupling (see Sec.2.2.2). Note that output coupling is performed symmetrically with respect to the center of the atom cloud. Therefore the flux at small Δz reflects the density in the center of the trap, whereas larger separations probe the density further out. Directly after the end of the shock cooling stage, the flux is independent of the separation Δz . This reflects the homogeneous density distribution in the probed center of the thermal cloud. With a size of about $9 \mu\text{m}$ it is much smaller than the spatial extent of the whole thermal cloud. The situation is markedly different in the equilibrium situation at times later than 500 ms. A small condensate has formed in the center of the trap. The density distribution shows a higher value in the center of the trap which decreases significantly

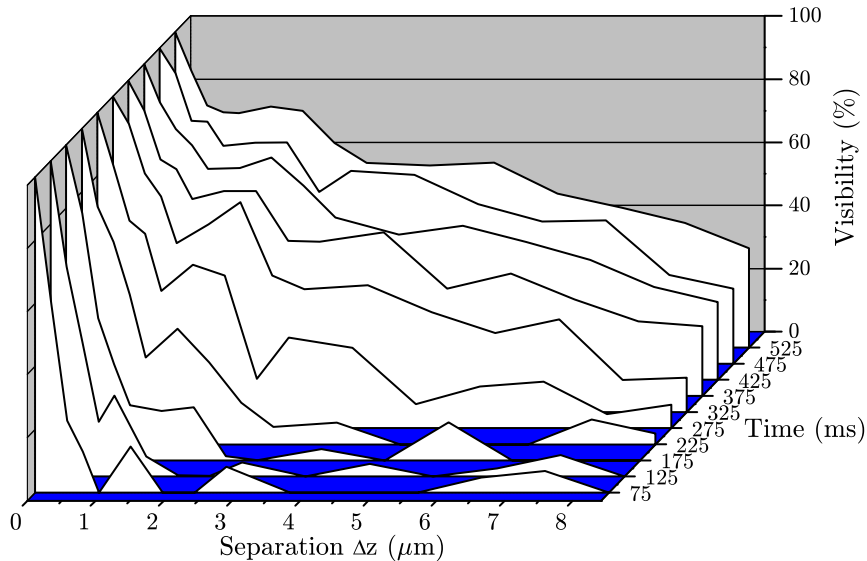


Figure 4.9: Formation of long-range order. Shown is the visibility of a matter wave interference pattern originating from two regions separated by Δz inside a trapped cloud. This is a measure of the first-order spatial correlation function of the atom cloud. By shock cooling the gas is prepared in a highly nonequilibrium state at time $t = 0$ and then relaxes towards thermal equilibrium. Initially ($t = 75$ ms) the correlations are short ranged and thermal-like. The onset of Bose-Einstein condensation is marked by the appearance of long-range order extending over all measured distances ($t = 275$ ms). The largest measured distance corresponds to half of the Thomas-Fermi diameter of the final condensate. The data are taken for constant separations versus time. The substructure of the curves reflects the scatter of the initial conditions for each separation. The resulting variance in the onset of condensation is about 30 ms.

on a length scale given by the Thomas-Fermi radius, which is about the size of the probed region of $\Delta z = 9 \mu\text{m}$. This effect is reduced but not negated by the fact that the density of the BEC alone is still smaller than the central density of the thermal component (compare Fig. 4.6). In addition, the probability for an output coupled atom to be detected increases with decreasing temperature from about 1% for atoms about 10% above T_c to 25% for atoms from the condensate. This effect contributes to the decrease of the atom flux with increasing Δz . In between the two limiting situations of a thermal gas and the partly condensed system in equilibrium, a continuous growth of the density on all lengths scales is observed.

In Fig. 4.11 we show the growth of the density reflected in the mean atom flux and

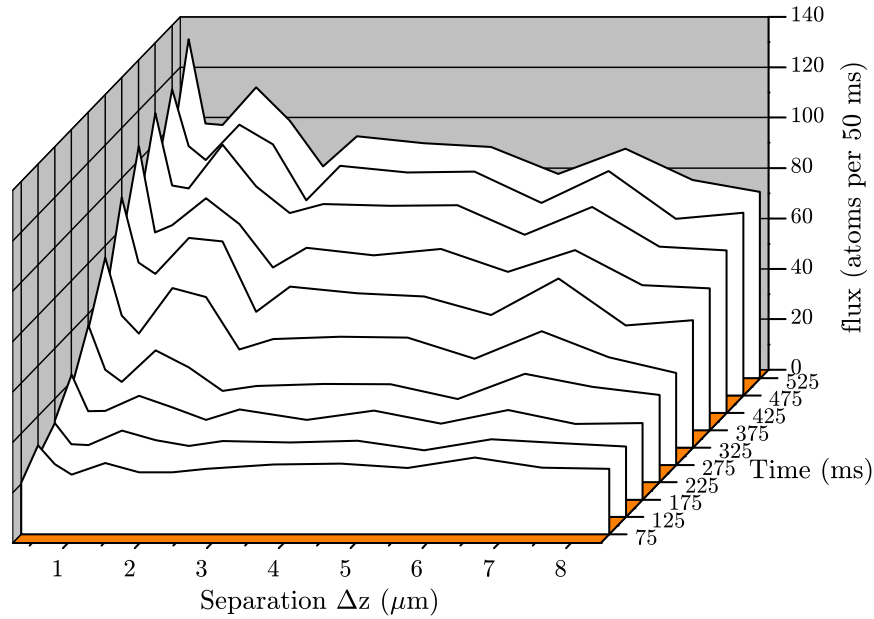


Figure 4.10: Evolution of the atom flux after shock cooling. This plot is analogous to Fig. 4.9 but shows the atom flux instead of the visibility. The flux and therewith the atom density grows rather uniformly. Starting from a nearly homogeneous situation immediately after the end of the shock cooling stage ($t = 0$) the flux grows by about a factor of 5 until thermal equilibrium is reached ($t > 500$ ms). The flux in equilibrium reflects the significantly altered density distribution due to the presence of a small condensate.

of the visibility for a given separation of the output coupling regions. This corresponds to a section of constant $\Delta z = 1.9 \mu\text{m}$ in Fig. 4.9. We have analyzed both the delay of the formation with respect to the shock cooling stage and the speed of the formation for density and off-diagonal long-range order. We fit a function

$$g(t) = A_2 + (A_1 - A_2) / [1 + (t/\tau)^p] \quad (4.23)$$

to the data to quantify the growth, where τ denotes the time after which 50% of the increase in flux or visibility are reached.

The time after which 10%, 50%, and 90% of the total increase of the atom flux (a) and visibility (b) are reached for different separations Δz is plotted in Fig. 4.12. As can be seen already from Fig. 4.10, the atom flux is only very weakly dependent on the slit separation Δz . From a linear fit, one finds a slope of $(3 \pm 1, 11 \pm 2, 22 \pm 6)$ ms/ μm for the 10%, 50% and 90% curves respectively. This in turn means that the atom density grows approximately simultaneously across the investigated inner region of the trapped cloud. For the visibility, the times after which a certain percentage of the growth has

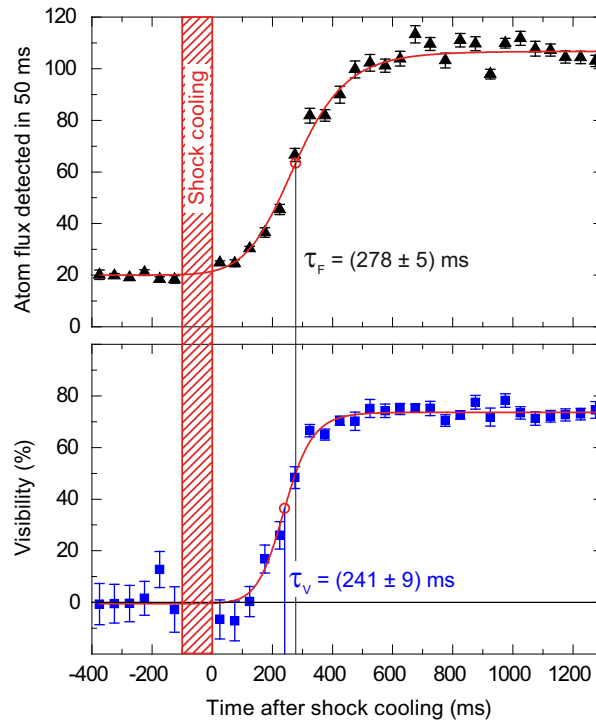


Figure 4.11: Growth curves for atom flux and visibility of the interference pattern during the formation of a Bose-Einstein condensate. The separation Δz between the two output coupling regions is $1.9 \mu\text{m}$. Before the shock cooling stage there is a low flux of thermal atoms and no interference. The growth in atom flux is significantly slower than the growth of the interference pattern. The data are averaged over 20 repetitions and the error bars indicate the statistical error of these measurements which are within a factor of 2 of the theoretical shot-noise limit.

been reached, increases with larger slit separation by $(19 \pm 4, 23 \pm 4, 23 \pm 6)$ ms/ μm for the three percentages. It is therefore approximately constant during the whole formation process. The much larger offset between the three curves in Fig. 4.12(a) in comparison to Fig. 4.12(b) reflects the slower growth of the atom flux as compared to the growth of the visibility.

The duration of the condensate formation can be quantified by the time needed for an increase of both the flux and the visibility from 10% to 90% of the total increase. We find the duration to be approximately independent of the separation Δz of the two output coupling regions. For the flux this time is (421 ± 47) ms whereas the visibility of the interference pattern grows faster in a time of (267 ± 48) ms.

The growth of the visibility can be compared to the atom flux by looking at the time differences between the points in Fig. 4.12. This has the advantage that systematic

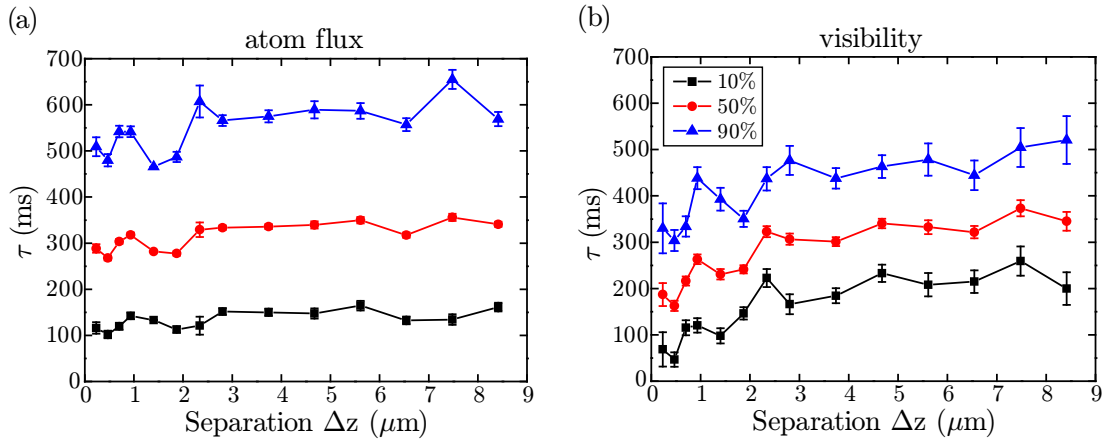


Figure 4.12: Temporal evolution of the atom flux (a) and visibility (b) during condensate formation. Plotted are the times after which 10 % (black squares), 50 % (red circles) and 90 % (blue triangles) of the total growth has been reached. For the flux, there is nearly no dependence of these times on the separation Δz of the probed regions. For the visibility however, a significantly increasing delay for larger separations can be observed.

errors which simultaneously affect flux and visibility, as for example nonconstant initial conditions, cancel. The corresponding graphs are shown in Fig. 4.13. Positive values of $\Delta\tau$ indicate that the atom flux establishes earlier than the visibility. This is the case for the onset of the growth (defined by the 10 % values, black squares) if one neglects small separations with $\Delta z < 1.5 \mu\text{m}$. For all other separations, the onset of the growth starts approximately 40 ms earlier for the density than for the coherence. In contrast, the visibility saturates (90 % values, blue triangles) about 120 ms earlier than the density. This applies for all separations Δz larger than the de Broglie wavelength λ_{dB} . Separations $\Delta r \leq \lambda_{\text{dB}}$ are special, because as expected they show a nonzero visibility even immediately after the shock cooling stage. In summary, we observe that a coherent region grows outwards and subsequently the density in this region increases towards the final condensate density. This supports the picture of a kinetic evolution of the cloud [205]. It is opposed to the picture of condensate formation via quasicondensates, where the growth of the density precedes the formation of long-range order [204, 7].

To learn about the spatial growth process, the dependence of $\Delta\tau$ on the separation Δz needs to be examined. From the data we find that the coherent region grows with a velocity of about 0.1 mm/s, which is approximately a factor of 5 slower than the speed of sound at the peak density of the thermal cloud. The speed of sound imposes a natural speed limit for the expansion of the coherent region.

Moreover we find that τ decreases with increasing size of the final condensate. This is

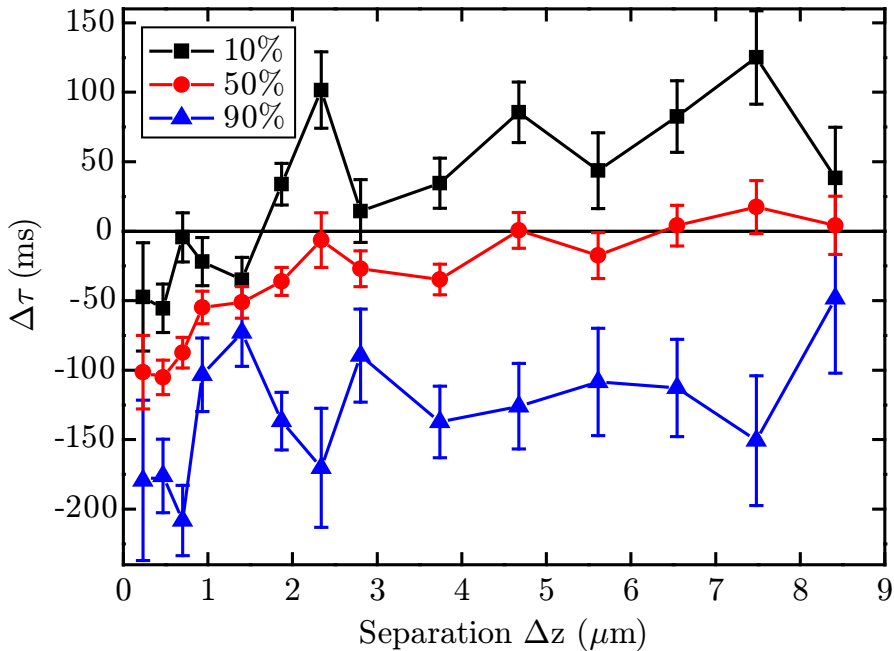


Figure 4.13: Delay of the visibility compared to the atom flux. The difference between each curve in Fig. 4.12(b) and the corresponding curve in Fig. 4.12(a) is plotted. Looking at the 50% points (red circles), the visibility precedes the density for small distances Δz , while for large Δz they are approximately concurrent. The large separation between the 10% and 90% curves is a consequence of the different durations of the growth processes (see text).

illustrated by the data in Fig. 4.14. To obtain a larger final condensate fraction, larger initial clouds or the removal of a larger fraction of the atoms in the shock cooling process are necessary. The first accelerates the process via an increased collision rate, and the latter results in a larger difference in the chemical potentials of thermal component and condensate. Both result in a faster equilibration process and therefore in a faster condensate growth. Starting with an initial temperature closer to T_c is a third option. Of course, all these changes have mutual interdependencies [219].

As the limiting cases we find for a final condensate number of 2.5×10^5 atoms $\tau = (282, 320)$ ms and for 8.9×10^5 atoms $\tau = (57, 114)$ ms, where the first number in the bracket refers to the visibility and the latter to the flux. The numbers are averaged over all slit separations. This decrease of the formation time for larger condensates is proportional to the increase of the elastic collision rate due to the higher final density.

It is instructive to study the evolution of the vertical momentum distribution $n(k)$ during the thermalization process. The average momentum distribution is given by the Fourier transform of the spatially integrated single particle correlation function

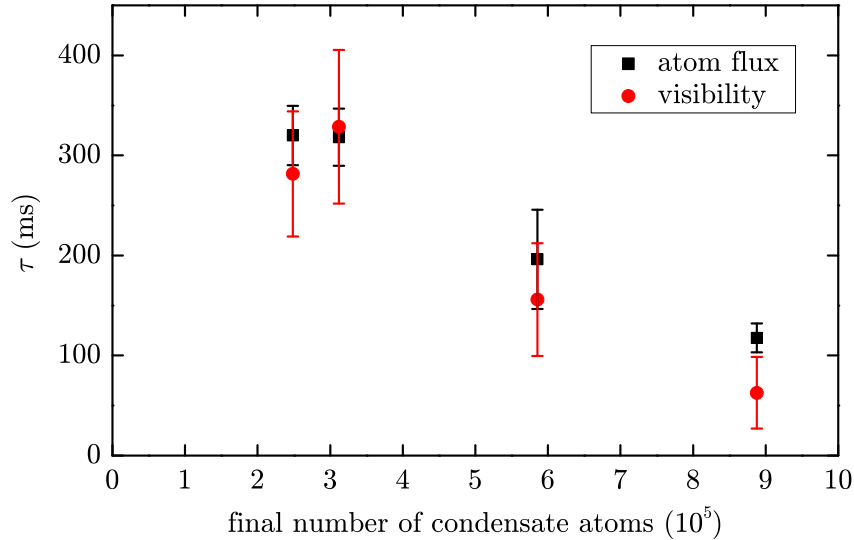


Figure 4.14: Dependence of the duration of condensate formation on its final size. Plotted are the times τ after which the atom flux (black squares) and the visibility (red circles) have grown by 50 % as a function of the final number of condensed atoms. The equilibration process towards larger condensates develops faster than that with a small final condensate number.

[62]. Therefore we can infer the distribution $n(k)$ of the detected atoms from the Fourier transform of the visibility data of Fig.4.9 multiplied by the average flux [228]. The result is shown in Fig.4.15. For the initial state directly after the quench, the momentum distribution is well approximated by a thermal distribution (dashed line). The thermalization process after the shock cooling leads to the formation and the growth of a low-momentum peak which in equilibrium corresponds to the condensate.

Using the theory presented in Sec.2.1.4 it can be calculated whether for our equilibrium parameters a true condensate or a quasicondensate with strong residual phase fluctuations is expected. The parameter δ_L^2 introduced in eqn.(2.24) represents the phase fluctuations on a length scale given by the size of the system [60]. For $\delta_L^2 \ll 1$ the fluctuations are small. Using $T \approx T_c$ and a condensate fraction of 3 % one finds $\delta_L^2 \approx 0.2$ for our equilibrium parameters. In equilibrium, we therefore expect a true condensate without strong residual phase fluctuation.

In Fig.4.15, we focus on the beginning of the condensate formation. After 225 ms of evolution, we observe a broader low-momentum peak (width in $k \sim 0.8 \mu\text{m}^{-1}$) than for the final distribution. In contrast to the previous results, this is what one expects to characterize a quasicondensate. Further measurements with higher resolution are

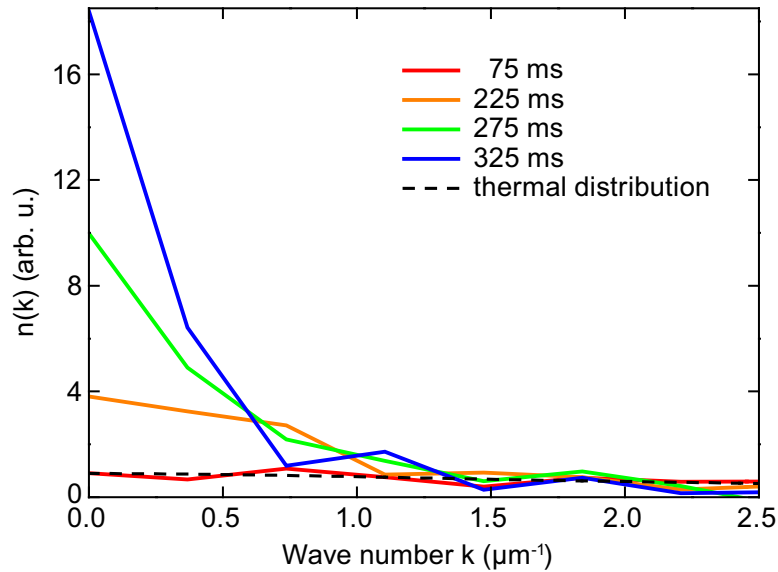


Figure 4.15: Temporal evolution of the momentum distribution of the detected atoms. The distribution is obtained by Fourier transformation of the visibility data. The thermal distribution is calculated for the parameters before shock cooling including a normalization factor.

required to consistently resolve the question of the existence of quasicondensates during the formation of a Bose-Einstein condensate. For evolution times of 325 ms and larger, the width of the low momentum peak is limited by our measurement resolution of $2\pi/(16\ \mu\text{m})$, which takes into account that the correlation function is symmetric with respect to $\Delta z = 0$.

4.5 Summary

Our experiments have shown that quantum gases give unique access to nonequilibrium phenomena. The technique of counting single atoms extracted from a Bose-Einstein condensate is minimally invasive and the time evolution of a quantum system can be followed over seconds. We have studied the fundamental question of phase ordering during the formation of a Bose-Einstein condensate. Our data are in agreement with the expectation that every atom undergoes several collisions before the ensemble has thermalized and long-range order has developed. We have obtained quantitative measurements which show that a coherent region grows outwards and subsequently the density in this region increases towards the final condensate density, supporting the picture of a kinetic evolution of the cloud [205]. The growth of the coherent region is found to be faster than the increase of the density. In addition, we presented the momentum

distribution of the atoms inferred from the visibility data. The emergence of a large peak at low momenta from the broad background of thermal atoms was observed.

5 Correlations and counting statistics of an atom laser

We demonstrate time-resolved counting of single atoms extracted from a weakly interacting Bose-Einstein condensate of ^{87}Rb atoms. The atoms are detected with a high-finesse optical cavity and single atom transits are identified. An atom laser beam is formed by continuously output coupling atoms from the Bose-Einstein condensate. We investigate the full counting statistics of this beam and measure its second-order correlation function $g^{(2)}(\tau)$ in a Hanbury Brown and Twiss type experiment. For the monoenergetic atom laser we observe a constant correlation function $g^{(2)}(\tau) = 1.00 \pm 0.01$ and an atom number distribution close to a Poissonian statistics. A pseudothermal atomic beam shows a bunching behavior and a Bose distributed counting statistics.

In addition, we determine the conditional and the unconditional detection probabilities for the atoms in the two beams and find good agreement with the theoretical predictions.

This chapter has been published at large in [101]: A. Öttl, S. Ritter, M. Köhl, and T. Esslinger. ‘Correlations and Counting Statistics of an Atom Laser’. *Physical Review Letters* **95**(9), 090404 (2005).

and [229]: M. Köhl, A. Öttl, S. Ritter, T. Donner, T. Bourdel, and T. Esslinger. ‘Time interval distributions of atoms in atomic beams’. *Applied Physics B* **86**, 391–393 (2007).

5.1 Introduction

Correlations between identical particles were first observed by Hanbury Brown and Twiss in light beams [20]. Their idea was that intensity fluctuations and the resulting correlations reveal information about the coherence and the quantum statistics of the probed system. This principle has found applications in many fields of physics [230] such as astronomy [231], high-energy physics [232], atomic physics [58] and condensed matter physics [233, 234]. In optics the reduced intensity fluctuations of a laser have been observed by Arecchi [235] only a few years after its invention, thereby disclosing the

extraordinary properties of this light source. The bunching of photons from a thermal source has been observed [236, 237] as well as antibunching of photons emitted by single atoms [238].

With the realization of Bose-Einstein condensation in dilute atomic gases a novel weakly interacting quantum system is available. The interpretation of a Bose-Einstein condensate representing a single, macroscopic wave function has been supported in numerous experiments highlighting its phase coherence [17, 220, 221, 104]. Correspondingly, atom lasers are atomic beams which are coherently extracted from Bose-Einstein condensates [75, 76, 77, 79]. Their first-order phase coherence has been observed both in space [17] and time [100]. However, only the second-order coherence reveals whether atom lasers exhibit a truly laser-like behavior. Thermal sources can be made to resemble a laser by filtering their output spatially and in frequency space. The result will be a highly collimated, bright and monochromatic beam, characteristic of a laser. However, the underlying statistics are not altered by the filtering. Therefore looking at the statistical properties of an atom laser beam “is how to tell [a] genuine [atom] laser . . . from a cheap imitation”—as put in a scintillatingly witty introduction to atom lasers by D. Kleppner[239]. In this respect there are no differences between optical and atom lasers. Here we present a measurement of the second-order correlation function $g^{(2)}(\tau)$ of an atom laser in a Hanbury Brown and Twiss type experiment.

The second-order correlation function $g^{(2)}(\tau)$ represents the conditional likelihood for detecting a particle a time τ later than a previously detected particle and quantifies second-order coherence [59, 240]. For a thermal source of bosons $g^{(2)}(\tau)$ equals 2 for $\tau = 0$ and decreases to 1 on the time scale of the correlation time which is given by its energy spread. For a coherent source $g^{(2)}(\tau) = 1$ holds for all times and therefore intensity fluctuations are reduced to the shot noise limit. Higher-order coherence in quantum degenerate samples was so far only studied in the spatial domain where atom-atom interactions reveal the short-distance correlations [224, 223]. Information on the second-order coherence was extracted from the release energy of condensates in time of flight measurements [223]. The different decay rates of BECs and thermal clouds due to three-body collisions were shown to be compatible with short-range third-order coherence of the BEC [224]. In an interferometric measurement $g^{(2)}(r)$ has been determined for elongated, phase-fluctuating condensates [64], and recently spatial correlation effects in expanding atom clouds were observed [241, 22, 23]. Moreover, atom-atom correlations have also been observed in the dissociation process of ultracold molecules [242].

We demonstrate detection of single atoms from a weakly interacting quantum gas by employing a high-finesse optical cavity [26, 123] (see Fig. 5.1). A different technique with the potential of single atom detection in quantum degenerate samples has been demonstrated with metastable Helium atoms [127]. Detecting the arrival times of all atoms at the cavity explicitly gives access to the full counting statistics that reveals the

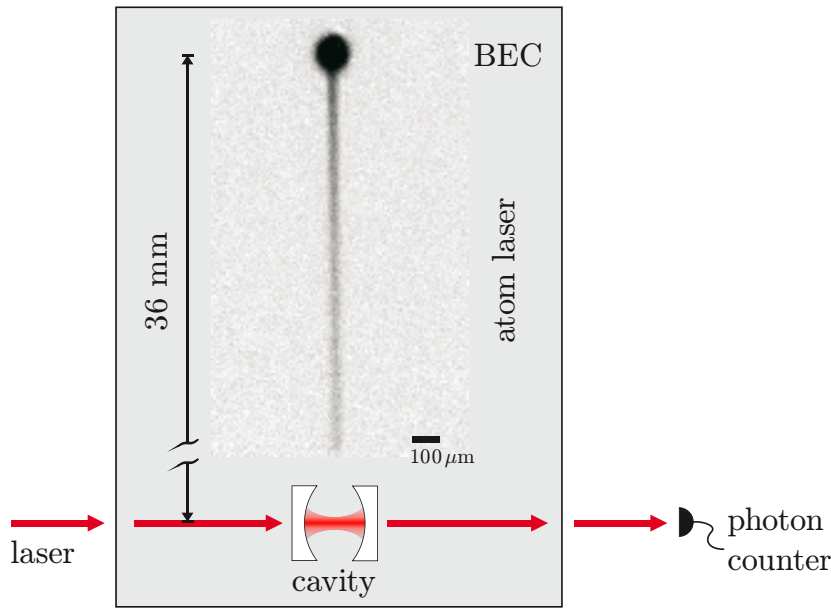


Figure 5.1: Schematic of the experimental setup. A weak continuous atom laser beam is released from a Bose-Einstein condensate. After dropping a distance of 36 mm the atoms enter a high-finesse optical cavity and single atoms in the beam are detected. For the actual measurement the atomic flux is reduced by a factor 10^4 as compared to the image.

atom number distribution function and its statistical moments [243, 244]. Determining the full counting statistics goes far beyond a measurement of the intensity correlation function only, because it represents the full statistical information about the quantum state. Despite recent progress, especially in mesoscopic electronic systems [245], the full counting statistics has not been measured for massive particles before. For neutral atoms this quantity is of special interest, since the strength of the interaction does not overwhelm the quantum statistics as it is often the case for electrons.

5.2 Methods

Our new experimental design combines the techniques for the production of atomic Bose-Einstein condensates with single atom detection by means of a high-finesse optical cavity. The apparatus consists of an ultrahigh vacuum (UHV) chamber which incorporates a separated enclosure with a higher background pressure. Here we collect 10^9 ^{87}Rb atoms in a vapor cell magneto-optical trap which is loaded from a pulsed dispenser source. After polarization gradient cooling and optical pumping into the $|F = 1, m_F = -1\rangle$ hyperfine ground state we magnetically transfer the atoms over a distance of 8 cm out

of the enclosure into a magnetic trap. All coils for the magnetic trapping fields are placed inside the UHV chamber and are cooled to below 0°C. In the magnetic trap we perform radio frequency induced evaporative cooling of the atomic cloud and obtain almost pure Bose-Einstein condensates with 1.5×10^6 atoms. After evaporation we relax the confinement of the atoms to the final trapping frequencies $\omega_x = 2\pi \times 38.6$ Hz, $\omega_y = 2\pi \times 7.2$ Hz and $\omega_z = 2\pi \times 29.1$ Hz, with the vertical z -axis defined by gravity.

For output coupling an atom laser beam we apply a weak, continuous microwave field to locally spin-flip atoms inside the Bose-Einstein condensate into the $|F = 2, m_F = 0\rangle$ state. These atoms do not experience the magnetic trapping potential but are released from the trap and form a well collimated beam which propagates downwards due to gravity [79]. The output coupling is performed near the center of the Bose condensate for a duration of 500 ms during which we extract on the order of 3×10^3 atoms. After dropping a distance of 36 mm the atoms enter the high finesse optical cavity (see Fig. 5.1). Fine tuning of the relative position between the atom laser beam and the cavity mode is obtained by tilting the vacuum chamber. We maintain a magnetic field along the trajectory of the atom laser, which at the position of the cavity is oriented vertically and has a strength of approximately 15 G.

The cavity consists of two identical mirrors separated by 176 μm . Their radius of curvature is 75 mm resulting in a Gaussian TEM₀₀ mode with a waist of $w_0 = 25$ μm . The coupling strength between a single Rb atom and the cavity field is $g_0 = 2\pi \times 10.6$ MHz on the $|F = 2\rangle \rightarrow |F' = 3\rangle$ transition of the D₂ line. The cavity has a finesse of 3×10^5 and the decay rate of the cavity field is $\kappa = 2\pi \times 1.3$ MHz. The spontaneous emission rate of the rubidium atom is $\Gamma = 2\pi \times 6$ MHz. Therefore we operate in the strong coupling regime of cavity QED. The cavity mirrors are mounted inside a piezo tube which enables precise mechanical control over the length of the resonator [123]. Four radial holes in the piezo element allow atoms to enter the cavity volume and also provide optical access perpendicular to the cavity axis. The cavity resides on top of a vibration isolation mount which ensures excellent passive stability. The cavity resonance frequency is stabilized by means of a far-detuned laser with a wavelength of 830 nm using a Pound-Drever-Hall locking scheme.

The cavity is probed by a weak, near resonant laser beam, whose transmission is monitored by a single photon counting module. We find a shot-noise-limited transmission of photons through the empty cavity. The presence of an atom inside the cavity results in a drop of the transmission (see Fig. 5.2). The stabilization light is blocked from the single photon counter by means of optical filters with an extinction of 120 dB. The probe laser and the cavity are red-detuned from the atomic $|F = 2\rangle \rightarrow |F' = 3\rangle$ transition by 40 MHz and 41 MHz, respectively. The polarization of the laser is aligned horizontally and the average intracavity photon number is 5. These settings are optimized to yield a maximum detection efficiency for the released atoms which is $(24 \pm 5)\%$. This number

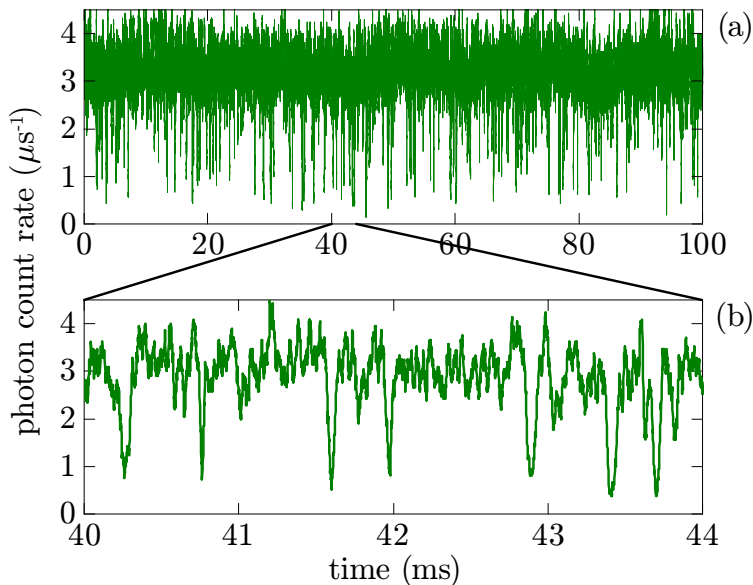


Figure 5.2: (a) Light transmission through the high-finesse optical cavity when an atom laser beam is traversing. (b) Details of the single atom transits. The photon count rate is averaged over $20\ \mu\text{s}$.

is primarily limited by the size of the atom laser beam which exceeds the cavity mode cross section. The atoms enter the cavity with a velocity of $84\ \text{cm/s}$ giving rise to an interaction time with the cavity mode of typically $45\ \mu\text{s}$, which determines the dead time of our detector. The dead time is short compared to the time scale of the correlations, which allows us to perform Hanbury Brown and Twiss type measurements with a single detector [246].

We record the cavity transmission for the period of the atom laser operation and average the photon counting data over $20\ \mu\text{s}$ (see Fig. 5.2). Using a peak detection routine we determine the arrival time of an atom in the cavity, requiring that the cavity transmission drops below its background value by at least four times the standard deviation of the photon shot noise. From the arrival times of all atoms we compute the second-order correlation function $g^{(2)}(\tau)$ by generating a histogram of all time differences within a single trace and normalizing it by the mean atomic flux. Due to the finite duration of the measurement T , the number of events with a time difference τ_i is reduced according to $1 - \tau_i/T$, which is taken into account by dividing the correlation function by this factor. This correction increases the total number of events in the histogram $\sum_{i=0}^{T/\Delta\tau} g^{(2)}(\tau_i)$ by a factor of 2. For N detected atoms the number of entries in the histogram is $N(N-1)/2$. Taking the influence of the aforementioned correction factor into account, normalization of the correlation function is achieved by dividing the histogram of M time bins by $N(N-1)/M$. This normalization to an average of 1 is

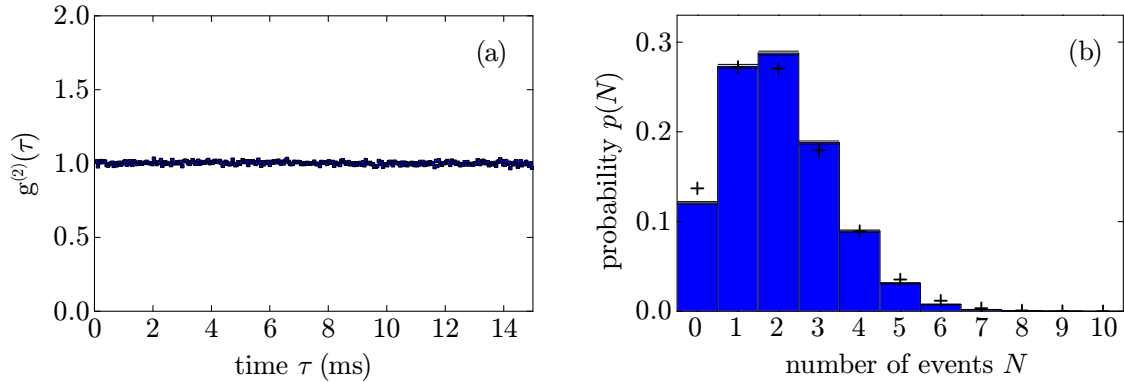


Figure 5.3: (a) Second-order correlation function of an atom laser beam. The data are binned with a time bin size of $50 \mu\text{s}$. The average count number is 2×10^5 per bin. We have omitted the first two data points since they are modified by the dead time of our detector. (b) Probability distribution $p(N)$ of the atom number N detected within a time interval of $T = 1.5 \text{ ms}$. The (+) symbols show a Poissonian distribution for the same mean value of $\langle n \rangle = 1.99$ as the measured data. The errors indicate statistical errors.

basically equivalent to $g^{(2)}(\tau \rightarrow \infty) = 1$, because the measurement duration T is much longer than the time scale on which correlations or anticorrelations can be expected. We average these histograms over many repetitions of the experiment to obtain $g^{(2)}(\tau)$ with a high signal-to-noise ratio.

5.3 Results

5.3.1 Second-order correlation function and counting statistics

Figure 5.3(a) shows the measured second-order correlation function of an atom laser beam. The value of the correlation function is $g^{(2)}(\tau) = 1.00 \pm 0.01$ which is expected for a coherent source. The second-order correlation function being equal to unity reveals the second-order coherence of the atom laser beam and is intimately related to the property that it can be described by a single wave function. Residual deviations from unity could arise from technical imperfections. Magnetic field fluctuations either due to current noise in the magnetic trapping coils or due to external fluctuations could imprint small intensity fluctuations onto the atom laser beam. We employ a low noise current source and magnetic shielding to minimize these effects. In addition, we use a highly stable microwave source which is stabilized to a GPS disciplined oscillator. A further contribution to a potential modification of the second-order correlation function could be due to the output coupling process itself. The spatial correlation function of atoms output coupled from a weakly interacting condensate has been studied theoretically in a

situation neglecting gravity [247]. The modification from a constant unity second-order correlation function was on the order of 1%, which is on the same order of magnitude as the uncertainty in our data.

Measuring the second-order correlation function requires to detect the particles within their coherence time and coherence volume [246]. The uncertainty of the detection time of an atom must be smaller than the correlation time, because otherwise the correlations vanish [58]. We estimate that the acquired time delays resulting from a possibly misaligned detector are shorter than the dead time of our detector. It has been measured that the coherence time of the atom laser is given by the duration of output coupling at least for durations of 1.5 ms [100].

Trapped Bose-Einstein condensates have been demonstrated to be phase coherent and to have a uniform spatial and temporal phase [220, 221, 104]. The atom laser beam has been theoretically described by a single wave function [247, 248] and its spatial coherence was observed [17]. Moreover, a full contrast interference pattern was observed between two atom laser beams extracted from separate locations inside a condensate [104]. This indicates a high degree of spatial overlap between the two propagating modes and a negligible distortion of the uniform spatial phase due to interactions with the remaining condensate. From this we conclude that the atom laser leaves the condensate region with a well defined spatial wavefront.

Many overlapping spatial modes at the detector wash out the correlations. In our experimental geometry this is the case when output coupling from a thermal source, since we can not resolve a single diffraction limited spatial mode. Therefore we do not observe thermal bunching of non-condensed atoms.

Determining the arrival times of all detected atoms explicitly allows us to extract the full counting statistics of the atoms. We choose a time bin length of $T=1.5$ ms in which we count the number N of detected atoms and plot the probability distribution $p(N)$ [see Fig. 5.3(b)]. The distribution is close to a Poissonian distribution

$$p(N) = \langle n \rangle^N e^{-\langle n \rangle} / N! \quad (5.1)$$

with a mean of $\langle n \rangle = 1.99$. For the measured distribution we have calculated the second, third and fourth cumulant to be $\kappa_2 = 1.75$, $\kappa_3 = 1.34$ and $\kappa_4 = 0.69$, respectively. We attribute the small deviation from the Poissonian distribution to having two or more atoms arriving within the dead time of our detector. For the total flux of 5.2 atoms per ms this probability is 5%.

We realize a direct comparison with a pseudothermal beam of atoms by output coupling a beam with thermal correlations from a Bose-Einstein condensate. This is in close analogy to changing the coherence properties of a laser beam by means of a rotating ground glass disc [235]. Instead of applying a monochromatic microwave field for

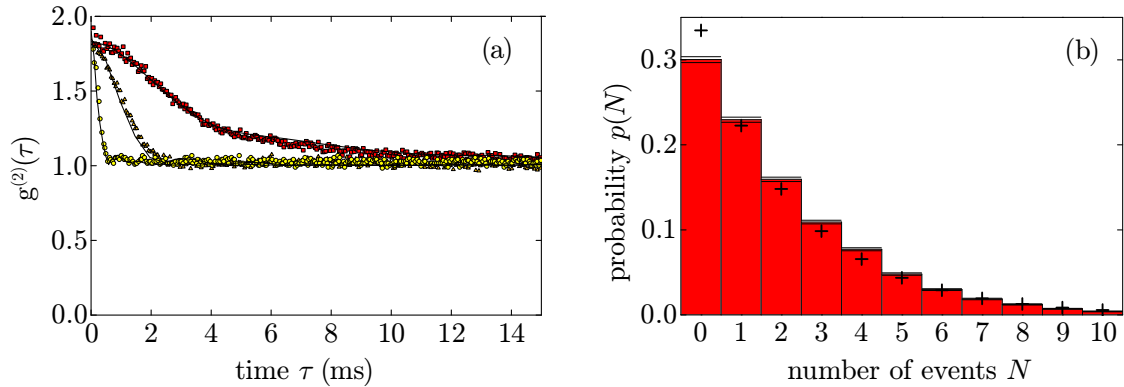


Figure 5.4: (a) Second-order correlation functions of pseudothermal atomic beams. The red square symbols correspond to a filter band width (FWHM) of 90 Hz, the orange triangles to a bandwidth of 410 Hz, and the yellow circles to a bandwidth of 1870 Hz. The data are binned with a time bin size of $50 \mu\text{s}$ in which the average count number is 8×10^4 . We have omitted the first two data points since they are modified by the dead time of our detector. The lines are the experimentally determined correlation functions of the broadband microwave fields. (b) Probability distribution $p(N)$ of the atom number N within a time interval of $T = 1.5 \text{ ms}$ for the 90 Hz bandwidth data. The (+) symbols indicate a Bose distribution with the same mean value of $\langle n \rangle = 1.99$. The errors indicate the statistical errors.

output coupling we have used a broadband microwave field with inherent frequency and intensity noise. We have employed a white noise generator in combination with quartz crystal bandpass filters which set the bandwidth of the noise. The filters operate at a frequency of a few MHz and the noise signal is subsequently mixed to a fixed frequency signal at 6.8 GHz to match the output coupling frequency. For atomic beams prepared in such a way we observe bunching with a time constant set by the bandpass filter [see Fig. 5.4(a)]. To compare our data with the theoretically expected correlation function we have measured the power spectra of the bandpass filters and calculated $|g^{(1)}(\tau)|^2$ of the rf field before frequency mixing. In Fig. 5.4(a) we plot $1 + \beta|g^{(1)}(\tau)|^2$. The normalization factor $\beta = 0.83$ accounts for the deviation of the experimental data from $g^{(2)}(0) = 2$ due to imperfections in the frequency mixing process.

For the pseudothermal beam we also calculate the counting statistics and find a significantly different behavior than for the atom laser case. For a filter with a spectral width (FWHM) of 90 Hz we have chosen a time bin length of $T=1.5 \text{ ms}$, smaller than the correlation time. The atomic flux with a mean atom number $\langle n \rangle = 1.99$ is equal to the case of the atom laser. We compare the measured probability distribution to a Bose distribution

$$p(N) = \langle n \rangle^N / (1 + \langle n \rangle)^{1+N}, \quad (5.2)$$

which is expected for a thermal sample and find good agreement [see Fig. 5.4(b)]. From

the distribution we have extracted the second, third and fourth cumulant to be $\kappa_2 = 4.6$, $\kappa_3 = 14.5$ and $\kappa_4 = 50.6$, respectively.

5.3.2 Time interval distributions of atoms

In this section, measurements of the the conditional and the unconditional probabilities for atom detection are presented and compared to theory. This constitutes a complementary view on two-particle correlations as compared to an analysis of the second-order correlation function. A famous example of how the statistics vary for different quantum states of light is the distinct difference of photon correlations in thermal light beams and laser beams [235, 249]. For ideal bosonic atoms the same quantum statistical properties are expected as for the case of photons.

We first investigate the distribution function of the time intervals between successive atom counting events. This represents a “start-stop” measurement, where a time counter is triggered by an atom detection event and stopped by the next detection event [249]. From the histogram of the measured time intervals we obtain the conditional probability $p(t|t + \tau)$ of detecting the *next* atom a time τ later than an initial atom observed at t . These exclusive pair correlations, for which we restrict ourselves to consecutive atom detection events, are distinguished from the non-exclusive pair correlations measured by the second-order correlation function $g^{(2)}(\tau)$. There the pairwise time differences between *all* atoms are evaluated.

For an average count rate ν the conditional detection probability density for a coherent beam is given by [250]

$$p_{\text{coh}}(0|\tau) = \nu e^{-\nu\tau}. \quad (5.3)$$

In contrast, for a thermal state of bosons one finds [250]

$$p_{\text{th}}(0|\tau) = \frac{2\nu}{(1 + \nu\tau)^3}. \quad (5.4)$$

For $\tau = 0$ the thermal probability density is twice as large as the coherent probability density. This reflects the increased thermal fluctuations and the bunching behavior in pair correlations of bosonic particles.

In Fig. 5.5(a) we compare our data with this theory. For the pseudothermal atomic beam we have chosen a bandwidth of $\Delta f = 90$ Hz and analyzed time intervals short compared to the coherence time $\tau_c = 1/\Delta f = 11$ ms. We normalize the measured probability by the measured count rate $\nu_{\text{exp}} = 1.5 \times 10^3 \text{ s}^{-1}$ and fit the result with the functions given in equation (5.3) and equation (5.4) allowing for some overall scaling factor. From the fits we obtain the average count rates $\nu = 1.4 \times 10^3 \text{ s}^{-1}$ and $\nu = 1.6 \times 10^3 \text{ s}^{-1}$ for the atom laser beam and the pseudothermal beam, respectively, which compares well with the experimentally determined flux ν_{exp} for both cases. For $\tau = 0$

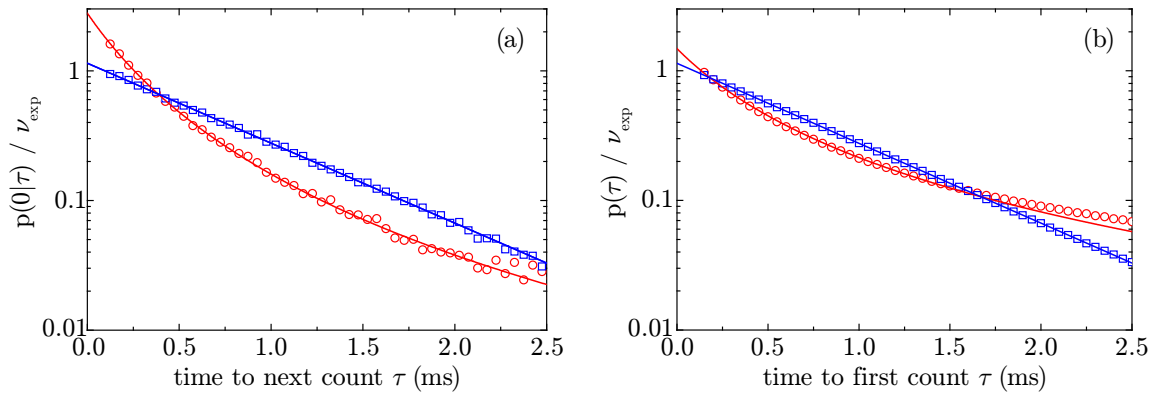


Figure 5.5: Exclusive detection probabilities for an atom laser (blue squares) and for a pseudothermal beam with a bandwidth of $\Delta f = 90$ Hz (red circles). (a) Conditional detection probability $p(0|\tau)$, which is the frequency distribution of the time intervals between two successive atom counts. The lines are fits according to equations (5.3) and (5.4). (b) Unconditional detection probability $p(\tau)$, given by the frequency distribution of the length of intervals between a randomly chosen start point and the subsequent atom detection. The lines are fits according to equations (5.5) and (5.6).

we find that the data for the atom laser beam exceed $p(0|\tau)/\nu_{\text{exp}} = 1$ by approximately 15%. Similarly, the results for the pseudothermal beam exceed $p(0|\tau)/\nu_{\text{exp}} = 2$ by approximately 30%. This could be attributed to the dead time of our detector—which is about 70 μs (see Sec. 3.5.3)—during which we cannot detect a possible consecutive event. We estimate the probability for a second atom arriving within the dead time of the detector to be 5% for the atom laser beam and 10% for atoms in the pseudothermal beam. With this probability a later atom might falsely be identified being consecutive to the initial event which overestimates the number of time intervals larger than the detector dead time. Moreover, the experimental count rate is underestimated by the same factor contributing also to the enhancement of the data above the theoretical expectation.

Next we study the unconditional probability of a single atom detection event. The unconditional probability assumes that the timer is started at a randomly chosen time and records the time to the next atom detection event. For a coherent beam of atoms the unconditional probability for a detection event $p(\tau)$ is equal to the conditional probability investigated above [250]

$$p_{\text{coh}}(\tau) = \nu e^{-\nu\tau}. \quad (5.5)$$

This reflects the absence of any density correlations in a coherent atomic beam. For a thermal state one finds

$$p_{\text{th}}(\tau) = \frac{\nu}{(1 + \nu\tau)^2}, \quad (5.6)$$

which for $\tau = 0$ differs from the corresponding conditional probability by a factor of 2. The physical reason for this difference lies in the bunching of thermal bosons, which enhances the detection probability only for two nearby events measured by the conditional probability. The unconditional probability measures a single particle property and does not reveal a bunching effect. In Fig. 5.5(b) we show our measurements of the atom detection probability for a randomly chosen initial start point and find good agreement with the theoretical prediction. Similarly to the results for the conditional probability we observe that the experimental data for $\tau = 0$ are larger than the theoretically expected result of $p(\tau)/\nu_{\text{exp}} = 1$ by the same relative amount as in Fig. 5.5(a). We attribute this again to the dead time of our detector as discussed above. The apparently better data quality of Fig. 5.5(b) as compared to Fig. 5.5(a) is due to the larger number of available time intervals for the unconditional probability.

6 Cavity QED detection of interfering matter waves

We observe the build-up of a matter wave interference pattern from single atom detection events in a double-slit experiment. The interference arises from two overlapping atom laser beams extracted from a rubidium Bose-Einstein condensate. Our detector is a high-finesse optical cavity which realizes a quantum measurement of the presence of an atom and thereby projects delocalized atoms into a state with zero or one atom in the resonator. The experiment reveals simultaneously the granular and the wave nature of matter. We present a setup which is suited for applications in atom interferometry and cavity QED.

This chapter has been published as [187]: T. Bourdel, T. Donner, S. Ritter, A. Öttl, M. Köhl, and T. Esslinger. ‘Cavity QED detection of interfering matter waves’. *Physical Review A* **73**(4), 043602 (2006).

6.1 Introduction

The prediction of the duality between particles and waves by de Broglie [251] is a cornerstone of quantum mechanics. The simple picture that matter waves show interferences just like classical waves neglects the granularity of matter. This analogy is valid only if the detector is classical and integrates the signal in such a way that the result is a mean particle flux. With quantum detectors that are sensitive to individual particles the discreteness of matter has to be considered. The probability to detect a particle is proportional to the square amplitude of the wave function and interferences are visible only after the signal is averaged over many particles. Interference of single massive particles have been observed using electrons [252, 253], neutrons [254], atoms [255, 256, 257] and even large molecules [258].

In the regime of atom optics, single atom detection has been achieved for example by fluorescence [259], using a microchannel plate detector for metastable atoms [260] and high-finesse optical cavities [26]. Only very recently the single atom detection capability

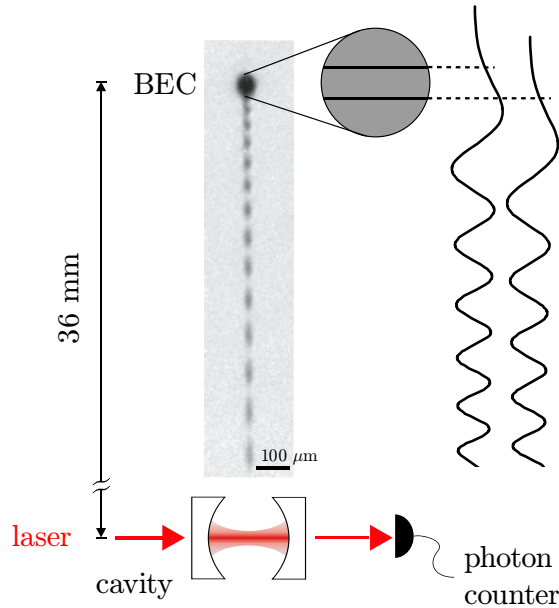


Figure 6.1: Schematic of the experimental setup. From two well defined regions in a Bose-Einstein condensate (BEC), we couple atoms to an untrapped state. The real parts of the resulting atom laser wave functions are sketched on the right hand side. The absorption image shows an interference pattern corresponding to $\Delta f = 1$ kHz and an atom flux $\sim 10^6$ times larger than in the actual single atom interference experiment. Monitoring the transmission of a probe laser through a high-finesse optical cavity with a photon counter, single atom transits are detected.

has been achieved together with quantum degenerate samples reaching the regime of quantum atom optics [101, 22]. In our experiment, we detect single atoms from a coherent matter-wave field using a high-finesse optical cavity in the strong coupling regime of cavity quantum electrodynamics (QED) [121, 134, 132].

For atoms with a spatially extended wave function, such as in a Bose-Einstein condensate or in an atom laser beam, a measurement projects the delocalized atom into a state localized at the detector [261]. This quantum measurement requires dissipation in the detection process. For our cavity QED detection method, we study the open quantum system composed of coupled matter-wave and light fields. The two sources of dissipation are cavity losses and spontaneous emission. In particular, we calculate the time needed for the localization of an atom along the beam in the cavity measurement process. We then experimentally investigate atomic interferences using our detector which can resolve single atom transits in time. The high detection efficiency opens new perspectives for atom interferometry such as quantum limited detection of amplitude and phase of a matter-wave [262].

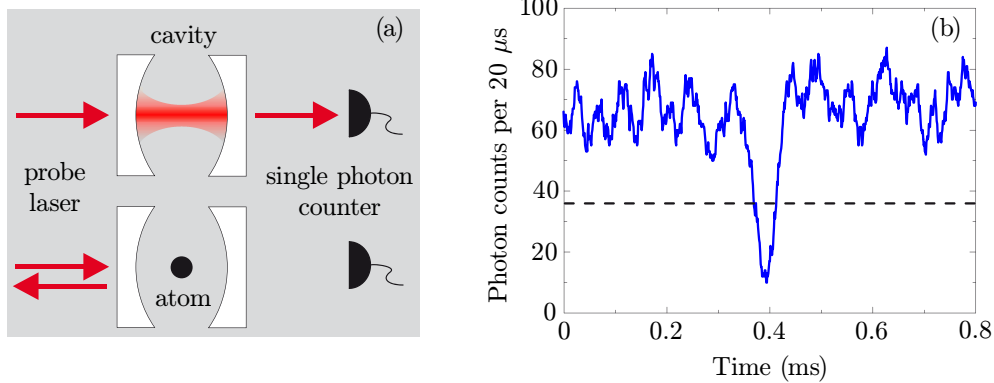


Figure 6.2: (a) Cavity single atom detection principle. An atom detunes the high-finesse cavity from resonance and the cavity transmission consequently drops. (b) Photon flux through the high-finesse optical cavity when an atom is detected. The photon count rate is averaged over $20\ \mu\text{s}$. The detection threshold is set to be four times the standard deviation of the photon shot noise (dashed line).

A schematic of our experimental setup is shown in Fig. 6.1. We output couple two weak atom laser beams from a Bose-Einstein condensate and their wave functions overlap and interfere [104]. The flux is adjusted in such a way that there is on average only one atom at a time in the interferometer. Using the high-finesse cavity we measure single atom arrival times in the overlapping beams. We observe the gradual appearance of a temporal high-contrast matter-wave interference pattern as more and more detection events are accumulated.

6.2 Quantum measurement in a cavity QED system

Single atom detection in an optical cavity can be captured in a classical picture: an atom changes the index of refraction in the cavity and thereby shifts it out of resonance from the probe laser frequency. In the absence of an atom, the probe beam is resonant with the cavity and its transmission is maximal. Experimentally we use a probe power corresponding to five photons on average in the cavity. The cavity lock is sufficiently stable for the cavity transmission to be at the photon shot noise limit. The presence of an atom results in a drop of the cavity transmission (see Fig. 6.2). We set the threshold for an atom detection event to a drop in transmission of four times the standard deviation of the photon shot noise in our $20\ \mu\text{s}$ integration time. Then the overall detection efficiency of atoms extracted from a Bose-Einstein condensate is measured to be $0.23(8)$. It is mainly limited by the size of the atom laser which exceeds the dimension of the cavity mode and can be increased using a laser to guide the atoms into the detector.

Our cavity has been described before (see Sec. 3.3.1 and Sec. 3.4.4) and we only recall here its main figures of merit. Its length is $176\ \mu\text{m}$, the mode waist radius is $25\ \mu\text{m}$, and its finesse is 3×10^5 . The maximum coupling strength between a single ^{87}Rb atom and the cavity field $g = 2\pi \times 10.4\ \text{MHz}$ is larger than the cavity field decay rate $\kappa = 2\pi \times 1.4\ \text{MHz}$ and the atom dipole decay rate $\gamma = 2\pi \times 3\ \text{MHz}$. The probe laser and the cavity are red-detuned as compared to the atomic resonance so that the light force pulls the atoms to regions where the coupling is large, therefore enhancing the detection efficiency.

To understand the actual detection process we study the dynamics of the atom-cavity quantum system taking into account dissipation. We first consider a classical atom entering a simplified square shaped cavity mode so that its coupling to the cavity field increases suddenly to a constant value g . Thereby we do not take into account the atom dynamics due to the dipole potential of the standing-wave cavity mode. The cavity field is initially coherent with a few photons. We use a two level approximation for the atom description and assume a $30\ \text{MHz}$ red-detuning of the probe laser compared to the atomic resonance. Our probe beam is linearly polarized orthogonally to the magnetic field direction. We therefore do not probe on a cycling transition. The $30\ \text{MHz}$ detuning is an effective value chosen to match the experimental conditions. In the case of strong coupling the following dynamics occur. On a short time scale given by $1/g$, the atom-cavity system exhibits coherent oscillations. It progressively reaches an equilibrium state on a time scale given by $1/\kappa$ and $1/\gamma$ due to cavity loss and atomic spontaneous emission. These are the two sources of dissipation. In the equilibrium state, the mean photon number in the cavity is reduced and the cavity transmission drops.

To evaluate this drop quantitatively, we find the steady-state of the master equation for the density matrix numerically [116, 263, 119, 264]. For our parameters the transmission as a function of the coupling strength g is plotted in Fig. 6.3(a). For a maximally coupled atom $g = 2\pi \times 10.4\ \text{MHz}$, the average intracavity photon number is found to be reduced from 5 to 0.8, and the number of detected photons is then reduced by the same ratio. Such a reduction corresponds well to the largest observed transmission drops. An example is shown in Fig. 6.2. The detection threshold corresponds to a coupling of $g = 2\pi \times 6.5\ \text{MHz}$. Experimentally, unlike in our model, an atom feels a position dependent coupling as it transverses the mode profile. However, the atom transit time through the cavity mode ($45\ \mu\text{s}$) is long compared to the cavity relaxation time scales $1/\kappa$ and $1/\gamma$ and the atom-cavity system adiabatically follows a quasiequilibrium state. Therefore the experimental transmission drops can be compared to the calculated ones.

Specific to our experiment is that a longitudinally extended matter wave and not a classical atom enters the cavity [100]. Our system allows us to realize a quantum measurement of the presence of an atom. For our low atom flux, we can neglect the probability of having more than one atom at a time in the cavity. The incoming con-

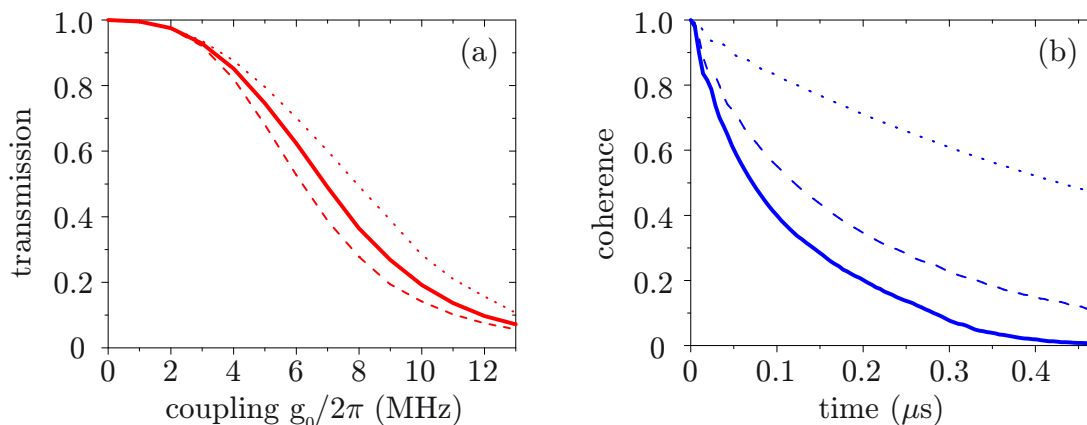


Figure 6.3: (a) Normalized transmission as a function of coupling strength. The solid line corresponds to our probe strength of 5 photons in the cavity in the absence of an atom. The dashed line is the weak probe limit. The dotted line corresponds to 10 photons in the cavity. (b) Coherence between the states with one and no atom as a function of time. The initial coherence is normalized to 1. Solid line: $g = 2\pi \times 10$ MHz. Dashed line: $g = 2\pi \times 6.5$ MHz. Dotted line: $g = 2\pi \times 3$ MHz.

tinuous wave function is thus projected into a state with one or zero atom in the cavity. This evolution from a pure quantum state to a statistical mixture involves decoherence. The latter is introduced by spontaneous scattering and cavity photon loss. The origin of the decoherence can be understood as unread measurements in the environment [263, 261]. For example, if a spontaneously emitted photon is detected, there is necessarily an atom in the cavity and the wave function is immediately projected. Similarly, the more different the light field with an atom in the cavity is from the field of an empty cavity, the more different is the scattered radiation out of the cavity, and the projection occurs correspondingly faster.

We now quantify the time needed for the projection to occur. For simplicity, rather than a continuous wave function, we consider a coherent mixture of one and zero atom entering a square shaped cavity at a given time. We take the limit when the probability to have one atom is low. The initial cavity field is the one of an empty cavity. Dissipation effects are studied by computing the time evolution of the density matrix [119]. The degree of projection of the initial state can be extracted from the off-diagonal terms between states with one atom and no atom in the density matrix. More precisely, we define the coherence as the square-root of the sum of the squared modulus of the off-diagonal terms mentioned above. This quantity is maximal for a pure quantum state with equal probability to have an atom or not. The coherence is zero for a statistical mixture.

In Fig. 6.3(b) the temporal evolution of the coherence is plotted. As expected, it

decays to zero at long times due to dissipation. The decay time increases as the coupling to the cavity is weakened. In the limit where the coupling vanishes, the coherence is preserved. The atomic wave function then evolves as if there was no cavity. For $g > 2\pi \times 6.5$ MHz, the decoherence time is found to be a fraction of a microsecond. This time is much shorter than the 45 μ s transit time of an atom through the cavity, and for all our detected atomic transits the wave function is thus well projected to a state with one atom. Our detection scheme realizes a quantum measurement of the presence of an atom in the cavity. However during an atom transit some photons are spontaneously scattered and the velocity of the atom is slightly modified.

6.3 Single atom interference

Using our cavity detector we can observe matter wave interferences on the single atom level. The starting point of the experiment is a quasi pure Bose-Einstein condensate with 1.5×10^6 rubidium atoms in the hyperfine ground state $|F = 1, m_F = -1\rangle$ [101]. The atoms are magnetically trapped with frequencies $\omega_x = 2\pi \times 38.6$ Hz, $\omega_y = 2\pi \times 7.2$ Hz and $\omega_z = 2\pi \times 29.1$ Hz with the vertical z -axis defined by gravity. A weak and continuous microwave field locally spin-flips atoms from the Bose-Einstein condensate into the untrapped $|F = 2, m_F = 0\rangle$ state. This process is resonant for a section of the condensate where the magnetic field is constant. Because the magnetic moment of the spin flipped atoms vanishes, they fall due to gravity and form a continuous atom laser [79].

When we apply two microwave fields of different frequencies, we are able to output couple atom laser beams from two well defined slices of the condensate [104]. The two distinct atom laser wave functions overlap and interfere. At the entrance of the cavity, the atomic wave function ψ is well described by the sum of two plane waves with the following time dependence

$$\begin{aligned} \psi(t) &\propto \exp(i\omega_1 t) + \exp(i(\omega_2 t + \phi)) \\ &\propto \cos((\omega_2 - \omega_1)t/2 + \phi/2) \end{aligned} \quad (6.1)$$

where $\hbar\omega_1$ and $\hbar\omega_2$ are the energies of the two laser beams and ϕ is a fixed phase difference. The radial dependence of the wave function is neglected. The probability to detect an atom is given by the square norm of the wave function which is modulated in time and behaves like a cosine squared. The modulation frequency of the interference signal is given by the energy difference between the two atom lasers. Experimentally, it is determined by the frequency difference of the two microwave fields and is chosen to be $\Delta f = 10$ Hz, which corresponds to a distance of 5 nm between the two output coupling regions. The two microwave fields are generated such that the interference pattern is phase stable from one experimental run to the other.

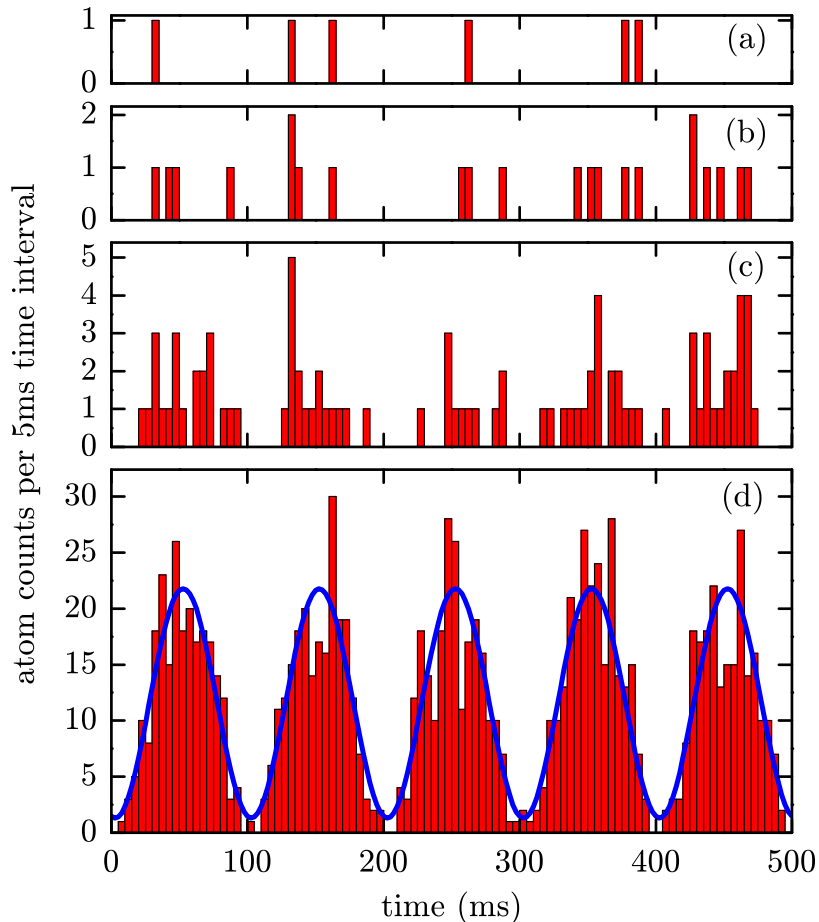


Figure 6.4: Histograms of the atoms detected in 5 ms time intervals. (a) Single experimental run. (b) Sum of 4 runs. (c) Sum of 16 runs. (d) Sum of 191 runs, the line is a sinusoidal fit. Please note the different scales.

The results of the experiment are presented in Fig. 6.4. Each experimental run corresponds to output coupling from a new condensate. On average ~ 6 atoms are detected in 0.5 s. After the detection of a few atoms, the interference pattern is not yet visible [Fig. 6.4(a)]. Nevertheless, after adding the results of several runs, it progressively appears [Figs. 6.4(b)–6.4(d)]. Experimentally, the atom number fluctuation is found to be dominated by the atomic shot noise and the signal to noise ratio of the interference increases as more data are included. A fit to the histogram yields a contrast of $0.89(5)$. The slight reduction of contrast is explained by a detected flux of about one atom every 3 runs in the absence of output coupling. We attribute this effect to artifact detection events and to atoms output coupled from stray microwave fields. Using a higher flux,

we were able to detect an interference contrast in excess of 0.97.

Here, we work with a flux of one detected atom per 83 ms, which is about the time an atom needs to travel from the condensate region to the cavity. We are thus in a regime where the atoms fall one by one in the interferometer. Thereby a single atom interferes with itself. It behaves both like a wave because its time arrival probability shows an interference pattern and like a particle when detected. This can be similarly expressed by saying that each individual atom is released from both slits simultaneously. Our experiment is an atomic counterpart of Young's double slit experiment with individual photon detection.

6.4 Summary

In conclusion, we detect matter wave interferences with a high-finesse optical cavity detector which realizes a quantum measurement of the presence of an atom. We explain how dissipation plays a crucial role in the detection process and for the localization of the atom inside the cavity. Using this detector, we are able to detect a high contrast atom interference pattern at the single atom level. The coupling of a matter wave to a cavity QED system opens the route to the quantum control not only of the internal state of the atoms but also of their positions [265]. Using the presented detection technique we can probe an atomic gas with a good quantum efficiency and introduce only a minimum perturbation through the measurement. This could facilitate nondestructive and time-resolved studies of the coherence of a quantum gas, for example during the formation of a Bose-Einstein condensate. With our setup quantum limited detection of the phase between two distinct condensates would permit investigations of their relative phase evolution [266, 267], build-up [268, 51, 52], or diffusion [269].

7 Conclusions and outlook

We presented an apparatus that achieves the fusion of BEC production with the single atom detection ability in the strong coupling regime of cavity QED. The challenge to experimentally merge these two fields was overcome by forging new paths for the Bose-Einstein condensation setup and the ultrahigh finesse optical cavity design [157]. The cavity can be used as a highly sensitive probe for precision measurements of numerous condensate properties. Atom lasers with accurately controllable flux can be output coupled from the BEC, directed into the cavity and detected with single atom resolution using the cavity.

This setup allowed us to observe the formation of long-range order in a Bose gas crossing the phase transition to a Bose-Einstein condensate [153]. A thermal cloud of atoms closely above the phase transition temperature was prepared in a highly nonequilibrium situation by removing the most energetic third of the atoms. In the subsequent free evolution of the system, it crossed the phase transition. Two atom lasers of different energy, originating from different regions within the atom cloud, were output coupled simultaneously. While the visibility of the resulting interference pattern signaled the degree of coherence of the trapped cloud, the flux of atoms gave information on the density of the sample. The growth of the coherence in time and space was studied and compared to the increase in the flux of atoms. The speed of the growth and its spatial dependence could be quantified. A particular strength of this novel measuring method is that it yields real time information, and that at the same time the system is only minimally disturbed.

The ability to detect single atoms with high efficiency allowed us to measure the second-order correlation function of an atom laser and to confirm its second-order coherence as opposed to the bunching behavior of a pseudothermal beam [101, 229]. This absence of excess intensity fluctuations is the clearest distinction between a laser and a thermal beam. Together with measurements proving the first-order coherence of an atom laser [100, 187] it proves the close analogy between an atom laser and an optical laser. A very interesting extension of our measurements would be to study the change of the two particle correlation function in close vicinity of the Bose-Einstein phase transition.

Study of a trapped, interacting Bose gas in the critical regime

The described method used to study the growth of a BEC is also perfectly suited to investigate the coherence of a Bose gas in the critical regime near the Bose-Einstein phase transition. In this regime, the length scale of critical fluctuations of the order parameter is larger than the thermal de Broglie wavelength and the critical fluctuations completely govern the system.

To gain a better understanding of such a system, it is instructive to look at a non-interacting Bose gas above the critical temperature trapped in the harmonic potential $V(\mathbf{r})$, for which the first-order correlation function $g^{(1)}$ can be calculated making a few assumptions. Here we will concentrate on the correlations as measured when output coupling symmetrically with respect to the center of the trap ($x = x' = y = y' = 0$), and only investigating distances along the vertical axis ($z = -z'$). This most closely resembles our experimental situation (see Sec. 4.3.3). Under the assumption that the thermal energy of the system is much larger than the energy spacing of the trap levels $k_B T \gg \hbar\omega$ and in the local density approximation the result is [56]:

$$g^{(1)}(z, z') = \frac{g_{3/2} \left[\exp\left(\frac{\mu}{k_B T}\right), \exp\left(-\pi \frac{(z-z')^2}{\lambda_{\text{dB}}^2}\right) \right]}{g_{3/2} \left[\exp\left(\frac{\mu}{k_B T}\right), 1 \right]}, \quad (7.1)$$

where the generalized Bose function is defined as $g_\alpha(x, y) = \sum_{m=1}^{\infty} x^m y^{1/m} m^{-\alpha}$. The chemical potential is denoted by μ and λ_{dB} is the thermal de Broglie wavelength. A mean-field treatment of the interactions gives a similar result, but with μ replaced by $\mu(\mathbf{r}) = \mu - 2U_0 n_T(\mathbf{r})$, where $n_T(\mathbf{r})$ is the local density of the thermal atoms [56].

In the limit of $\mu/(k_B T) \gg 1$, i.e. for a thermal cloud far above T_c , we can replace the sum by its lowest-order term:

$$g^{(1)}(z, z') \approx \exp\left(-\pi \frac{(z-z')^2}{\lambda_{\text{dB}}^2}\right). \quad (7.2)$$

This is the well known result for the first-order correlation function of a thermal Bose gas: It has the form of a Gaussian with the width given by the thermal de Broglie wavelength. As can be seen from eqn. (7.1), a very different behavior is to be expected for temperatures close to the critical temperature T_c [for the dependence of μ on T see eqn. (4.9)].

The experimental starting point is a BEC heated very slowly with a rate of only about 4 nK/s. With such a low heating rate and a temperature resolution of about $0.002 T_c$ we are able to access the critical regime. Applying the method discussed in detail in chapter 4 allows us to measure the coherence of the trapped Bose gas as a function of temperature and position, but now in a nearly stationary situation.

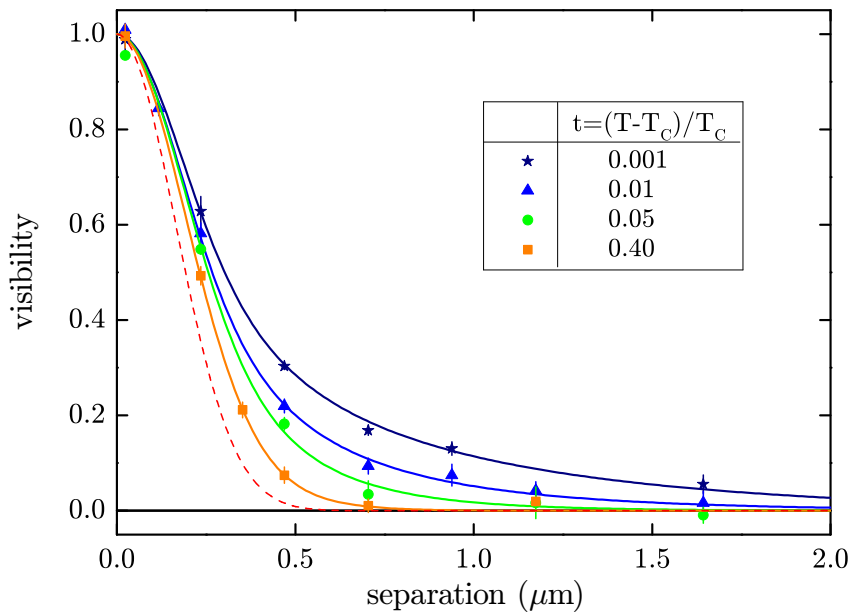


Figure 7.1: Correlation function for a trapped thermal Bose gas at different temperatures above T_c . The points are the measured visibility of an interference pattern, while the solid lines are fits of a theory describing a non-interacting trapped Bose gas (see text). In contrast to a thermal gas far above T_c , the data can clearly not be described by a Gaussian with its width given by the thermal de Broglie wavelength (red dashed line).

Preliminary results of such a measurement are presented in Fig. 7.1. We have sampled the first-order correlation function for four different temperatures between 1.4 and 1.001 T_c . The particle number and therefore $T_c = 126$ nK is approximately the same for all curves. The solid lines are fits of eqn. (7.1) to the data with μ and T as free parameters. The dashed red line is the result according to eqn. (7.2) with the thermal de Broglie wavelength $\lambda_{dB} = 0.41$ μm calculated at T_c . Obviously, the decay of the correlation function is not Gaussian any more very close to the critical temperature. Rather, the region of large coherence is extended beyond λ_{dB} and the tail of the correlation function decays significantly slower. To our knowledge, this measurement is the first observation of the non-Gaussian behavior of the correlation function in close proximity to the phase transition.

In the critical regime very close to T_c , the mean-field theory outlined above is not applicable any more. For $t = (T - T_c)/T_c \rightarrow 0$ and $r > \lambda_{dB}$, the correlation function in “Ornstein-Zernike form” is given by [6]

$$g^{(1)}(\mathbf{r}) = r^{-p} \exp(-r/\xi). \quad (7.3)$$

The correlation length ξ diverges close to the critical temperature as

$$\xi \propto \left| \frac{T - T_c}{T_c} \right|^{-\nu} = |t|^{-\nu}, \quad (7.4)$$

with the critical exponent ν describing the form of the divergence. The correlation function decays as a power-law at $t = 0$, with the exponent given by $p = d - 2 + \eta$. Here d is the dimensionality of space. The critical exponent η is zero according to mean-field theory and a Gaussian model and its potential deviation from this value is too small to be measured with our setup. However, it is possible to infer the critical exponent ν from the behavior of the correlation function ξ determined in the apparatus presented here. This is especially interesting since the critical exponent ν of the correlation length in a trapped, interacting system has neither been measured directly nor do theoretical predictions exist.

The theory for the non-interacting trapped case presented above gives $\nu = 1/2$, but measurements of the critical exponent α of the specific heat in liquid Helium as well as renormalization group theory calculations suggest $\nu = 0.67$ for a homogeneous, interacting system. The same critical exponents apply to very different physical systems whose critical temperatures may differ by orders of magnitude. This universality distinguishes the critical exponents and makes our results interesting not only to the cold atoms community but to many different fields in physics. In liquid helium, the analysis of the critical exponents is considered the strongest evidence for BEC [55]. With the apparatus presented here, we could very recently determine the critical exponent of a trapped, dilute atomic Bose gas to be $\nu = 0.67 \pm 0.13$ [154].

Transport of the BEC into the cavity

In the experiments presented so far, the cavity has been used as a single atom detector for atoms from an atomic beam. This has facilitated research on Bose-Einstein condensates with unprecedented resolution, allowing for previously impossible experiments. However, single atom detection is by far not the only possible application for an ultra-high finesse cavity in the strong coupling regime. Therefore we decided to extend the experimental setup with a mechanism to transport the BEC into the cavity. There, the BEC can be held in various trap geometries, allowing for the exploration of the rich physics provided by the ultrastrong coupling between the atomic matter wave and the quantized light field of the cavity mode.

Two vertical, counterpropagating laser beams are focused through the cavity forming an optical dipole trap. They are frequency stabilized to a ^{133}Cs transition at $\lambda_t = 852.35 \text{ nm}$, red-detuned from the ^{87}Rb D₁ and D₂ lines. With an elliptical focus of $(25 \times 50) \mu\text{m}^2$ inside the cavity and a maximum power of 80 mW per beam the resulting standing wave potential is deep enough to support the atoms against gravity, even at

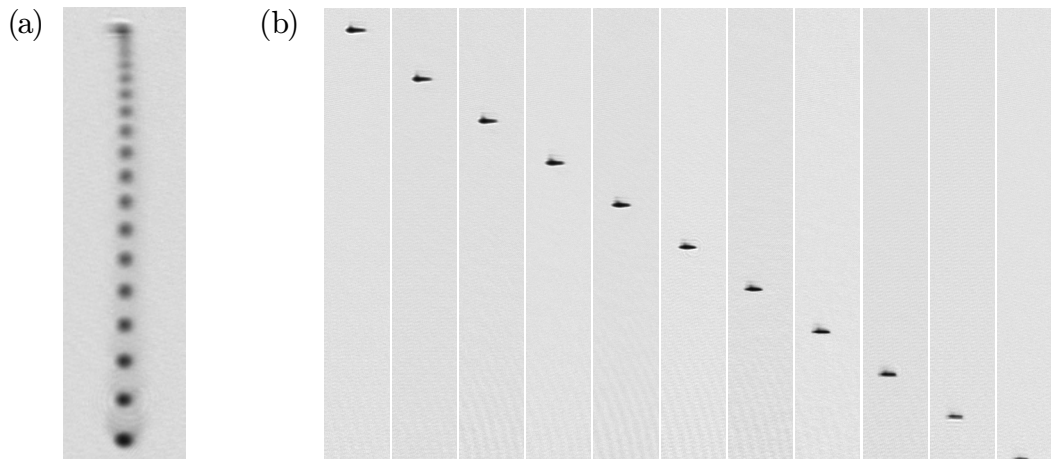


Figure 7.2: Absorption images of a BEC held in a one-dimensional, horizontal optical lattice (gravity points downwards). (a) The trapped BEC (top spot) is held in a weak standing wave. The other atom pulses are due to quantum interference between the vertical array of BECs trapped in the antinodes of the standing wave (not resolved). (b) Transport of the atoms. The distance between the atom cloud in successive images is $500\ \mu\text{m}$.

the position of the magnetic trap $36\ \text{mm}$ above the cavity. The exact frequency of both beams is set independently using two acousto-optical modulators controlled by two homebuilt direct digital synthesis (DDS) generators [270]. By introducing a frequency difference δ between the two beams, the standing wave pattern can be shifted in a controlled way. Each potential well moves at a velocity $v = \delta\lambda_t/2$.

In an initial experiment, the BEC was loaded into a weak stationary lattice. We observed a train of atom pulses originating from it as shown in Fig. 7.2(a). Due to Bloch oscillations [271, 272], a fraction of the atoms undergoes Landau-Zener tunneling to the continuum band [76]. As expected, the frequency of the Bloch oscillations $\omega_J = mg\lambda_t/(2\hbar)$ is independent of the lattice depth. m is the atomic mass and g the acceleration due to gravity. Figure 7.2(b) shows the transport of the atoms trapped in several antinodes of the standing wave. This vertical array of small traps is not resolved due to the limited imaging resolution of about $10\ \mu\text{m}$. In the leftmost image, the position of the atoms is the same as in the QUIC trap. The length of the transport is increased by $500\ \mu\text{m}$ from one image to the next. Due to limited optical access, only the first $5\ \text{mm}$ of the transport are covered.

Inside the cavity, the atoms can be trapped either in the transport lattice, the standing wave of the cavity stabilization light at $830\ \text{nm}$ or an additional dipole trap at $852\ \text{nm}$ on the third orthogonal axis. We find that all three traps independently are sufficient to hold the transported cloud against gravity. A combination of the horizontal dipole

trap perpendicular to the cavity axis plus one of the two counterpropagating transport beams however provide the best confinement of the atoms to ensure good overlap with the cavity mode. The transport of single atoms [125] should also be feasible, but we favor to transport the whole cloud and to reduce the atom number subsequently by forced evaporation if required. The largest condensates inside the cavity can be achieved by transporting an only partly condensed cloud. Subsequent recondensation of the atoms by evaporative cooling can compensate heating during the transport and we obtain nearly pure condensates of more than 10^5 atoms at the position of the cavity mode.

In the future, the combination of the trapped atoms with the cavity detector could allow for the preparation of atomic Fock states by exploiting the dependence of the coupling constant on the number of atoms. Once the discrimination between one, two and no atom inside the cavity is implemented, which is definitely feasible, measurement induced entanglement of two atoms could be realized [273]. A particularly attractive proposal is the cooling of a single atom by immersion in a BEC [274]. The single atom would have to be in a state strongly coupled to the cavity, e.g. in the $|F = 2\rangle$ hyperfine state with the cavity set to the $|F = 2\rangle \rightarrow |F = 3\rangle$ transition. The BEC formed by the remaining atoms would be in a more weakly coupling state, for example $|F = 1\rangle$. This technique has the potential of preserving the internal state of the single atom, which in turn would constitute an excellent qubit. Using heterodyne detection, the phase shift of the detection light imposed by the atoms can be detected. Especially in the case of large detuning between detection light and atom, one can hope to non-destructively read out the internal state of an atom. A scheme for the deterministic production of photon Fock states has also been proposed [275]. Adiabatic dark state passage for N atoms will generate N photons in the cavity mode. Our system offers the optical access necessary for a 3D optical lattice inside the cavity. Therefore the creation of a Mott-insulating state [276] inside the cavity seems feasible. It would serve as an excellent starting point for quantum state engineering [277, 278] and the implementation of quantum gates [279]. Five coils placed around the cavity can create magnetic field configurations with the potential of position dependent single atom addressability using tomography techniques and read out using the cavity. This is an extremely promising setup for studying strongly correlated systems with single site resolution.

A Appendix

A.1 Physical constants and ^{87}Rb data

- Unless otherwise stated all physical constants used in this thesis can be found at <http://physics.nist.gov/constants> and are published in:
P. J. Mohr and B. N. Taylor. ‘CODATA recommended values of the fundamental physical constants: 2002’. *Rev. Mod. Phys.* **77**(1), 1–107 (2005).
- All data about physical properties of ^{87}Rb , especially the optical properties of the D₂ line ($5^2\text{S}_{1/2} \rightarrow 5^2\text{P}_{3/2}$ transition), have been taken from:
D. A. Steck. ‘Rubidium 87 D Line Data’. <http://steck.us/alkalidata/> (2003).

Bibliography

- [1] M. H. Anderson, J. R. Ensher, M. R. Matthews, C. E. Wieman, and E. A. Cornell. ‘Observation of Bose-Einstein Condensation in a Dilute Atomic Vapor’. *Science* **269**, 198–201 (1995).
- [2] K. B. Davis, M.-O. Mewes, M. R. Andrews, N. J. van Druten, D. S. Durfee, D. M. Kurn, and W. Ketterle. ‘Bose-Einstein condensation in a gas of sodium atoms’. *Phys. Rev. Lett.* **75**(22), 3969–3973 (1995).
- [3] C. C. Bradley, C. A. Sackett, J. J. Tollett, and R. G. Hulet. ‘Evidence of Bose-Einstein Condensation in an Atomic Gas with Attractive Interactions’. *Phys. Rev. Lett.* **75**(9), 1687–1690 (1995). Erratum: *Phys. Rev. Lett.* **79**, 1170 (1997).
- [4] O. Penrose and L. Onsager. ‘Bose-Einstein Condensation and Liquid Helium’. *Phys. Rev.* **104**, 576–584 (1956).
- [5] C. N. Yang. ‘Concept of Off-Diagonal Long-Range Order and the Quantum Phases of Liquid He and of Superconductors’. *Rev. Mod. Phys.* **34**, 694–704 (1962).
- [6] K. Huang. *Statistical Mechanics* (John Wiley & Sons, 1987).
- [7] Y. Kagan and B. V. Svistunov. ‘Kinetics of the onset of long-range order during Bose condensation in an interacting gas’. *Sov. Phys. JETP* **78**(2), 187–194 (1994).
- [8] C. W. Gardiner, P. Zoller, R. J. Ballagh, and M. J. Davis. ‘Kinetics of Bose-Einstein Condensation in a Trap’. *Phys. Rev. Lett.* **79**(10), 1793–1796 (1997).
- [9] D. W. Snoke and J. P. Wolfe. ‘Population dynamics of a Bose gas near saturation’. *Phys. Rev. B* **39**(7), 4030 (1989).
- [10] D. V. Semikoz and I. I. Tkachev. ‘Kinetics of Bose condensation’. *Phys. Rev. Lett.* **74**(16), 3093–3097 (1995).
- [11] D. V. Semikoz and I. I. Tkachev. ‘Condensation of bosons in the kinetic regime’. *Phys. Rev. D* **55**(2), 489–502 (1997).

- [12] M. Holland, J. Williams, and J. Cooper. ‘Bose-Einstein condensation: Kinetic evolution obtained from simulated trajectories’. *Phys. Rev. A* **55**(5), 3670–3677 (1997).
- [13] H.-J. Miesner, D. M. Stamper Kurn, M. R. Andrews, D. S. Durfee, S. Inouye, and W. Ketterle. ‘Bosonic Stimulation in the Formation of a Bose-Einstein Condensate’. *Science* **279**(5353), 1005–1007 (1998).
- [14] M. Köhl, M. J. Davis, C. W. Gardiner, T. W. Hänsch, and T. Esslinger. ‘Growth of Bose-Einstein Condensates from Thermal Vapor’. *Phys. Rev. Lett.* **88**(8), 080402 (2002).
- [15] I. Shvarchuck, C. Buggle, D. S. Petrov, K. Dieckmann, M. Zielonkowski, M. Kemmann, T. G. Tiecke, W. von Klitzing, G. V. Shlyapnikov, and J. T. M. Walraven. ‘Bose-Einstein Condensation into Nonequilibrium States Studied by Condensate Focusing’. *Phys. Rev. Lett.* **89**(27), 270404 (2002).
- [16] M. Hugbart, J. A. Retter, A. F. Varón, P. Bouyer, A. Aspect, and M. J. Davis. ‘Population and phase coherence during the growth of an elongated Bose-Einstein condensate’. *Phys. Rev. A* **75**(1), 011602 (2007).
- [17] M. R. Andrews, C. G. Townsend, H.-J. Miesner, D. S. Durfee, D. M. Kurn, and W. Ketterle. ‘Observation of Interference Between Two Bose Condensates’. *Science* **275**(5300), 637–641 (1997).
- [18] D. E. Miller, J. R. Anglin, J. R. Abo Shaeer, K. Xu, J. K. Chin, and W. Ketterle. ‘High-contrast interference in a thermal cloud of atoms’. *Phys. Rev. A* **71**(4), 043615 (2005).
- [19] R. Hanbury Brown and R. Q. Twiss. ‘A New Type of Interferometer for Use in Radio Astronomy’. *Philos. Mag.* **45**(366), 663–682 (1954).
- [20] R. Hanbury Brown and R. Q. Twiss. ‘Correlation Between Photons in 2 Coherent Beams of Light’. *Nature (London)* **177**(4497), 27–29 (1956).
- [21] R. Hanbury Brown and R. Q. Twiss. ‘Question of Correlation Between Photons in Coherent Light Rays’. *Nature (London)* **178**(4548), 1447–1448 (1956).
- [22] M. Schellekens, R. Hoppeler, A. Perrin, J. V. Gomes, D. Boiron, A. Aspect, and C. I. Westbrook. ‘Hanbury Brown Twiss Effect for Ultracold Quantum Gases’. *Science* **310**(5748), 648–651 (2005).
- [23] T. Jelten, J. M. McNamara, W. Hogervorst, W. Vassen, V. Krachmalnicoff, M. Schellekens, A. Perrin, H. Chang, D. Boiron, A. Aspect, and C. I. Westbrook. ‘Comparison of the Hanbury Brown-Twiss effect for bosons and fermions’. *Nature* **445**(7126), 402–405 (2007).

-
- [24] R. J. Thompson, G. Rempe, and H. J. Kimble. ‘Observation of normal-mode splitting for an atom in an optical cavity’. *Phys. Rev. Lett.* **68**(8), 1132–1135 (1992).
- [25] A. Boca, R. Miller, K. M. Birnbaum, A. D. Boozer, J. McKeever, and H. J. Kimble. ‘Observation of the Vacuum Rabi Spectrum for One Trapped Atom’. *Phys. Rev. Lett.* **93**(23), 233603 (2004).
- [26] H. Mabuchi, Q. A. Turchette, M. S. Chapman, and H. J. Kimble. ‘Real-time detection of individual atoms falling through a high-finesse optical cavity’. *Opt. Lett.* **21**(17), 1393–1395 (1996).
- [27] C. J. Hood, T. W. Lynn, A. C. Doherty, A. S. Parkins, and H. J. Kimble. ‘The Atom-Cavity Microscope: Single Atoms Bound in Orbit by Single Photons’. *Science* **287**(5457), 1447–1453 (2000).
- [28] P. W. H. Pinkse, T. Fischer, P. Maunz, and G. Rempe. ‘Trapping an atom with single photons’. *Nature (London)* **404**(6776), 365–368 (2000).
- [29] P. Maunz, T. Puppe, I. Schuster, N. Syassen, P. W. H. Pinkse, and G. Rempe. ‘Cavity cooling of a single atom’. *Nature (London)* **428**(6978), 50–52 (2004).
- [30] A. Kuhn, M. Hennrich, and G. Rempe. ‘Deterministic Single-Photon Source for Distributed Quantum Networking’. *Phys. Rev. Lett.* **89**(6), 067901 (2002).
- [31] J. McKeever, A. Boca, A. D. Boozer, R. Miller, J. R. Buck, A. Kuzmich, and H. J. Kimble. ‘Deterministic Generation of Single Photons from One Atom Trapped in a Cavity’. *Science* **303**(5666), 1992–1994 (2004).
- [32] T. Campey, C. J. Vale, M. J. Davis, N. R. Heckenberg, H. Rubinsztein Dunlop, S. Kraft, C. Zimmermann, and J. Fortagh. ‘Atom counting in ultracold gases using photoionization and ion detection’. *Phys. Rev. A* **74**(4), 043612 (2006).
- [33] T. Gericke, C. Utfeld, N. Hommerstad, and H. Ott. ‘A Scanning Electron Microscope for Ultracold Atoms’. *Laser Phys. Lett.* **3**(8), 415–419 (2006).
- [34] H. Mabuchi, J. Ye, and H. Kimble. ‘Full observation of single-atom dynamics in cavity QED’. *Appl. Phys. B* **68**(6), 1095–1108 (1999).
- [35] A. Öttl. ‘Correlations and Counting Statistics of an Atom Laser’. Ph.D. thesis, ETH Zürich (2006).
- [36] M. Köhl. ‘Observing correlated quantum matter with atomic gases’. Habilitation, ETH Zürich (2005).

- [37] S. N. Bose. ‘Plancks Gesetz und Lichtquantenhypothese’. *Z. Phys.* **26**(1), 178–181 (1924).
- [38] A. Einstein. ‘Quantentheorie des einatomigen idealen Gases. Zweite Abhandlung.’ *Sitzungsberichte der Preussischen Akademie der Wissenschaften* **1**, 3–14 (1925).
- [39] F. London. ‘The λ -Phenomenon of Liquid Helium and Bose-Einstein Degeneracy’. *Nature (London)* **141**, 643–644 (1938).
- [40] F. London. ‘On the Bose-Einstein condensation’. *Phys. Rev.* **54**, 947 (1938).
- [41] F. Dalfovo, S. Giorgini, L. P. Pitaevskii, and S. Stringari. ‘Theory of Bose-Einstein condensation in trapped gases’. *Rev. Mod. Phys.* **71**(3), 463–512 (1999).
- [42] Y. Castin. *Coherent atomic matter waves*, volume 72, chapter Course 1: Bose-Einstein Condensates in Atomic Gases: Simple Theoretical Results, pp. 1–136 (Springer Berlin, 2001).
- [43] C. J. Pethick and H. Smith. *Bose-Einstein Condensation in Dilute Gases* (Cambridge University Press, 2002).
- [44] L. Pitaevskii and S. Stringari. *Bose-Einstein Condensation* (Oxford University Press, 2003).
- [45] W. Ketterle, D. S. Durfee, and D. M. Stamper Kurn. ‘Making, probing and understanding Bose-Einstein condensates’. In *Bose-Einstein Condensation in Atomic Gases*, edited by M. Inguscio, S. Stringari, and C. Wieman, volume CXL of *Proceedings of the International School of Physics Enrico Fermi*, pp. 67–176 (IOS Press, Amsterdam, 1999).
- [46] A. J. Leggett. ‘Bose-Einstein condensation in the alkali gases: Some fundamental concepts’. *Rev. Mod. Phys.* **73**(2), 307–50 (2001). Erratum: *Rev. Mod. Phys.* **75**, 1083 (2003).
- [47] J. L. Roberts, N. R. Claussen, J. P. Burke, Jr., C. H. Greene, E. A. Cornell, and C. E. Wieman. ‘Resonant Magnetic Field Control of Elastic Scattering in Cold Rb’. *Phys. Rev. Lett.* **81**(23), 5109–5112 (1998).
- [48] E. Gross. ‘Structure of a quantized vortex in boson systems’. *Nuovo Cimento* **20**, 454 (1961).
- [49] L. Pitaevskii. ‘Vortex lines in an imperfect Bose gas’. *Sov. Phys. JETP* **13**, 451 (1961).
- [50] W. Hoston and L. You. ‘Interference of two condensates’. *Phys. Rev. A* **53**(6), 4254 (1996).

-
- [51] J. I. Cirac, C. W. Gardiner, M. Naraschewski, and P. Zoller. ‘Continuous observation of interference fringes from Bose condensates’. *Phys. Rev. A* **54**(5), R3714–R3717 (1996).
- [52] Y. Castin and J. Dalibard. ‘Relative phase of two Bose-Einstein condensates’. *Phys. Rev. A* **55**(6), 4330–4337 (1997).
- [53] E. H. Lieb, R. Seiringer, and J. Yngvason. ‘Bose-Einstein Condensation and Spontaneous Symmetry Breaking’. arXiv:math-ph/0610034 (2006).
- [54] O. Penrose. ‘On the Quantum Mechanics of Helium .2.’ *Philos. Mag.* **52**, 1373–1377 (1951).
- [55] A. Griffin, D. W. Snoke, and E. S. Stringari. *Bose-Einstein Condensation* (Cambridge University Press, 1995).
- [56] M. Naraschewski and R. J. Glauber. ‘Spatial coherence and density correlations of trapped Bose gases’. *Phys. Rev. A* **59**(6), 4595–4607 (1999).
- [57] R. Hanbury Brown and R. Q. Twiss. ‘Interferometry of the Intensity Fluctuations in Light II. An Experimental Test of the Theory for Partially Coherent Light’. *Proc. R. Soc. London, Ser. A* **243**(1234), 291–319 (1958).
- [58] M. Yasuda and F. Shimizu. ‘Observation of Two-Atom Correlation of an Ultracold Neon Atomic Beam’. *Phys. Rev. Lett.* **77**(15), 3090–3093 (1996).
- [59] R. J. Glauber. ‘Quantum Theory of Optical Coherence’. *Phys. Rev.* **130**(6), 2529–2539 (1963).
- [60] D. S. Petrov, G. V. Shlyapnikov, and J. T. M. Walraven. ‘Phase-Fluctuating 3D Bose-Einstein Condensates in Elongated Traps’. *Phys. Rev. Lett.* **87**(5), 050404 (2001).
- [61] S. Dettmer, D. Hellweg, P. Ryytty, J. J. Arlt, W. Ertmer, K. Sengstock, D. S. Petrov, G. V. Shlyapnikov, H. Kreutzmann, L. Santos, and M. Lewenstein. ‘Observation of Phase Fluctuations in Elongated Bose-Einstein Condensates’. *Phys. Rev. Lett.* **87**(16), 160406 (2001).
- [62] D. Hellweg, S. Dettmer, P. Ryytty, J. Arlt, W. Ertmer, K. Sengstock, D. Petrov, G. Shlyapnikov, H. Kreutzmann, L. Santos, and M. Lewenstein. ‘Phase fluctuations in Bose-Einstein condensates’. *Appl. Phys. B* **73**(8), 781–789 (2001).
- [63] H. Kreutzmann, A. Sanpera, L. Santos, M. Lewenstein, D. Hellweg, L. Cacciapuoti, M. Kottke, T. Schulte, K. Sengstock, J. Arlt, and W. Ertmer. ‘Characterization and control of phase fluctuations in elongated Bose-Einstein condensates’. *Applied Physics B: Lasers and Optics* **V76**(2), 165–172 (2003).

- [64] D. Hellweg, L. Cacciapuoti, M. Kottke, T. Schulte, K. Sengstock, W. Ertmer, and J. J. Arlt. ‘Measurement of the Spatial Correlation Function of Phase Fluctuating Bose-Einstein Condensates’. *Phys. Rev. Lett.* **91**(1), 010406 (2003).
- [65] L. Cacciapuoti, D. Hellweg, M. Kottke, T. Schulte, W. Ertmer, J. J. Arlt, K. Sengstock, L. Santos, and M. Lewenstein. ‘Second-order correlation function of a phase fluctuating Bose-Einstein condensate’. *Phys. Rev. A* **68**(5), 053612 (2003).
- [66] H. M. Wiseman. ‘Defining the (atom) laser’. *Phys. Rev. A* **56**(3), 2068–2084 (1997). Erratum: *Phys. Rev. A* 57, 674 (1998).
- [67] J. Fujita, M. Morinaga, T. Kishimoto, M. Yasuda, S. Matsui, and F. Shimizu. ‘Manipulation of an atomic beam by a computer-generated hologram’. *Nature* **380**(6576), 691–694 (1996).
- [68] M. Morinaga, M. Yasuda, T. Kishimoto, F. Shimizu, J.-i. Fujita, and S. Matsui. ‘Holographic Manipulation of a Cold Atomic Beam’. *Phys. Rev. Lett.* **77**(5), 802–805 (1996).
- [69] H. M. Wiseman and M. J. Collett. ‘An atom laser based on dark-state cooling’. *Phys. Lett. A* **202**(4), 246–252 (1995).
- [70] C. J. Bordé. ‘Amplification of atomic fields by stimulated emission of atoms’. *Phys. Lett. A* **204**(3-4), 217–222 (1995).
- [71] R. Spreew, T. Pfau, U. Janicke, and M. Wilkens. ‘Laser-like scheme for atomic-matter waves’. *Europhys. Lett.* **32**(6), 469–474 (1995).
- [72] M. Holland, K. Burnett, C. Gardiner, J. I. Cirac, and P. Zoller. ‘Theory of an atom laser’. *Phys. Rev. A* **54**(3), R1757–R1760 (1996).
- [73] M. Olshanii, Y. Castin, and J. Dalibard. ‘A model for an atom laser’. In *Proceedings of the 12th International Conference on Laser Spectroscopy* (World Scientific, 1995).
- [74] R. Ballagh and C. M. Savage. ‘The Theory of Atom Lasers’. *Mod. Phys. Lett. B* **14**(Suppl. Issue 1), 153–188 (2000).
- [75] M.-O. Mewes, M. R. Andrews, D. M. Kurn, D. S. Durfee, C. G. Townsend, and W. Ketterle. ‘Output Coupler for Bose-Einstein Condensed Atoms’. *Phys. Rev. Lett.* **78**(4), 582–585 (1997).
- [76] B. P. Anderson and M. A. Kasevich. ‘Macroscopic Quantum Interference from Atomic Tunnel Arrays’. *Science* **282**(5394), 1686–1689 (1998).

-
- [77] E. W. Hagley, L. Deng, M. Kozuma, J. Wen, K. Helmerson, S. L. Rolston, and W. D. Phillips. ‘A Well-Collimated Quasi-Continuous Atom Laser’. *Science* **283**(5408), 1706–1709 (1999).
- [78] N. P. Robins, C. Figl, S. A. Haine, A. K. Morrison, M. Jeppesen, J. J. Hope, and J. D. Close. ‘Achieving Peak Brightness in an Atom Laser’. *Phys. Rev. Lett.* **96**(14), 140403 (2006).
- [79] I. Bloch, T. W. Hänsch, and T. Esslinger. ‘Atom Laser with a cw Output Coupler’. *Phys. Rev. Lett.* **82**(15), 3008–3011 (1999).
- [80] G. Cennini, G. Ritt, C. Geckeler, and M. Weitz. ‘All-Optical Realization of an Atom Laser’. *Phys. Rev. Lett.* **91**(24), 240408 (2003).
- [81] A. P. Chikkatur, Y. Shin, A. E. Leanhardt, D. Kielpinski, E. Tsikata, T. L. Gustavson, D. E. Pritchard, and W. Ketterle. ‘A Continuous Source of Bose-Einstein Condensed Atoms’. *Science* **296**(5576), 2193–2195 (2002).
- [82] T. Lahaye, J. M. Vogels, K. J. Günter, Z. Wang, J. Dalibard, and D. Guéry Odelin. ‘Realization of a Magnetically Guided Atomic Beam in the Collisional Regime’. *Phys. Rev. Lett.* **93**(9), 093003– (2004).
- [83] T. Lahaye, Z. Wang, G. Reinaudi, S. P. Rath, J. Dalibard, and D. Guéry Odelin. ‘Evaporative cooling of a guided rubidium atomic beam’. *Phys. Rev. A* **72**(3), 033411 (2005).
- [84] J. Schneider and A. Schenzle. ‘Output from an atom laser: theory vs. experiment’. *Appl. Phys. B* **69**(5– 6), 353–356 (1999).
- [85] J. Schneider and A. Schenzle. ‘Investigations of a two-mode atom-laser model’. *Phys. Rev. A* **61**(5), 053611 (2000).
- [86] T. Kramer, C. Bracher, and M. Kleber. ‘Matter waves from quantum sources in a force field’. *Journal of Physics A: Mathematical and General* **35**(40), 8361–8372 (2002).
- [87] T. Kramer and M. Rodriguez. ‘Quantum theory of an atom laser originating from a Bose-Einstein condensate or a Fermi gas in the presence of gravity’. *Phys. Rev. A* **74**(1), 013611 (2006).
- [88] D. A. Steck. ‘Rubidium 87 D Line Data’ (2003). Revision 1.6, <http://steck.us/alkalidata>.
- [89] G. Breit and I. I. Rabi. ‘Measurement of Nuclear Spin’. *Phys. Rev.* **38**(11), 2082–2083 (1931).

- [90] Y. Le Coq, J. H. Thywissen, S. A. Rangwala, F. Gerbier, S. Richard, G. Delannoy, P. Bouyer, and A. Aspect. ‘Atom Laser Divergence’. *Phys. Rev. Lett.* **87**(17), 170403 (2001).
- [91] J. Dugué, N. P. Robins, C. Figl, M. Jeppesen, P. Summers, J. J. Hope, and J. D. Close. ‘Investigation and comparison of multi-state and two-state atom laser output-couplers’. arXiv:cond-mat/0608449 (2006).
- [92] Y. B. Band, P. S. Julienne, and M. Trippenbach. ‘Radio-frequency output coupling of the Bose-Einstein condensate for atom lasers’. *Phys. Rev. A* **59**(5), 3823–3831 (1999).
- [93] R. Graham and D. F. Walls. ‘Theory of strong outcoupling from Bose-Einstein condensates’. *Phys. Rev. A* **60**(2), 1429–1441 (1999).
- [94] T. Esslinger, I. Bloch, and T. W. Hänsch. ‘Bose-Einstein condensation in a quadrupole-Ioffe-configuration trap’. *Phys. Rev. A* **58**(4), R2664–R2667 (1998).
- [95] H. Steck, M. Naraschewski, and H. Wallis. ‘Output of a Pulsed Atom Laser’. *Phys. Rev. Lett.* **80**(1), 1–5 (1998).
- [96] N. P. Robins, A. K. Morrison, J. J. Hope, and J. D. Close. ‘Limits to the flux of a continuous atom laser’. *Phys. Rev. A* **72**(3), 031606 (2005).
- [97] T. Busch, M. Köhl, T. Esslinger, and K. Mølmer. ‘Transverse mode of an atom laser’. *Phys. Rev. A* **65**(4), 043615 (2002). Erratum: *Phys. Rev. A* **65**, 069902 (2002).
- [98] J.-F. Riou, W. Guerin, Y. L. Coq, M. Fauquembergue, V. Josse, P. Bouyer, and A. Aspect. ‘Beam Quality of a Nonideal Atom Laser’. *Phys. Rev. Lett.* **96**(7), 070404 (2006).
- [99] M. Köhl, T. Busch, K. Mølmer, T. W. Hänsch, and T. Esslinger. ‘Observing the profile of an atom laser beam’. *Phys. Rev. A* **72**(6), 063618 (2005).
- [100] M. Köhl, T. W. Hänsch, and T. Esslinger. ‘Measuring the Temporal Coherence of an Atom Laser Beam’. *Phys. Rev. Lett.* **87**(16), 160404 (2001).
- [101] A. Öttl, S. Ritter, M. Köhl, and T. Esslinger. ‘Correlations and Counting Statistics of an Atom Laser’. *Phys. Rev. Lett.* **95**(9), 090404 (2005).
- [102] H. M. Wiseman and L. K. Thomsen. ‘Reducing the Linewidth of an Atom Laser by Feedback’. *Phys. Rev. Lett.* **86**(7), 1143–1147 (2001).

-
- [103] S. A. Haine, A. J. Ferris, J. D. Close, and J. J. Hope. ‘Control of an atom laser using feedback’. *Phys. Rev. A* **69**(1), 013605 (2004). Erratum: *Phys. Rev. A* **70**, 039902 (2004).
- [104] I. Bloch, T. W. Hänsch, and T. Esslinger. ‘Measurement of the spatial coherence of a trapped Bose gas at the phasetransition’. *Nature (London)* **403**(6766), 166–170 (2000).
- [105] H. J. Kimble. ‘Structure and Dynamics in Cavity Quantum Electrodynamics’. In *Cavity Quantum Electrodynamics*, edited by P. Berman, number Supplement 2 in Advances in Atomic, Molecular and Optical Physics, pp. 203–266 (Academic Press Inc., 1993).
- [106] H. J. Kimble. ‘Strong interactions of single atoms and photons in cavity QED’. *Physica Scripta* **T76**, 127–137 (1998).
- [107] J. M. Raimond, M. Brune, and S. Haroche. ‘Colloquium: Manipulating quantum entanglement with atoms and photons in a cavity’. *Rev. Mod. Phys.* **73**(3), 565–18 (2001).
- [108] H. Mabuchi and A. C. Doherty. ‘Cavity Quantum Electrodynamics: Coherence in Context’. *Science* **298**(5597), 1372–1377 (2002).
- [109] O. Svelto and D. C. Hanna. *Principles of Lasers* (Plenum Press, 1998), 4th edition.
- [110] A. E. Siegman. *Lasers* (University Science Books, 1986).
- [111] H. Kogelnik and T. Li. ‘Laser beams and resonators’. *Appl. Opt.* **5**(10), 1550–1567 (1966).
- [112] E. Jaynes and F. Cummings. ‘Comparison of quantum and semiclassical radiation theories with application to the beam maser’. *Proc. IEEE* **51**(1), 89–109 (1963).
- [113] B. W. Shore and P. L. Knight. ‘The Jaynes-Cummings Model’. *J. Mod. Optics* **40**(7), 1195–1238 (1993).
- [114] P. Meystre and M. Sargent III. *Elements of Quantum Optics*, chapter 18, pp. 377–390 (Springer, 1998).
- [115] W. Vogel and D.-G. Welsch. *Quantum Optics* (Wiley-VCH, 2006).
- [116] C. W. Gardiner and P. Zoller. *Quantum Noise* (Springer, 1991).
- [117] P. Horak, G. Hechenblaikner, K. M. Gheri, H. Stecher, and H. Ritsch. ‘Cavity-Induced Atom Cooling in the Strong Coupling Regime’. *Phys. Rev. Lett.* **79**(25), 4974–4977 (1997).

- [118] G. Hechenblaikner, M. Gangl, P. Horak, and H. Ritsch. ‘Cooling an atom in a weakly driven high-Q cavity’. *Phys. Rev. A* **58**(4), 3030 (1998).
- [119] K. Mølmer, Y. Castin, and J. Dalibard. ‘Monte Carlo wave-function method in quantum optics’. *J. Opt. Soc. Am. B* **10**, 524 (1993).
- [120] G. Puebla Hellmann. ‘Dissipation Effects in a High-Finesse Cavity’. Semesterarbeit, ETH Zürich (2005).
- [121] C. J. Hood, M. S. Chapman, T. W. Lynn, and H. J. Kimble. ‘Real-Time Cavity QED with Single Atoms’. *Phys. Rev. Lett.* **80**(19), 4157–4160 (1998).
- [122] Christina J. Hood. ‘Real-Time Measurement and trapping of Single Atoms by Single Photons’. Ph.D. thesis, California Institute of Technology (2000).
- [123] P. Münstermann, T. Fischer, P. Pinkse, and G. Rempe. ‘Single slow atoms from an atomic fountain observed in a high-finesse optical cavity’. *Opt. Commun.* **159**, 63–67 (1999).
- [124] N. Schlosser, G. Reymond, I. Protsenko, and P. Grangier. ‘Sub-poissonian loading of single atoms in a microscopic dipole trap’. *Nature* **411**(6841), 1024–1027 (2001).
- [125] S. Kuhr, W. Alt, D. Schrader, M. Müller, V. Gomer, and D. Meschede. ‘Deterministic Delivery of a Single Atom’. *Science* **293**(5528), 278–280 (2001).
- [126] T. Bondo, M. Hennrich, T. Legero, G. Rempe, and A. Kuhn. ‘Time-resolved and state-selective detection of single freely falling atoms’. *Optics Communications* **264**(2), 271–277 (2006).
- [127] A. Robert, O. Sirjean, A. Browaeys, J. Poupard, S. Nowak, D. Boiron, C. I. Westbrook, and A. Aspect. ‘A Bose-Einstein Condensate of Metastable Atoms’. *Science* **292**(5516), 461–464 (2001).
- [128] P. Pinkse, T. Fischer, P. Maunz, T. Puppe, and G. Rempe. ‘How to catch an atom with single photons’. *J. Mod. Optics* **47**(14-15), 2769–2787 (2000).
- [129] L. A. Lugiato. ‘Theory of optical bistability’. In *Progress in optics. Volume 21. Amsterdam, North-Holland Physics Publishing*, pp. 69–216 (1984).
- [130] A. T. Rosenberger, L. A. Orozco, H. J. Kimble, and P. D. Drummond. ‘Absorptive optical bistability in two-state atoms’. *Phys. Rev. A* **43**(11), 6284 (1991).
- [131] G. Rempe, R. J. Thompson, R. J. Brecha, W. D. Lee, and H. J. Kimble. ‘Optical bistability and photon statistics in cavity quantum electrodynamics’. *Phys. Rev. Lett.* **67**(13), 1727–1730 (1991).

-
- [132] J. A. Sauer, K. M. Fortier, M. S. Chang, C. D. Hamley, and M. S. Chapman. ‘Cavity QED with optically transported atoms’. *Phys. Rev. A* **69**(5), 051804–4 (2004).
- [133] C. Savage and H. Carmichael. ‘Single atom optical bistability’. *IEEE J. Quantum Electron.* **24**(8), 1495–1498 (1988).
- [134] P. Münstermann, T. Fischer, P. Maunz, P. W. H. Pinkse, and G. Rempe. ‘Dynamics of Single-Atom Motion Observed in a High-Finesse Cavity’. *Phys. Rev. Lett.* **82**(19), 3791–3794 (1999).
- [135] P. Münstermann, T. Fischer, P. Maunz, P. W. H. Pinkse, and G. Rempe. ‘Observation of Cavity-Mediated Long-Range Light Forces between Strongly Coupled Atoms’. *Phys. Rev. Lett.* **84**(18), 4068 (2000).
- [136] C. Salomon, J. Dalibard, A. Aspect, H. Metcalf, and C. Cohen Tannoudji. ‘Channeling atoms in a laser standing wave’. *Phys. Rev. Lett.* **59**(15), 1659–1662 (1987).
- [137] T. Fischer, P. Maunz, T. Puppe, P. W. H. Pinkse, and G. Rempe. ‘Collective light forces on atoms in a high-finesse cavity’. *New J. Phys.* **3**, 11–11 (2001).
- [138] P. Horak, H. Ritsch, T. Fischer, P. Maunz, T. Puppe, P. W. H. Pinkse, and G. Rempe. ‘Optical Kaleidoscope Using a Single Atom’. *Phys. Rev. Lett.* **88**(4), 043601 (2002).
- [139] Peter Münstermann. ‘Dynamik einzelner Atome in einem optischen Resonator höchster Finesse’. Ph.D. thesis, Universität Konstanz (1999).
- [140] Peter L. W. Maunz. ‘Cavity cooling and spectroscopy of a bound atom-cavity system’. Ph.D. thesis, Technische Universität München (2005).
- [141] S. J. van Enk, J. McKeever, H. J. Kimble, and J. Ye. ‘Cooling of a single atom in an optical trap inside a resonator’. *Phys. Rev. A* **64**(1), 013407 (2001).
- [142] J. Ye, D. W. Vernooy, and H. J. Kimble. ‘Trapping of Single Atoms in Cavity QED’. *Phys. Rev. Lett.* **83**(24), 4987–4990 (1999).
- [143] H. W. Chan, A. T. Black, and V. Vuletić. ‘Observation of Collective-Emission-Induced Cooling of Atoms in an Optical Cavity’. *Phys. Rev. Lett.* **90**(6), 063003 (2003).
- [144] B. Nagorny, Th. Elsasser, and A. Hemmerich. ‘Collective Atomic Motion in an Optical Lattice Formed Inside a High Finesse Cavity’. *Phys. Rev. Lett.* **91**(15), 153003 (2003).

- [145] D. Kruse, C. von Cube, C. Zimmermann, and P. W. Courteille. ‘Observation of Lasing Mediated by Collective Atomic Recoil’. *Phys. Rev. Lett.* **91**(18), 183601 (2003).
- [146] J. McKeever, J. R. Buck, A. D. Boozer, A. Kuzmich, H.-C. Nagerl, D. M. Stamper Kurn, and H. J. Kimble. ‘State-Insensitive Cooling and Trapping of Single Atoms in an Optical Cavity’. *Phys. Rev. Lett.* **90**(13), 133602 (2003).
- [147] S. Nußmann, K. Murr, M. Hijkema, B. Weber, A. Kuhn, and G. Rempe. ‘Vacuum-stimulated cooling of single atoms in three dimensions’. *Nat. Phys.* **1**(2), 122–125 (2005).
- [148] A. D. Boozer, A. Boca, R. Miller, T. E. Northup, and H. J. Kimble. ‘Cooling to the Ground State of Axial Motion for One Atom Strongly Coupled to an Optical Cavity’. *Phys. Rev. Lett.* **97**(8), 083602 (2006).
- [149] I. Teper, Y.-J. Lin, and V. Vuletic. ‘Resonator-Aided Single-Atom Detection on a Microfabricated Chip’. *Phys. Rev. Lett.* **97**(2), 023002 (2006).
- [150] T. Steinmetz, Y. Colombe, D. Hunger, T. W. Hansch, A. Balocchi, R. J. Warburton, and J. Reichel. ‘Stable fiber-based Fabry-Pérot cavity’. *Appl. Phys. Lett.* **89**(11), 111110 (2006).
- [151] P. Horak, B. G. Klappauf, A. Haase, R. Folman, J. Schmiedmayer, P. Domokos, and E. A. Hinds. ‘Possibility of single-atom detection on a chip’. *Phys. Rev. A* **67**(4), 043806 (2003).
- [152] S. Eriksson, M. Trupke, H. Powell, D. Sahagun, C. Sinclair, E. Curtis, B. Sauer, E. Hinds, Z. Moktadir, C. Gollasch, and M. Kraft. ‘Integrated optical components on atom chips’. *Eur. Phys. J. D* **35**, 135–139 (2005).
- [153] S. Ritter, A. Öttl, T. Donner, T. Bourdel, M. Köhl, and T. Esslinger. ‘Observing the Formation of Long-Range Order during Bose-Einstein Condensation’. *Phys. Rev. Lett.* **98**(9), 090402 (2007).
- [154] T. Donner, S. Ritter, T. Bourdel, A. Öttl, M. Köhl, and T. Esslinger. ‘Critical Behavior of a Trapped Interacting Bose Gas’. *Science* **315**(5818), 1556–1558 (2007).
- [155] M. Greiner, I. Bloch, T. W. Hänsch, and T. Esslinger. ‘Magnetic transport of trapped cold atoms over a large distance’. *Phys. Rev. A* **63**(3), 031401 (2001).
- [156] H. J. Lewandowski, D. M. Harber, D. L. Whitaker, and E. A. Cornell. ‘Simplified System for Creating a Bose-Einstein Condensate’. *J. Low Temp. Phys.* **132**(5 - 6), 309–367 (2003).

-
- [157] A. Öttl, S. Ritter, M. Köhl, and T. Esslinger. ‘Hybrid apparatus for Bose-Einstein condensation and cavity quantum electrodynamics: Single atom detection in quantum degenerate gases’. *Rev. Sci. Instrum.* **77**, 063118 (2006).
- [158] C. Wieman, G. Flowers, and S. Gilbert. ‘Inexpensive laser cooling and trapping experiment for undergraduate laboratories’. *Am. J. Phys.* **63**(4), 317–330 (1995).
- [159] J. Fortágh, A. Grossmann, T. W. Hänsch, and C. Zimmermann. ‘Fast loading of a magneto-optical trap from a pulsed thermal source’. *J. Appl. Phys.* **84**(12), 6499–6501 (1998).
- [160] S. Turner (editor). *CERN Accelerator School: Vacuum Technology*, 99-05 (CERN, Genève, 1999).
- [161] J. M. Laurent and G. Losch. ‘Bake-out Procedure for Lab Work’. Technical report, CERN (1997). Private communication.
- [162] T. Bergeman, G. Erez, and H. J. Metcalf. ‘Magnetostatic trapping fields for neutral atoms’. *Phys. Rev. A* **35**(4), 1535–1546 (1987).
- [163] E. Baum and J. Bork. ‘Systematic design of magnetic shields’. *J. Magn. Magn. Mater.* **101**(1-3), 69–74 (1991).
- [164] A. Marte, T. Volz, J. Schuster, S. Durr, G. Rempe, E. G. M. van Kempen, and B. J. Verhaar. ‘Feshbach Resonances in Rubidium 87: Precision Measurement and Analysis’. *Phys. Rev. Lett.* **89**(28), 283202 (2002).
- [165] C. M. Harris and A. G. Piersol (editors). *Shock and Vibration Handbook* (McGraw-Hill, 2002), 5th edition.
- [166] C. Gerber, G. Binnig, H. Fuchs, O. Marti, and H. Rohrer. ‘Scanning tunneling microscope combined with a scanning electron microscope’. *Rev. Sci. Instrum.* **57**(2), 221–224 (1986).
- [167] M. Okano, K. Kajimura, S. Wakiyama, F. Sakai, W. Mizutani, and M. Ono. ‘Vibration isolation for scanning tunneling microscopy’. *J. Vac. Sci. Technol. A* **5**(6), 3313–3320 (1987).
- [168] A. I. Oliva, Victor Sosa, R. de Coss, Raquel Sosa, N. Lopez Salazar, and J. L. Pena. ‘Vibration isolation analysis for a scanning tunneling microscope’. *Rev. Sci. Instrum.* **63**(6), 3326–3329 (1992).
- [169] A. I. Oliva, M. Aguilar, and Víctor Sosa. ‘Low- and high-frequency vibration isolation for scanning probe microscopy’. *Meas. Sci. Technol.* **9**(3), 383–390 (1998).

- [170] L. Ricci, M. Weidemüller, T. Esslinger, A. Hemmerich, C. Zimmermann, V. Vuletic, W. König, and T. W. Hänsch. ‘A compact grating-stabilized diode laser system for atomic physics’. *Opt. Commun.* **117**(5-6), 541–549 (1995).
- [171] U. Schünemann, H. Engler, R. Grimm, M. Weidemüller, and M. Zielonkowski. ‘Simple scheme for tunable frequency offset locking of two lasers’. *Rev. Sci. Instrum.* **70**(1), 242–243 (1999).
- [172] G. C. Bjorklund, M. D. Levenson, W. Lenth, and C. Ortiz. ‘Frequency modulation (FM) spectroscopy’. *Appl. Phys. B* **32**(3), 145–152 (1983).
- [173] W. Wohlleben, F. Chevy, K. Madison, and J. Dalibard. ‘An atom faucet’. *Eur. Phys. J. D* **15**, 237–244 (2001).
- [174] K. Lindquist, M. Stephens, and C. Wieman. ‘Experimental and theoretical study of the vapor-cell Zeeman optical trap’. *Phys. Rev. A* **46**(7), 4082 (1992).
- [175] K. E. Gibble, S. Kasapi, and Chu. S. ‘Improved magneto-optic trapping in a vapor cell’. *Opt. Lett.* **17**, 526 (1992).
- [176] H. Metcalf and P. van der Straten. ‘Laser cooling and trapping of atoms’. *J. Opt. Soc. Am. B* **20**(5), 887–908 (2003).
- [177] C. J. Lee. ‘Quantum-mechanical analysis of atom lithography’. *Phys. Rev. A* **61**(6), 063604 (2000).
- [178] V. I. Balykin and V. S. Letokhov. ‘The possibility of deep laser focusing of an atomic beam into the A-region’. *Opt. Commun.* **64**(2), 151–156 (1987).
- [179] R. B. Doak, R. E. Grisenti, S. Rehbein, G. Schmahl, J. P. Toennies, and C. Woll. ‘Towards Realization of an Atomic de Broglie Microscope: Helium Atom Focusing Using Fresnel Zone Plates’. *Phys. Rev. Lett.* **83**(21), 4229–4232 (1999).
- [180] R. W. P. Drever, J. L. Hall, F. V. Kowalski, J. Hough, G. M. Ford, A. J. Munley, and H. Ward. ‘Laser phase and frequency stabilization using an optical resonator’. *Appl. Phys. B* **31**(2), 97–105 (1983).
- [181] Eric D. Black. ‘An introduction to Pound–Drever–Hall laser frequency stabilization’. *Am. J. Phys.* **69**(1), 79–87 (2001).
- [182] M. Prevedelli, T. Freegarde, and T. W. Hänsch. ‘Phase Locking of Grating-Tuned Diode Lasers’. *Appl. Phys. B* **60**, S241–S248 (1995).
- [183] J. F. Kelly and A. Gallagher. ‘Efficient electro-optic modulator for optical pumping of Na beams’. *Rev. Sci. Instrum.* **58**(4), 563–566 (1987).

-
- [184] P. Bohlouli Zanjani, K. Afrousheh, and J. D. D. Martin. ‘Optical transfer cavity stabilization using current-modulated injection-locked diode lasers’. *Rev. Sci. Instrum.* **77**(9), 093105 (2006).
- [185] <http://emtoolbox.nist.gov/Wavelength/ciddor.asp>.
- [186] C. J. Hood, H. J. Kimble, and J. Ye. ‘Characterization of high-finesse mirrors: Loss, phase shifts, and mode structure in an optical cavity’. *Phys. Rev. A* **64**(3), 033804 (2001).
- [187] T. Bourdel, T. Donner, S. Ritter, A. Öttl, M. Köhl, and T. Esslinger. ‘Cavity QED detection of interfering matter waves’. *Phys. Rev. A* **73**(4), 043602 (2006).
- [188] A. Spinelli, L. M. Davis, and H. Dautet. ‘Actively quenched single-photon avalanche diode for high repetition rate time-gated photon counting’. *Rev. Sci. Instrum.* **67**(1), 55–61 (1996).
- [189] A. Czitrovszky, A. Sergienko, P. Jani, and A. Nagy. ‘Measurement of quantum efficiency using correlated photon pairs and a single-detector technique’. *Metrologia* **37**(5), 617–620 (2000).
- [190] M. Ware and A. Migdall. ‘Single-photon detector characterization using correlated photons: the march from feasibility to metrology’. *Journal of Modern Optics* **51**(9–10), 1549–1557 (2004).
- [191] M. Lindenthal and J. Kofler. ‘Measuring the absolute photodetection efficiency using photon number correlations’. *Appl. Opt.* **45**(24), 6059–6064 (2006).
- [192] A. C. Doherty, A. S. Parkins, S. M. Tan, and D. F. Walls. ‘Motion of a two-level atom in an optical cavity’. *Phys. Rev. A* **56**(1), 833 (1997).
- [193] A. C. Doherty, A. S. Parkins, S. M. Tan, and D. F. Walls. ‘Motional states of atoms in cavity QED’. *Phys. Rev. A* **57**(6), 4804 (1998).
- [194] D. A. Gedcke. ‘How Counting Statistics Controls Detection Limits and Peak Precision’. Application Note AN59, Ortec, Oak Ridge, TN, USA (2005).
- [195] J. McKeever, J. R. Buck, A. D. Boozer, and H. J. Kimble. ‘Determination of the Number of Atoms Trapped in an Optical Cavity’. *Phys. Rev. Lett.* **93**(14), 143601 (2004).
- [196] S. Seidelin, J. Viana Gomes, R. Hoppeler, O. Sirjean, D. Boiron, A. Aspect, and C. I. Westbrook. ‘Getting the Elastic Scattering Length by Observing Inelastic Collisions in Ultracold Metastable Helium Atoms’. *Phys. Rev. Lett.* **93**(9), 090409 (2004).

- [197] A. S. Tychkov, T. Jelten, J. M. McNamara, P. J. J. Tol, N. Herschbach, W. Hogervorst, and W. Vassen. ‘Metastable helium Bose-Einstein condensate with a large number of atoms’. *Phys. Rev. A* **73**(3), 031603 (2006).
- [198] D. S. Jin, J. R. Ensher, M. R. Matthews, C. E. Wieman, and E. A. Cornell. ‘Collective Excitations of a Bose-Einstein Condensate in a Dilute Gas’. *Phys. Rev. Lett.* **77**(3), 420 (1996).
- [199] M. Edwards, P. A. Ruprecht, K. Burnett, R. J. Dodd, and C. W. Clark. ‘Collective Excitations of Atomic Bose-Einstein Condensates’. *Phys. Rev. Lett.* **77**(9), 1671 (1996).
- [200] S. Stringari. ‘Collective Excitations of a Trapped Bose-Condensed Gas’. *Phys. Rev. Lett.* **77**(12), 2360–2363 (1996).
- [201] S. Jochim, M. Bartenstein, A. Altmeyer, G. Hendl, S. Riedl, C. Chin, J. Hecker Denschlag, and R. Grimm. ‘Bose-Einstein Condensation of Molecules’. *Science* **302**(5653), 2101–2103 (2003).
- [202] T. Stöferle, H. Moritz, C. Schori, M. Köhl, and T. Esslinger. ‘Transition from a Strongly Interacting 1D Superfluid to a Mott Insulator’. *Phys. Rev. Lett.* **92**(13), 130403 (2004).
- [203] M. Bartenstein, A. Altmeyer, S. Riedl, S. Jochim, C. Chin, J. H. Denschlag, and R. Grimm. ‘Collective Excitations of a Degenerate Gas at the BEC-BCS Crossover’. *Phys. Rev. Lett.* **92**(20), 203201 (2004).
- [204] Y. M. Kagan, B. V. Svistunov, and G. V. Shlyapnikov. ‘Kinetics of Bose condensation in an interacting Bose gas’. *Sov. Phys. JETP* **75**(2), 387–393 (1992). Erratum for *Sov. Physics JETP* 74, 279 (1992).
- [205] B. Svistunov. ‘Strongly non-equilibrium Bose-Einstein condensation in a trapped gas’. *Phys. Lett. A* **287**(1–2), 169–174 (2001).
- [206] P. D. Drummond and J. F. Corney. ‘Quantum dynamics of evaporatively cooled Bose-Einstein condensates’. *Phys. Rev. A* **60**(4), R2661–R2664 (1999).
- [207] D. Jaksch, C. W. Gardiner, and P. Zoller. ‘Quantum kinetic theory. II. Simulation of the quantum Boltzmann master equation’. *Phys. Rev. A* **56**(1), 575–586 (1997).
- [208] M. J. Bijlsma, E. Zaremba, and H. T. C. Stoof. ‘Condensate growth in trapped Bose gases’. *Phys. Rev. A* **62**(6), 063609 (2000).
- [209] H. T. C. Stoof. ‘Coherent Versus Incoherent Dynamics During Bose-Einstein Condensation in Atomic Gases’. *J. Low Temp. Phys.* **114**(1–2), 11–108 (1999).

-
- [210] N. G. Berloff and B. V. Svistunov. ‘Scenario of strongly nonequilibrated Bose-Einstein condensation’. *Phys. Rev. A* **66**(1), 013603 (2002).
- [211] H. T. C. Stoof. ‘Initial Stages of Bose-Einstein Condensation’. *Phys. Rev. Lett.* **78**(5), 768–771 (1997).
- [212] S. Khlebnikov. ‘Strong acoustic turbulence and the speed of Bose-Einstein condensation’. *Phys. Rev. A* **66**(6), 063606 (2002).
- [213] R. Lacaze, P. Lallemand, Y. Pomeau, and S. Rica. ‘Dynamical formation of a Bose-Einstein condensate’. *Physica D* **152–153**, 779–786 (2001).
- [214] C. W. Gardiner and P. Zoller. ‘Quantum kinetic theory: A quantum kinetic master equation for condensation of a weakly interacting Bose gas without a trapping potential’. *Phys. Rev. A* **55**(4), 2902 (1997).
- [215] C. W. Gardiner and P. Zoller. ‘Quantum kinetic theory. III. Quantum kinetic master equation for strongly condensed trapped systems’. *Phys. Rev. A* **58**(1), 536 (1998).
- [216] H. Wu, E. Arimondo, and C. J. Foot. ‘Dynamics of evaporative cooling for Bose-Einstein condensation’. *Phys. Rev. A* **56**(1), 560–569 (1997).
- [217] C. W. Gardiner, M. D. Lee, R. J. Ballagh, M. J. Davis, and P. Zoller. ‘Quantum Kinetic Theory of Condensate Growth: Comparison of Experiment and Theory’. *Phys. Rev. Lett.* **81**(24), 5266–5269 (1998).
- [218] M. D. Lee and C. W. Gardiner. ‘Quantum kinetic theory. VI. The growth of a Bose-Einstein condensate’. *Phys. Rev. A* **62**(3), 033606 (2000).
- [219] M. J. Davis, C. W. Gardiner, and R. J. Ballagh. ‘Quantum kinetic theory. VII. The influence of vapor dynamics on condensate growth’. *Phys. Rev. A* **62**(6), 063608 (2000).
- [220] J. Stenger, S. Inouye, A. P. Chikkatur, D. M. Stamper Kurn, D. E. Pritchard, and W. Ketterle. ‘Bragg Spectroscopy of a Bose-Einstein Condensate’. *Phys. Rev. Lett.* **82**(23), 4569–4573 (1999). Erratum: *Phys. Rev. Lett.* **84**, 2283(E) (2000).
- [221] E. W. Hagley, L. Deng, M. Kozuma, M. Trippenbach, Y. B. Band, M. Edwards, M. Doery, P. S. Julienne, K. Helmerson, S. L. Rolston, and W. D. Phillips. ‘Measurement of the Coherence of a Bose-Einstein Condensate’. *Phys. Rev. Lett.* **83**(16), 3112–3115 (1999).
- [222] S. Richard, F. Gerbier, J. H. Thywissen, M. Hugbart, P. Bouyer, and A. Aspect. ‘Momentum Spectroscopy of 1D Phase Fluctuations in Bose-Einstein Condensates’. *Phys. Rev. Lett.* **91**(1), 010405 (2003).

- [223] W. Ketterle and H.-J. Miesner. ‘Coherence properties of Bose-Einstein condensates and atom lasers’. *Phys. Rev. A* **56**(4), 3291–3293 (1997).
- [224] E. A. Burt, R. W. Ghrist, C. J. Myatt, M. J. Holland, E. A. Cornell, and C. E. Wieman. ‘Coherence, Correlations, and Collisions: What One Learns about Bose-Einstein Condensates from Their Decay’. *Phys. Rev. Lett.* **79**(3), 337–340 (1997).
- [225] M. J. Davis and C. W. Gardiner. ‘Growth of a Bose-Einstein condensate: a detailed comparison of theory and experiment’. *J. Phys. B* **35**(3), 733–742 (2002).
- [226] Y. Kagan and B. V. Svistunov. ‘Evolution of Correlation Properties and Appearance of Broken Symmetry in the Process of Bose-Einstein Condensation’. *Phys. Rev. Lett.* **79**(18), 3331–3334 (1997). Erratum: *Phys. Rev. Lett.* **80**, 892 (1998).
- [227] O. Zobay and B. M. Garraway. ‘Two-Dimensional Atom Trapping in Field-Induced Adiabatic Potentials’. *Phys. Rev. Lett.* **86**(7), 1195 (2001).
- [228] F. Gerbier, J. H. Thywissen, S. Richard, M. Hugbart, P. Bouyer, and A. Aspect. ‘Momentum distribution and correlation function of quasicondensates in elongated traps’. *Phys. Rev. A* **67**(5), 051602 (2003).
- [229] M. Köhl, A. Öttl, S. Ritter, T. Donner, T. Bourdel, and T. Esslinger. ‘Time interval distributions of atoms in atomic beams’. *Applied Physics B: Lasers and Optics* **86**(3), 391–393 (2007).
- [230] G. Baym. ‘The physics of Hanbury Brown-Twiss intensity interferometry: From stars to nuclear collisions’. *Acta Phys. Pol. B* **29**(7), 1839–1884 (1998).
- [231] R. Hanbury Brown and R. Q. Twiss. ‘Test of a New Type of Stellar Interferometer on Sirius’. *Nature (London)* **178**(4541), 1046–1048 (1956).
- [232] G. Goldhaber, S. Goldhaber, W. Lee, and A. Pais. ‘Influence of Bose-Einstein Statistics on the Antiproton-Proton Annihilation Process’. *Phys. Rev.* **120**(1), 300–312 (1960).
- [233] M. Henny, S. Oberholzer, C. Strunk, T. Heinzl, K. Ensslin, M. Holland, and C. Schönberger. ‘The Fermionic Hanbury Brown and Twiss Experiment’. *Science* **284**(5412), 296–298 (1999).
- [234] W. D. Oliver, J. Kim, R. C. Liu, and Y. Yamamoto. ‘Hanbury Brown and Twiss-Type Experiment with Electrons’. *Science* **284**(5412), 299–301 (1999).
- [235] F. T. Arecchi. ‘Measurement of the Statistical Distribution of Gaussian and Laser Sources’. *Phys. Rev. Lett.* **15**(24), 912–916 (1965).

-
- [236] B. L. Morgan and L. Mandel. ‘Measurement of Photon Bunching in a Thermal Light Beam’. *Phys. Rev. Lett.* **16**(22), 1012–1015 (1966).
- [237] D. T. Phillips, H. Kleiman, and S. P. Davis. ‘Intensity-Correlation Linewidth Measurement’. *Phys. Rev.* **153**, 113–115 (1967).
- [238] H. J. Kimble, M. Dagenais, and L. Mandel. ‘Photon antibunching in resonance fluorescence’. *Phys. Rev. Lett.* **39**(11), 691–695 (1977).
- [239] Daniel Kleppner. ‘A Beginner’s Guide to the Atom Laser’. *Phys. Today* **50**(8), 11–13 (1997).
- [240] R. J. Glauber. ‘Optical Coherence and Photon Statistics’. In *Quantum Optics and Electronics*, edited by V. DeWitt, A. Blandin, and C. Cohen Tannoudji, Lectures at Les Houches 1964, pp. 63–185 (Gordon and Breach, New York, 1965).
- [241] S. Fölling, F. Gerbier, A. Widera, O. Mandel, T. Gericke, and I. Bloch. ‘Spatial quantum noise interferometry in expanding ultracold atom clouds’. *Nature (London)* **434**(7032), 481–484 (2005).
- [242] M. Greiner, C. A. Regal, J. T. Stewart, and D. S. Jin. ‘Probing Pair-Correlated Fermionic Atoms through Correlations in Atom Shot Noise’. *Phys. Rev. Lett.* **94**(11), 110401 (2005).
- [243] L. S. Levitov, H. Lee, and G. B. Lesovik. ‘Electron counting statistics and coherent states of electric current’. *J. Math. Phys.* **37**(10), 4845–4866 (1996).
- [244] W. Belzig, C. Schroll, and C. Bruder. ‘Density correlations in ultracold atomic Fermi gases’. In *AIP Conf. Proc.*, volume 780, pp. 817–820 (AIP, Salamanca, Spain, 2005).
- [245] B. Reulet, J. Senzier, and D. E. Prober. ‘Environmental Effects in the Third Moment of Voltage Fluctuations in a Tunnel Junction’. *Phys. Rev. Lett.* **91**(19), 196601 (2003).
- [246] L. Mandel and E. Wolf. ‘Coherence Properties of Optical Fields’. *Rev. Mod. Phys.* **37**(2), 231–287 (1965).
- [247] S. Choi, Y. Japha, and K. Burnett. ‘Adiabatic output coupling of a Bose gas at finite temperatures’. *Phys. Rev. A* **61**(6), 063606 (2000).
- [248] F. Gerbier, P. Bouyer, and A. Aspect. ‘Quasicontinuous atom laser in the presence of gravity’. *Phys. Rev. Lett.* **86**(21), 4729–4732 (2001). Erratum: *Phys. Rev. Lett.* **93**, 059905(E) (2003).

- [249] F. T. Arecchi, E. Gatti, and A. Sona. ‘Time distribution of photons from coherent and Gaussian sources’. *Phys. Lett.* **20**(1), 27–29 (1966).
- [250] R. J. Glauber. ‘Photon Statistics’. In *Laser Handbook*, edited by F. T. Arecchi and E. O. Schulz Dubois, volume I, chapter A1, pp. 1–43 (North-Holland, 1972).
- [251] L. de Broglie. ‘Waves and Quanta’. *Nature* **112**, 540 (1923).
- [252] C. Jönsson. ‘Elektroneninterferenzen an mehreren künstlich hergestellten Feinspalten’. *Z. Phys.* **161**(4), 454–474 (1961).
- [253] A. Tonomura, J. Endo, T. Matsuda, T. Kawasaki, and H. Ezawa. ‘Demonstration of single-electron buildup of an interference pattern’. *Am. J. Phys.* **57**(2), 117–120 (1989).
- [254] A. Zeilinger, R. Gähler, C. G. Shull, W. Treimer, and W. Mampe. ‘Single- and double-slit diffraction of neutrons’. *Rev. Mod. Phys.* **60**(4), 1067–1073 (1988).
- [255] O. Carnal and J. Mlynek. ‘Young’s double-slit experiment with atoms: A simple atom interferometer’. *Phys. Rev. Lett.* **66**(21), 2689–2692 (1991).
- [256] D. W. Keith, C. R. Ekstrom, Q. A. Turchette, and D. E. Pritchard. ‘An interferometer for atoms’. *Phys. Rev. Lett.* **66**(21), 2693–2696 (1991).
- [257] F. Shimizu, K. Shimizu, and H. Takuma. ‘Double-slit interference with ultracold metastable neon atoms’. *Phys. Rev. A* **46**(1), R17–R20 (1992).
- [258] M. Arndt, O. Nairz, J. Vos Andreae, C. Keller, G. van der Zouw, and A. Zeilinger. ‘Wave-particle duality of C60 molecules’. *Nature* **401**(6754), 680–682 (1999).
- [259] Z. Hu and H. J. Kimble. ‘Observation of a Single-Atom in a Magneto-optical Trap’. *Opt. Lett.* **19**(22), 1888–1890 (1994).
- [260] J. L. Wiza. ‘Microchannel plate detectors’. *Nucl. Instrum. Methods* **162**(1–3), 587–601 (1979).
- [261] A. M. Herkommer, H. J. Carmichael, and W. P. Schleich. ‘Localization of an atom by homodyne measurement’. *Quantum Semiclass. Opt.* **8**(1), 189–203 (1996).
- [262] P. Bouyer and M. A. Kasevich. ‘Heisenberg-limited spectroscopy with degenerate Bose-Einstein gases’. *Phys. Rev. A* **56**(2), R1083–R1086 (1997).
- [263] Jean Dalibard, Yvan Castin, and Klaus Mølmer. ‘Wave-function approach to dissipative processes in quantum optics’. *Phys. Rev. Lett.* **68**(5), 580–583 (1992).
- [264] H. J. Carmichael. *An Open Systems Approach to Quantum Optics*. Lecture Notes in Physics, New Series M (Springer, Berlin, 1993).

-
- [265] P. Horak, S. M. Barnett, and H. Ritsch. ‘Coherent dynamics of Bose-Einstein condensates in high-finesse optical cavities’. *Phys. Rev. A* **61**(3), 033609 (2000).
- [266] M. Saba, T. A. Pasquini, C. Sanner, Y. Shin, W. Ketterle, and D. E. Pritchard. ‘Light Scattering to Determine the Relative Phase of Two Bose-Einstein Condensates’. *Science* **307**(5717), 1945–1948 (2005).
- [267] M. Albiez, R. Gati, J. Fölling, S. Hunsmann, M. Cristiani, and M. K. Oberthaler. ‘Direct Observation of Tunneling and Nonlinear Self-Trapping in a Single Bosonic Josephson Junction’. *Phys. Rev. Lett.* **95**(1), 010402 (2005).
- [268] J. Javanainen and S. M. Yoo. ‘Quantum phase of a Bose-Einstein condensate with an arbitrary number of atoms’. *Phys. Rev. Lett.* **76**(2), 161–164 (1996).
- [269] J. Javanainen and M. Wilkens. ‘Phase and Phase Diffusion of a Split Bose-Einstein Condensate’. *Phys. Rev. Lett.* **78**(25), 4675–4678 (1997).
- [270] R. Jördens. ‘A Radio Frequency Source for the Preparation of Quantum States’. Master’s thesis, ETH Zürich (2006).
- [271] M. Ben Dahan, E. Peik, J. Reichel, Y. Castin, and C. Salomon. ‘Bloch oscillations of atoms in an optical potential’. *Phys. Rev. Lett.* **76**(24), 4508–4511 (1996).
- [272] O. Morsch, J. H. Müller, M. Cristiani, D. Ciampini, and E. Arimondo. ‘Bloch Oscillations and Mean-Field Effects of Bose-Einstein Condensates in 1D Optical Lattices’. *Phys. Rev. Lett.* **87**(14), 140402 (2001).
- [273] A. S. Sørensen and K. Mølmer. ‘Measurement Induced Entanglement and Quantum Computation with Atoms in Optical Cavities’. *Phys. Rev. Lett.* **91**(9), 097905 (2003).
- [274] A. J. Daley, P. O. Fedichev, and P. Zoller. ‘Single-atom cooling by superfluid immersion: A nondestructive method for qubits’. *Phys. Rev. A* **69**(2), 022306 (2004).
- [275] K. R. Brown, K. M. Dani, D. M. Stamper Kurn, and K. B. Whaley. ‘Deterministic optical Fock-state generation’. *Phys. Rev. A* **67**(4), 043818 (2003).
- [276] M. Greiner, O. Mandel, T. Esslinger, T. W. Hänsch, and I. Bloch. ‘Quantum phase transition from a superfluid to a Mott insulator in a gas of ultracold atoms’. *Nature (London)* **415**(6867), 39–44 (2002).
- [277] O. Mandel, M. Greiner, A. Widera, T. Rom, T. W. Hänsch, and I. Bloch. ‘Coherent Transport of Neutral Atoms in Spin-Dependent Optical Lattice Potentials’. *Phys. Rev. Lett.* **91**(1), 010407 (2003).

- [278] A. Widera, O. Mandel, M. Greiner, S. Kreim, T. W. Hansch, and I. Bloch. ‘Entanglement Interferometry for Precision Measurement of Atomic Scattering Properties’. *Phys. Rev. Lett.* **92**(16), 160406 (2004).
- [279] T. Pellizzari, S. A. Gardiner, J. I. Cirac, and P. Zoller. ‘Decoherence, Continuous Observation, and Quantum Computing: A Cavity QED Model’. *Phys. Rev. Lett.* **75**(21), 3788 (1995).

Publications related to this thesis

1. *Correlations and Counting Statistics of an Atom Laser*
Anton Öttl, Stephan Ritter, Michael Köhl, and Tilman Esslinger
Physical Review Letters **95**, 090404 (2005).
2. *Cavity QED detection of interfering matter waves*
Thomas Bourdel, Tobias Donner, Stephan Ritter, Anton Öttl, Michael Köhl, and
Tilman Esslinger
Physical Review A **73**, 043602 (2006).
3. *Hybrid Apparatus for Bose-Einstein condensation and cavity quantum
electrodynamics: Single atom detection in quantum degenerate gases*
Anton Öttl, Stephan Ritter, Michael Köhl, and Tilman Esslinger
Review of Scientific Instruments **77**, 063118 (2006).
4. *Time interval distributions of atoms in atomic beams*
Michael Köhl, Anton Öttl, Stephan Ritter, Tobias Donner, Thomas Bourdel, and
Tilman Esslinger
Applied Physics B: Lasers and Optics **86**, 391 (2006).
5. *Observing the Formation of Long-Range Order during Bose-Einstein
Condensation*
Stephan Ritter, Anton Öttl, Tobias Donner, Thomas Bourdel, Michael Köhl, and
Tilman Esslinger
Physical Review Letters **98**, 090402 (2007).
6. *Critical Behavior of a Trapped Interacting Bose gas*
Tobias Donner, Stephan Ritter, Thomas Bourdel, Anton Öttl, Michael Köhl, and
Tilman Esslinger
Science **315**, 1504 (2007).

Acknowledgements

The excellent circumstances under which I could carry out my doctorate were on no account natural. I was fortunate to have numerous colleagues, coworkers and friends who played an essential role in the completion of this work. I would like to use this opportunity to thank them:

Tilman Esslinger gave me the opportunity to pursue this PhD. He presented me with the idea for a great experimental setup, a large, empty lab, all necessary resources and had formed a great team. I cannot think of any better circumstances for a researcher. In addition, his friendly, bright and positive personality provides a superb atmosphere, for which I would especially like to thank him. His continuous flow of new scientific ideas has been much inspiration.

Michael Köhl provided the experimental and theoretical expertise and assistance necessary for setting up and running the apparatus, and he was vital for the success of the experiments. Even though he was supervising two laboratories, he worked on both projects with such commitment that I could count on his full attention and excellent support at all times.

Anton ‘Toni’ Öttl, my fellow PhD student, shared the will to build a setup that will last for long. His designs of our apparatus are famous for their sturdiness and style. His true interest in physical insight and his vitality in and outside the lab are enriching.

Tobias Donner and Ferdinand Brennecke joined the experiment two and one year ago, respectively. Discussing and working with them is a great pleasure and enrichment. I am thankful and happy to be part of such a team. Undoubtedly, they will continue with the setup in the best possible way. Thomas Bourdel contributed to the experiment as a postdoc for nearly two years and brought much insight, especially on the theoretical aspects of the experiment.

Henning Moritz and Thilo Stöferle were part of the Quantum Optics group in Zurich from the first days on and paved the way for us. I am indebted to them for their generous helpfulness and for introducing me to the physics of atomic gases in optical lattices.

Since I started my doctorate, the team has grown a lot. Kenneth Günter, Niels Strohmeier, Robert Jördens, Bruno Zimmermann and Torben Müller are the current PhD students working on other projects. They are very much responsible for the lively atmosphere in the group and have helped me to think outside the box, in physical and non-physical matters. The same is true for the former postdocs Christian Schori and Yosuke Takasu.

Alexander Frank has provided us with very professional electronic equipment as well as deeper insight into the wizardry of electronic design. Jean-Pierre Stucki and Paul Herrmann helped in numerous ways in setting up the lab, and Peter Brühwiler and his team at the mechanical workshop of the ETH Physics Department did a great job in building all the bits and pieces so vital to our apparatus. Stimulating discussions with Wolfgang Belzig, Christoph Bruder, Yuri Kagan, Anatoly Kuklov, Klaus Mølmer, Helmut Ritsch and many others have contributed to my understanding and the direction of our experiments.

Veronica Bürgisser takes care of all administrative work in the group in an impressively well-organized way. Her support in various fields gave me the freedom to concentrate on physics rather than paperwork.

Finally, I would like to thank my parents and my brother Henning for who and what they are and for all they have done for me.

Curriculum Vitae

Stephan Ritter

Born: 17 January, 1975 in Itzehoe, Germany

Nationality: german

Education

- 2002 – 2007 Graduate studies at the ETH Zürich, Switzerland
under the supervision of Prof. Dr. T. Esslinger
PhD thesis: *‘Probing Coherence During Bose-Einstein Condensation’*
- 2001 – 2002 Diploma Thesis in the group of Prof. Dr. A. Hemmerich
at the Institute of Laser-Physics, University of Hamburg, Germany
*‘Entwicklung präziser Laserlichtquellen für Experimente mit
ultrakalten Calciumatomen’*
- 1999 – 2001 Graduate studies in physics at the University of Hamburg
- 1998 – 1999 Exchange student, Imperial College London, England
- 1996 – 1998 Undergraduate studies in physics at the University of Hamburg
- 1994 – 1995 Civil service
- 1985 – 1994 High school, Otto-Hahn-Gymnasium in Geesthacht, Germany
- 1981 – 1985 Elementary school in Geesthacht, Germany

Awards

- 1995 – 2002 Scholar of the German National Merit Foundation
 (“Studienstiftung des deutschen Volkes”)
- 1998 – 1999 ERASMUS scholarship at Imperial College, London

Teaching

- 2002 – 2003 Physics I & II for chemistry and biology students
- 2003 – 2004 Introductory lab courses in experimental physics
- 2004 – 2005 Physics I & II for chemistry and biology students
- 2005 – 2007 Physics I – III for physics students

